Crystals and nanoparticles of a BODIPY derivative : spectroscopy and microfluidic precipitation

Yuanyuan Liao

EDSP
École Doctorale
Sciences Pratiques

ENSC-(n° d'ordre)

ENS CACHAN

THESE DE DOCTORAT
DE L'ECOLE NORMALE SUPERIEURE DE CACHAN

Présentée par

YuanYuan LIAO

pour obtenir le grade de

DOCTEUR DE L'ECOLE NORMALE SUPERIEURE DE CACHAN

Domaine :
CHIMIE

Sujet de la thèse :

Crystals and Nanoparticles of a BODIPY derivative: spectroscopy and microfluidic precipitation.

Thèse présentée et soutenue à Cachan le 12 Novembre 2013 devant le jury composé de :

Suzanne Fery-Forgues	Directeur de Recherches	Rapporteur (ITAV-Toulouse)
Cyril Aymonier	Chargé de recherche	Rapporteur (ICMCB, Bordeaux)
Patrick Baldeck	Directeur de Recherches	Examinateur (ENS-Lyon)
Sandrine Lacombe	Maitre de conférences	Examinateur (Université Paris Sud 11)
Robert B. Pansu	Directeur de Recherches	Directeur de thèse (ENS-Cachan)
Valérie Génot	Maitre de conférences	Co-Encadrant de thèse (ENS-Cachan)

Laboratoire de photophysique et photochimie supramoléculaires et macromoléculaires
PPSM-UMR 8531
Ecole Normale Superieure de CACHAN
61, avenue du Président Wilson, 94235 CACHAN CE

Acknowledgement

This dissertation bears only one name, however it was accomplished under many people's help. This work would not have been possible without the collaboration, help, and support of many people.

Foremost, I would like to give my deepest gratitude to my supervisor Dr. Robert Pansu and also my co-supervisor, Dr. Valérie Génot, for giving me the opportunity to do this research in ENS Cachan. They are the one who are always available for questions, and always ready to give advice and to help in overcoming difficulties either in the study or in life during my staying in France. And they inspired me to do my best in performing experiments, preparing talks and writing report, also offer me many opportunities to participate conference and summer school. It is their intellectual support, encouragement, enthusiasm, and intelligent guidance, which made this dissertation possible.

I would like to thank the past and present members of the PPSM. I would like to express my heartfelt thanks to Dr. Thanh Truc Vu and Dr. Rachel Méallet-Renault, who help me get familiar with the lab, taught me hand by hand during my internship of master. They are always warmhearted to help me out of the difficulty, and for assisting me every aspect of life in the last three years.

I really appreciate to Dr Gilles Clavier for this amazing molecule Adambodipy and the guidance for TDDFT calculation, also for taking the time to read my dissertation and useful discussion.

I am very grateful to Jean-frederic Audibert, who was very experienced in microscope and photonic and he explained a lot about the time-resolved single photon counting spectroscopy and the AFM to new Ph. D student like me, great thanks to his useful discussion, patience and inspiration. I am also thankful to Jean-Pierre Lefévre for his patient training in microfluidic fabrication. Also I would like to give great thanks to Dr. Jean-Pierre Lemaistre for his kind help and guidance for our exciton theory, and to Arnaud Brosseau for his kind help in time-resolved spectroscopy.

I would like to extend my gratitude to my committee: Dr. Suzanne Fery-Forgues, Dr. Cyril Aymonier, Dr. Patrice Baldeck, Dr. Keitaro Nakatani, Dr. Sandrine Lacombe for taking the time to read my dissertation and useful discussion.

I would like to thank Prof. Keitaro Nakatani, Prof. Jacques Delaire, Nicolas Bogliotti, Rémi Métivier, Prof. Pierre Audebert, Valérie Alain-Rizzo, Clémence Allain,

Fabien Miomandre for their help in my work; to Jacky Fromont for handling my computer problems; to Andrée Husson and Christian Jean-Baptiste for their administrative help. Also thanks to Dr. Ludivine Houel-Renault who taught me how to use microtome and Pascal Retailleau who provide useful X-ray diffraction data for our crystal.

I also learned much from the international program SERP-Chem during a two-years stay in Paris as a master student; during this wonderful experience, I met outstanding scientists and friends from France, Poland and Italy. I would like to give my sincere thanks to my Prof. Jun Yao for the recommendation and Prof. Sandrine Lacombe for accepting me in this program.

I appreciate the help from the members of PPSM: Yanhua Yu, Yang Si, Yuan Li, for their friendship and support. Djibril Faye, Laura Jonusauskaite, Issa Samb, Olivier Noël, Sandrine Peyrat, Ni Ha Nguyen, Karima Ouhenia, Jia Su, Jonathan Piard, Chloé Grazon, Eva Jullien, Jérémy Malinge, Cassandre Quinton, Johan Saba, who made it all so much more fun at work and beyond. I extend my thanks to all the colleagues in my office, such as Haitao Zhang, Olivier Francais, Bruno Le Pioufle, Feriel Hamdi, Wei Wang for their nice friendship and support and the best crepe party in the lab.

Here in the Paris as well as in France, I got to know many people from the "Chinese-speaking community", with whom I had pleasant time on various occasions. I wish to convey my thanks to Qinggele Li, Feifei Shi, Yao Wang, Xiao Wu, Zhenzhen Yi, Jiayi Gao, Zongwei Tang, Fangzhou Zhang, Zhikai Xu, Yibin Ruan, Xiaoqian Xu, He Huang, Lue Huang, Zhe Sun, Fan Yang, Yingying Chen, Xiaoju Ni for their companion and valuable friendship. Keeping a close contact with you, guys, you help me a lot in the daily life and make me never feel homesick while living abroad.

Lastly but certainly not least, At last, I would like to thank my parents for their continuous support and encouragement.

The list of teachers, colleagues and friends who should be gratefully acknowledged for their advice and encouragement would be too long, during all my study and internship, there are so many people help a lot and remarkable.

Content

List of Symbol and Abbreviation

$\epsilon(v)$	extinction coefficient
ϕ	quantum yield
∇	del operator
∇c	concentration gradient
$\nabla\varepsilon$	Franck-Condon bandwidth
$\nabla\varepsilon'$	individual vibronic bandwidth
$\Delta\varepsilon$	exciton splitting term
ε_o	permittivity of free space
ΔW	difference in Van der Waals energy
2U	exciton bandwidth
μ	viscosity
μ-TAS	micro-total-analysis systems
$\vec{\mu}$	dipole moment operator
$\vec{\mu}_{di}$	transition dipole moment operator
ψ_e	molecular excited eigenstate
ψ_g	molecular ground eigenstate
ψ_{AO}	electronic states in an atom
ψ_{MO}	electronic states in a molecule
ψ_E^+	symmetric coupling
ψ_E^-	anti-symmetric coupling
ρ	fluid density
$\rho(\vec{r})$	electron density
a	particle size, radius
a_0	diffusion length of exciton
A	Absorbance, (§ 5.1.3) cross sectional area
AFM	Atomic force microscopy
BODIPY	4,4-Difluoro-4-bora-3a, 4a-diaza-s-indacene
c	speed of light
CMC	critical micelle concentration
CTACl	hexadecyltrimethylammonium chloride

d_Q	density of quenching sites
D	diffusion coefficient
DLS	dynamic light scattering
D_{ij}	Maxwell-Stefan binary diffusion coefficient
D_{W-E}	diffusion coefficient for water-ethanol binary system
e	charge of an electron
EET	electronic excitation energy transfer
EtOH	ethanol
E_E	energy of the excited state for a dimer
E_G	energy of the ground state for a dimer
f	oscillator strength
FLIM	fluorescence lifetime imaging
FONs	fluorescence organic nanoparticles
FRET	Förster resonance energy transfer
GTOs	Gaussian Type Orbitals
h	Planck's constant
H	Hamiltonian operator
HOMO	highest occupied molecular orbital
HF	Hartree Fock
I	light intensity
IC	internal conversion
ID	inner diameter of the channel
ISC	intersystem crossing
J	diffusion flux of the particles
J_{ij}	exciton transfer matrix element
k_B	Boltzmann constant
k_f	fluorescence rate
k_Q	quenching rate
LUMO	lowest unoccupied molecular orbital
L	most relevant length scale for flow
m_e	mass of an electron
M	transition moment for the singlet-singlet transition
M	total average molar mass of the mixture(kg/mol)

MEMS	microelectromechanical systems
MFD	micro-fluidic-device
MO	molecular orbital
N	Avogadro's number
n_0	refractive index
$n(a)$	number of quenching sites
NPs	nanoparticles
NCs	nanocrystals
OD	optical density, out side diameter of the channel (Chapter 4)
P	pressure
ΔP	pressure drop
PDMS	polydimethylsiloxane
P_w	wetted perimeter of the channel
Q	volumetric flow rate
Qc	center volumetric flow rate
Qs	side volumetric flow rate
Re	Reynolds number
s	refractive index of the substrate
SE	Schrödinger equation
STOs	Slater Type Orbitals
T	kinetic energy (§ 3.8.1.1), absolute temperature (§ 4.2.1)
$T_{max}(\lambda)$	maxima transmittance spectrum along wavelength
$T_{min}(\lambda)$	minima transmittance spectrum along wavelength
TDDFT	time-dependent density functional theory
THF	tetrahydrofuran
TRANES	time resolved area-normalized emission spectroscopy
UV	ultra-violet
$\boldsymbol{u}$	local velocity of the fluid
u_{avg}	average velocity of the flow
v	frequency
$v_{ext}(\vec{r})$.	external potential
$\tilde{v}$	energy in wavenumber
V_{ij}	dipole-dipole interaction operator

V_{ne}	nuclear-electron interaction
V_{ee}	electron-electron interaction
w	mass fraction
x, x_W, x_E	mole fraction, mole fraction of water, EtOH

Abstract

During this work, we have addressed two aspects of the properties of the fluorescent organic nanoparticles made of Adambodipy : their spectroscopy and their production with controlled sizes.

We have produced micro-crystals ($100x10x1\mu m^3$) by precipitation in solutions of low supersaturation. We have measured their spectroscopy under microscope in the range 380nm to 900nm. The microcrystals are birefringent and dichroic. By adding polarizers on a microscope we have measured their refraction index along the two neutral axes according to the method of Swanepoel.

We have measured the two absorption spectra along the neutral axis. We have calculated these absorption spectra using the model of the dipolar coupling for Frenkel excitons. The amplitude of this coupling has been estimated according to the classic model. Bu t for two particular pairs of the cell, we have compared this estimation with the value that can be deduced from the quantum calculation of a dimer by TDDFT.

The calculated spectra reproduce the dichroism, the spectral broadening of the absorption spectra but not the experimental peak shape probably because our micro-spectrophotometer levels up at high absorbance. The calculated fluorescence spectra predict a polarized transition along the b direction of the cell. The experiment shows two other red shifted bands. The study of their polarization, as well as their fluorescence lifetime allows us to attribute them to defects in the crystal. The spectra of the nanoparticles produced in the second part of this work are not those of crystals. We have been able to reproduce them theoretically by introducing an orientation disorder inside the periodic structure.

The 3D hydrodynamic focusing enables us to produce nanoparticles with controlled size without precipitation of Adambodipy on the wall. We have used the PDMS technology and we the moved to a glass tube approach, in order to avoid the diffusion of fluorescence into the PDMS. By adjusting the flow ratio between the inner organic solution of the dye and outer aqueous solution, we can control the size of the nanoparticle between 100nm and 300nm. The stability of the colloidal suspension is maintained by the surfactant CTACl below the CMC. Indeed above the CMC, the nanoparticles exist together with dyes dispersed in micelles.

We have simulated using COMSOL the precipitation of the nanoparticles. We have introduced in the calculation the hydrodynamic and mutual diffusion of water and ethanol, as well as the diffusion of the Adambodipy. From our studies of the solubility of Adambodipy in water/ethanol mixtures, we have obtained the saturation curve and we have built the supersaturation maps in the micro-device. We have used Fluorescence lifetime imaging microscopy to follow *in situ* the precipitation process. From the decay collected in different positions can be attributed to the coexistence of three species : the monomers, the nanoparticles and an intermediate species supposed to be the nuclei. The FLIM shows a precipitation in the diffusion area of the two solvents as well as a massive precipitation after a few hundred of millisecond. The FLIM images are very close to the COMSOL predictions.

Résumé

Pendant cette thèse nous avons travaillé sur deux aspects des nanoparticules organiques fluorescentes d'AdamBodipy : leur spectroscopie et leur production avec des tailles contrôlées.

La structure cristallographique des cristaux d'Adambodipy a été obtenue par diffraction-X. Nous avons produit des microcristaux ($100\times10\times1\mu m^3$) par précipitation dans des solutions de sursaturation faible. Nous avons mesuré leur spectroscopie sous microscope dans la gamme 380nm à 900nm. Les microcristaux sont biréfringents et dichroïques. Nous avons mesuré leur biréfringence en déterminant leurs indices de réfraction suivant les deux axes neutres par le méthode de Swanepoel.

Nous avons mesuré des spectres d'absorption suivant les axes neutres. Nous avons calculé ces spectres d'absorption en utilisant la théorie du couplage dipolaire pour les exciton de Frenkel. La valeur du couplage intermoléculaire a été estimée par le modèle classique. Mais pour deux paires particulaires de la maille nous avons comparé cette estimation classique du couplage avec la valeur qui peut être déduite du calcul quantique du dimère par TDDFT. L'ordre de grandeur est vérifié.

Le programme s'applique à des nanoparticules formées de N×N×N (N<11) mailles cristallines. Les spectres calculés reproduisent le dichroïsme, l'élargissement des spectres d'absorption, mais il apparaît que les spectres expérimentaux sont écrêtés par la faible dynamique de notre spectrophotomètre sous microscope. Le calcul du spectre de fluorescence prédit une bande polarisée selon la direction b de la maille. L'expérience en distingue deux autres décalée dans le rouge. L'étude de leur polarisation ainsi que de leur dynamique de fluorescence permet d'attribuer ces bandes rouges à des défauts dans la structure cristalline. Les spectres des nanoparticules produites dans la deuxième partie ne sont pas ceux de la forme cristalline. Nous avons pu reproduire ces spectres en introduisant un désordre d'orientation à l'intérieur la structure des N×N×N mailles.

La focalisation hydrodynamique 3D, nous a permis de produire des nanoparticules de taille contrôlée sans qu'il y ait précipitation de l'AdamBodipy sur les parois. En réglant le rapport des flux entre la solution organique de colorant et la solution aqueuse non solvant, nous avons pu ajuster la taille des nanoparticules entre 100 et 300nm. La stabilité colloïdale des nanoparticules est assurée par du CTACl en dessous de la CMC. En effet au dessus de la CMC les nanoparticules coexistent avec des micelles chargées en colorant.

Les spectroscopies d'absorption et de fluorescence des nanoparticules montrent qu'elles sont amorphes.

Nous avons simulé la précipitation des nanoparticules par COMSOL en introduisant une l'hydrodynamique de mélange par diffusion mutuelle de l'eau et de l'éthanol et de diffusion du colorant dans ce mélange. Nos études de la solubilité de l'Adambodipy dans des mélanges organiques/eau, nous ont permis de déterminer la loi de solubilité et d'obtenir des cartes de la super-saturation dans le microdispositif. Nous avons utilisé l'imagerie de fluorescence pour suivre le processus de précipitation. Les images obtenues sont semblables à celles calculées par COMSOL On observe une précipitation à l'interface entre les deux solvants ainsi qu'une précipitation en masse après un temps de résidence qui dépend du rapport des flux. Les déclins de fluorescence collectés en différents points du canal microfluidique peuvent être attribués à trois espèces : le monomère, la nanoparticule et une espèce intermédiaire, un germe.

General Introduction

Fluorescence nano-objects have attracted great attention for decades due to their potential applications in and labeling and sensing in the fields of bio-analysis[1,2], electronic device[3], and also photonic[4].

Fluorescence nanoparticles are of great interest because they present much brighter optical properties due to the high local concentration of dyes in particle, but also due to the high sensitivity with respect to the increased surface-to-volume ratio compared to bulk materials.

Among the competitive nanoparticles, the pure organic nanoparticles are usually less toxic than quantum dots and better sensitivity than the dye-doped nanoparticles. However, compared to the inorganic nanoparticles (semiconductors and metals) that have been extensively investigated in various fields, the preparation method and characterization of nanoparticles of organic dyes have not yet drawn many attentions.

This work focused on the nanoparticles made of BODIPY (4-Difluoro-4-bora-3a, 4a-diaza-s-indacene derivative, which are interesting fluorophores due to their relatively large extinction coefficients (ε> 50,000) and high fluorescence quantum yields (ϕ>70%)[5]. Their properties are described and compared to the other well-known popular fluorescence organic molecules in Chapter 1. They are widely used in applications as laser dyes, biological labeling of DNA, proteins and lipids[6].

Among the BODIPY derivatives (with boron dipyrromethene), the aim of our research is to produce Adamantyl mesityl BODIPY (4,4-Difluoro-3,5-di-(adamantyl)-8-mesityl-4-bora-3a,4a-diaza-s-indacene) nanoparticles. The molecule was synthesized in our lab, with the bulky alkyl substituent (Adamantane group), the Adambodipy can limit the π-π stacking to overcome the fluorescence quenching in solid state, and also easy to crystallize. The basic spectroscopic properties of the molecule in solvent were presented in Chapter 2.

In the solid state, the optical properties depend on the molecular packing in the solid. The abilities to define the optical properties from the geometry of molecular packing in solid state and to tune the geometry from the fabrication methods represent

a quite important challenge. As Kasha[7] describe the effect of dimerization on the absorption spectra according to the different packing types of dimer, the Frenkel exciton theory[8] can be applied to solid state. The theoretical studies are suitable for organic crystals as their bonding are mainly weak Van der Waals interaction. Based on the crystallography information from X-ray diffraction on the large crystal, the theoretical model can be built on the molecular crystalline structure.

With the model we computed the optical properties of Adambodipy in nanoparticles and crystalline structure and compared them with results of emission polarizations and time resolved fluorescence experiments. We detailed the studies in Chapter 3.

On the other hand, a suitable nanoparticle preparation method that can well control the nano-precipitation process using microfluidic system was developed here. Thanks to the continuous mode with laminar flow, combined with the fluorescence spectroscopy and microscopy, we can study the kinetics.

After a general introduction in Chapter 1 on the most popular preparation methods reported in the literature, including the reprecipitation method, the design of the hydrodynamic microfluidic and the production of nanoparticles are detailed in the Chapter 4. Chapter 5 was dedicated to the experimental kinetic study using fluorescence lifetime imaging (FLIM) and its simulation using COMSOL® software.

Reference:

[1] Liu, J. S.; Wang, L.; Gao, F.; Li, Y. X.; Wei, Y. *"Novel fluorescent colloids as a DNA fluorescence probe."* Analytical and bioanalytical chemistry, **2003**, *377*, 346-349.

[2] Taylor, J. R.; Fang, M. M.; Nie, S. M. *"Probing specific sequences on single DNA molecules with bioconjugated fluorescent nanoparticles."* Anal Chem, **2000**, *72*, 1979-1986.

[3] Menard, E.; Meitl, M. A.; Sun, Y. G.; Park, J. U.; Shir, D. J. L.; Nam, Y. S.; Jeon, S.; Rogers, J. A. *"Micro- and nanopatterning techniques for organic electronic and optoelectronic systems."* Chem Rev, **2007**, *107*, 1117-1160.

[4] Zhang, Y.-Q.; Wang, J.-X.; Ji, Z.-Y.; Hu, W.-P.; Jiang, L.; Song, Y.-L.; Zhu, D.-B. *"Solid-state fluorescence enhancement of organic dyes by photonic crystals."* J Mater Chem, **2007**, *17*, 90-94.

[5] Bencini, A.; Bernardo, M. A.; Bianchi, A.; Fusi, V.; Giorgi, C.; Pina, F.; Valtancoli, B. *"Macrocyclic polyamines containing phenanthroline moieties - Fluorescent chemosensors for H+ and Zn2+ ions."* Eur J Inorg Chem, **1999**, 1911-1918.

[6] Burghart, A.; Kim, H. J.; Welch, M. B.; Thoresen, L. H.; Reibenspies, J.; Burgess, K.; Bergstrom, F.; Johansson, L. B. A. *"3,5-diaryl-4,4-difluoro-4-bora-3a,4a-diaza-s-indacene (BODIPY) dyes: Synthesis, spectroscopic, electrochemical, and structural properties."* J Org Chem, **1999**, *64*, 7813-7819.

[7] Kasha, M. *"Energy Transfer Mechanisms and the Molecular Exciton Model for Molecular Aggregates."* Radiat Res, **1963**, *178*, Av27-Av34.

[8] Knox, R. S. *"Theory of excitons."* Academic Press, **1963**.

Chapter 1. Introduction to fluorescence organic molecules and their solid state: crystalline, micro-, nano- particles

1.1. General introduction on the fluorescence of organic molecules

During the last few decades, there has been a remarkable growth in the use of fluorescence methodology in biotechnology and medical diagnostics[1]. The key characteristic of fluorescence detection is its high sensitivity. Fluorimetry may achieve limits of detection several orders of magnitude lower than most of other techniques. The limits of detection could be lower as 10^{-10}M for intensely fluorescent molecules, even could reach the ultimate limit of detection (a single molecule) when reducing the observed volume to 100μm×100μm×10μm. With these properties, fluorescence is widely used for the detection of trace constituents of biological and environmental samples, and is also used to detect non-fluorescent molecules that have been tagged by fluorescent labels (such as biological tissues and DNA sequencing[2]).

Excitation of a molecule doesn't automatically produce fluorescence, and most molecules exhibit very weak fluorescence. That makes it important to find intensely fluorescent organic molecules. Commonly used fluorescence compounds have emission with energies from UV to near infrared. Among them, blue is less used in biology because of confusion with the autofluorescence coming from the constituent of the cell (Tryptophan, NADH, flavine), also red ones have been used only comparatively recently with the development of silicon based detectors, while green and yellow fluorochromes are widely used in many fields especially in labeling and sensing. Near-infrared fluorochromes have been used mainly in bioluminescent imaging,[3] since the absorption coefficient of tissue is considerably smaller in the near infrared region. [4]

The fluorescence spectrum and intensity of a molecule also strongly depend on the environment, these include pH[5], temperature[6], the presence of oxidizing agents,[7] polarity or hydrogen-bonding ability of a solvent, to name just a few. Thus, the fluorescence characteristics of probe molecules may be used to make inferences about their immediate microenvironments.

According to the objective of the thesis, we will give a brief overview of the widely used organic fluorophore families which usually emit beyond 500 nm, which comprise fluoresceins, rhodamines, cyanines, and 4,4-difluoro-4-bora-3a, 4a-diaza-s-indacene (BODIPY) dyes.[8]

1.1.1. Fluoresceins

Fluorescein (3, 6 –dihydrospiro, [isobenzofuran − 1(3H), 9 − [9H]xanthen] -3-one, Dictionary of Organic Compound, 1996) sodium is a yellow dyes which is widely used as a fluorescence tracer for many applications[9] due to its ease of detection, relatively temperature insensitive, and relatively low susceptibility to adsorption. It has an excitation maximum at 494 nm, which is closed to the 488 nm spectral line of argon-ion laser, making it an important fluorophore for confocal scanning microscopy[10], also flow cytometry applications[11,12]. The quantum yield of this molecule is 0.92 at pH 9[13], which is relatively high, and it also has a high molar absorptivity. There is a wide array of fluorescein derivatives and they have found a lot of applications in biotechnology due to their high quantum yield and relatively good water solubiliy[14], although they have disadvantages due to their photochemical instability and pH sensitivity[15,16].

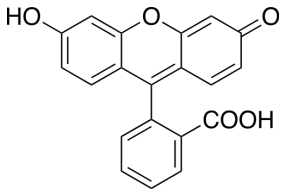

Figure 1. 1: Fluorescein

1.1.2. Rhodamines

Rhodamines (**Fig. 1.2**) is a diamino analogue of Fluorescein that exhibits spectral properties similar to those of Fluorescein.[17] It is well known as fluorescence tracer dye within water[18] to determine the rate and direction of flow. It was also widely used as laser dye and fluorescent compounds for labeling proteins and nucleic acids[19] in biology. Some readily available and inexpensive rhodamines, for instance, rhodamines 6G, B and 101 are especially photo- chemical stable, with high fluorescence quantum yields[20,21] (ϕ=41%-97%), and emit at 500-600 nm. Like fluorescein dyes, rhodamines dyes also exhibit small Stoke shift, around 20-30 nm[20], but they are in general far more stable than fluoresceins[22].

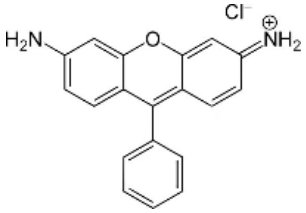

Figure 1. 2: Rhodamines

1.1.3. Cyanines

Cyanine is one of the most commonly used long-wavelength fluorophore with non-systematic name of a synthetic dye family belonging to polymethine group. Cyanine dyes have high extinction coefficient (>100000 $M^{-1}.cm^{-1}$)[23] but moderate quantum yield (usually ϕ<25%). They are usually long wavelength fluorophore with emission wavelength range about 500nm to 900 nm. It was characterized by good photostability for the usage in biolabelling applications and cell imaging[24,25]. Cyanine C3 and Cyanine 5 are the dyes that are universally used for DNA Bioschips[26].

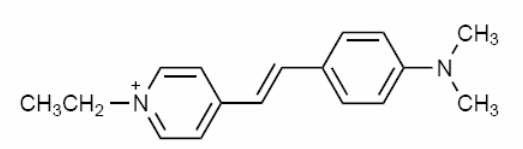

Figure 1. 3: Basic structure of cyanine dye

1.1.4 BODIPYs

4,4-Difluoro-4-bora-3a, 4a-diaza-s-indacene (abbreviated to BODIPY) dyes were first discovered in 1968 by Treibs and Kreuzer[18], and the name BODIPY was derived from BOron DIPYrromethenes. The core structure of the BODIPY fluorophore is based on the 4,4-difluoro-4-bora-3a, 4a-diaza-s-indacene platforms shown in **Fig. 1.4**. They are relatively insensitive to the polarity and pH of their environment and are reasonably stable under physiological conditions,[27] its absorption and emission characteristics do not change much by changing the solvent.

Only since 1980s, certain attentions were given to this discovery. Then these dyes have steadily increased in popularity over the past two decades and have been considered as substitute for those fluorophore families that where mentioned above, for their remarkable properties such as the large extinction coefficients (ε> 50,000), small stokes shifts and high quantum yield (ϕ>70%)[28], high photostability and chemical stability, sharp emission peak, also the insensitivity to solvent polarity and pH.

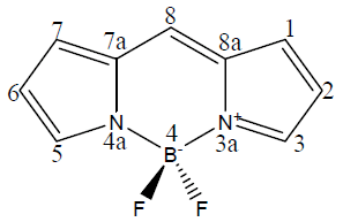

Figure 1. 4: BODIPY core structure.

Furthermore, the BODIPY platform offers outstanding synthetic versatility that enable small modifications to their structures tuning their fluorescence characteristics, for instance, when substituents that yield additional conjugation are added to the parent molecule, both absorption and emission spectra of the resulting derivatives can shift to significantly longer wavelengths, with emission maximum extend in 510-800 nm can be now possible obtained[29]. Such modifications to the BODIPY framework will lead to probes that can be used more effectively for imaging in living cells and whole organisms.[30]

Those properties enable BODIPY based fluorophore to be applied in many application, to produce highly fluorescent labels and probes[8,31], fluorescent switches[32,33], chemical sensor[34,35], two-photon exited probes[36,37]. It can replace fluoresceins for the design of assays that measure fluorescence polarization[38,39] because of its similarity in absorption and emission characteristic and long fluorescence lifetime.

1.2. State of art on solid-state fluorescence organic dyes

Solid-state fluorescent organic dyes with π–conjugated structure have attracted a considerable amount of attention due to applications in electroluminescence (EL) device, such as organic light-emitting diodes[40-42] and photoelectric conversion systems[43,44]. They have also been successfully used for sensing applications of explosives, ions[45] and DNA hybridization[46].

In spite of their numerous uses in analytical and material sciences, however, little is known about the influence of the molecular packing on their solid-state fluorescence properties. We shall see that the spectra can be calculated but the fluorescence yield is not predictable.

For many solid-state fluorescence organic dyes, the absorption and fluorescence properties are highly dependent on molecular orientation, and usually undergo a red-shifted emission and a loss of vibrational structure in comparison with the corresponding fluorescence spectra that are observed in solution[47,48]. Several fundamental researches on solid-state photochemistry are done to understand the correlation between solid-state fluorescence properties and molecular packing structures on the basis of the X-ray diffraction measurements[47,49]. The research helps to find the key points in designing new strong solid-state emissive fluorophores, and one of the most important, is to reduce the fluorescence quenching, that is due to the strong intermolecular $\pi - \pi$ interactions[50-52]. Theoretical studies

for the fluorescence properties of fluorescence organic dyes in various solid states are of a great importance for a better understanding of π -electron delocalization between molecules in supramolecular structure.

1.2.1. General introduction to fluorescence organic nanoparticles (FONs)

Recently, the nanotechnology has explored unique or improved properties dependent on the diameter, and the composition of nanometric structures. It is highly desirable to introduce novel fluorescent composite that possess several superior optical properties, such as a bright luminescence, high photo stability and a large Stokes shift.

For the detection of single particles, the key parameter is the brightness, which is the product of the molar extinction coefficient by the fluorescence quantum yield. In an assembly of fluorescent molecules, the brightness will scale with the number of dyes in the particle. In case of a strong coupling between the molecules the absorption spectrum can change and can be bigger than the sum of the constituting molecules[53].

The physico-chemical properties of organic dye nanoparticles considerably differ not only from those of individual molecules, but also from those of bulk crystals.

On the energy stand of point, the decrease in the particle size results in an increase in the fraction of the surface energy in its chemical potential[54,55]. In this respect, FONs can be interesting materials bridging the gaps between molecules and bulk materials. For biosensor application, the key property that makes them ideal for nanosensors is the increased surface to volume ratio of NPs, depending on surface reactions. As a result, it is very important to be able to accurately control size and size distributions within NPs suspensions.

In addition, the size of the nanoparticle will become smaller than that of the diffusion length of the exciton. The diffusion of the exciton toward the surface will make all those particles react to surface events. This leads to the realization of ultra bright sensors[56]. In the case of an exciton moving through FRET (Förster resonance energy transfer) between molecules dispersed in a matrix, the diffusion length of the exciton is the Förster distance[57,58]. In the case of a strong coupling between the molecules, the diffusion length can be few hundreds nanometers[59,60]

The optical properties of the organic dyes depend on their electronic transitions that reflect molecular geometries and can be tuned by elaborate molecular design strategies[54]. It

also helps the developments of the technology in many applications such as bioanalysis[61,62], photocatalysis[63], pharmacology[64], photonic[65] and microelectronics[66].

In this thesis, we have studied NPs made of pure organic molecules, while other structures also exist in competition, among which are quantum dots, fluorescent latex particles and dye-doped nanoparticles[67,68].

As we are wondering about the Adambodipy molecules, which are widely used as a type of biosensor, the key property that makes them ideal for nanosensors is the increased surface to volume ratio of NPs, depending on surface reactions. As a result, it is very important to be able to accurately control size and size distributions within NP suspensions.

1.2.1.1. Quantum dots

Quantum dots (QDs) are tiny, bright, photostable light-emitting particles on the nanometer scale, which composed of semiconductor materials. They bridge the gap between individual atoms and bulk semiconductor solids. It composed of atoms from groups II-VI, III-V, or IV-VI of the periodic table. Compared to fluorescence organic dyes and proteins, QDs have unique optical and electronic property such as the broad excitation spectra and size-tunable photoluminescence (PL) spectra with narrow emission bandwidths that span the visible spectrum.

QD can be threats to living cells, but are part of the fluorescent toolbox for biological application where they have shown their non toxicity [60]. But because of the public suspicion against heavy metals, they may not be a clinical solution for improving diagnosis or therapy.

1.2.1.2. FloDots

Another well-known type of FONs is Luminescent dye-doped silica nanoparticles (FloDots)[69], which have been developed for ultrasensitive bioanalysis and diagnosis. Dye molecules can be either luminescent organic or inorganic molecules dispersed within the silica matrix. Besides the facts that silica do no swell or change porosity with a change of pH, FloDots have many advantages over other luminescent probes such as the high emission intensity, and water solubility and efficient conjugation. It can be easily synthesized through reverse microemulsion method[70] or by Stöber method[71,72]. But the density of dyes in the FloDots is not high, thus the brightness of these particle and the mobility of the exciton are not expected to be high.

1.2.2. Method for preparation of crystal and nanoparticles made of pure dyes

The organic nanomaterial fabrication can be divided in to two types: (1) bottom-up and (2) top-down methods.[73,74] The bottom-up approach deals with the controlled assembly of small building blocks, such as atomic and molecular aggregates into larger structures (e.g. clusters, organic lattices, supermolecular structures and synthesized macromolecules.) This covers the popular synthetic methods like: chemical synthesis,[75] laser induced assembly,[76] self-assembly,[77] colloidal aggregation, 2-photon confocal processing[78,79], leading to the formation of particles, molecules, cosmetics, fuel additives, crystals, films, tubes, displays, atomic or molecular devices.

Whereas the top-down approach deals with the reduction in structure sizes of microscopic elements to the nanometer scale by applying lithography technique[80] (e.g., photolithography, UV laser,[81] electron or ion-beam. Scanning probe, optical near field) laser ablation[82] and mechanical techniques (e.g., cutting, etching, grinding, polishing etc.,) giving rise to electronic devices, chip masks, quantum well lasers, computer chips, MEMS, precision engineered surfaces, high quality optical mirrors. Mechanical techniques are in principle unsuitable for the production of narrow size distribution nanomaterials, because with the decrease in the particle size, it becomes increasingly difficult to use applied mechanical energy in the form of shearing and cavitation forces for particle milling without simultaneously inducing particle agglomeration[74]. A recent development in Laser ablation technology may overcome such energy problem although an expensive short-pulse laser system is required[83,84].

1.2.2.1. Reprecipitation Method

There are several methods for the preparation of organic nanoparticles including evaporation, microemulsion[85,86] and solvent displacement methods.[74] Among the latest ones, the reprecipitation method would be one of the easiest, size-controllable and widely used method for the production of a colloidal dispersion of nanoparticles solution of the target dye compound. This method was first reported by Nakanishi and co-workers in 1992[87,88]. They demonstrated the possibility to produce nanoparticles with sizes under 100 nm dispersed in water.[89] Since then, this method has been widely used in nanoparticle preparation, especially to control the size, shape of the resulting organic nanocrystals and dispersity in a medium by varying the condition of reprecipitation[90-92]. This includes the reprecipitation during the sol-

gel phase transition where both the change in solubility and in viscosity are used to reduce the size of the nanocrystals.[93]

Reprecipitation methods include "Routine Reprecipitation Method", "Supercritical Reprecipitation Method", "Reprecipitation-Microwave Irradiation Method" and also "Inverse Reprecipitation Method" [81,82]. In a Routine Reprecipitation Method, a rapid mixing of a small amount of the concentrated dye solution (namely, the target dye compound dissolved in a "good" solvent) with an excess of a "poor" solvent was achieved at a constant temperature.

One of the most popular and simple reprecipitation method used in fluid phase, is to obtain colloidal dispersions of nano-particles by pouring a saturated solution into a non-solvent, which has been used for a long time[94]. Most of the time, water is used as the non-solvent in which the BODIPY derivative is weakly soluble. And the nano- or microcrystals are formed immediately after combining the solutions. The nanocrystal size can be controlled by varying the concentration of solution, temperature, use of surfactant and mixing methodology[95]. However, it is difficult to control the reaction conditions precisely on a large scale in a liquid-phase synthesis. There is a need for using micro-fluidic-reactor-based synthetic methods where a better control of a defined size, shape, and crystal structure without recourse to multipurification steps[96].

1.2.3. Methods of nanoparticle stabilization

Nanoparticles in solution present typical colloidal systems consisting of a continuous phase (solvent) and a dispersed phase (NPs). They experience strong van der Waals attraction, which make the particle dispersion unstable and particles intend to aggregate. So far, one of the most important goals is to raise the stability of nanoparticles during storage and transportation. For nanoparticles to remain well and stably dispersed in liquid dispersion, a stabilizing repulsive force must be present between two particles to counteract the attraction and prevent particle aggregation. This repulsive force can be either electrostatic or steric[97].

To achieve sufficient interparticle separation, the method could be the coating of the nanoparticle with ionic compounds in order to increase electrostatic repulsion, or coating them with large molecules, such as polymers or surfactants. The long chain hydrocarbons in polymers or surfactants greatly increase the steric repulsion when particles get closer, efficiently preventing them from aggregation.[98]

Various stabilizers are used in many applications, they can be low-molecular organic compounds such as carbonic acids, alcohols, amides. Or they can be neural polymers including gelatin, gum Arabic, agar-agar, starch, cellulose[99]. We have chosen small cationic surfactants as stabilizers because of their high solubility in water. This allows a fast equilibrium of the surfactant between the surface of the nanoparticle and the solvent and a fast equilibrium of the surfactant among nanoparticles[100]. Thus if the stability can be achieved, it will be independent of the preparation history of the sample.

1.2.4. Organic dyes in surfactant micelles.

Surfactants mainly consisting of a non-polar, hydrophobic tail and a polar, hydrophilic head group, in which the hydrophobic tail is usually a branched or linear long-chain hydrocarbon residue with a chain length in the range of 8-18 carbon atoms[101].

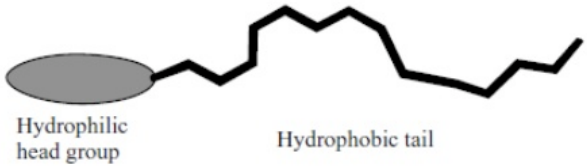

Figure 1. 5: A typical illustration of a surfactant molecule[102].

With this typical structure, when surfactants are dissolved in water at low concentration, they accumulate at the surface and orient themselves with the polar, hydrophilic head groups interacting with the water and with the hydrophobic tails removed from the aqueous system. So the surfactants disrupt the cohesive forces of water molecules at the surface and thus lower the surface tension.

One important characteristic of surfactant is their tendency to form aggregate, also named micelle in the solution, since surfactant molecules behave very differently when present as micelle or as monomer. Only monomers contribute to surface and interfacial tension lowering and dynamic phenomena[102]. An illustration of a micelle's structure is given in **Fig. 1. 6**. The concentration at which micelles start to form is called the critical micelle concentration, or CMC, and at such concentration the surface becomes completely loaded with surfactant, thus it is also the highest concentration value of surfactant monomer, regardless of the amount of surfactant added to the solution.

Many physical properties of surfactant are depends on the concentration, and will have abrupt changes above this critical concentration, which is shown in **Fig. 1.7**

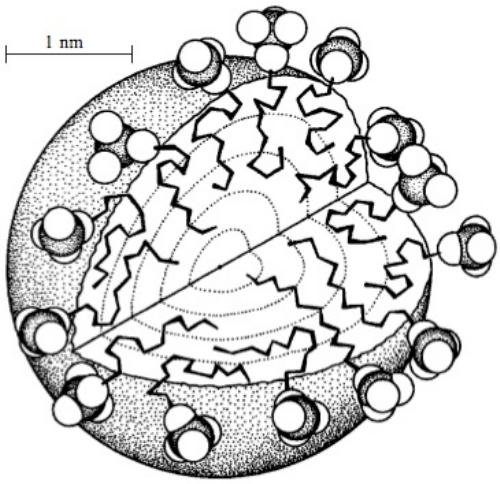

Figure 1. 6: An typical illustration of a spherical micelle (dodecyl sulfate)[102].

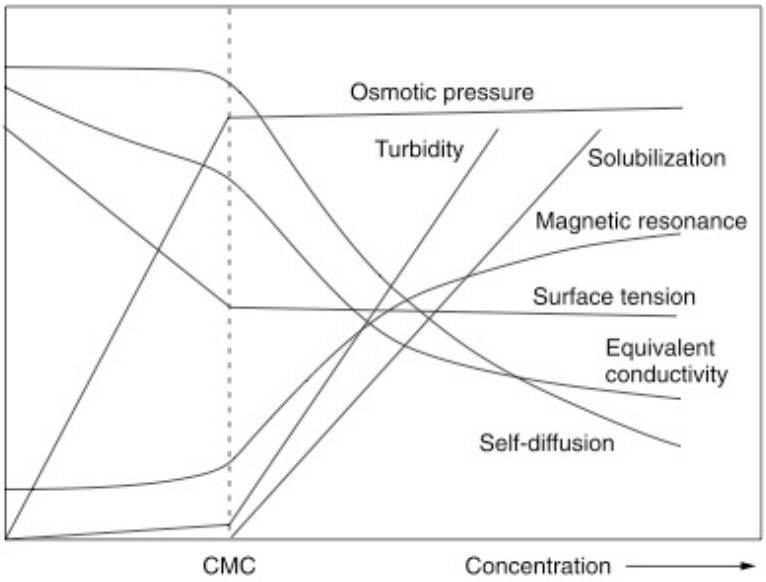

Figure 1. 7: Physico-chemical changes around the critical micelle concentration (CMC) dependence of a wide range of concentration[103].

Dye molecules can be dissolved as monomer in micelles[104]. We have thus chosen to use the surfactant at concentration lower than the CMC. We expect that, because of the hydrophobic nature of the surface of the FON, surfactant molecules will be adsorbed at their surface forming pre-micellar aggregates.

CTACl (hexadecyltrimethylammonium chloride) was used here as surfactant for Adambodipy nanoparticle samples, and the chemical structure is shown as follow:

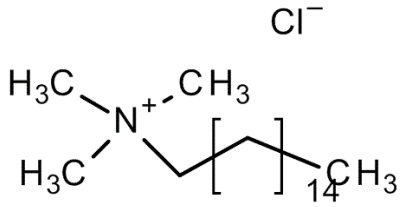

Figure 1. 8: CTACl (hexadecyltrimethylammonium chloride)

In order to stabilize the nanoparticle suspension while reducing the effects of surfactant, the value of concentration is very important and always kept below CMC. CMC depends on chemical structure of the surfactant, and according to the list of CMC values of some selected surfactants at 25 degrees[102], the CMC is 1.47×10^{-3} mol/L for CTACl.

The CMC of CTACl has been measured by monitoring the change is the absorbance of crystal violet as a function of surfactant concentration that gives a value of $1.0\pm0.3\times10^{-3}$ mol/L. [105] It has also been measured through conductivity and gave a value of 1.47×10^{-3} mol/L[106].

In the thesis, we have used a concentration of 10^{-3}mol/L except indicated otherwise (**§ 4.2.3**).

1.3. State of the arts of microfluidic technology

Micro-fluidics was initially developed as a part of microelectromechanical systems (MEMS), which in turn used the established technologies and infrastructure of microelectronics[107]. Then the new fluid phenomena that is not possible in traditional device attracted researchers in many field, etc. chemical synthesis, biosensing (biological analysis), drug discovery, basic science and a broad range of applications[108,109].

As the microfluidics is defined as fluid flow with the scale in the range 10-1000μm[110], the fundamental physics of fluid flow in microfluidics is largely identical to macroscale fluid dynamics. And one of the characteristics of microfluidics is the large surface area-to-volume ratio compared to the typical macro flow system. Thus, such systems are dominated more by interactions of the fluid with the channel surfaces and the viscous interactions with the surfaces cause very large pressure drops for even modest flow velocities. According to these surface forces, most flows in microfluidics are laminar[110]. In order to take the main advantages of microfluidics, analytical chemists, biochemists and chemical engineers, for

years working in the field of surface science, came to microfluidics to take advantage of the new effect and better performance[107]. But the scale is large enough compared to all the molecules in the system, and the continuum flow assumptions are valid.

The micro-fluidic device demonstrates its ability to achieve rapid diffusion with the cross-sectional dimensions on the order of 10-100 μm[111], able of short diffusive mixing time less than 10μs, and predictable fluidic dynamics. This allows the progress of chemical reactions to be followed and controlled in a few milliseconds after initiating the mixing[112]. We have been interested by microfluidic since it has allowed us to produce very small inner flow and thus a rapid mixing. But at the same time, the laminar flow is maintained, that allows a good reproducibility and an easy modeling[107].

Also micro-fluidic devices are designed to manipulate fluids in microchannels with reduced consumption and efficient heat and mass transfer due to the high surface- area-to-volume ratios, so as to have better control of the synthesis conditions and parameters.

Furthermore, microfluidics has a great potential advantage to approach for chemical analysis, synthesis by combining processes such as mixing, separation[113], reaction and also detection in one single system.[114] It has been connected to several spectroscopic probes such as FTIR[115] and NMR[116] in order to reach the spectroscopy of intermediate states in reactions. Combining a microfluidic device with fluorescence lifetime imaging (FLIM) functions as "labs-on-a-chip", builds up a technology to follow the kinetic of a number of physical processes, such as concentration diffusion[117], chemical reaction[114], molecular assembly[118]. The fluorescence time-resolved techniques could provide the appropriate lifetime information to map the molecule's reactions with its surroundings, as the lifetime is sensitive to pH changes[119], Calcium[120], diffusion[121], quenching[122] and also conformation changes[123].

Valérie Génot and Serge Desportes have been pioneers in the development of a microfluidic device for the production of FON by precipitation. They have shown that the size of the rubrene nanoparticle could be controlled by controlling the flow ratio between the good solvent and the non solvent [94]. Most of the time, water is used as the non-solvent in which the BODIPY derivative is weakly soluble. And the nano- or microcrystals are formed immediately after combining the solutions. The nanocrystal size can be controlled by varying the concentration of solution, temperature, use of surfactant and mixing methodology[95]. However, it is difficult to control the reaction conditions precisely on a large scale in a liquid-phase synthesis. There is a need for using micro-fluidic-reactor-based synthetic methods

where a better control of a defined size, shape, and crystal structure without recourse to multipurification steps[96].

In spite of the conventional application fields as mentioned, there are also novel use of microfluidics for distributed energy supply, distributed thermal management, and chemical production. It shows the future trend of nanotechnology.

Reference

[1] R.Lakowicz, J. *"Principles of Fluorescence Spectroscopy."* Third Edition ed.; Springer, **2006**; *Vol*. 1.

[2] Proudnikov, D.; Mirzabekov, A. *"Chemical methods of DNA and RNA fluorescent labeling."* Nucleic Acids Res, **1996**, *24*, 4535-4542.

[3] Rost, F. W. D. *"Fluorescence Microscopy. I."* Cambridge University Press, **1995**; *Vol*. 2.

[4] Grosenick, D.; Wabnitz, H.; Rinneberg, H. H.; Moesta, K. T.; Schlag, P. M. *"Development of a time-domain optical mammograph and first in vivo applications."* Appl Optics, **1999**, *38*, 2927-2943.

[5] Boens, N.; Qin, W. W.; Basaric, N.; Orte, A.; Talavera, E. M.; Alvarez-Pez, J. M. *"Photophysics of the fluorescent pH indicator BCECF."* J Phys Chem A, **2006**, *110*, 9334-9343.

[6] Barilero, T.; Le Saux, T.; Gosse, C.; Jullien, L. *"Fluorescent Thermometers for Dual-Emission-Wavelength Measurements: Molecular Engineering and Application to Thermal Imaging in a Microsystem."* Anal Chem, **2009**, *81*, 7988-8000.

[7] Naguib, Y. M. A. *"A fluorometric method for measurement of oxygen radical-scavenging activity of water-soluble antioxidants."* Anal Biochem, **2000**, *284*, 93-98.

[8] Sameiro, M.; Goncalves, T. *"Fluorescent Labeling of Biomolecules with Organic Probes."* Chem Rev, **2009**, *109*, 190-212.

[9] Chua, L. H. C.; Robertson, A. P.; Yee, W. K.; Shuy, E. B.; Lo, E. Y. M.; Lim, T. T.; Tan, S. K. *"Use of fluorescein as a ground water tracer in brackish water aquifers."* Ground Water, **2007**, *45*, 85-88.

[10] Wells, S. J., I.;: Fluorescent Labels for Confocal Microscopy. In *Three-Dimensional Confocal Microscopy: Volume Investigation of Biological Specimens*; Academic Press, 1994; pp 101-129.

[11] Sahagun, G.; Moore, S. A.; Fabry, Z.; Schelper, R. L.; Hart, M. N. *"Purification of Murine Endothelial-Cell Cultures by Flow-Cytometry Using Fluorescein-Labeled Griffonia Simplicifolia Agglutinin."* Am J Pathol, **1989**, *134*, 1227-1232.

[12] Makrigiorgos, G. M.; Kassis, A. I.; Mahmood, A.; Bump, E. A.; Savvides, P. *"Novel fluorescein-based flow-cytometric method for detection of lipid peroxidation."* Free Radical Bio Med, **1997**, *22*, 93-100.

[13] Mottram, L. F. B., S; Kovel, R. E.; Peterson, B. R. *"The Pennsylvania Green Fluorophore: A Hybrid of Oregon Green and Tokyo Green for the Construction of Hydrophobic and pH-Insensitive Molecular Probes."* Org. Lett. , **2006**, *8*, 581-584.

[14] Kasten, F. H.: Introduction to Fluorescent Probes: Properties, History and Applications. In *Fluorescent and Luminescent Probes for Biological Activity: A Practical Guide to Technology for Quantitative Real-Time Analysis*; Academic Press, 1999; pp 17-39.

[15] Smith, S. A.; Pretorius, W. A. *"The conservative behaviour of fluorescein."* Water Sa, **2002**, *28*, 403-406.

[16] Zhu, H.; Derksen, R. C.; Krause, C. R.; Fox, R. D.; Brazee, R. D.; Ozkan, H. E. *"Fluorescent intensity of dye solutions under different pH conditions."* Am Soc Test Mater, **2006**, *1470*, 191-197.

[17] Leytus, S. P. M., L. L.; Mangel, W. F.;. *"Rhodamine-based compounds as fluorogenic substrates for serine proteinases."* Biochem J., **1983**, *209*, 299-307.

[18] Smart, P. L. L., M. S.;. *"An Evaluation of Some Fluorescent Dyes for Water Tracing."* Water Resources Research, **1977**, *13*, 15-33.

[19] Boyarskiy, V. P.; Belov, V. N.; Medda, R.; Hein, B.; Bossi, M.; Hell, S. W. *"Photostable, Amino Reactive and Water-Soluble Fluorescent Labels Based on Sulfonated Rhodamine with a Rigidized Xanthene Fragment."* Chemistry – A European Journal, **2008**, *14*, 1784-1792.

[20] Sauer, M.; Han, K. T.; Müller, R.; Nord, S.; Schulz, A.; Seeger, S.; Wolfrum, J.; Arden-Jacob, J.; Deltau, G.; Marx, N. J.; Zander, C.; Drexhage, K. H. *"New fluorescent dyes in the red region for biodiagnostics."* J Fluoresc, **1995**, *5*, 247-261.

[21] Karstens, T.; Kobs, K. *"Rhodamine B and rhodamine 101 as reference substances for fluorescence quantum yield measurements."* The Journal of Physical Chemistry, **1980**, *84*, 1871-1872.

[22] Davidson, R. S.; Hilchenbach, M. M. *"THE USE OF FLUORESCENT PROBES IN IMMUNOCHEMISTRY*."* Photochem Photobiol, **1990**, *52*, 431-438.

[23] Ernst, L. A.; Gupta, R. K.; Mujumdar, R. B.; Waggoner, A. S. *"Cyanine dye labeling reagents for sulfhydryl groups."* Cytometry, **1989**, *10*, 3-10.

[24] Escobedo, J. O.; Rusin, O.; Lim, S.; Strongin, R. M. *"NIR dyes for bioimaging applications."* Curr Opin Chem Biol, **2010**, *14*, 64-70.

[25] Gadjev, N. I.; Deligeorgiev, T. G.; Kim, S. H. *"Preparation of monomethine cyanine dyes as noncovalent labels for nucleic acids."* Dyes Pigments, **1999**, *40*, 181-186.

[26] Redon, R. F., T.; CarterC, N. P.;. *"Comparative Genomic Hybridization: DNA labeling, hybridization and detection."* Methods Mol Biol. , **2009**, 267-278.

[27] Xu, Z. C.; Yoon, J.; Spring, D. R. *"Fluorescent chemosensors for Zn2+."* Chem Soc Rev, **2010**, *39*, 1996-2006.

[28] Bencini, A.; Bernardo, M. A.; Bianchi, A.; Fusi, V.; Giorgi, C.; Pina, F.; Valtancoli, B. *"Macrocyclic polyamines containing phenanthroline moieties - Fluorescent chemosensors for H+ and Zn2+ ions."* Eur J Inorg Chem, **1999**, 1911-1918.

[29] Ulrich, G.; Ziessel, R.; Harriman, A. *"The Chemistry of Fluorescent Bodipy Dyes: Versatility Unsurpassed."* Angewandte Chemie International Edition, **2008**, *47*, 1184-1201.

[30] Loudet, A.; Burgess, K. *"BODIPY dyes and their derivatives: Syntheses and spectroscopic properties."* Chem Rev, **2007**, *107*, 4891-4932.

[31] Rostron, J. P.; Ulrich, G.; Retailleau, P.; Harriman, A.; Ziessel, R. *"Engineering of an electronically decoupled difluoroindacene-pyrene dyad possessing high affinity for DNA."* New J Chem, **2005**, *29*, 1241-1244.

[32] Shao, J.; Sun, H.; Guo, H.; Ji, S.; Zhao, J.; Wu, W.; Yuan, X.; Zhang, C.; James, T. D. *"A highly selective red-emitting FRET fluorescent molecular probe derived from BODIPY for the detection of cysteine and homocysteine: an experimental and theoretical study."* Chemical Science, **2012**, *3*, 1049-1061.

[33] Ragab, S. S.; Swaminathan, S.; Baker, J. D.; Raymo, F. M. *"Activation of BODIPY fluorescence by the photoinduced dealkylation of a pyridinium quencher."* Phys Chem Chem Phys, **2013**.

[34] Peng, X.; Du, J.; Fan, J.; Wang, J.; Wu, Y.; Zhao, J.; Sun, S.; Xu, T. *"A Selective Fluorescent Sensor for Imaging Cd2+ in Living Cells."* J Am Chem Soc, **2007**, *129*, 1500-1501.

[35] QI, X.; KIM, S. K.; JUN, E. J.; XU, L.; KIM; #160; Sung-Jin; YOON; #160; Juyoung. *"A New BODIPY Derivative Bearing Piperazine Group."* Korean Chemical Society, **2007**; *Vol*. 28.

[36] Zheng, Q.; He, G. S.; Prasad, P. N. *"A novel near IR two-photon absorbing chromophore: Optical limiting and stabilization performances at an optical communication wavelength."* Chemical Physics Letters, **2009**, *475*, 250-255.

[37] Atilgan, S.; Ozdemir, T.; Akkaya, E. U. *"A Sensitive and Selective Ratiometric Near IR Fluorescent Probe for Zinc Ions Based on the Distyryl−Bodipy Fluorophore."* Org Lett, **2008**, *10*, 4065-4067.

[38] Chen, C. S. C., W. N.; Zhou, M.; Arttamangkul, S.; Haugland, R. P.;. *"Probing the cathepsin D using a BODIPY FL-pepstatin A: applications in fluorescence polarization and microscopy."* J. Biochem. Biophys. Methods, **2000**, *42*, 137-151.

[39] Schade, S. Z.; Jolley, M. E.; Sarauer, B. J.; Simonson, L. G. *"BODIPY–α-Casein, a pH-Independent Protein Substrate for Protease Assays Using Fluorescence Polarization."* Anal Biochem, **1996**, *243*, 1-7.

[40] Tang, C. W.; VanSlyke, S. A. *"Organic electroluminescent diodes."* Appl Phys Lett, **1987**, *51*, 913-915.

[41] Shi, J.; Tang, C. W. *"Doped organic electroluminescent devices with improved stability."* Appl Phys Lett, **1997**, *70*, 1665-1667.

[42] Wong, K.-T.; Chien, Y.-Y.; Chen, R.-T.; Wang, C.-F.; Lin, Y.-T.; Chiang, H.-H.; Hsieh, P.-Y.; Wu, C.-C.; Chou, C. H.; Su, Y. O.; Lee, G.-H.; Peng, S.-M. *"Ter(9,9-diarylfluorene)s: Highly Efficient Blue Emitter with Promising Electrochemical and Thermal Stability."* J Am Chem Soc, **2002**, *124*, 11576-11577.

[43] Wang, Z.-S.; Li, F.-Y.; Huang, C.-H.; Wang, L.; Wei, M.; Jin, L.-P.; Li, N.-Q. *"Photoelectric Conversion Properties of Nanocrystalline TiO2 Electrodes Sensitized with Hemicyanine Derivatives."* The Journal of Physical Chemistry B, **2000**, *104*, 9676-9682.

[44] Ehret, A.; Stuhl, L.; Spitler, M. T. *"Spectral Sensitization of TiO2 Nanocrystalline Electrodes with Aggregated Cyanine Dyes."* The Journal of Physical Chemistry B, **2001**, *105*, 9960-9965.

[45] Sumner, J. P.; Aylott, J. W.; Monson, E.; Kopelman, R. *"A fluorescent PEBBLE nanosensor for intracellular free zinc."* Analyst, **2002**, *127*, 11-16.

[46] Hartmann, L.; Kumar, A.; Welker, M.; Fiore, A.; Julien-Rabant, C.; Gromova, M.; Bardet, M.; Reiss, P.; Baxter, P. N. W.; Chandezon, F.; Pansu, R. B. *"Quenching Dynamics in CdSe Nanoparticles: Surface-Induced Defects upon Dilution."* Acs Nano, **2012**, *6*, 9033-9041.

[47] Stevens, B. *"Some effects of molecular orientation on fluorescence emission and energy transfer in crystalline aromatic hydrocarbons."* Spectrochimica Acta, **1962**, *18*, 439-448.

[48] Sonoda, Y.; Kawanishi, Y.; Ikeda, T.; Goto, M.; Hayashi, S.; Yoshida, Y.; Tanigaki, N.; Yase, K. *"Fluorescence Spectra for the Microcrystals and Thin Films of trans,trans,trans-1,6-Diphenyl-1,3,5-hexatrienes."* The Journal of Physical Chemistry B, **2003**, *107*, 3376-3383.

[49] Langhals, H.; Potrawa, T.; Nöth, H.; Linti, G. *"The Influence of Packing Effects on the Solid-State Fluorescence of Diketopyrrolopyrroles."* Angewandte Chemie International Edition in English, **1989**, *28*, 478-480.

[50] Yoshida, K.; Ooyama, Y.; Miyazaki, H.; Watanabe, S. *"Heterocyclic quinol-type fluorophores. Part 1. Synthesis of new benzofurano[3,2-b]naphthoquinol derivatives and their photophysical properties in solution and in the crystalline state."* Journal of the Chemical Society, Perkin Transactions 2, **2002**, 700-707.

[51] Ooyama, Y.; Nakamura, T.; Yoshida, K. *"Heterocyclic quinol-type fluorophores. Synthesis of novel imidazoanthraquinol derivatives and their photophysical properties in benzene and in the crystalline state."* New Journal of Chemistry, **2005**, *29*, 447-456.

[52] Yeh, H.-C.; Wu, W.-C.; Wen, Y.-S.; Dai, D.-C.; Wang, J.-K.; Chen, C.-T. *"Derivative of α,β-Dicyanostilbene: Convenient Precursor for the Synthesis of Diphenylmaleimide Compounds, E−Z Isomerization, Crystal Structure, and Solid-State Fluorescence."* The Journal of Organic Chemistry, **2004**, *69*, 6455-6462.

[53] Würthner, F.; Kaiser, T. E.; Saha-Möller, C. R. *"J-Aggregates: From Serendipitous Discovery to Supramolecular Engineering of Functional Dye Materials."* Angewandte Chemie International Edition, **2011**, *50*, 3376-3410.

[54] Yao, H. *"Prospects for Organic Dye Nanoparticles."* Springer-Verlag **2010** pp 455.

[55] Gubin, S. P.; Koksharov, Y. A.; Khomutov, G. B.; Yurkov, G. Y. *"Magnetic nanoparticles: Preparation methods, structure and properties."* Usp Khim+, **2005**, *74*, 539-574.

[56] Thomas, S. W.; Joly, G. D.; Swager, T. M. *"Chemical Sensors Based on Amplifying Fluorescent Conjugated Polymers."* Chem Rev, **2007**, *107*, 1339-1386.

[57] Binder, F.; Calzaferri, G.; Gfeller, N. *"Dye molecules in zeolites as artificial antenna."* Solar Energy Materials and Solar Cells, **1995**, *38*, 175-186.

[58] Meallet-Renault, R.; Pansu, R.; Amigoni-Gerbier, S.; Larpent, C. *"Metal-chelating nanoparticles as selective fluorescent sensor for Cu2+."* Chem Commun, **2004**, 2344-2345.

[59] Simpson, O. *"Electronic Properties of Aromatic Hydrocarbons. III. Diffusion of Excitons."* Proceedings of the Royal Society of London. Series A. Mathematical and Physical Sciences, **1957**, *238*, 402-411.

[60] Dubuisson, E.; Badré, S.; Gautier Luneau, I.; Ulrich, G.; Lemaistre, J. P.; Pansu, R.; Ibanez, A. *"Elaboration, structure and fluorescence spectroscopy of iodophenyl-BODIPY crystals."* Dyes Pigments, **2013**, *96*, 296-303.

[61] Tapec, R. Z., X. J.; Tan, W. *"Development of organic dye-doped silica nanoparticles for bioanalysis and biosensors."* J Nanosci Nanotechnol., **2002**, *2*, 405-9.

[62] Ronit, F.; Bilha, W.; Itamar, W. *"Biomolecule/Nanoparticle Hybrid Systems for Bioanalysis and Nanomedicine."* American Chemical Society, **2012**; *Vol*. 1112. pp 1-31.

[63] Kim, H. Y.; Bjorklund, T. G.; Lim, S. H.; Bardeen, C. J. *"Spectroscopic and Photocatalytic Properties of Organic Tetracene Nanoparticles in Aqueous Solution."* Langmuir, **2003**, *19*, 3941-3946.

[64] He, X. D., J.; Wang, K.; Tan, W.; Lin, X.; He, C.;. *"A novel fluorescent label based on organic dye-doped silica nanoparticles for HepG liver cancer cell recognition."* J Nanosci Nanotechnol., **2004**, *4*, 585-9.

[65] Cordovilla, C.; Swager, T. M. *"Strain Release in Organic Photonic Nanoparticles for Protease Sensing."* J Am Chem Soc, **2012**, *134*, 6932-6935.

[66] Ozaydin-Ince, G.; Coclite, A. M.; Gleason, K. K. *"CVD of polymeric thin films: applications in sensors, biotechnology, microelectronics/organic electronics, microfluidics, MEMS, composites and membranes."* Reports on Progress in Physics, **2012**, *75*, 016501.

[67] Chan, W. C. W.; Nie, S. M. *"Quantum dot bioconjugates for ultrasensitive nonisotopic detection."* Science, **1998**, *281*, 2016-2018.

[68] Yang, J.; Sandoval, S.; Alfaro, J. G.; Aschemeyer, S.; Liberman, A.; Martin, D. T.; Makale, M.; Kummel, A. C.; Trogler, W. C. *"Red-luminescent europium (III) doped silica nanoshells: synthesis, characterization, and their interaction with HeLa cells."* Journal of biomedical optics, **2011**, *16*.

[69] Yao, G.; Wang, L.; Wu, Y. R.; Smith, J.; Xu, J. S.; Zhao, W. J.; Lee, E. J.; Tan, W. H. *"FloDots: luminescent nanoparticles."* Analytical and bioanalytical chemistry, **2006**, *385*, 518-524.

[70] Zhao, X. J.; Bagwe, R. P.; Tan, W. H. *"Development of organic-dye-doped silica nanoparticles in a reverse microemulsion."* Adv Mater, **2004**, *16*, 173-+.

[71] Tapec, R.; Zhao, X. J. J.; Tan, W. H. *"Development of organic dye-doped silica nanoparticles for bioanalysis and biosensors."* J Nanosci Nanotechno, **2002**, *2*, 405-409.

[72] Werner, S. A., F.;. *"Controlled Growth of Monodisperse Silica Spheres in the Micron Size Range."* J Colloid Interface Sci, **1968**, *26*, 62-69.

[73] Rotello, V. M. *"Nanoparticles : building blocks for nanotechnology."* Kluwer Academic/Plenum Publishers, **2004**.

[74] Horn, D.; Rieger, J. *"Organic nanoparticles in the aqueous phase - theory, experiment, and use."* Angew Chem Int Edit, **2001**, *40*, 4331-4361.

[75] Schmidt, H. *"Nanoparticles by chemical synthesis, processing to materials and innovative applications."* Appl Organomet Chem, **2001**, *15*, 331-343.

[76] Wang, J. B.; Yang, G. W.; Zhang, C. Y.; Zhong, X. L.; Ren, Z. H. A. *"Cubic-BN nanocrystals synthesis by pulsed laser induced liquid-solid interfacial reaction."* Chem Phys Lett, **2003**, *367*, 10-14.

[77] Rodriguez-Hernandez, J.; Checot, F.; Gnanou, Y.; Lecommandoux, S. *"Toward 'smart' nano-objects by self-assembly of block copolymers in solution."* Prog Polym Sci, **2005**, *30*, 691-724.

[78] Tribuzi, V.; Correa, D. S.; Avansi, W.; Ribeiro, C.; Longo, E.; Mendonca, C. R. *"Indirect doping of microstructures fabricated by two-photon polymerization with gold nanoparticles."* Opt Express, **2012**, *20*, 21107-13.

[79] Lin, C. T.; Fan, H.; Bouriau, M.; Liao, C. Y.; Lin, C. L.; Masclet, C.; Leon, J. C.; Chung, T. T.; Baldeck, P. L. *"Simulation and Correction of Angular Defects in Two-Photon Lithography."* J Photopolym Sci Tec, **2011**, *24*, 651-655.

[80] Haynes, C. L.; Van Duyne, R. P. *"Nanosphere lithography: A versatile nanofabrication tool for studies of size-dependent nanoparticle optics."* J Phys Chem B, **2001**, *105*, 5599-5611.

[81] Wachulak, P. W.; Capeluto, M. G.; Marconi, M. C.; Menoni, C. S.; Rocca, J. J. *"Patterning of nano-scale arrays by table-top extreme ultraviolet laser interferometric lithography."* Opt Express, **2007**, *15*, 3465-3469.

[82] Vitrant, G.; Zaiba, S.; Vineeth, B. Y.; Kouriba, T.; Ziane, O.; Stephan, O.; Bosson, J.; Baldeck, P. L. *"Obstructive micro diffracting structures as an alternative to plasmonics nano slits for making efficient microlenses."* Opt Express, **2012**, *20*, 26542-26547.

[83] Asahi, T.; Sugiyama, T.; Masuhara, H. *"Laser Fabrication and Spectroscopy of Organic Nanoparticles."* Accounts Chem Res, **2008**, *41*, 1790-1798.

[84] Yasukuni, R.; Asahi, T.; Sugiyama, T.; Masuhara, H.; Sliwa, M.; Hofkens, J.; Schryver, F. C.; Auweraer, M.; Herrmann, A.; Müllen, K. *"Fabrication of fluorescent nanoparticles of dendronized perylenediimide by laser ablation in water."* Appl. Phys. A, **2008**, *93*, 5-9.

[85] Debuigne, F.; Jeunieau, L.; Wiame, M.; Nagy, J. B. *"Synthesis of organic nanoparticles in different W/O microemulsions."* Langmuir, **2000**, *16*, 7605-7611.

[86] Debuigne, F.; Cuisenaire, J.; Jeunieau, L.; Masereel, B.; Nagy, J. B. *"Synthesis of nimesulide nanoparticles in the microemulsion Epikuron/isopropyl myristate/water/n-butanol (or isopropanol)."* J Colloid Interf Sci, **2001**, *243*, 90-101.

[87] Kasai, H.; Kamatani, H.; Okada, S.; Oikawa, H.; Matsuda, H.; Nakanishi, H. *"Size-dependent colors and luminescences of organic microcrystals."* Jpn J Appl Phys 2, **1996**, *35*, L221-L223.

[88] Kasai, H.; Kamatani, H.; Yoshikawa, Y.; Okada, S.; Oikawa, H.; Watanabe, A.; Itoh, O.; Nakanishi, H. *"Crystal size dependence of emission from perylene microcrystals."* Chem Lett, **1997**, 1181-1182.

[89] Masuhara, H. N., Hachiro; Sasaki, Keiji *"Single Organic Nanoparticles."* Springer, **2003**.

[90] Zhao, G.; Ishizaka, T.; Kasai, H.; Oikawa, H.; Nakanishi, H. *"Fabrication of Unique Porous Polyimide Nanoparticles Using a Reprecipitation Method."* Chem Mater, **2007**, *19*, 1901-1905.

[91] Ji, X.-H.; Fu, H.-B.; Xie, R.-M.; Xiao, D.-B.; Yao, J.-N. *"Perylene Nanoparticles Prepared by Reprecipitation Method."* Chinese Journal of Chemistry, **2002**, *20*, 123-126.

[92] Chung, H.-R.; Kwon, E.; Oikawa, H.; Kasai, H.; Nakanishi, H. *"Effect of solvent on organic nanocrystal growth using the reprecipitation method."* J Cryst Growth, **2006**, *294*, 459-463.

[93] Ibanez, A.; Maximov, S.; Guin, A.; Chaillout, C.; Baldeck, P. L. *"Controlled nanocrystallization of organic molecules in sol-gel glasses."* Adv Mater, **1998**, *10*, 1540-+.

[94] Desportes, S.; Yatabe, Z.; Baumlin, S.; Genot, V.; Lefevre, J. P.; Ushiki, H.; Delaire, J. A.; Pansu, R. B. *"Fluorescence lifetime imaging microscopy for in situ observation of the nanocrystallization of rubrene in a microfluidic set-up."* Chem Phys Lett, **2007**, *446*, 212-216.

[95] Szuromi, P. D. *"Handbook of nanostructured materials and nanotechnology."* Science, **2000**, *288*, 1596-1596.

[96] Watts, P.; Haswell, S. J.; Pombo-Villar, E. *"Electrochemical effects related to synthesis in micro reactors operating under electrokinetic flow."* Chem Eng J, **2004**, *101*, 237-240.

[97] Yi, L. D., J. S.; Daisuke, S.;. *"Handbook Of Advanced Magnetic Materials, 4."* Tsinghua University Press, Springer, **2005**; *Vol*. 4.

[98] Corain, C., Schmid, G., Toshima, N.,. *"Metal Nanoclusters in Catalysis and Materials Science: The Issue of Size Control: The Issue of Size Control."* Elsevier, **2011**.

[99] Pomogailo, A. D. K., V.N. . *"Metallopolymer Nanocomposites."* Springer, **2005**.

[100] PANSU, R. B. *"Kinetic versus thermodynamic control of dodac vesicles formation."* CNRS, **1990**; *Vol*. 14.

[101] Rajdeep, S. *"Solubilization of Organic Dyes in Surfactant Micelles (Master thesis)."* Department of Chemical and Biological Engineering,, **2012**.

[102] K. Holmberg, B. J., B. Kronberg and B. Lindman. *"Surfactants and Polymers in Aqueous Solution."* 2nd Ed ed.; Wiley, Chichester, **2003**.

[103] Tharwat, F. T. *"Applied Surfactants: Principles and Applications."* WILEY-VCH, **2005**.

[104] Aamodt, M.; Landgren, M.; Joensson, B. *"Solubilization of uncharged molecules in ionic surfactant aggregates. 1. The micellar phase."* The Journal of Physical Chemistry, **1992**, *96*, 945-950.

[105] Rio, L. G.; Godoy, A. *"Influence of CTACl cationic micelles on the spectral behavior of crystal violet."* Chem Phys, **2006**, *327*, 361-367.

[106] García-Río, L.; Leis, J. R.; López-Fontán, J. L.; Mejuto, J. C.; Mosquera, V.; Rodríguez-Dafonte, P. *"Mixed micelles of alkylamines and cetyltrimethylammonium chloride."* J Colloid Interf Sci, **2005**, *289*, 521-529.

[107] Nam-Trung, N. S., T. W.;. *"Fundamentals and Applications of Microfluidics."* ARTECH HOUSE, INC., **2002**.

[108] Maluf, N. *"An Introduction to Microelectromechanical Systems Engineering."* 2nd ed.; Artech House Print on Demand, **2000**.

[109] Minhang, B. *"Analysis and Design Principles of MEMS Devices."* Elsevier Science, **2005**.

[110] Keith, E. H., A. R.;. *"Lab on a Chip Technology: Fabrication and Microfluidics."* Horizon Scientific Press, **2009**.

[111] Knight, J. B.; Vishwanath, A.; Brody, J. P.; Austin, R. H. *"Hydrodynamic focusing on a silicon chip: Mixing nanoliters in microseconds."* Phys Rev Lett, **1998**, *80*, 3863-3866.

[112] Hessel, V.; Lowe, H.; Schonfeld, F. *"Micromixers - a review on passive and active mixing principles."* Chem Eng Sci, **2005**, *60*, 2479-2501.

[113] Harrison, D. J.; Fluri, K.; Seiler, K.; Fan, Z. H.; Effenhauser, C. S.; Manz, A. *"Micromachining a Miniaturized Capillary Electrophoresis-Based Chemical-Analysis System on a Chip."* Science, **1993**, *261*, 895-897.

[114] Hibara, A.; Nonaka, M.; Tokeshi, M.; Kitamori, T. *"Spectroscopic analysis of liquid/liquid interfaces in multiphase microflows."* J Am Chem Soc, **2003**, *125*, 14954-14955.

[115] Kakuta, M.; Hinsmann, P.; Manz, A.; Lendl, B. *"Time-resolved Fourier transform infrared spectrometry using a microfabricated continuous flow mixer: application to protein conformation study using the example of ubiquitin."* Lab Chip, **2003**, *3*, 82-85.

[116] Kakuta, M.; Jayawickrama, D. A.; Wolters, A. M.; Manz, A.; Sweedler, J. V. *"Micromixer-based time-resolved NMR: Applications to ubiquitin protein conformation."* Anal Chem, **2003**, *75*, 956-960.

[117] Kamholz, A. E.; Schilling, E. A.; Yager, P. *"Optical measurement of transverse molecular diffusion in a microchannel."* Biophysical journal, **2001**, *80*, 1967-72.

[118] Teixeira, R.; Andrade, S. M.; Serra, V. V.; Paulo, P. M. R.; Sanchez-Coronilla, A.; Neves, M. G. P. M. S.; Cavaleiro, J. A. S.; Costa, S. M. B. *"Reorganization of Self-Assembled Dipeptide Porphyrin J-Aggregates in Water-Ethanol Mixtures."* J Phys Chem B, **2012**, *116*, 2396-2404.

[119] Lin, H. J.; Herman, P.; Lakowicz, J. R. *"Fluorescence lifetime-resolved pH imaging of living cells."* Cytometry. Part A : the journal of the International Society for Analytical Cytology, **2003**, *52*, 77-89.

[120] Schoutteten, L.; Denjean, P.; Faure, J.; Pansu, R. B. *"Photophysics of Calcium Green 1 in vitro and in live cells."* Phys Chem Chem Phys, **1999**, *1*, 2463-2469.

[121] Roth, C. M.; Heinlein, P. I.; Heilemann, M.; Herten, D. P. *"Imaging diffusion in living cells using time-correlated single-photon counting."* Anal Chem, **2007**, *79*, 7340-7345.

[122] Boreham, A.; Kim, T. Y.; Spahn, V.; Stein, C.; Mundhenk, L.; Gruber, A. D.; Haag, R.; Welker, P.; Licha, K.; Alexiev, U. *"Exploiting Fluorescence Lifetime Plasticity in FLIM: Target Molecule Localization in Cells and Tissues."* Acs Med Chem Lett, **2011**, *2*, 724-728.

[123] Calleja, V.; Ameer-Beg, S. M.; Vojnovic, B.; Woscholski, R.; Downward, J.; Larijani, B. *"Monitoring conformational changes of proteins in cells by fluorescence lifetime imaging microscopy."* The Biochemical journal, **2003**, *372*, 33-40.

Chapter 2. Introduction to BODIPY derivatives

2.1. General introduction of molecular fluorescence[1,2] and absorption

Fluorescence spectroscopy technology has been widely used in the study of the structure and dynamics of molecules and considered to be primarily tools in biochemistry and biophysics due to its high sensitivity and universality. As fluorophores play the central role in fluorescence spectroscopy technology, imaging, and also the main subject in our study, we will start with an investigation of their manifold interactions with light. So in the very beginning, an elementary introduction to the various aspects of transition process is presented.

The basic concepts of absorption and fluorescence starts from the definitions of the processes involved in the electronic transitions and their relations in the presence of electron transfer, with different types of electronic transitions are presented by the example of formaldehyde as following **Fig. 2. 1**.

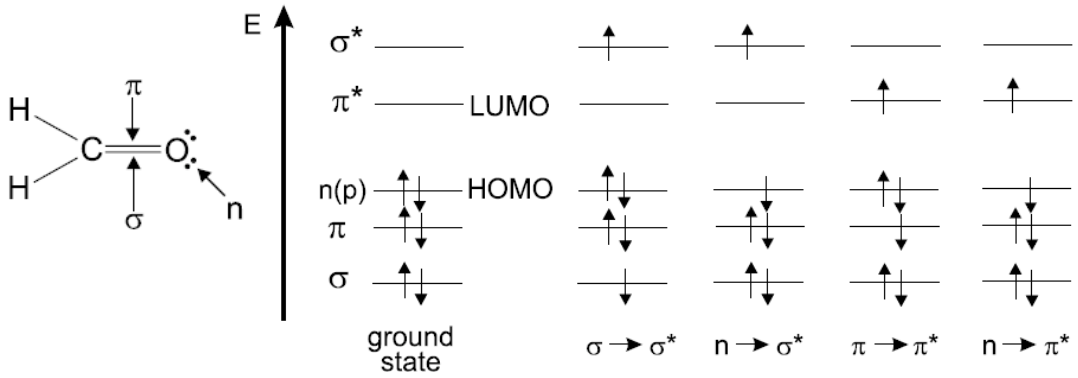

Figure 2. 1: Energy levels of molecular orbitals in formaldehyde.

In **Fig. 2. 1**, σ orbital can be formed either from two σ atomic orbitals, or from one σ and one π atomic orbital, or from two π atomic orbitals having a collinear axis of symmetry. The bond formed in this way is called a σ bond. A π orbital is formed from two π atomic orbitals overlapping laterally. The resulting bond is called a π bond.

Two important types of orbitals are considered with respect to absorption and fluorescence spectroscopy, that is the Highest Occupied Molecular Orbital (HOMO) and Lowest Unoccupied Molecular Orbital (LUMO)[1]. Indeed the LUMO and HOMO are the orbitals that describe most of the S_1 state.

The possible transitions processes that occur between the absorption and emission of light are usually illustrated by the well-known Perrin-Jablonski diagram[3] in **Fig. 2. 2**, also called the electronic transitions diagram. That includes: photon absorption, internal conversion (denoted as IC), fluorescence, intersystem crossing (denoted as ISC), phosphorescence,

delayed fluorescence and triplet–triplet transitions. The singlet electronic states are denoted S_0 (Fundamental electronic state), S_1; S_2; . . . and the triplet states, T_1; T_2; . . . Vibrational levels are associated with each electronic state.

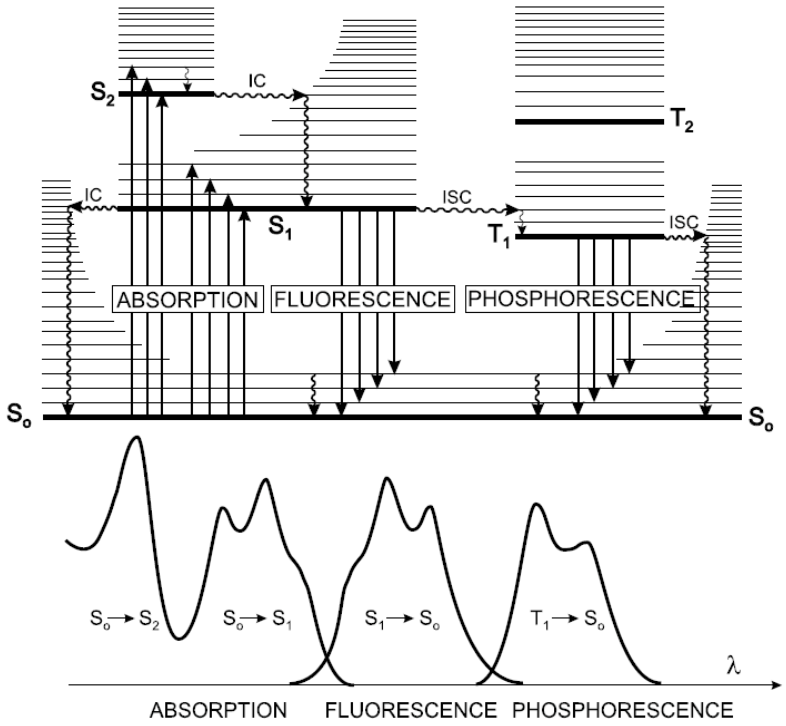

Characteristic times:
Absorption: 10^{-15}s
Vibrational relaxation: $10^{-15} – 10^{-10}$ s
Intersystem crossing: $10^{-10} – 10^{-8}$ s
Internal conversion: $10^{-15} – 10^{-10}$ s

Lifetime of the excited state S_1: 10^{-9}-10^{-7}s →Fluorescence
Lifetime of the excited state T_1: 10^{-6}-1s →Phosphorescence

Figure 2. 2: Perrin–Jablonski diagram. Most of photophysical pathways to the ground state after an electronic excitation are shown schematically. S_0, S_1, S_2, T_1, T_2 are singlet ground state, singlet first and second excited state, triplet first and second excited state respectively. Characteristic time scales of individual pathways are shown behind the diagram.

2.1.1. Molecular fluorescence and competition process[4]

According to the Perrin–Jablonski diagram, absorption allows a chromophore to absorb a photon, so the electron of a molecule in the ground state is excited to an orbital with higher energy level and the electron in the excited orbital is paired (by opposite spin) to the second electron in the ground-state orbital, that is an excited state S_n. An excited molecule will return to the ground state by following two successive steps[5]:

1. The molecule at S_n returns to the lowest excited state S_1 by dissipating a part of its energy in the surrounding environment. This phenomenon is usually called internal conversion.
2. The de-excitation of molecule in S_1 occurs through different competitive processes: fluorescence emission with a radiative rate constant k_r, inter-system crossing, with a rate constant k_{isc}, collisional quenching with a rate constant k_q, and probably electron transfer, and energy transfer

Consequently, from the excited state S_1, the molecule will reach the ground state S_0 during a spin allowed process and occurs rapidly by emission of a photon, and the emission of a photon (fluorescence emission process) with a radiative rate constant k_r :

$1/k_r$ are typically in the range of 10^{-9}-10^{-7}s as in the illustration after **Fig.2. 2**, thus, the emission process is a very fast process, and so in order to observe fluorescence emission, the fluorophore should be excited continuously.

Emission occurs from the excited state S_1, and is independent from the excitation wavelength. Since not all the molecules present at the excited states will participate in the fluorescence process, a fluorescence quantum yield Φ_f exist and can be calculated as mentioned in Chapter 6.

2.1.2. Kinetics of fluorescence

Considering a diluted solution of fluorophore A with a concentration of $[A]$ (mol L^{-1}), after excitation by a short pulse of light, a number of excited molecules A remain in the excited state S_1, for a short time before returning to the ground state either radiatively or non-radiatively. The fluorescence decay rate is the rate of population decay of the S_1 state. Thus, the fluorescence decay rate k_f is the sum of radiative (k_r) and non-radiative (k_{nr}) decay rate:

$$k_f = k_r + k_{nr} \qquad \text{Eq. 2. 1}$$

And the rate of disappearance of excited molecules is expressed by the following differential equation:

$$-\frac{d[A^*]}{dt} = (k_r + k_{nr})[A^*] \qquad \text{Eq. 2. 2}$$

where $[A^*]$ represents the concentration of the excited molecules at S_1 state, and integration of **Eq. 2.3** yields the time evolution of the concentration of excited molecules$[A^*]$

$$[A^*] = [A^*]_0 exp\left(-\frac{t}{\tau_f}\right) \qquad \text{Eq. 2.3}$$

where $[A^*]$ is the concentration of excited molecules at time 0 after pulse light excitation.

The fluorescence intensity I_t at time t can be given as:

$$I_t = k_r[A^*]_0 exp\left(-\frac{t}{\tau_f}\right) \qquad \text{Eq. 2.4}$$

with $\tau_f = {}^1/_{k_r + k_{nr}}$

In the case of the fluorescence of solid sample, the fluorescence decay cannot be described as a simple exponential for most cases. Indeed, in solid samples, each chromophore defers from the other one by a different local environment and a different distance to the first quencher. Thus distributions of exponentials are expected, and intensity decays are typically fit to the multi-exponential model[2]:

$$I_t = \sum_i \alpha_i \, exp\left(-\frac{t}{\tau_i}\right) \qquad \text{Eq. 2.5}$$

Where the $\sum_i \alpha_i$ is normalized to unity.

In practice, the numerical analysis of this distribution of exponentials is not possible. On the reverse this means that most decay-associated spectra can be numerically approximated by a sum of finite number of exponentials. In our case, the decay can be constructed for maximum of three species[6,7].

2.1.3. Electronic transition and transition dipole moment

In the quantum mechanical approach, an electronic transition will occur within the molecule when the molecule interacts with light of suitable frequency, and here a transition moment is introduced for characterizing the transition between an initial state and a final state. The transition moment represents the transient dipole resulting from the displacement of charges during the transition and it is not strictly a dipole moment.

The classical electrical theory defines the dipole moment of two charges (+q and -q) of the distance $\vec{r}$ as $\vec{\mu} = q\vec{r}$. So for multi-electron system, the dipole moment of electrons is

related to the sum over the electrons (n) in the system: $\sum e\vec{r}_n$, where e is the charge of one electron. In quantum mechanics, the transition dipole moment could be expressed as:

$$\langle \mu_{di} \rangle = \langle \psi_g | \vec{\mu} | \psi_e \rangle \qquad \text{Eq. 2.6}$$

where $\vec{\mu}$ is the dipole moment operator, ψ_g is the molecular ground eigenstate and ψ_e is the excited eigenstate.

The radiative transition probability between two electronic states, which determine the intensities of spectral lines, is proportional to the square of the transition dipole moment and is shown as follow:

$$\mathrm{k}_r \propto |\langle \vec{\mu}_{di} \rangle|^2 = \propto \left| \langle \psi_g | \vec{\mu} | \psi_e \rangle \right|^2 \qquad \text{Eq. 2.7}$$

if $\langle \vec{\mu}_{di} \rangle \neq 0$, it is called the "dipole allowed", otherwise if $\langle \vec{\mu}_{di} \rangle = 0$, it is called the "dipole forbidden". The proportionality factor is obtained through the Einstein theory[8-10] of the absorption/emission of light and the Plank theory of the radiation of black body, under the vacuum condition it gives:

$$\mathrm{k}_r = \mathrm{A}_{ij} = \frac{2{w_{ij}}^3}{3\varepsilon_0 hc^3} |\langle \vec{\mu}_{di} \rangle^2| \qquad \text{Eq. 2.8}$$

where A_{ij} is Einstein coefficient (s^{-1}), w_{ij} is the pulsation of the resonant light. ε_0 (C $N^{-1}m^{-2}$) is the permittivity of free space, h is the Planck's constant; the unit of transition dipole $\vec{\mu}_{di}$ is $C \cdot m$. The order of magnitude of the value is in the range of $10^{-29}\ C \cdot m$ (1 electron charge × 1 Å).

In the case of a transition in a medium with refraction index n_0, the relation becomes:

$$\mathrm{k}_r = \mathrm{A}_{ij} = \frac{8\pi\delta n_0 {w_{ij}}^3}{3\varepsilon_0 hc^3} |\langle \vec{\mu}_{di} \rangle^2| \qquad \text{Eq. 2.9}$$

where δ is a scalar factor and the actual value of which depends on the cavity model[10].

2.1.4. Light absorption and oscillator strength[8]

The transition dipole also governs the absorption of the light by the molecules in a dielectric. It can be related to molar extinction coefficient of a solution of molecules. Experimentally, the efficiency of light absorption at a wavelength λ by an absorbing medium is defined by the absorbance A(λ) or the transmittance T(λ).

To define the absorption characteristic, as the total energy absorbed per unit length is proportional to the integral of the absorption cross-section over the atomic frequency response, the well-known Lambert-Beer law correlates and characterized the light intensity to the

concentration C of the absorbing species and the thickness d that is passed, relating to absorption spectrometry of the crystal. And that could be written as:

$$I(v) = I_0 \times e^{-\alpha(v)\times d} \leftrightarrow \log\left(\frac{I_0}{I}\right) = \epsilon(v)\times C \times d \qquad \text{Eq. 2.10}$$

where $\alpha(v) = 2.303\times \epsilon(v)\times C$ is defined as absorption coefficient of the medium for light of the frequency v and $\epsilon(v)$ is the extinction coefficient or the molar extinction coefficient with molarity concentration, and absorptivity is measured as absorbance A, or optical density (OD).

Chemists prefer to use a dimensionless quantity: the oscillator strength f to express the probability of absorption or emission of electromagnetic radiation in transitions between energy levels. f tends toward 1 for a perfectly allowed single electron transition. A perfectly allowed single electron transition is that expected for an electron oscillating inside a harmonic potential using classical electromagnetism.

Because the experimentally observed transition probabilities are often close to the classical spontaneous emission or radiative decay rate γ, an emission oscillator strength f_{ji} is defined by the relation as follow[8]:

$$\text{Aji} = -3 f_{ji} \gamma \qquad \text{Eq. 2.11}$$

The relation are given by comparing the emission rate or absorption rate of the atom with the emission or absorption rate of a classical, single- electron oscillator[11-13], where

$$\gamma = \frac{e^2 {w_{ij}}^2}{6\pi\varepsilon_0 m_e c^3} \qquad \text{Eq. 2.12}$$

Then

$$f_{ji} = -\frac{2\pi\varepsilon_0 m_e c^3}{e^2 {w_{ij}}^2}\text{Aji} \qquad \text{Eq. 2.13}$$

and according to **Eq. 2.8**

$$f_{ji} = \left(\frac{4\pi m_e w_{ij}}{3he^2}\right)|\langle\vec{\mu}_{di}\rangle^2|_{SI} \cong 4.702\times10^{-7}(cm\ D^2)\times\tilde{v}_{ij}\times|\langle\vec{\mu}_{di}\rangle^2|_{Debye} \qquad \text{Eq. 2.14}$$

The relationships between A, f_{ji} and $|\langle\vec{\mu}_{di}\rangle^2|_{SI}$ were given[14] in SI units, where m_e is the mass of the electron ($\approx 9.109\times10^{-28}g$), e is the charge ($\approx 1.602\times10^{-19}$C), h is the Planck's constant, and $|\langle\vec{\mu}_{di}\rangle^2|_{SI}$ is in m^2C^2 respectively. Then the value could be calculated with electric dipole in Debye (D), and $\tilde{v}_{ij}$ is the energy of the transition (in cm^{-1}) that is given by

$\tilde{v}_{ij} = {}^{w_{ij}}/_{2\pi c}$. That is because the transition dipole moment is conveniently measured in units of Debye, where 1 D = 3.336 x 10^{-30}C•m.

Oscillator strength can be expressed in many ways, and it can be calculated from the experimentally known molar decadic extinction coefficient[15] $\epsilon(\tilde{v})$ (L $mol^{-1}cm^{-2}$)by integrating over the absorption band in cgs units in **Eq. 2.15**

$$f = \frac{2303 m_e c^2}{N\pi n_0 e^2} \int \epsilon(\tilde{v}) \mathrm{d}(\tilde{v}) = \frac{4.319\times10^{-9}}{n_0} \int \epsilon(\tilde{v}) \mathrm{d}(\tilde{v}) \qquad \text{Eq. 2.15}$$

Where m_e is the mass of an electron, e is the charge of an electron respectively, and n_0 is the refractive index of the medium, c is the speed of light; N is Avogadro's number. $\tilde{v}$ (cm^{-1}) can be given in units of 1/λ and denotes wavenumbers. Factor 2303 involves the conversion from natural logarithms as well as the number of cubic centimeters in a liter required by the introduction of the molar absorption coefficient. **Eq. 2.15** will be used in this thesis to calculate the oscillator strength of BODIPY from the experimental spectra.

Then combining the classical and quantum-mechanical calculations, the transition probability can be evaluated from the absorption spectrum by:

$$|\langle \vec{\mu}_{di} \rangle^2| = \frac{9.185\times10^{-3}}{n_0 \tilde{v}} \int \epsilon(\tilde{v}) \mathrm{d}(\tilde{v}) \qquad \text{Eq. 2.16}$$

2.1.5. Quantum yield

Quantum yield is one of the most important photophysical data of a chromophore for many applications. It is not only the characteristic of a photon emitter but also a good indication showing the properties of environment and the interaction among chromophore and environment[16].

The quantum yield is defined as the ratio of the rate at which photon are emitted to the rate at which molecule are excited or desexcited, and it can be expressed by using photophysical parameters as follow:

$$\Phi_f = \frac{I_F}{I_{abs}} = \frac{V_F}{V_F + V_{NR}} = \frac{k_r}{k_r + k_{nr}} = k_r \tau_f \qquad \text{Eq. 2.17}$$

2.1.6. Fluorescence Anisotropy measurements: [2]

Fluorescence anisotropy, which was first described by Perrin, 1926, are based on the principle of photoselective excitation of fluorophores by polarized light. The probability that

a molecule is excited will be equal to the square of the projection of excitation electric field along the transition moment. Molecules with their absorption axis aligned parallel to the electric field of the polarized excitation have the highest probability of excitation. Starting from an isotropic population we create an anisotropic population of excited molecules.

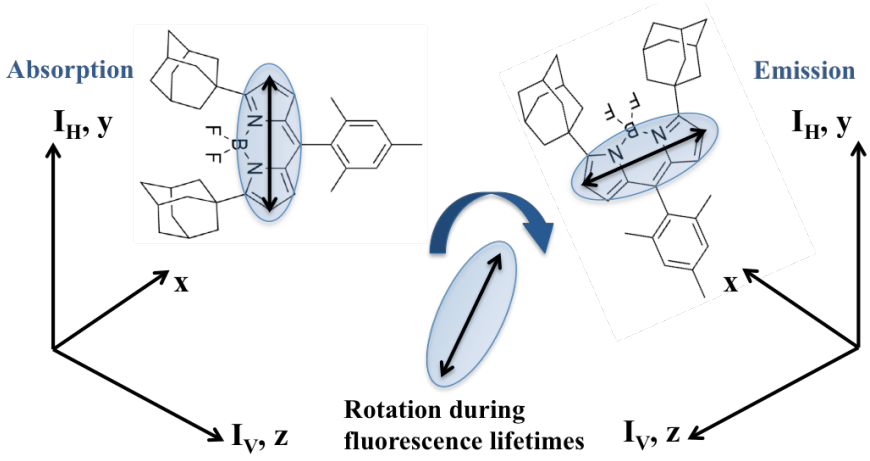

Figure 2. 3: Fluorescence anisotropy experiment. The fluorophore is excited by a polarized laser pulse, and then undergoes rotational diffusion during its fluorescence lifetime. Finally, the dye emits a photon in a possibly changed orientation.

The fluorescence anisotropy (r) are defined by:

$$r = \frac{I_V - I_H}{I_V + 2I_H} \qquad \text{Eq. 2. 18}$$

The denominator I_V+2I_H is due to the axial symmetry of the photoselection in an isoptropic solution.

In the case of polarized fluorescence of flat crystals, we record I(theta1,Theta2) where theta1 is the angle of the excitation with respect to the long axis of the crystal and theta2 is the angle of the fluorescence with respect with the same axis.

The intrinsic anisotropy of a fluorophore is related to the angle between the excitation transition dipole and the emission transition dipole. It is given by:

$$r_0 = \frac{2}{5}\left(\frac{3\langle cos^2\theta\rangle - 1}{2}\right) \qquad \text{Eq. 2. 19}$$

where θ is the angle between the absorption and emission transitions. According to the equation, when θ=0°, $r_0 = 0.4$; when θ=54.7°, $r_0 = 0$, and when θ exceeds 54.7, the

anisotropy becomes negative. The maximum negative value -0.2 is found for θ=90°. Since the transition moment depends on the excited state, studying the variation of θ as a function of wavelength can be use to separate excited states in a spectrum.

2.2. BODIPY dye conjugation and their solid phase

Emissive solids are highly demanded for various applications, but difficult to produce. That is due to the general tightly packing structure of fluorophore in crystalline state or amorphous solid phase leading to a very significant quenching[17,18]. Just like most of the other fluorophores, certain limitations can arise for BODIPY dyes, because of fluorescence quenching and decreased quantum yields in solid states.[19] As previously reported for fluorescent dyes used for solar cells[20] the strategic placement of very bulky groups on the BODIPY core structure should hinder π-π stacking of the chromophores, which is likely to be responsible for the quenching of the fluorescence emission in the solid state for most aromatic fluorophores.

Advances in imaging technique now make fluorescence one of the most powerful tools for many applications that were not previously possible. Experiments ranging from environmental field to biomedical diagnostic connect to interacting protein or with living cells are now common due to the improvement made on the techniques of the observation of similar events on a single molecule level. There is a growing realization that the molecular probes available limit imaging events.

2.3. Adamantyl mesityl BODIPY

2.3.1. Adambodipy synthesis method

Motivated by the attractive potentials of fluorescence organic nanoparticle, we have been engaged in the synthesis of a new fluorescent BODIPY derivative dye (from Dr.Gilles Clavier and Dr. Marina Dvorko), Adamantyl mesityl BODIPY (Adambodipy or 4,4-Difluoro-3, 5-di-(adamantyl)-8-mesityl-4-bora-3a, 4a-diaza-*s*-indacene). The bulky alkyl subtituent (adamantine group) is introduced at the periphery of the fluorophore structure (see **Fig.2-c**). It limits the π-π stacking and overcome the fluorescence quenching in solid state and also helps in crystallization.

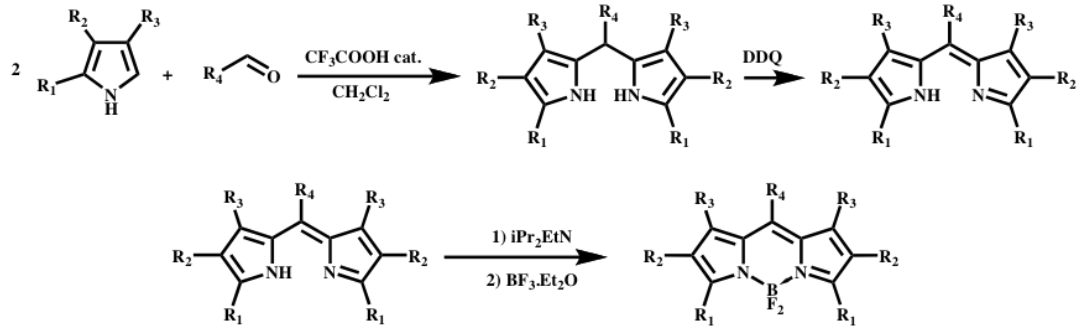

a). Classical synthetic method

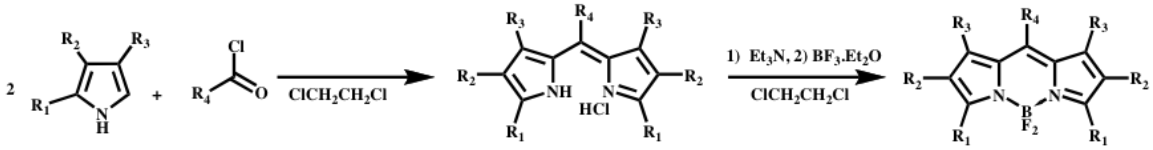

b). Optimised method

Scheme 1. 1 Synthetic method of Adambodipy

The spectroscopic properties of Adambodipy have been first studied in solution. The time decay, absorption and fluorescence spectra in THF/EtOH (3:7) with CTACl are shown on the **Fig.2. 4.**

2.3.2. The spectroscopic properties of Adambodipy in solution

The **Fig.2. 4** exhibits the typical spectroscopy of the Adamantyl Mesityl BODIPY in dichloromethane. The main absorption band, centered at 515 nm, is attributed to the strong S0->S1 transition. There is also one more absorption band near 490 nm, assignable to vibrational structure. A second vibrational structure can be guessed at 450nm. The vibration can also be seen in fluorescence as a mirror image at 555nm. The fluorescence spectrum shows a main and intense emission band centered at 523 nm due to the transition S1->S0 and reveals a quite high quantum yield (0.79).

The fluorescence lifetime decay is one of the most important characteristics of a fluorescent molecule because it defines the time window of observation of dynamic phenomena.[1] The decay of Adambodipy in solution can be fitted by mono-exponential decay law and the fluorescence lifetime is 5.7 ns. From these data a few parameters can be obtained, such as the radiative deactivation rate (1.2 x 108 s) and the non radiative deactivation rate (3.2 x 107 s).

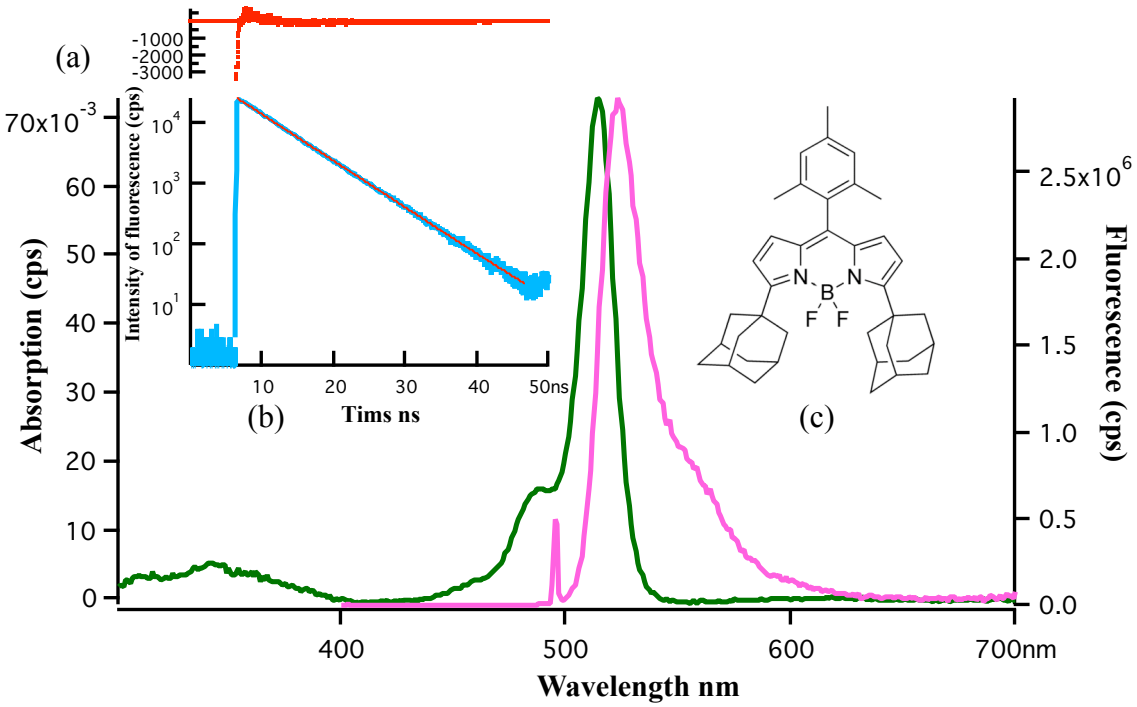

Figure 2. 4: Absorption and fluorescence spectra of Adambodipy in THF/EtOH= 3:7&CTACl (10^{-3}M) solvent

In (a), (b)
- Absorption spectrum, maximum at 515nm
- Fluorescence spectrum, excited at 515nm, maximum at 523nm
- Fluorescence decay, with mono-exponential fitting

Figure (c) is the structure of the Adambodipy molecule.

2.3.3. Fluorescence Anisotropy measurements:

As the anisotropy can be decreased by extrinsic factors (that act during the lifetime of the excited state,) such as rotational diffusion of the fluorophore and the resonance energy transfer, to decrease the rotation diffusion, we can use low temperature or high viscosities squalane, diluted solution to avoid the energy transfer effect.

We have studied the anisotropy of a solution of Adambodipy in squalane (n'=1,4474)[21]. The largest anisotropy values are observed for excitation at the longest wavelength absorption band, because the lowest singlet state is generally responsible for the observed fluorescence, and this state is also responsible for the long wavelength absorption band according to Kasha's rule. We have measured a value of 0.14 but not the expected value of 0.4, since the viscosity of the squalane is not infinite.

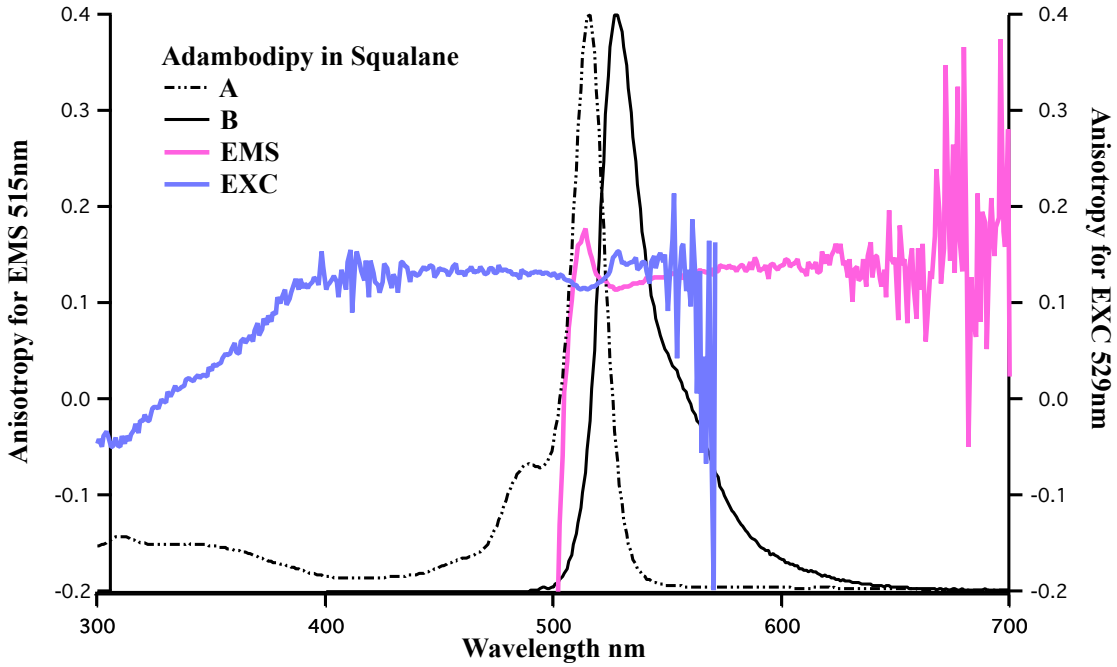

Figure 2. 5: A and B represent the absorption and fluorescence spectra of Adambodipy in squalane solvent respectively, and one-photon excitation anisotropy spectrum (EXC), emission anisotropy spectrum (EMS) in squalane are presented in the figure.

The excitation anisotropy is relatively constant within the long wavelength absorption bands (400-540nm) around 0.14 correspond to the first electronic transition, S_0-> S_1. Below 400nm, a gradual decrease in r_0 is observed as the excitation wavelength is decreased, indicating the position of the second electronic transition S_0->S_2, and it goes down to -0.07, that is the negative half of the 0.14. This is the value expected for an angle of 90° between the excitation and the emission dipole according to **Eq. 2.19**.

The anisotropy is constant across the emission spectrum, which is typical of emission anisotropy spectra.

2.3.4 Fluorescence of molecular nanocrystals prepared with Adambodipy

BODIPY derivatives are widely used to design highly sensitive sensors for many fields such as medicine, biology and environment[22]. The limitation of this fluorophore would be fluorescence quenching and decreased quantum yields in solid state[19]. Comparatively speaking, organic crystals or pigments are quite attractive candidates, since they allow getting assemblies of fluorescent molecules in micro- or nano-sized particles and such NP may provide even more responsive sensors due to their high absorption cross-section and their capability of quenching more than one fluorophore per sensor[23]. The preparation and

properties of fluorescent micro- or nano-sized particles have given rise to number of applications. The main benefits of nanoparticle labels are stronger luminescence and also a better anti-photobleaching due to the fact that each particle contains a lot of luminescent molecules and are usually protected with a coating layer. Their good photostability and long fluorescence lifetime make them appropriate labels for long term labeling[24].

Many strategies are built to synthesize fluorescent assemblies; one popular method is on a cast film prepared by evaporation of a droplet of the dye solution in dichloromethane spread out on a microscope slide. Microcrystals grown right after the synthesis were also studied[25]. The fluorescent organic nanocrystals synthesis have been reported using reprecipitation method, laser ablation, ion sputtering, photochemical synthesis and many other methods[26]. Crystal size dependence of spectroscopics properties was also found in several applications.

Our main objective is to build assemblies of the adamantly mesityl BODIPY. This derivative was obtained in solid state by reprecipitation method. For the comparison the antisolvent precipitation was done by bulk method and the process was also implemented in a micro-fluidic device. The products were analyzed to compare their fluorescent properties and size distribution. We have also prepared crystals by reprecipitation in water. From the fluorescent properties, we hope to deduce the molecular organization of the molecules in the NPs. Furthermore we are wondering whether or not the NPs are crystaline or amorphous and to what extend.

2.3.5. Adambodipy particles obtained by bulk technology

There are many approaches to synthesize NP, and aqueous bulk method is no doubt to be one of the most traditional **(§ 1.2.2.1)**. In order to compare the size distribution of the NPs synthesized by different methods, we analysed the samples collected by this bulk method. At the initial stage when Adambodipy solution (in THF/EtOH with or without CTACl) was added, a large amount of water (with or without CTACl) was kept in turbulence with vortex oscillator. As the size distribution of the NPs may be controlled by the concentration and the surfactant, we changed the volume ratio of the Adambodipy solution and water; the concentration was also taken into account.

Among several samples, four of them are presented (see **Table 2.1**). They were obtained by pouring 100µl of organic solution in 5mL of aqueous solution (water with 10^{-2}M CTACl or without surfactant)

Sample-NO.	Conditions	Main peak/nm	Range/nm
3	Adambodipy 0.1mg/ml in THF/EtOH (3:7 v/v) No CTACl	130	100-200
6	Adambodipy 0.1mg/ml in THF/EtOH (3:7 v/v) With CTACl	320	200-400
8	Adambodipy 0.5mg/ml in THF/EtOH (3:7 v/v) No CTACl	520	200-700
7	Adambodipy 0.5mg/ml in THF/EtOH (3:7 v/v) With CTACl	250	150-600

Table 2. 1: Operating conditions to prepared bulk samples and the size distribution of the NPs obtained (with CTACl 10^{-2}M).

However, from the NPs size distribution, we didn't get a very obvious trend to say whether or not the surfactant is important to control the size of the NPs. The spectroscopic properties are more relevant when we compare the samples prepared with and without surfactant.

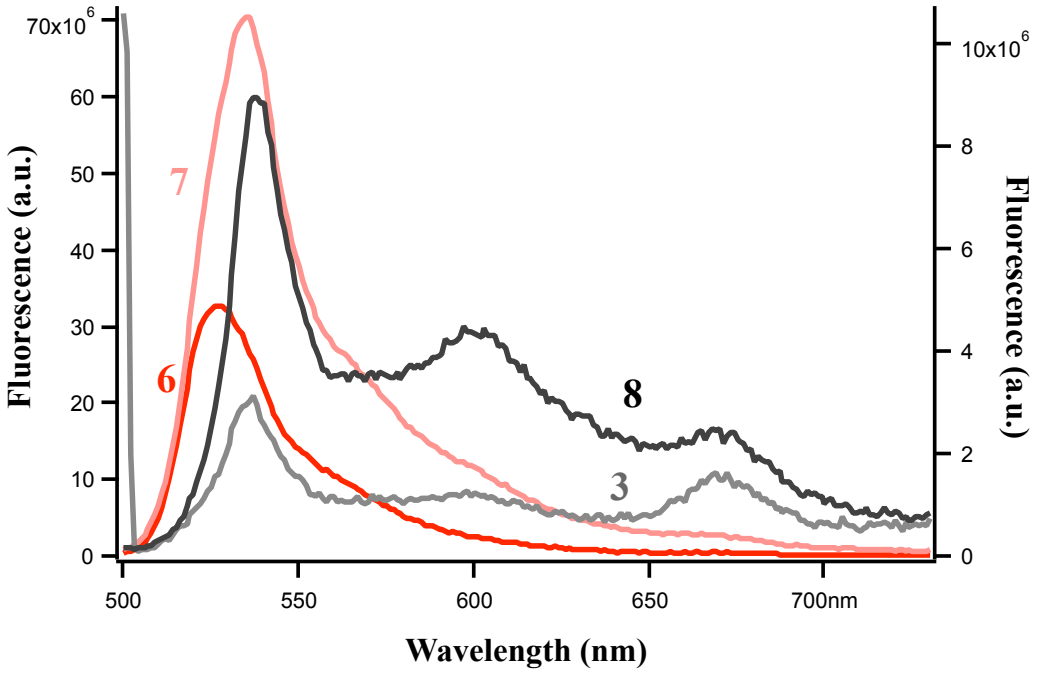

Figure 2. 6: Fluorescence spectra according to the samples from bulk method (Operating conditions in Table 2.1) the numbers with respect to the curve are related to the samples in Table 2.1.

When no surfactant is added (samples 3 and 8, black lines), the fluorescence intensity is 7 times lower compared to when surfactant is present, the band detected between 525 and 545 nm is red shifted and bands at higher wavelength are detected (600- and 670 nm). The similarity between the spectrum with CTACl and that in THF/EtOH (3:7 v/v) along suggests

that in presence of CTACl surfactant Admbodipy molecules are dissolved in micelles since the CTACl concentration is ten times higher than its CMC.

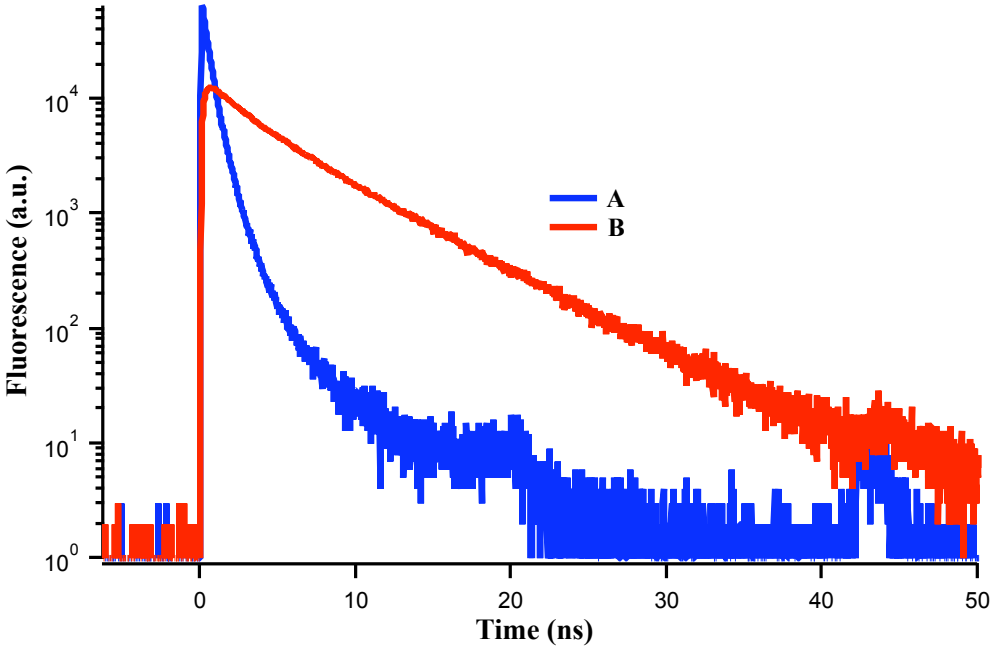

Figure 2. 7: Fluorescence decay curves for the sample from bulk method recorded A at 539nm, and B at 670nm separately.

Fig.2.7 shows typical decays for all the samples collected by bulk method (no matter with or without surfactant). They look similar to the decay curves recorded for the samples collected by MFD1. They would be analyzed further in the MFD parts in the next section.

2.3.6. Solubility of Adambodipy in solution

The driving force for nucleation and growth of one-component crystals in liquid solutions is supersaturation. In order to obtain single crystal of Adambodipy at low supersaturation, a solubility curve of Adambodipy was produced from a previous work (unpublished data.)

The dissolution of raw Adambodipy crystals was done in several THF-EtOH-water mixtures. The clear supernatant was then collected, analyzed by spectrophotometry and compared to a calibration curve. The following graph **Fig. 2.8** was done by Dmoore, PPSM.

We are using binary water-ethanol mixture in the simulation, although the solubility behavior in such binary system is still a challenging area these days. A predictive model to predict solubility curve of dye Adambodipy in a binary mixture of ethanol and water was describe by the Jouyban-Acree model [27,28]with the following form:

$$logC_{eq} = flogC_E + (1-f)logC_W + J - Afactor \qquad \text{Eq. 2. 20}$$

where C_{eq}, T, C_E, T, and C_W,T are the solute solubility at temperature T in the mixture solvent, neat cosolvent and water, respectively. And f denotes the solute free (in the absence of solute) volume fraction of ethanol, V_E, in the cosolvent (ethanol) and water V_W:

$$f = \frac{V_E}{V_W + V_E} \qquad \text{Eq. 2. 21}$$

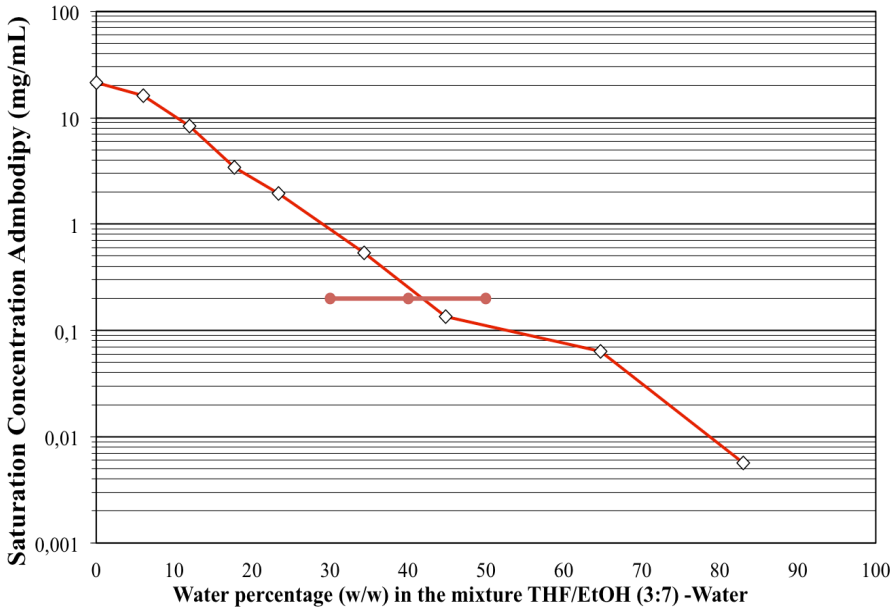

Figure 2. 8: Saturation curve obtained by a dissolution process in a THF-EtOH-water mixtures

and the Jouyban-Acree factor is defined as :

$$J - Afactor = f(1-f)\left[\frac{724.21}{T} + \frac{485.17\big(f-(1-f)\big)}{T} + \frac{194.41(f-(1-f))^2}{T}\right] \qquad \text{Eq. 2. 22}$$

We have adjusted the data that shown in **Fig. 2.8** according to the Jouyban-Acree model as logarithm relation, where T=298K, and the expression would be:

$$g(f) = \exp\left(Af + B(1-f) + f(1-f)\right.$$
$$\left. * \left[\frac{724.21}{298} + \frac{485.17\big(f-(1-f)\big)}{298} + \frac{194.41(f-(1-f))^2}{298}\right]\right. \qquad \text{Eq. 2. 23}$$

The result of the fit is displayed on **Fig. 2.9.**

We obtained for the adjustable parameters values of **Eq. 2.23**: $A=logS_E$, $B=logS_W$, while $A=3.07$, $B=-10.116$ according to the concentration of Adambodipy when percentage of water equals to 0.

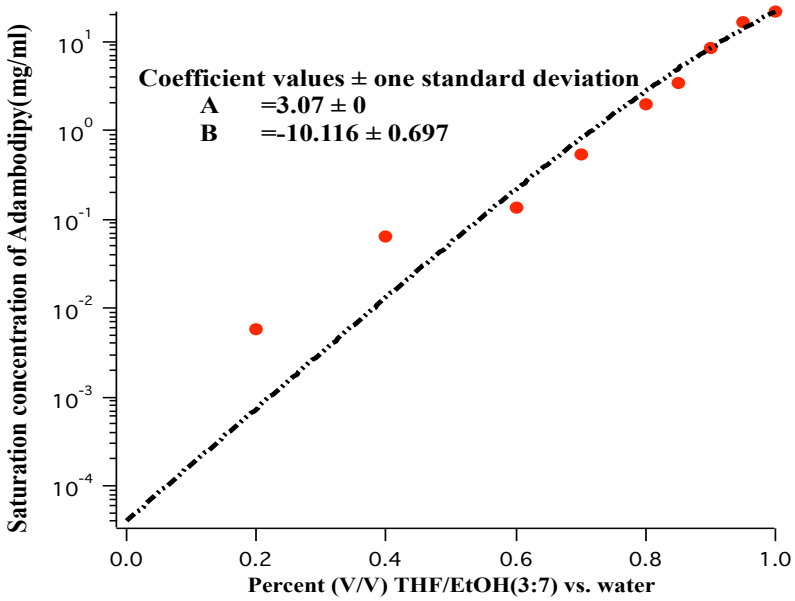

Figure 2. 9: Experimental solubility points for Adambodipy in the mixture of THF/ethanol =3/7 &water, fitting with Jouyban-Acree model as logarithm relation

Then with the formula we can calculate the saturation solubility of Adambodipy in a known composition of water-ethanol solvent, where in this experiment, the mass composition of water-ethanol mixture could be simulated with COMSOL using "Maxwell-Stefan Diffusion and Convection" module.

Reference:

[1] Valeur, B. *"Molecular Fluorescence Principles and Applications."* Wiley-VCH PlacePublished, **2001**.

[2] R.Lakowicz, J. *"Principles of Fluorescence Spectroscopy."* Third Edition ed.; Springer: PlacePublished, **2006**; *Vol*. 1.

[3] Nickel, B. *"From the Perrin Diagram to the Jablonski Diagram."* EPA Newsletter **1997**, *61*, 27-60.

[4] Sauer, M. H., J.; Enderlein, J.; . *"Handbook of Fluorescence Spectroscopy and Imaging."* WILEY-VCH, Verlag & Co. KGaA: PlacePublished, **2011**

[5] Albani, J. R. *"Principles and Applications of Fluorescence Spectroscopy."* **2007**, 270.

[6] Krishna, M. M. G.; Periasamy, N. *"Spectrally constrained global analysis of fluorescence decays in biomembrane systems."* Anal Biochem **1997**, *253*, 1-7.

[7] Boens, N.; Van der Auweraer, M. *"Identifiability of models for fluorescence quenching in aqueous micellar systems."* Chemphyschem : a European journal of chemical physics and physical chemistry **2005**, *6*, 2352-2358.

[8] Corney, A. *"Atomic and Laser Spectroscopy."* OUP Oxford: PlacePublished, **2006**.

[9] Perrin, F. *"Polarisation de la lumiere de fluorescence: Vie moyenne des molecules dans l'etat excite."* J. Phys. Radium Serie 6, 7 **1926**, *12*, 390-401.

[10] Toptygin, D. *"Effects of the solvent refractive index and its dispersion on the radiative decay rate and extinction coefficient of a fluorescent solute."* J Fluoresc **2003**, *13*, 201-219.

[11] Robinson, G. W. *"In Experimental Methods of Molecular Physics."* Academic Press Inc.: PlacePublished, **1962**; *Vol*. 3.

[12] John, R. S. E. J., B.;. *"Advanced in Quantum Chemistry: Applications of Theoretical Methods to Atmospheric Science."* Science: PlacePublished, **2011**.

[13] Walter. Heitler. *"The Quantum Theory of Radiation "*; Oxford University Press, London: PlacePublished, **1954 edition**.

[14] Drake, G. W. F. *"Handbook of Atomic, Molecular, and Optical Physics."* Springer: PlacePublished, **2006**.

[15] Dogra, S. K. R., H. S.;. *"Atom, Molecule and Spectrum."* newagepublishers: PlacePublished, **2011**.

[16] Wan-Hee, G.: Single Molecule Study of Fluorescence from Organic Dyes at Interfaces. Emory University, 2007.

[17] Ozdemir, T.; Atilgan, S.; Kutuk, I.; Yildirim, L. T.; Tulek, A.; Bayindir, M.; Akkaya, E. U. *"Solid-State Emissive BODIPY Dyes with Bulky Substituents As Spacers."* Org Lett **2009**, *11*, 2105-2107.

[18] Ooyama, Y.; Kagawa, Y.; Harima, Y. *"Synthesis and Solid-State Fluorescence Properties of Structural Isomers of Novel Benzofuro[2,3-c]oxazolocarbazole-Type Fluorescent Dyes."* European Journal of Organic Chemistry **2007**, *2007*, 3613-3621.

[19] Meallet-Renault, R.; Clavier, G.; Dumas-Verdes, C.; Badre, S.; Shmidt, E. Y.; Mikhaleva, A. I.; Laprent, C.; Pansu, R.; Audebert, P.; Trofimov, B. A. *"Novel BODIPY preparations from sterically hindered pyrroles. Synthesis and photophysical behavior in solution, polystyrene nanoparticles, and solid phase."* Russ J Gen Chem+ **2008**, *78*, 2247-2256.

[20] Ooyama, Y.; Ishii, A.; Kagawa, Y.; Imae, I.; Harima, Y. *"Dye-sensitized solar cells based on novel donor-acceptor pi-conjugated benzofuro[2,3-c]oxazolo[4,5-a]carbazole-type fluorescent dyes exhibiting solid-state fluorescence."* New J Chem **2007**, *31*, 2076-2082.

[21] Tripathi, N. *"Densities, viscosities, and refractive indices of mixtures of hexane with cyclohexane, decane, hexadecane, and squalane at 298.15 K."* Int J Thermophys **2005**, *26*, 693-703.

[22] Haugland, R. P. *"Handbook of Fluorescent Probes and Research Chemicals."* Spence, M.T.Z., Ed., Eugene (OR): Molecular Probes, : PlacePublished, **1996**.

[23] Badre, S.; Monnier, V.; Meallet-Renault, R.; Dumas-Verdes, C.; Schmidt, E. Y.; Mikhaleva, A. I.; Laurent, G.; Levi, G.; Ibanez, A.; Trofimov, B. A.; Pansu, R. B. *"Fluorescence of molecular micro- and nanocrystals prepared with Bodipy derivatives."* J Photoch Photobio A **2006**, *183*, 238-246.

[24] Dubuisson, E.; Monnier, V.; Sanz-Menez, N.; Boury, B.; Usson, Y.; Pansu, R. B.; Ibanez, A. *"Brilliant molecular nanocrystals emerging from sol-gel thin films: towards a new generation of fluorescent biochips."* Nanotechnology **2009**, *20*.

[25] Qin, W. W.; Leen, V.; Rohand, T.; Dehaen, W.; Dedecker, P.; Van der Auweraer, M.; Robeyns, K.; Van Meervelt, L.; Beljonne, D.; Van Averbeke, B.; Clifford, J. N.; Driesen, K.; Binnemans, K.; Boens, N. *"Synthesis, Spectroscopy, Crystal Structure, Electrochemistry, and Quantum Chemical and Molecular Dynamics Calculations of a 3-Anilino Difluoroboron Dipyrromethene Dye."* J Phys Chem A **2009**, *113*, 439-447.

[26] C. N. Chintamani Nagesa Ramachandra Rao, P. J. T., G. U. Kulkarni. *"Nanocrystals: Synthesis Properties and Applications."* Springer: PlacePublished, **2007**.

[27] Jouyban, A.; Acree, W. E. *"In silico prediction of drug solubility in water-ethanol mixtures using Jouyban-Acree model."* J Pharm Pharm Sci **2006**, *9*, 262-269.

[28] Khoubnasabjafari, M.; Jouyban, A.; Acree, W. E. *"Mathematical representation of solubility of electrolytes in binary solvent mixtures using Jouyban-Acree model."* Chem Pharm Bull **2005**, *53*, 1591-1593.

Chapter 3: From single molecules to aggregates, and molecule crystal model

The models discussed in the previous section could well explain the photophysical properties of isolated small molecules. However, as soon as interactions between molecules have to be taken into account, they become more difficult to use since many molecular orbitals and the electron-electron interaction between these molecules need to be included in the new model. The nature of excited states of organic molecular crystal is mainly determined by the excited states of the corresponding isolated molecules.

The study always starts from the interaction of two adjacent molecules, the so-called dimer, as this is the smallest possible aggregate that shows some properties which are important for crystal formation. It leads to a stabilization of the ground and excited state due to columbic energy interaction of the two molecules.

3.1. The interaction between molecules

3.1.1. Electronic excitation energy transfer (EET) mechanism

An area of interest in physical chemistry related to polymer chemistry, photosynthesis, surface photochemistry and molecular crystal is to understand the redistribution process of the light energy that is absorbed by complex molecular system. An example of the process is known as the transfer of electronic excitation energy from the excited state of a molecule to another, it is called electronic excitation energy transfer (EET), and it is an important fundamental physical process. The EET can have practical application and the EET can be used as "spectroscopic ruler"[1] (Stryer and Haugland in 1967) for biological applications. It has become increasingly important to develop computational techniques that allow us to calculate the rate of charge or energy transport[2,3] for photovoltaic applications. The research of the EET process also rigorously elucidates the approximated models that were previously developed for different strength of coupling.

The relationship between the spectrum of a molecular crystal and the individual molecule spectra depends critically on the strength of the coupling between molecules. In order to investigate this relationship, Simpson and Peterson first propose the classification and criterion for the strong coupling, weak coupling case and intermediate coupling, conceptually obtained under Born-Oppenheimer framework.[4] The strong coupling criterion is $2U/\nabla\varepsilon >>1$, where $2U$ is the exciton bandwidth, and $\nabla\varepsilon$ is the Franck-Condon bandwidth of the corresponding molecular electronic transition in the individual molecular unit. While the

criterion for the weak coupling case is $2U/\nabla\varepsilon$ <<1 conversely, and the approximation is assured if the splitting from the interaction is small with respect to the vibrational energy increments. The intermediate coupling case is due to the existence of a transition region between strong and weak coupling where the interaction changes with suddenness. And the relation is $2U/\nabla\varepsilon$ <1.

In the strong coupling case, the band shift for the exciton states of a molecular aggregate is observed which is greater than the total electronic band width of the corresponding transition in the individual molecule. Thus, strong exciton coupling occurs when chromophores are in close contact[5] (Cantor and Schimmel, 1980), and a pair of chromophores, also called dimer, may share delocalized energy as if they were one unit. Conversely, in the weak coupling case, the energy can be localized on each monomer at a time such as the monomer tend to retain their spectra, respectively[6].

Later, Föster proposed a slightly modify to the Simpson and Petersons' designation of the energy transfer model. Instead of the two coupling cases, he reclassified the criteria as "strong-coupling" and "medium-coupling"(corresponding to the Simpson and Petersons' weak-coupling), and then reserved "weak-coupling" as a very weak-coupling term for his own vibrational-relaxation resonance transfer case, with energy coupling criterion $U/\nabla\varepsilon'$<<1, and $\nabla\varepsilon'$ is the individual vibronic bandwidth. However, Kasha pointed out the deficient of Föster's theory: firstly, the impossibility to distinguish the "weak" and the "very weak" coupling by direct spectral criterion, and secondly, the theoretical discontinuity in the transition to the Föster model[7].

3.1.2. Molecular orbital theory

A basic approximation of the electronic structure in molecules is known as molecular orbital (MO) theory, and each molecule can be described by a set of molecular orbitals. MO theory assumes that the electronic states in a molecule ψ_{MO} can be expressed in terms of orbitals of discrete energy, formed through the simple weighted linear combination of the n constituent atomic orbitals ψ_{AO}. It could be shown as follow:

$$\psi_{MO} = \sum_{i}^{n} c_i \psi_{AO} \qquad \text{Eq. 3.1}$$

Few more details about the theory are presented here, because although more sophisticated methods for simulating the electronic structure will be employed in this thesis

for example, TDDFT simulation, but the descriptions of the findings will be explained by MO theory. Also, in Chapter 2, the electronic transitions among the molecular orbitals illustrated the spectra properties.

In molecules, without π-bonds, the σ-electrons are tightly bound between the nuclei and cannot interact with adjacent molecules. In contrast, the major characteristic of organic aggregates is the extended π-system, which consists of organic, π-electron conjugated molecules.

The simple example of ethylene is given here to illustrate the formation of bonding and antibonding orbitals of π-bond by MO theory. The orbital configuration of ethylene contains *1s*-orbitals of four hydrogen atoms and the *2s, 2p*$_x$*, 2p*$_y$, and *2p*$_z$ orbitals of two carbon atoms. All the orbitals except of the *2p*$_z$ orbital contribute to the formation of MOs, which have a σ-bonding character for carbon-carbon and carbon-hydrogen interactions. The σ-bond is formed coplanar, between the two respective nuclei, and the *2p*$_z$ orbitals are perpendicular to the carbon-carbon σ bond and antisymmetric with respect to reflection through a mirror plane containing the bond axis. They are designated as bonding (π) and anti-bonding (π^*) orbitals. Orbitals that are symmetric through this plane are called σ and σ^*orbitals. The figure of illustration was shown as follow.

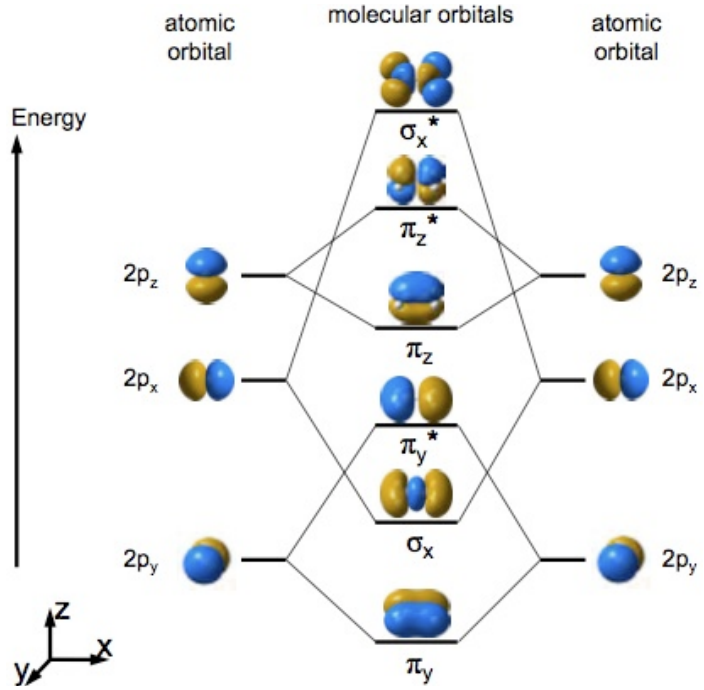

Figure 3. 1: Molecular orbitals of ethylene resulting of the overlap of the carbon p-orbitals (schematic representation on the left and right)[8].

Usually the MOs with π-character are the HOMO and the LUMO, which is due to the fact that the energetic stabilization in the bonding π-orbital as well as the destabilization in the corresponding anti-bonding orbitals π^* is small compared to respective σ-orbitals. This $\pi - \pi^*$ frontier orbitals have a strong impact on the optical and electrical properties of the fluorophore. According to the introduction of fluorescence properties in Chapter 2, lowest energetic optical excitation leads to a $\pi - \pi^*$ transition. The transition dipole moment of organic conjugated π-systems is usually large and leads to a very high absorption coefficient in the order of 10^5 cm^{-1}, without any symmetry restrictions. Thus, an aggregate of an organic dye with the thickness of only some hundred nanometers is already sufficient to absorb nearly the complete incident light in its absorption range.

3.1.3. Dimer and fluorophore dimerization effect

The electronic coupling between two adjacent molecules dominates the energy-transport properties in organic molecular solids. A physical dimer consists of two closely spaced molecules with purely physical interaction, and no chemical bonding is involved. A weak interaction of the molecules forming a dimer can be easily described using perturbation theory as done by Kasha. The theory is applied for dimers in the aggregate state, which result in the formation of mini-excitons upon excitation state[9].

The wavefunction of the dimer in ground state is:

$$\psi_G = \psi_1 \psi_2 \qquad \text{Eq. 3. 2}$$

where ψ_1 and ψ_2 represent the ground state wave-function of molecule 1 and 2 separately.

Taking the non-interacting molecules with their particular Hamiltonian H_1 and H_2 as a starting point, the Hamiltonian operator for the dimer is

$$H = H_1 + H_2 + V_{12} \qquad \text{Eq. 3. 3}$$

where the H_1 and H_2 are the Hamiltonian operators for the isolated molecules 1 and 2, and V_{12} describes the electronic intermolecular interaction.

The energy of the ground state of the dimer according to the Schrödinger equation is:

$$E_G = \iint \psi_1\psi_2 \mathrm{H}\, \psi_1\psi_2 d\tau_1\tau_2 \qquad \text{Eq. 3.4}$$

$$E_G = E_{G1} + E_{G2} + \iint \psi_1\psi_2(\mathrm{V}_{12})\, \psi_1\psi_2 d\tau_1\tau_2 \qquad \text{Eq. 3.5}$$

where the E_{G1} and E_{G2} are ground state energies of the isolated molecules 1 and 2, and the last term represents the Van der Waals interaction energy between the two molecules.

The excited state wavefunction could be described as:

$$\psi_E = c_1\psi_1^*\psi_2 + c_2\psi_1\psi_2^* \qquad \text{Eq. 3.6}$$

where ψ_1^* and ψ_2^* represent excited state wave-functions for molecules 1 and 2, corresponding to the arrows in **Fig. 3. 3**, and c_1 and c_2 are the coefficients to be determined. Then the Schrödinger equation of the excited state is:

$$H(c_1\psi_1^*\psi_2 + c_2\psi_1\psi_2^*) = E_E(c_1\psi_1^*\psi_2 + c_2\psi_1\psi_2^*) \qquad \text{Eq. 3.7}$$

where E_E is the excited state energy, and with an energetic lowering and splitting of the dimer states, the equation could be solve as follow:

$$E_E^+ = E_{G1} + E_{E1} + \iint \psi_1^*\psi_2\,(V_{12})\psi_1^*\psi_2 d\tau_1\tau_2 + \iint \psi_1^*\psi_2\,(V_{12})\psi_1\psi_2^* d\tau_1\tau_2 \qquad \text{Eq. 3.8}$$

$$E_E^- = E_{G1} + E_{E1} + \iint \psi_1^*\psi_2\,(V_{12})\psi_1^*\psi_2 d\tau_1\tau_2 - \iint \psi_1^*\psi_2\,(V_{12})\psi_1\psi_2^* d\tau_1\tau_2 \qquad \text{Eq. 3.9}$$

where E_{E1} is the excited-state energy of isolated molecule 1, which is the same as that of molecule 2 (E_{E2}).

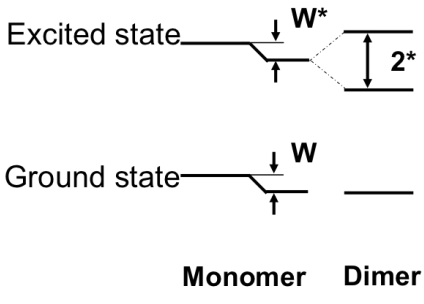

Figure 3. 2: Scheme of the molecular and dimer orbital levels

In **Eq. 3.8** and **3.9**, the third term represents the Van der Waals interaction between the molecule 1 of excited state and molecule 2 of ground state. In **Fig. 3. 2** the W and W* represent the Van der Waals interaction energy in the ground and excited state. The fourth

term is the most important energy term that characterizes the interaction energy due to exchange of excitation energy between molecule 1 and 2. This term is approximated as the point-dipole‑point-dipole interaction between the two exited dyes (Coulomb potential) in both Förster and Kasha theory.

$$\varepsilon = \iint \psi_1^* \psi_2 \, (V_{12}) \psi_1 \psi_2^* d\tau_1 \tau_2 \qquad \text{Eq. 3.10}$$

In the dipole-dipole approximation, according to the **Eq. 3.3-10** V_{12} represent interaction energy due to exchange of excitation energy between molecule 1 and 2. The transition energy for the dimer can be represented as:

$$\Delta E_{di} = \Delta E_m + \Delta W + \Delta\varepsilon \qquad Eq. 3.11$$

Where ΔW is the difference in Van der Waals energy between ground and excited states related to the third term in **Eq. 3.8- 9**, The exciton splitting term $\Delta\varepsilon$ in the point-dipole point-dipole approximation, is expressed as:

$$\Delta\varepsilon = \frac{\boldsymbol{M_1} \cdot \boldsymbol{M_2}}{r^3} - \frac{3(\boldsymbol{M_1} \cdot \boldsymbol{r})(\boldsymbol{M_2} \cdot \boldsymbol{r})}{r^5} \qquad \text{Eq. 3.12}$$

where M_1 and M_2 are the transition moments for the singlet-singlet transition in the monomer 1 and 2, respectively. *r* is the centre to centre distance between molecules 1 and 2 (position vector of the dipole 2 from dipole 1 as origin), and is the dot product or scalar product between two vectors. **Fig. 3. 4**. This energy is far greater than the Van der Waals interaction ΔW, ΔW ≪ Δε. We can neglect the third term of **Eq. 3.8-9**.

So the exciton model describes the resonance splitting of the aggregate molecular energy levels, which were non-degenerate in the individual molecules.

Upon the dimerization, the excited-state levels of the dimer split into two levels of symmetric (ψ_E^+) and anti-symmetric coupling (ψ_E^-), **Eq.3.13-14** according to the arrangements of the transition moments **Eq.3.8-9**.

$$\psi_E^+ = \sqrt{\frac{1}{2}}(\psi_1^* \psi_2 + \psi_1 \psi_2^*) \qquad \text{Eq. 3.13}$$

$$\psi_E^- = \sqrt{\frac{1}{2}}(\psi_1^* \psi_2 - \psi_1 \psi_2^*) \qquad \text{Eq. 3.14}$$

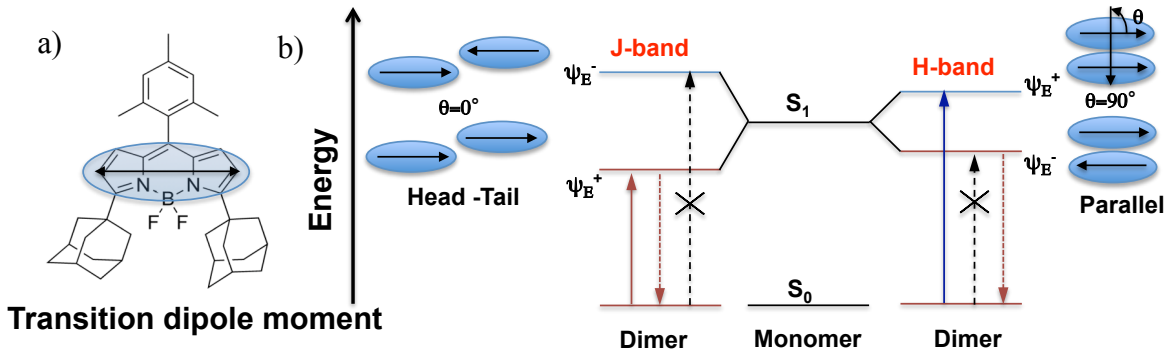

Figure 3. 3: a) Chemical structure of Adambodipy molecule. Arrow shows the transition moment b) The exciton-coupling model explains the spectral shifting related to the molecular packing structure. Excited-state levels of the monomer split into two levels in dimer, symmetric (ψ_E^+) and anti-symmetric coupling (ψ_E^-),) of excitons. Red, blue solid line correspond to red and blue shift, black dash line correspond to forbidden transition.

With the formation of a dimer, we will observe several spectral changes experimentally, and they are:

(a) Displacement of emission and absorption bands relative to the monomer,

(b) Splitting of spectral lines with a corresponding change in the polarization properties,

(c) Variation in the selection rules and oscillator strength for optical transitions.

And all these changes increase with the extent of the aggregation. The splitting will double in infinite stacks of molecules such as J- and H- aggregates. They will be observed in the crystalline phase of the Adambodipy in our study.

3.1.3.1 J-aggregate and H-aggregate

Some molecular aggregates consisting of organic dyes are remarkable in exhibiting an intense and very narrow absorption peak, which could be red-shifted compared to the absorption region of monomer, or else, shifted to higher energies. This red-shifted band are now usually referred to J-band, after its discoverer Jelly (1936), while H-band (hypsochromic shift) correspond to the blue shifted band. These appearances were ascribed to the formation of molecular aggregates. The appearance of J and H-band depends on the angle between the dipole moments of dye molecule in the aggregate and the long axis in the aggregate. And it is the strong Van der Waals force that causes aggregation of dye molecules.[10] The common forms of aggregations are J-type, H-type. (**Fig. 3. 3**)

According to the exciton theory of Kasha and co-wokers, for J-aggregate, only the transitions to the low energy states of the exciton band are allowed, see **Fig. 3. 4** J-aggregate

are characterized by a high fluorescence rate while H-aggregate are characterized by a large Stock-shifted fluorescence that has a low fluorescence rate. Assuming a constant non-radiative deactivation rate, it is often assumed that J aggregates have a better fluorescence yield than the corresponding H aggregates.

The exciton band splitting in a molecular dimer with parallel transition dipoles oriented like in **Fig. 3.4** is given by **Eq. 3.15**[11]

$$\Delta\varepsilon = \frac{2|\boldsymbol{M}|^2}{r^3}(1 - 3cos^2\theta) \qquad \text{Eq. 3.15}$$

Where θ is the angle between the two dipoles $\boldsymbol{M}_{1,2}$, r is the distance between the dipoles. The exciton splitting is zero when the value of $\theta = arccos\frac{1}{\sqrt{3}} = 54.7°$, so the dipole-dipole interaction is zero for this packing orientation of transition moments.

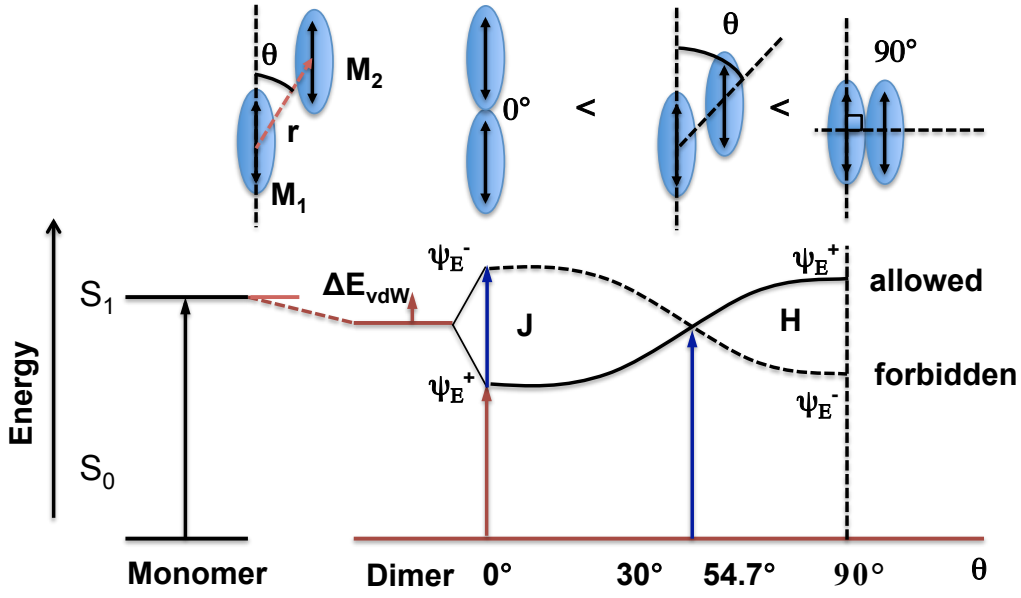

Figure 3. 4: Exciton band energy diagram for molecular dimers with coplanar transition dipoles inclined to interconnected axis by angle θ as illustrated above. For parallel-aligned dimers the optical excitation is only allowed from the ground state to one of the two excitonic states depending on the angle θ. When θ<54.7° the lower energy state is allowed leading to a J-band, while for θ>54.7° the allowed state is at higher energy leading to a H-band. ΔE_{vdW} represents the difference in Van der Waals interaction energies between ground and excited states. (full line: allowed electronic transition state; dotted line, forbidden electronic state; ovale-shaped object : monomer unit ; double arrow : transition moment) [11]

So the J- and H-aggregates are distinguished by the different angle θ between the molecular transition dipole moments and the long aggregate axis. When θ>54.7, H-aggregates are formed. In contrast, J-aggregates molecules are arranged in head-to-tail direction or coplanar displacements with θ<54.7. According to the **Fig. 3. 4**, for the special case of an H-aggregate, only transitions to the higher energetic excited state are allowed, whereas in a J-aggregate only transitions to the lower energetic state are allowed.

3.2. Organic Solids

3.2.1. History of the Exciton theory

We have started by considering the tutorial sample of a molecular dimer, and then have made the step to multi-molecular systems in one dimension. Excions theory in atomic lattices was further developed by Frenkel and then extended to molecular aggregate by Davydov (1948)[12], for which we deal with the Davydov splitting, and geometry-determined energy transfer. After, McRae has extended Simpson and Peterson's analysis of the interaction of vibronic excitons in dimers and crystals. [11,13]

3.2.2. Exciton theory for organic solids

Excitons are electronic excitations of dielectric solids and clusters that are important as a participant in phenomena of optical response of these materials, and responsible for energy transport processes, such as absorption, emission, photoconductivity and photovoltaic effect. Excitons are usually classified into two types, Frenkel excitons and Wannier–Mott excitons[14]. The difference lies in the typical separation between electron and hole.

As shown schematically in **Fig.3. 5**, for Frenkel excitons, a electron-hole pair occurs on the same molecule or atom, thus it is a small-radius exciton(<5Å) where the molecules are far apart compared with the orbit of the electron in the exciton state and the binding energy is large (~1ev).

In contrast, for the Wannier–Mott exciton, the electron–hole pair is delocalized on many molecules. The radius of the exciton is more than an order of magnitude lager than the intermolecular separation (~40-100 Å), thus the separation is much larger than a single molecule or atom with small binding energy (~1 meV).

For organic crystals, in which the intermolecular bonding is mainly of weak Van der Waals type, the Frenkel exciton theory is most widely used. In the other case, the Wannier-Mott exciton is important in inorganic semiconductors with strong bonding.

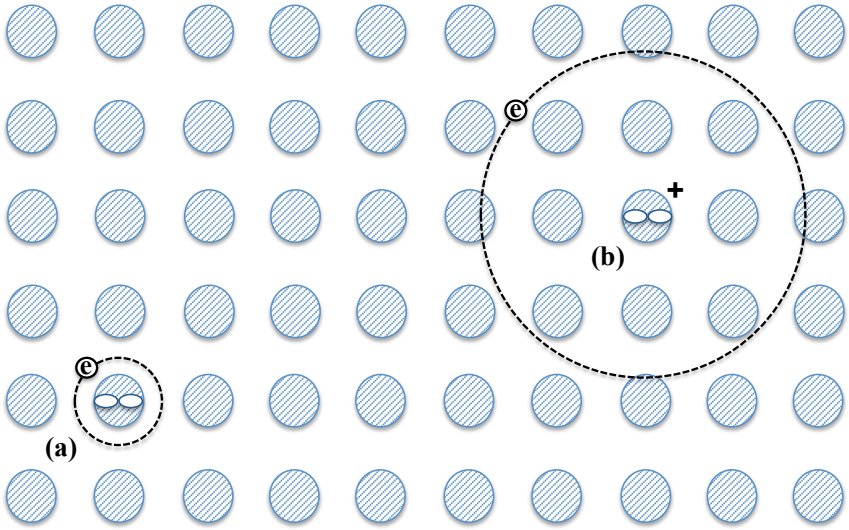

Figure 3. 5: Illustrating the limiting cases of small and large excitons radii for Frenkel excitons (a) and the Wannier-Mott exciton (b). In both cases, there is internal motion of an electron around a hole and the pair moves through the lattice as a unit.

3.2.3. The Frenkel exciton Hamiltonian

As stated in the introduction, we are interested in the optical properties of organic dye molecular aggregates, which have large transition dipole moments so that they interact strongly with light. Due to the strong interactions between the molecules, many molecules will coherently share an excitation in such an aggregate. In addition, the number of dye molecules can affect the spectroscopic behavior.

Let us expand the molecular exciton theory from a dimer to aggregate involving N molecules, by index $N=1,2,.....i,j$. Then assume that every molecule in the aggregate has only two states. The general Frenkel exciton Hamiltonian in the Heitler-London approximation is then given by[15,16]:

$$H = \sum_{i,j=1}^{N} H_i + V_{ij} = \sum_{i=1}^{N} E_i |i\rangle \langle i| + \sum_{i \neq j}^{N} J_{ij} |j\rangle \langle i| \quad \text{Eq. 3.16}$$

where $|i\rangle$ corresponds to a state where molecule i is in the excited state while all others are in their ground state, E_i is excitation energy of molecule i in the aggregates neglecting the dipolar interaction but including the inhomogeneous broadening due to the effect of disorder

imposed by the surrounding, and V_{ij} is the dipole-dipole interaction operator between molecules i and j. J_{ij} is the coupling element of the matrix that represents V_{ij} in the orbital base $|i\rangle$.

Assuming point dipoles, the matrix element can be written as:

$$J_{ij} = \frac{\vec{\mu}_i \cdot \vec{\mu}_j}{|\vec{r}_{ij}|^3} - 3\frac{(\vec{\mu}_i \cdot \vec{r}_{ij})(\vec{\mu}_j \cdot \vec{r}_{ij})}{|\vec{r}_{ij}|^5} \qquad \text{Eq. 3.17}$$

Where $\vec{\mu}_i = \mu_i \hat{e}_n$ is the transition dipole moment vector of molecule i with length μ_i, and $\vec{r}_{ij} = \vec{r}_i - \vec{r}_j$ is the relative position of the molecules i and j.

The equation could be rewritten in order to express transition dipole moments in Debye:

$$J_{ij} = A\,\frac{\vec{\mu}_i \cdot \vec{\mu}_j}{|\vec{r}_{ij}|^3} - 3\frac{(\vec{\mu}_i \cdot \vec{r}_{ij})(\vec{\mu}_j \cdot \vec{r}_{ij})}{|\vec{r}_{ij}|^5} \qquad \text{Eq. 3.18}$$

In which A=5.04cm^{-1}nm^3/Debye^2 is a numerical constant, J_{ij} is expressed in cm^{-1}, the transition moments $\vec{\mu}_i$ and $\vec{\mu}_j$ are in Debye (1 Debye =3.33×10^{-30} Coulomb meter), and r in nanometers, $\vec{r}_{ij}$ is the vector between the two molecules with a norm $|\vec{r}_{ij}|$ equal to their distance in nanometers.

Diagonalization of the N×N matrix H_{ij} Hamiltonian gives N eigenenergies and eigenvectors (one transition per chromophore):

$$H = \sum_k^N E_k |k\rangle \langle k| \qquad \text{Eq. 3.19}$$

$|k\rangle$ are the eigenvectors

$$|k\rangle = \sum_{i=1}^{N} c_i^k \, |i\rangle \qquad \text{Eq. 3.20}$$

Then the transition moments of the exciton k are given by

$$\vec{\mu}_k = \sum_i \mathrm{c}_\mathrm{i}^\mathrm{k}\, \vec{\mu}_i \qquad \text{Eq. 3.21}$$

where $\vec{\mu}_i$ is the transition moment of molecule *i* in the aggregate. The amplitude of the transition moment as well as the oscillator strengths can be obtained according to **Eq.2.14** in Chapter 2.

3.3. Adambodipy solid phase

3.3.1. Crystallization of Adambodipy derivatives

From a previous work **(§ 2.3.6.**), we got the curve of solubility of the Adambodipy molecule in a THF-EtOH-water mixture. The dissolution of raw Adambodipy crystals was done in several THF-EtOH-water mixtures. The clear supernatant was then collected, analyzed by spectrophotometry and compared to a calibration curve, and the graph was shown in **(§ 2.3.6. Fig. 2. 9)**

Based on this figure we have prepared samples at fixed Adambodipy concentration (0.2, 0.01 or 0.002 mg.mL^{-1}) in THF-water mixtures with various amount of water. For each Adambodipy concentration the water percentages in the mixtures were chosen in order to reach a low supersaturation. The lines drawn on the graph indicates the water percentage expected to reach the saturation. For example, for an Adambodipy concentration of 0.2 mg.mL^{-1}, the supersaturation must be reached for water content over 40% (over 70% for 0.01 mg.mL^{-1}, and over 80% for 0.002mg.mL^{-1}). The mixtures were done by adding water, under vigorous mixing by a vortex mixer, in a solution of Adambodipy in THF.

The Adambodipy-THF-water mixtures were prepared from two mother solutions of Adambodipy in THF at 1 and 0.2 mg.mL^{-1}, respectively noted S1 and S2. The following tables indicate the volumes added.

Sample	V_{S1} (1mg.mL^{-1}) µL	V_{THF} µL	V_{water} µL	WATER w/w %
C1	200	620	180	20
C2	200	526	274	30
C3	200	430	370	40
C4	200	332	468	50

Table 3. 1: Samples prepared to reach an Adambodipy concentration of 0.2 mg.mL^{-1} with water content from 20% to 50%.

Sample	V_{S2} (0.2mg.mL^{-1}) µL	V_{THF} µL	V_{water} µL	WATER w/w %
1	200	2700	1104	30
2	200	1916	1884	50
3	200	1513	2287	60
4	200	1100	2700	70
5	200	677	3123	80
6	200	244	3556	90

Table 3. 2: Samples prepared to reach a Adambodipy concentration of 0.01 mg.mL^{-1} with water content from 30% to 90%.

The more diluted solutions samples were prepared from the previous ones.

Sample	$V_{Sample\ i}$ (0.01mg.mL^{-1}) µL	V_{THF} µL	V_{water} µL	WATER w/w %
A	Sample 1: 1000	2896	1104	30
B	Sample 2: 1000	2116	1884	50
C	Sample 4: 1000	1300	2700	70
D	Sample 6: 1000	444	3556	90

Table 3. 3: Samples prepared to reach an Adambodipy concentration of 0.002 mg.mL^{-1} with water content from 30% to 90%.

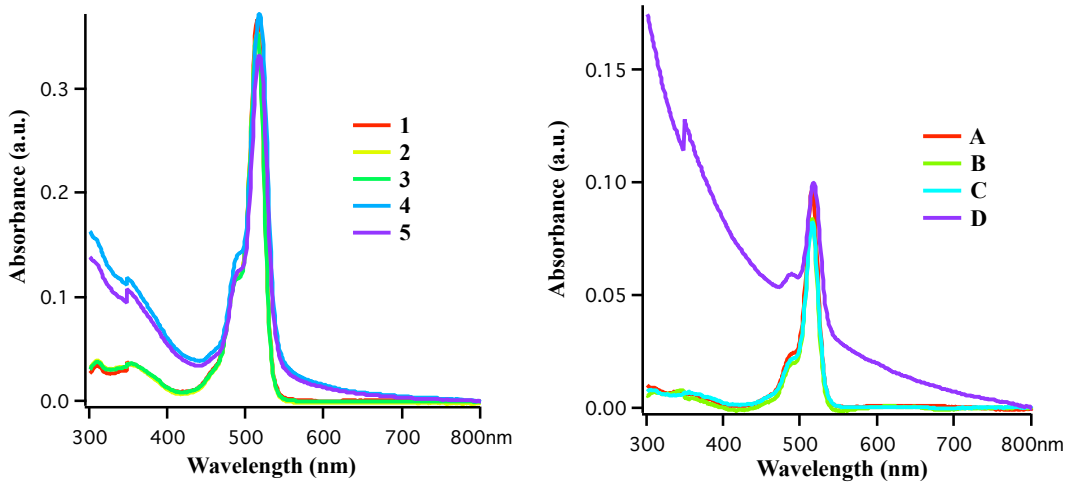

Figure 3. 6: Absorbance spectrum of the samples 1~5 and samples A~D, with conditions according to the tables above.

For the more diluted mixtures, (samples 1 to 3 and A to C), no micro-sized crystals were detected in the flask, but the absorption spectrum shows that particles were produced for samples 4,5 and D, as the baselines drift. The baseline drifts when there are particles with size in the same order of magnitude than the wavelength. Due to the presence of small particles, samples 4,5 and D exhibit pink color solution whereas the others still have the typical yellow color of the Adambodipy solution. The small decrease of the absorbance can be due to a shadowing effect or sedimentation.

According to the experiments, by pouring under vigorous mixing a volume of water into Adambodipy organic mixture of THF/EtOH (3/7 v/v) we obtain a 0.2 $g.L^{-1}$ of Adambodipy solution in a mixture containing water 40% w/w. This low supersaturation favours the formation of micro-sized needle-shaped crystals, which could be seen in the **Fig.3.7** below. The procedure was reproducible.

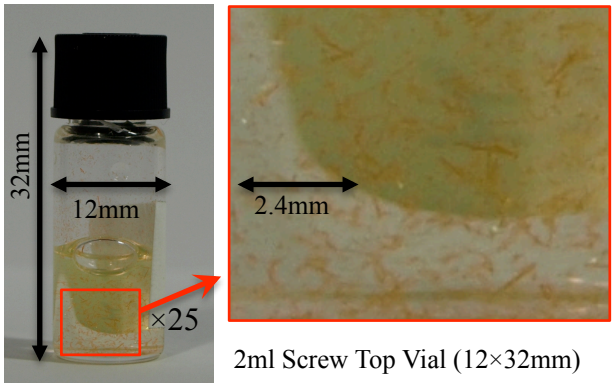

Figure 3. 7: micro-sized needle-shaped crystals samples in 2ml screw top vial.

3.3.2. Description of Adambodipy crystal

3.3.2.1. Single-crystal X-ray diffraction and crystallography

The large Adambodipy crystals suitable for X-ray diffraction analysis were obtained by evaporation of a solution of Adambodipy in CH_2Cl_2.

Then collected data are shown in **Table 3. 4,** also the stereo structure of one unit cell of this crystal was shown in **Fig. 3. 8 (a)**

Formula	$C_{38}H_{45}F_2N_2$
Mr $g.mol^{-1}$	578.57
Space Croup	P $2_1/c$

Cell Length (Å)	*a* 14.0557(3), *b* 11.4779(3), *c* 19.3737(13)
Cell Angles (°)	*a* 90.00, *b* 98.905, *c* 90.00
Volume ($Å^3$)	3087.9(2),
Z, Z'	Z: 4, Z': 0
ρcalcd $g.cm^{-3}$	1.245
m (mm^{-1})	0.626. 20448
measured reflections	(2qmax = 144.2°)
R_{int}	0.0586

Table 3. 4: Crystallographic data and structure refinement for Adambodipy crystal

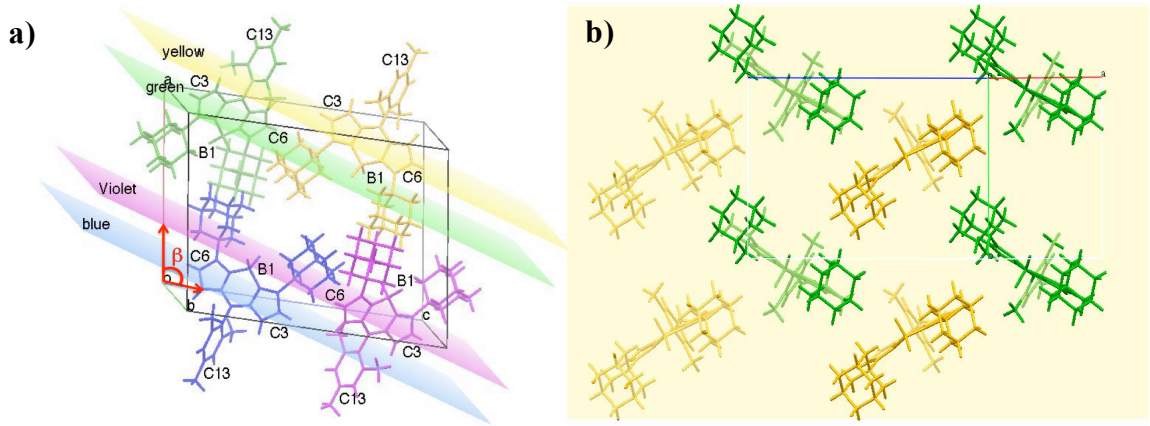

Figure 3. 8: (a) Stereo plot of the unit cell of Adambodiy crystal with the view on the plane hkl=703 defined by the transition moments. (b) herring bone packing structure of the crystal in the front view of the plane.

The Adambodipy molecules organize in a monoclinic structure with 4 molecules per cell. The chromophores make dense layers in the (1,0,0) plane separated by adamantane layers that occupy the centre of the cell. The transition of each molecule is aligned along the vector between the carbon atoms C3 and C6. Two pairs (yellow with blue, and green with violet) of molecule in each cell have one common centre of symmetry at the centre of the cell. For each pair the transition moments are parallel as shown on **Fig. 3. 8** (a) and define two directions in parallel plane with miller index equals to (7,0,3). From the front view of plane (7,0,3), there is a herringbone organization (**Fig. 3. 8** (b)) with an angle of 54.2°. From this

arrangement, we know that the crystal must be dichroic with its transition moments in that plane.[17]

3.3.2.2. Absorption spectra of the crystal

We were able to grow single crystals as thin plates (about 200x20x1 μm^3), and we have recorded the absorption spectra and the images of the micro-crystal (**Fig. 3. 12**) under the Microspectrometer set-up (Nikon TE2000+OceanOptics fiber spectrograph).

Both samples show a strong dichroism between spectra A1, A2 in **Fig. 3. 12,** and B1, B2 in **Fig. 3. 14.** They are recorded from a light polarized along each neutral axis. That agrees with the herringbone arrangement of two directions for the transition moments in the unit cell.

The spectra A and B differ in intensity and broadness because of the "saturation" of our microscopy absorption setup. The measured absorption ABS_M is related to the true absorption ABS_T and the Maximum absorption ABS_{Max} due to the crystal by:

$$ABS_M = ABS_T - \log_{10}(1 + 10^{-ABS_T - ABS_{Max}}) \qquad \text{Eq. 3.22}$$

α is the fraction of the light that is leaking around the sample. This "saturation" is due to the small size of the samples compared to the probing area of the spectrometer. Some part of the light, 10% (for the crystal) to 65% (for cleaved crystal) does reach our detector but does not pass through the sample. "Saturation" is true for both axes to the same extent. The effect of "saturation" on the spectra is more important for the natural crystal than for the cleaved one.

3.3.2.3. Neutral axis determinations

Orthorhombic, monoclinic and triclinic crystals are belonging to the biaxial optical class, and they are known to be birefringent, which means they exhibit two neutral axes with different refractive indexes. When light is polarized along these two neutral axes, there is no rotation of the polarization. According to the X-ray crystallography, the Adambodipy micro-crystal is monoclinic.

The neutral axes of the crystal can be defined by this property, with the crossed polarizer and analyser shown in the following figure.

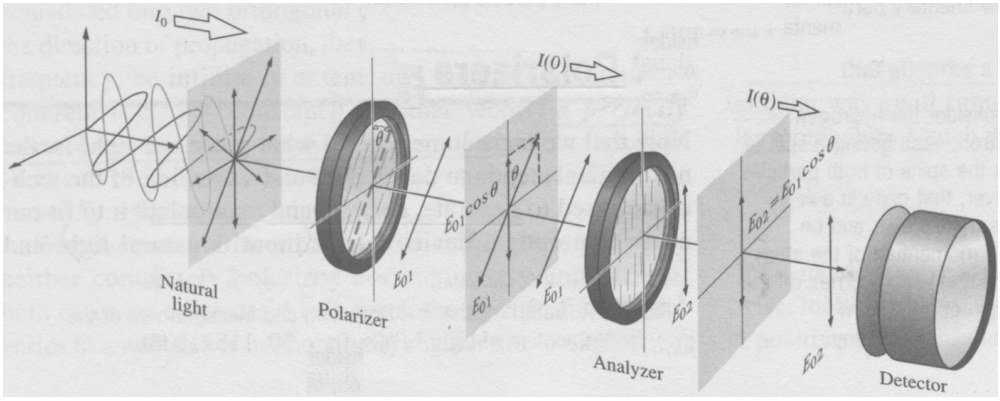

Figure 3. 9: Schematic illustration of a linearly polarized light passing through an analyzer[18].

Crystalline materials may have different indices of refraction associated with different crystallographic directions and propagation direction of light. This optical property of crystals is what we called Birefringence, and could be simply defined as the difference between the maximum and minimum refractive index values.[19]

The refractive index is defined as the velocity of the light in the crystal. According to the calculation, the crystal in **Fig.3. 13, 14** has two refractive indices: one higher, corresponding to slow propagation for light polarized in which charge can move, and another lower one is according to the light polarized perpendicular to this.

3.3.2.4. birefringent property

To determine these two axes, we equipped the microscope with a polarizer crossed to an analyser, with our crystal in between. Through the turning process of the crystal, we obtain two totally dark images, which correspond to the alignment of the polarization of the light with the neutral axes of the crystal. (**Fig. 3. 11**) The transmission images are taken after and noted as A1, A2 axes with angle of 84.2° separately, and shown as follow.

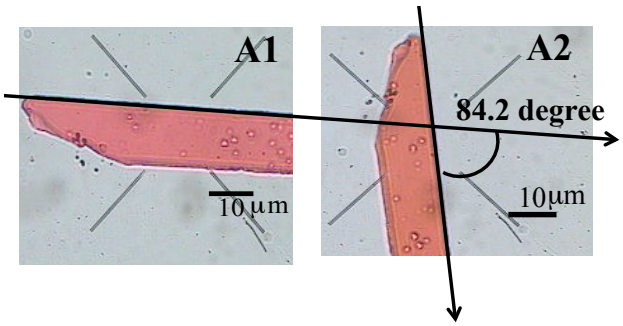

Figure 3. 10: Transmission images for k) and e) position that are obtained in Fig.10, with angle of 84.2°

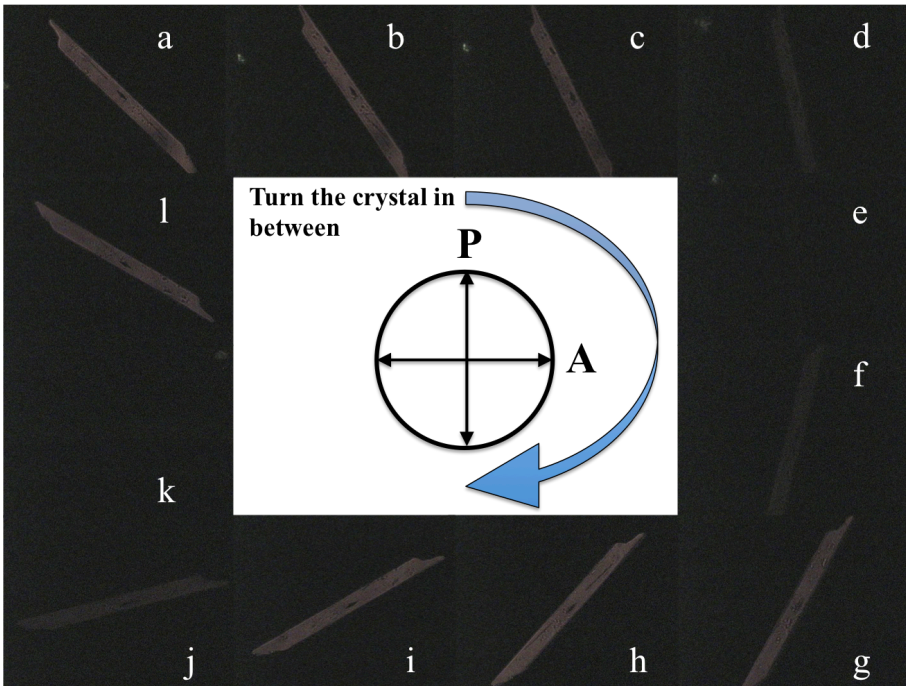

Figure 3. 11: When cross the polarizer and the analyzer, turn the crystal in the middle. Two total black images k) and e) are obtained with alignment of the polarization of the light with the neutral axes of the crystal.

3.3.3.3. Dichroïsm and Refractive index calculation

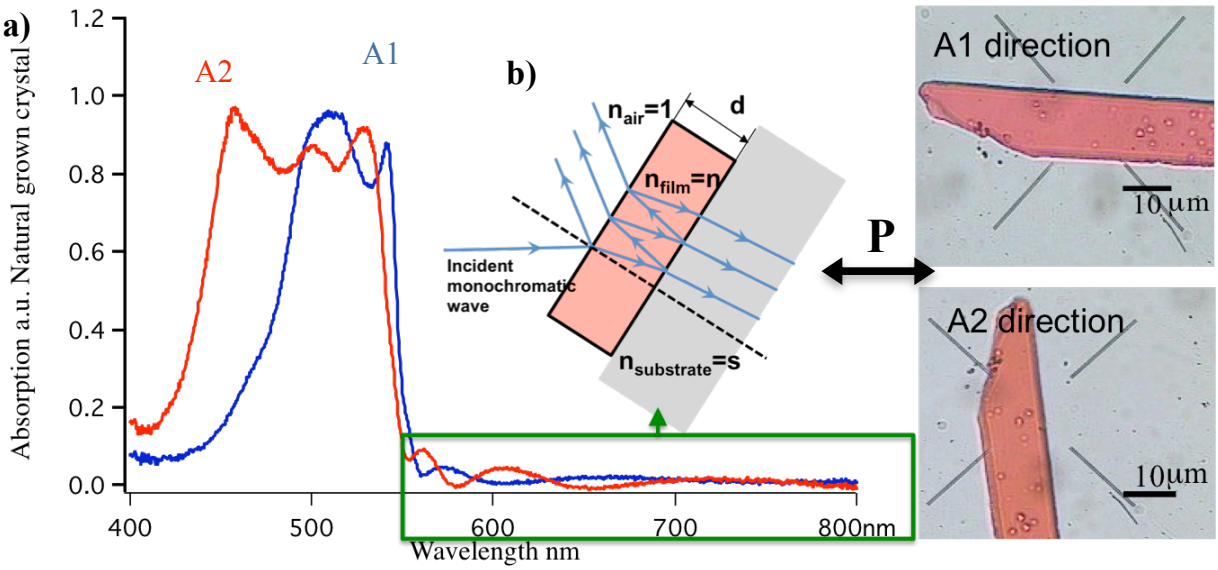

Figure 3. 12: a) Oscillations part of absorption spectra for a neat micro-crystal (A1, A2) with Pictures of the neat micro-crystal aligned according to his two neutral axes with the direction P of the polarizer; b) Reflection and transmission of light by a single film.

We see in **Fig. 3. 12 (a)** the oscillations of the transmitted intensity in a transparent domain beyond 600nm. This is due to reflections and interferences by the parallel faces of the crystal, see the **Fig. 3. 12 (b).** From them, the refractive index and the thickness can be calculated by using the method described by R. Swanepoel[20]. This method is limited to thin films deposited on transparent substrates several orders of magnitude thicker than the thin films, as in this study. **Fig. 3. 13 (a)** shows a magnified part of the transmittance spectrum for the crystal of Adambodipy along the A2 axis that is displayed in **Fig. 3. 12 (a)**. The first step is to calculate the envelope functions of the maximum and minimum transmittance T_M (λ) and T_m (λ). From these curves the refraction index can be calculated using **Eq. 3.23-24**. From the position of the oscillations, we can calculate the thickness of the sample using **Eq. 3.25**.

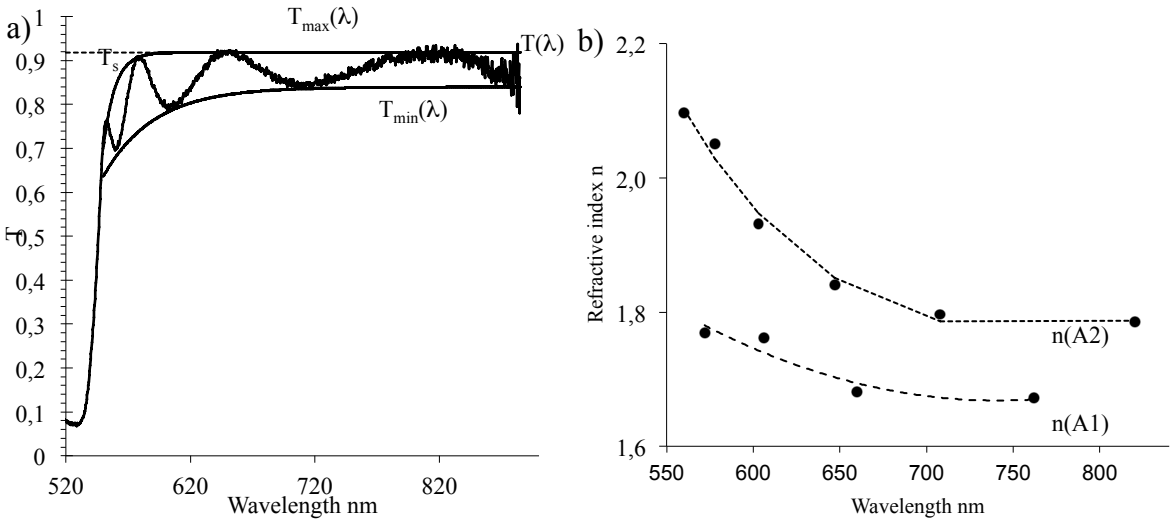

Figure 3. 13: (a) Transmittance spectrum for crystal along A2. The oscillation of the baseline is due to interferences between the two faces of the crystal. The positions and amplitudes of the Maxima and minima T_M and T_m, ($T_{max}(\lambda)$ and $T_{min}(\lambda)$ fit) are used to measure the refractive index and a thickness of 880±30nm. (b) Refractive index n as a function of wavelength along the axis A1 and A2. Dashed lines are fits using Cauchy expression[21] $n=A+B/\lambda^2$.

$$n = \left[N + (N^2 + s^2)^{1/2}\right]^{1/2} \qquad \text{Eq. 3.23}$$

Where

$$N = 2s\frac{T_M - T_m}{T_M T_m} + \frac{s^2 + 1}{2} \qquad \text{Eq. 3. 24}$$

s represents the refractive index of the substrate (in our case s=1.4906, for microscope cover slips No. 1 borosilicate glass, 25 mm × 50 mm, 0.15 mm thickness; VWR, cat. no. 631-0146), and the film thickness can be obtained through the following expression:

$$d = 2\frac{\lambda_1\lambda_2}{2(\lambda_1 n_2 - \lambda_2 n_1)} \qquad \text{Eq. 3. 25}$$

where n_1 and n_2 are the refractive indexes s at wavelengths λ_1 and λ_2 respectively, corresponding to two consecutive extrema. We get the thickness of the sample equals to 820±30nm.

The difference of the two refractive indexes along each neutral axis, Δn ranges from 0.13 to 0.23 according to wavelength ranges from 560 to 800 nm . This confirms the birefringence. It was reproducible for other samples with different thickness.

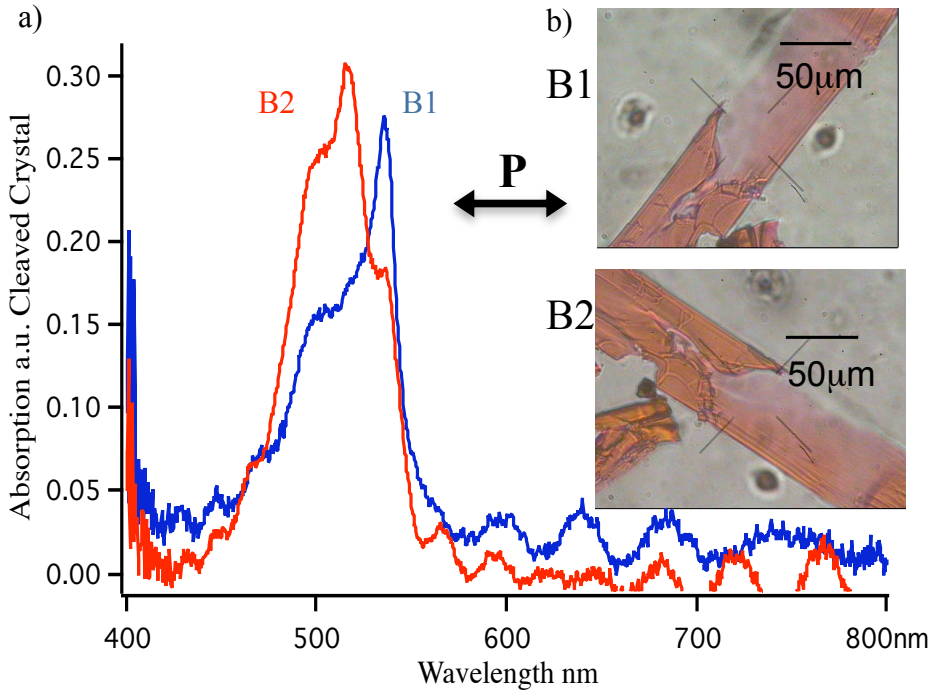

Figure 3. 14: Absorption spectra for a cleaved crystal (B1, B2) along the two neutral axes. b) Pictures of the cleaved crystal aligned according to his two neutral axes with the direction P of the polarizer. The oscillation transmission curves are due to the presence of the tape that is used to cleave the crystal and that cannot be removed without breaking it.

Due to the very high absorbance of Adambodipy crystals, we need thin samples. An "Organic Crystal Cleavage" method was used here to decrease the thickness from hundreds of nanometres to several tenths of nanometres.[22]

Indeed the thinner crystals collected were also smaller since the aspect ratio of the crystal Length/Width/Height is maintained during the crystal growth. In detail, naturally grown crystals were transferred between two transparent tapes. Then, the tape was torn several times until the adhesion force cleaves the crystal. The cleaved crystal remains on the sticky transparent tape. After the determination of the neutral axes by using crossed polarizer and analyser,[23] the spectra B1 and B2 of a crystal after cleavage are given on **Fig. 3. 14 (a).**

The thickness of the single crystal was also examined by intermediate-contact mode AFM, the method and the equipment was introduced in **Chapter 6**. The crystal terraces can be seen on **Fig. 3. 15 (a)** that shows the observation of the crystal surface. **Fig. 3. 15 (b)** gives the thickness plot as a function of the offset (position on the probe in µm). The thickness is 0.68±0.01µm, which fits the value calculated by the transmittance spectrum.

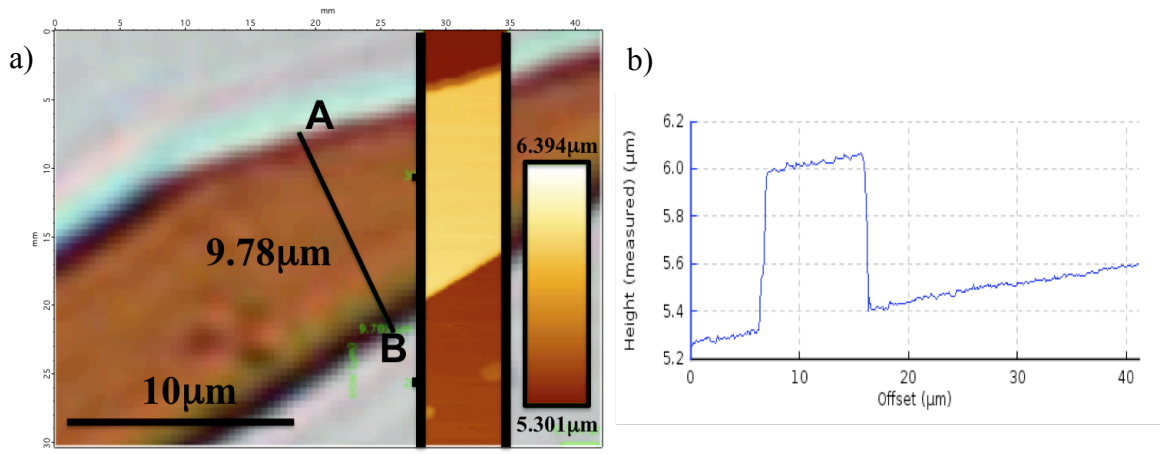

Figure 3. 15: a) Overlay of the transmission and AFM image of an Adambodipy crystal b) the height profile through the line AB. The measured thickness of 660nm can be compared with one deduced from the analysis of the interference pattern in Figure 8.

3.4. Computational model of Adambodipy

To calculate the spectra, we apply a model to describe the interaction between the molecules in the crystal.[24] Let us briefly recall here the molecular exciton theory within the

framework of Frenkel approximation.[25] Since Adambodipy has bulky substituents and despites relatively high oscillator strength of 0.29 (cf. Dipolar coupling calculation), the electronic intermolecular interactions are weak compared to the electronic transition energies. As the fundamental theory was introduced in exciton theory where we have Frenkel Hamiltonian of the aggregates.

3.4.1. Dipolar coupling calculation

The transition dipole moment of Adambodipy is calculated to be 5.6 D from an oscillator strength that is equal to 0.29 according to the absorption spectrum of adambodipy in dichloromethane. This differs from the TDDFT calculations that give a value of 0.56 for that oscillation strength **(§ 3.8.2.4)**

The discrepancy in the measured and the calculated oscillator strength is usual in quantum chemical calculation.[26,27] This is particularly true in the case of Bodipy according to Adamo[28] who explain this difficulty by saying the electronic transition in the case of Bodipy is "not vertical". However, if the absolute value is not correct, the calculation gives two important informations : it gives the vector for the transition dipole and it confirms that it is an intense single transition.

The direction and the magnitude of the transition moment with respect to the molecule can be calculated from TDDFT calculation, but not its position in the molecule. This would require additional computations[28]. For symmetry reasons, the transition moment has to be in the plane of the BODIPY chromophore and perpendicular to the B-C13 direction. There is some uncertainty on its position on the B-C13 line. We have tested various positions around the center of the chromophore. Moving the position of the transition moment inside the molecule does change the calculated spectrum. Assuming a quasi C2 symmetry of the BODIPY chromophore around the C3-C6 axis, we decided to place this position at the middle of the B-C9 segment.

We constructed the interaction matrixes J using the extended dipole approximation according to the **Eq. 3.17**. The positions of the atom have been extracted from the CIF files as crystallographic fractional coordinates. To calculate dipolar coupling, we need distances in nanometers. We have used, for the orthogonal Cartesian coordinates, the one with the X direction along the direction a of the cell and Z direction along c*. The transformation matrix from the crystallographic fractional coordinates to the orthogonal Cartesian coordinates is given by R.Diamond et al.[29]

We have compared the interaction term obtained by the **Eq. 3.17** with the energy splitting of the two first excited states, in a pair of Adambodipy in vacuum. Indeed the coupling element in the interaction matrix can be calculated independently from the full calculation of the dimer.[30,31] Nine pairs that are in Van der Waals contact in the crystal have been identified using Mercury 2.4®, and the energy splitting for two of them have been calculated.[32] We choose the first pair as the one with the strongest H type interaction where the dipolar interaction may fail due to the importance of higher multipolar terms. This pair corresponds to blue and violet molecules with the closest distance of 0.64 nm among the cells **(Fig. 3. 10(a))**. The second pair was chosen as the one with the strongest J type interaction.[33] This pair combines among the cells the closest yellow type molecule and the blue type with distance of 1.07nm **(Fig. 3. 10(a))**.

The results are gathered in table and more data and analysis from TDDFT calculation is provided in the section **§ 3.8.2.4**.

Splitting in cm-1	Dipolar approximation	TDDFT calculation
Closest H Pair	-513	451
Closest J Pair	99	142

Table 3. 5: The energy of interaction for two close pairs in the crystal calculated by the dipolar approximation **Eq. 18** and by a TDDFT calculation of the splitting of the two first LUMO levels of the same pairs in vacuum

The dipolar approximation appears to be a good one. We have thus used it for further calculation.

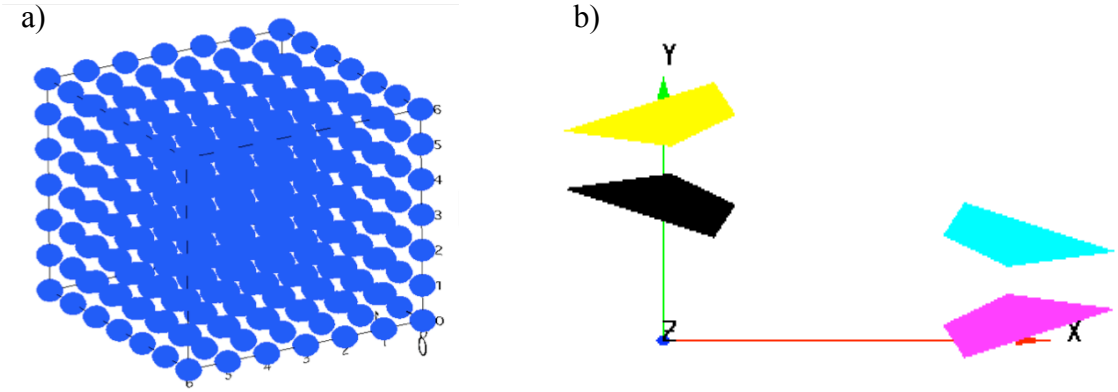

Figure 3. 16: 7×7×7 Cells crystal model (a) used in the computation, each cell contains 4 molecules in (b).

A 7×7×7 Cell crystal model was built and used in the computation. Each cell contains 4 molecules and contributes to 1372 molecules for the simulation. The interaction among those molecules can be calculated by **Eq. 3.18** as coupling term and represent values in matrix shown in **Fig. 3.17.**

Then with the coupling values, all the eigenvectors can be obtained as a linear combination of the localized excited states. Then, the transition dipole moments of the crystal are calculated from the computed eigenvectors from **Eq. 3.21**.

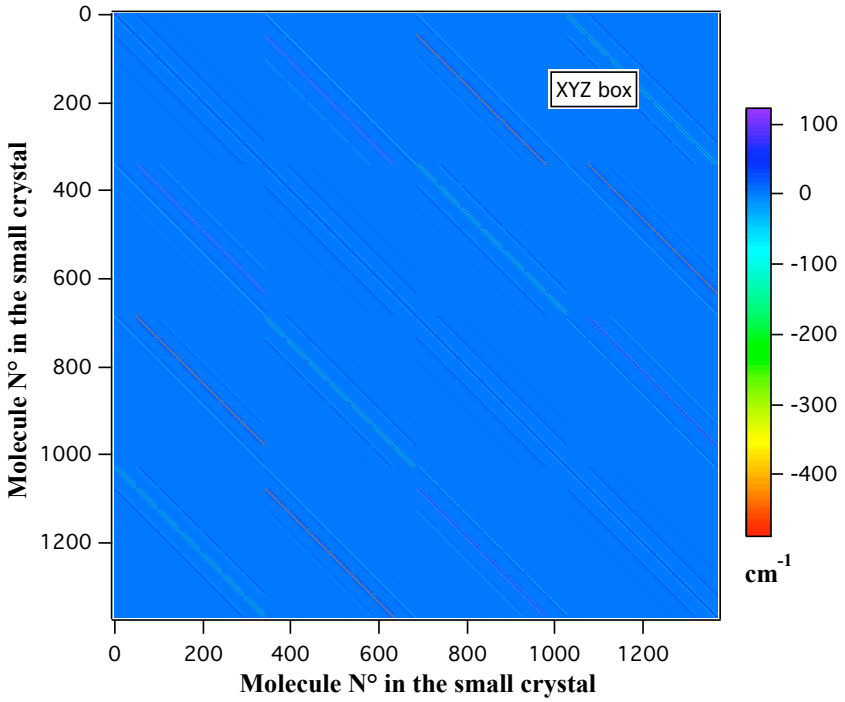

Figure 3. 17: Value matrix from dipole-dipole coupling term over 1372 molecules, with unit (cm^{-1}).

According to the **Fig. 3. 18** in each unit cell, there are 4 transition moments from C3 to C6 corresponding to 4 Adambodipy molecules. And all the contributing transition moments are in the same plane.

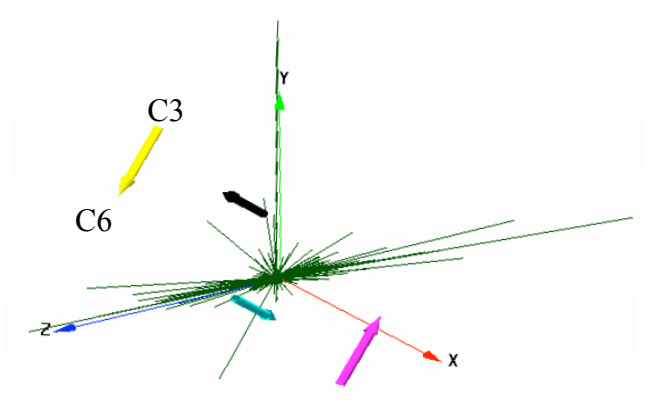

Figure 3. 18: 4 transition moments from C3 to C6 in one unit cell of Adambodipy crystal represented as four-color arrows. The contribution of the molecular transition moments has shown in green solid line on Cartesian coordinate system.

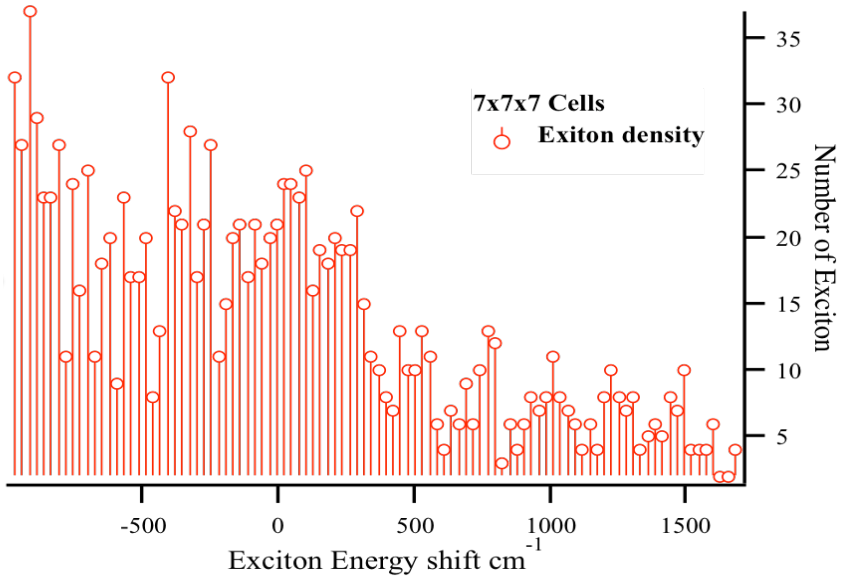

Figure 3. 19: The distribution of 1372 exciton states as a function of their energy (50cm^{-1} width bar).

The numerical diagonalization of $\mathbf{H_0}$ provides N=1372 eigen energies $\mathbf{E_k}$

In Fig. 3. 19, we summarize the calculated relative energies by plotting the density of the exciton states as a function of the exciton energy. We have 1372 eigen energies, which are spread from -800cm^{-1} to +1500cm^{-1}.

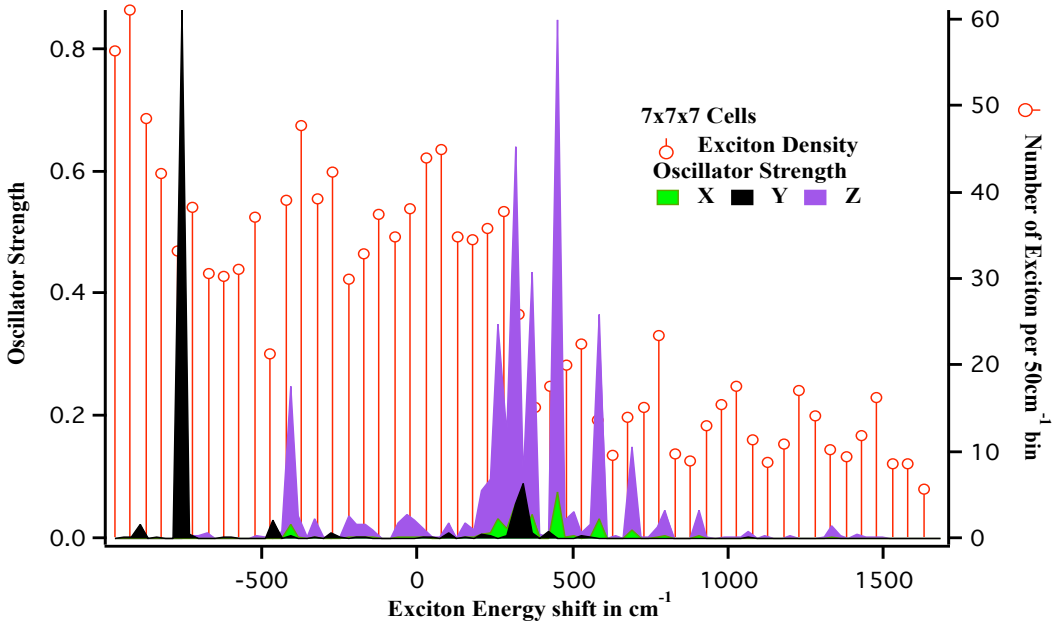

Figure 3. 20: The oscillator strength to each state is known from Eq. 7 and are represented their spectra for the three space directions. X and Y are along the *a* and *b* axis for crystal unit cell respectively. Z is orthogonal to a-b plane.

The oscillator strength can be computed from the eigen vector coordinate using **(§ 2.1.4 Eq. 14)**. Only few of these transitions bear significant oscillator strength. The smaller are the N×N×N crystals, the stronger are the intensities of the transitions at -400cm^{-1} and +325cm^{-1}. The molecules supporting these transitions are indeed at the surface of the nano-crystal (**Fig. 3. 21(b)**). Increasing the number of cells up to 11×11×11 does not significantly improve the calculated spectral density

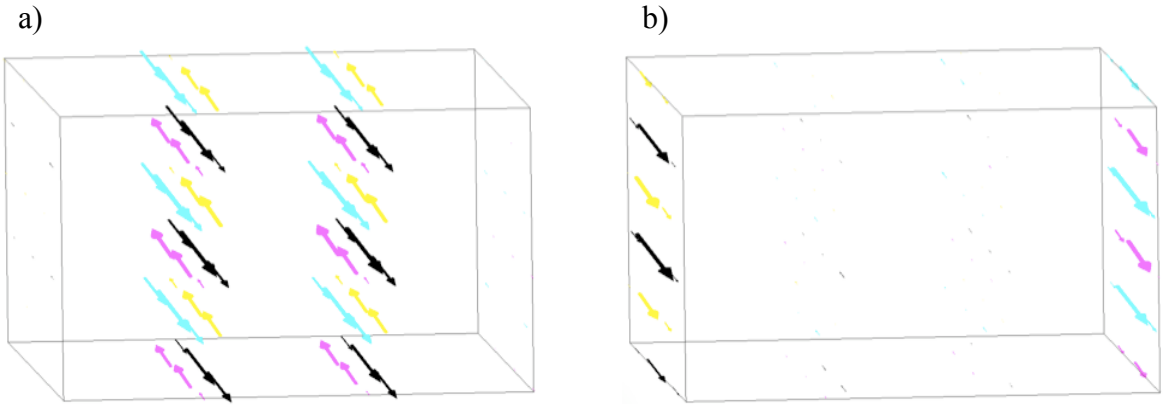

Figure 3. 21: a) The shape of the exciton at -810cm^{-1} in a nanoparticle 4x4x4 with no disorder. b) The shape of the exciton at -325cm^{-1} in a nanoparticle 4x4x4 with no disorder.

According to the calculation, there are three important excitonic transitions in the crystal at -745cm^{-1}, 326cm^{-1} and 460cm^{-1}. Transitions are mainly in the y and z plane. This agrees with the orientation of the molecules in the cell. The electronic transitions of the crystal are in the plane defined by the C3C6 directions (**Fig. 3. 10**).

The absorption spectra are calculated from the transition energies of the perfect crystal of **Fig. 3. 20** by taking into account the spectral broadening that occurs at room temperature. This spectral broadening is due to the limited lifetime of the phase of the excited state. This is the homogeneous line width of the transition. In addition, the fluctuations of the intermolecular interactions in the crystal induce an inhomogeneous broadening.[34] Different ways have been proposed to estimate these broadening.

a)

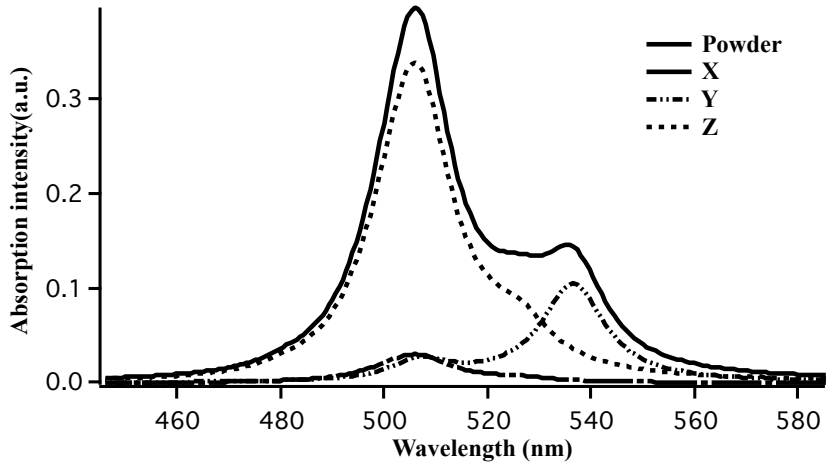

b)

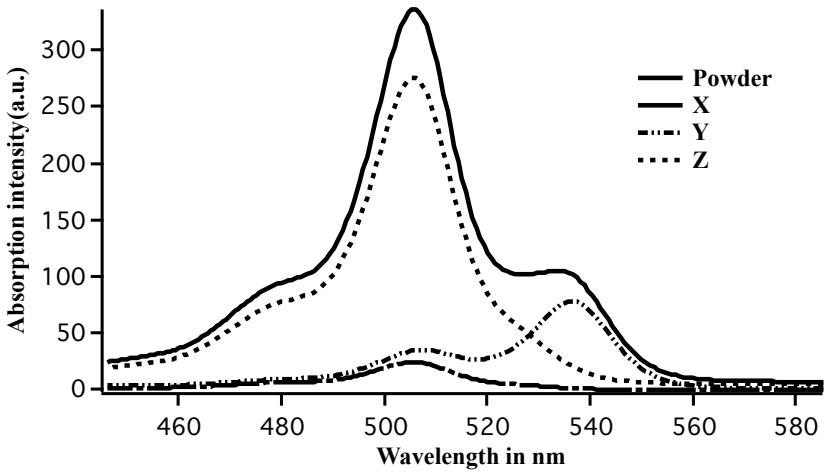

c)

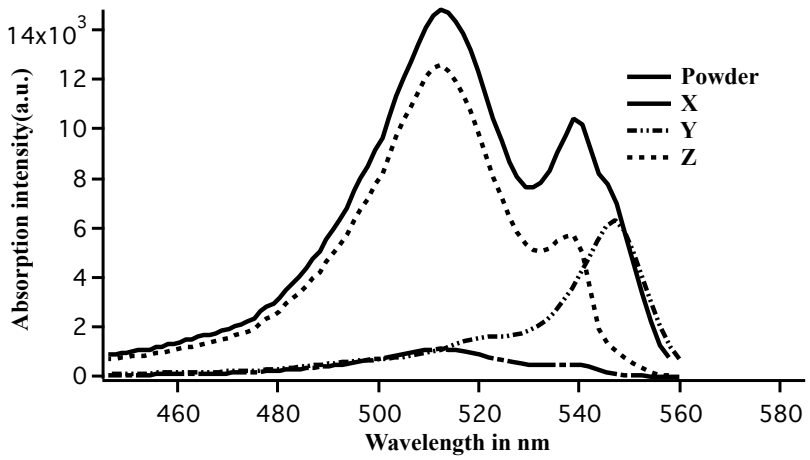

Figure 3. 22**:** Calculated absorption spectra from the transition oscillator strength. a) Lorentzian (linewidth =250cm^{-1}) convolution to account for the homogeneous and inhomogeneous broadening b) convolution by the absorption spectrum of the molecule in solution as an estimate of the broadening in crystal c) and adding a "diagonal disorder" in the coupling matrix before diagonalization. The distribution of the diagonal disorder is that of the molecule in solution.

First, on **Fig. 3. 22(a)** we have convoluted the oscillator strength spectra by a Lorentzian with a linewidth of 250cm^{-1} that fits with the width of the experimental transition at 540nm on spectrum B1 on **Fig. 3. 14**.[35]

Second, the molecules in the crystal interact through their transition moment. But in addition there are steric interactions of the molecule with its neighbors. Assuming that these steric interactions are similar in the solvent and in crystal, we can use the broadening of the absorption spectrum of the molecule in solution as an estimate of the broadening in crystal. We have convoluted the transition probability spectra by the molecule absorption spectrum.[36] (**Fig. 3. 22 (b)**)

Third we can include these steric interactions with neighbors into the calculation by adding a "diagonal disorder" in the coupling matrix before diagonalization. The diagonal elements represent the energy of the molecule not described by the dipolar coupling.[16] The energies where randomly chosen so that their distribution fits the absorption spectrum of the molecule in a solvent. The calculated spectra were then averaged over 500 random trials. The results are displayed on **Fig. 3. 22 (c)** The differences between the different spectra are smaller than the uncertainty of the experimental spectra.

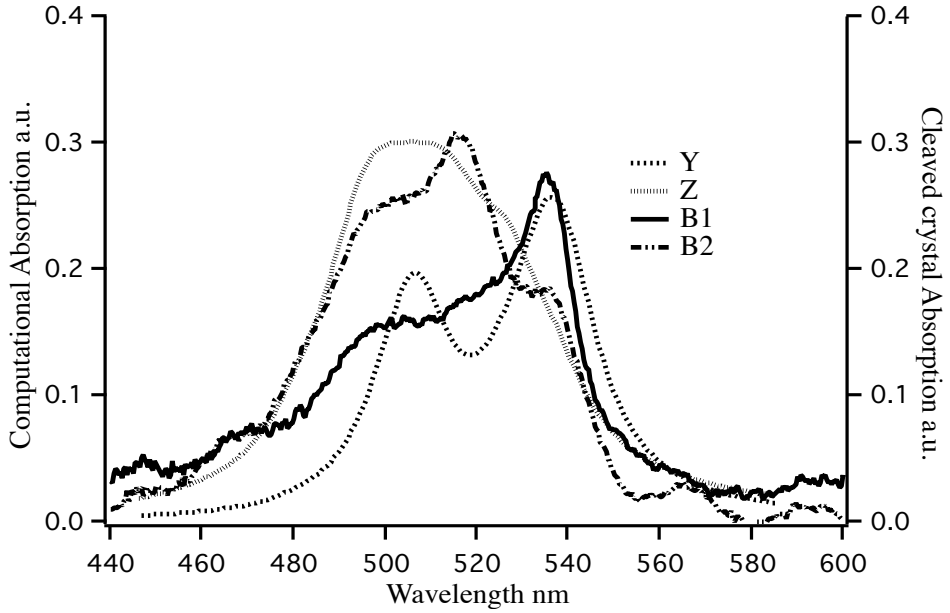

Figure 3. 23: Comparison of the absorption spectra along the two neutral axes B1 and B2 of a sliced crystal with the simulated absorption line shapes. Simulations have been done on a 343 cells Adambodipy crystal in the two orientations Y and Z. In the simulated spectra we have included the saturation effect of our microspectrometer using a fraction for a light leakage of 45% deduced from the measured spectra.

The experimental absorption spectra and the spectra predicted by the Frenkel exciton theory (from **Eq.3.16-21**.) at room temperature T=300 K were compared in **Fig. 3. 23**.

The saturation of the absorption spectra on single crystals prevents to compare precisely the shape of the spectra that have been calculated. But the comparison between experiment and theory confirms the magnitude of the broadening due to the dipolar coupling to a value of 2300cm^{-1} for the Z direction and 500000 cm^{-1} for the Y direction. Experiment and theory agrees about the dichroism and we can attribute the B1 neutral axis to the Y direction of the crystalline structure and the B2 direction to the Z direction. The plane 100 lay flat under the microscope.

After, we use the same formalism to generate the absorption spectrum of amorphous NPs. To generate the amorphous phase in the computer, we have simply allowed the molecule to rotate randomly in the plane of the BODIPY molecule around their center of mass with no translation. This is a simple way to generate amorphous phase with the same density as the crystal. We obtain the spectrum represented on **Fig. 3. 33(d)**. We see that

the amorphous spectrum appears as very close to the molecular spectrum **(Fig. 3. 33(a))** simply broadened by small dipolar interactions. The big difference between the crystalline and amorphous spectra can be explained since, even if the dipole density is the same, the probability to have the close pair with the strong coupling of 513cm^{-1} is much less frequent in the amorphous than in the crystal.

The calculations within the framework of Frenkel exciton theory give a good rationalization of experimental spectra

3.4.2. Emission polarization experiments

3.4.2.1. Linear polarized light

Light can be polarized when it passes through calcite material, sheet polarizers, prism polarizers or miscellaneous polarizers[37].

According to Malus's law, for a linearly polarized light passing through an analyzer , it can be written as: $I(\theta) = I_0 \cos^2 \theta$, where θ is the angle between the transmission axis of the linear polarizer and the polarization axis of the incident light, and $I(\theta)$ is the intensity of a linearly polarized light after it passes through the analyzer(polarizing plate) and I_0 is the intensity of the light incident on the analyzer. Fluorescence intensity changes under polarized illumination.

The two neutral axes from the flat plane of the single crystal with the bottom placed on the silica substrate were determined from the former study on the basis of the crystallographic structure of Adambodipy single crystal. Using this crystal we measured emissions in various directions, also polarized emissions were studied as well.

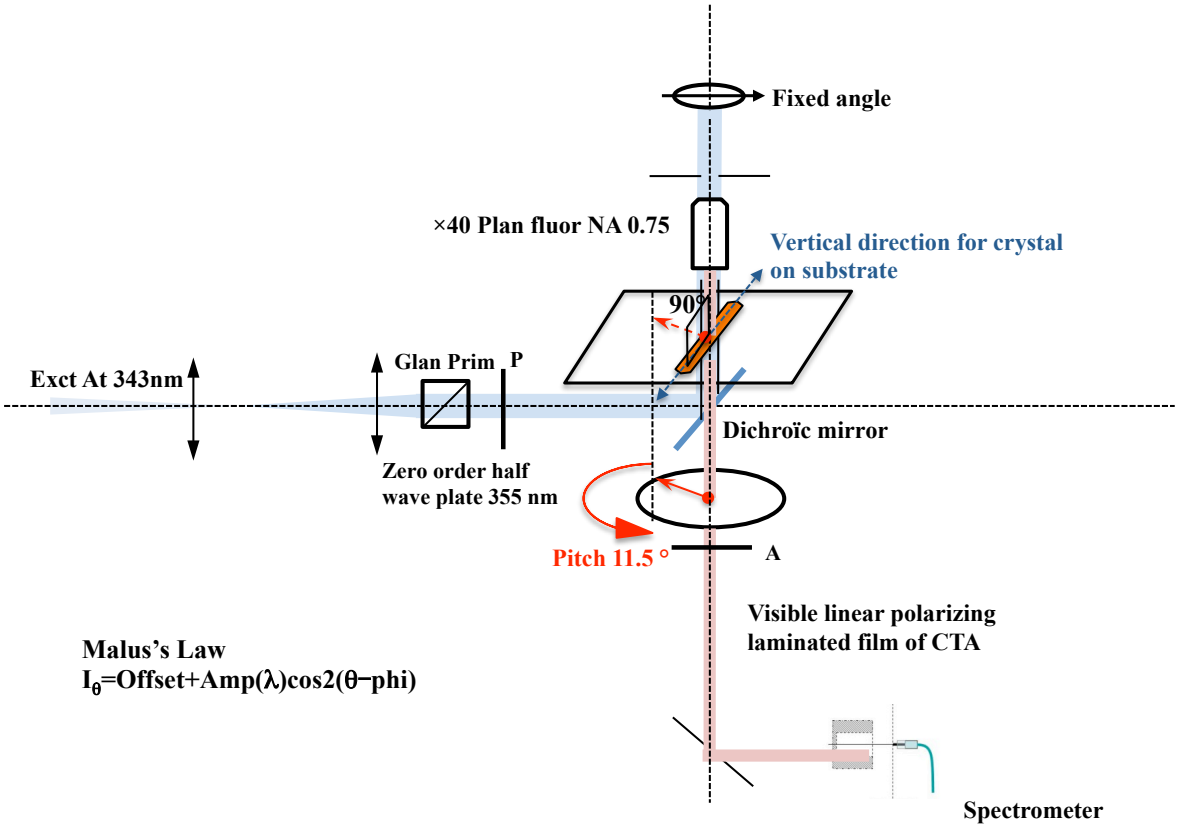

Figure 3. 24: Schematic diagram of experimental setup for emission polarization measurement for Adambodipy crystal.

Fig. 3. 24 schematically shows the experimental setup for the spectrum measurements of the crystal. The measurement was done with the crystal fixed on the substrate. The excitation light polarized with a fixed angle along the long crystal axis was incident perpendicularly on to the flat crystal plane.

3.4.2.2. Emission polarization property

To examine the polarization feature of the emission, the excitation polarization was fixed at 0°, 90°, and 135° with respect to long axis. The excitation wavelength was set at 343 nm, the third harmonic of our laser. The polarization direction of the polarizing plate, the analyzer was incrementally rotated from 0° (along the long axis of the crystal) to 180°, every 11.25°, with the excitation polarization direction disrotated. Below we summarize experimental results according to these measuring conditions in **Fig. 3. 25**:

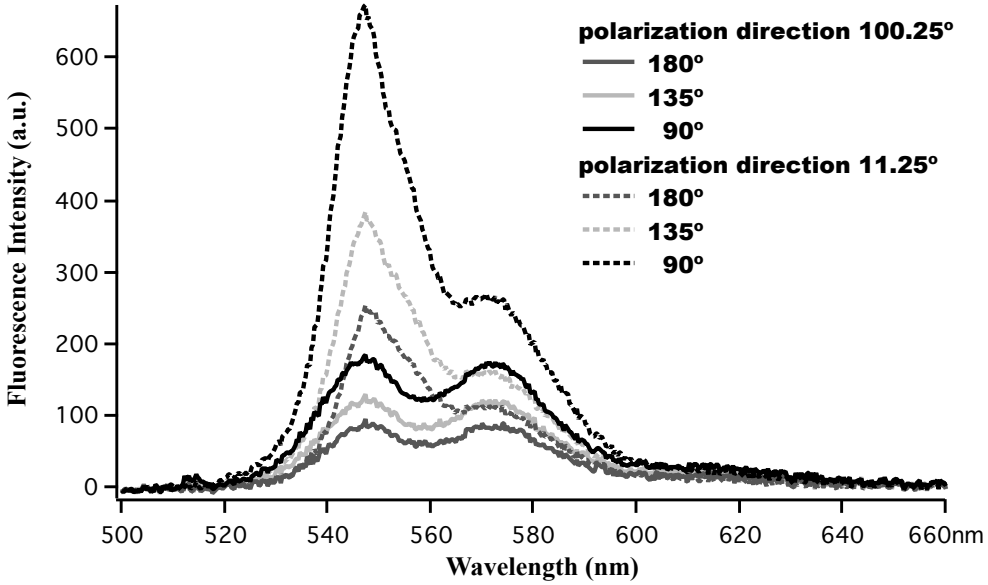

Figure 3. 25: Polarized emission spectra of the crystal excited with the polarization light at angle of 90°, 135° and 180°. Then for each angle, the fluorescence intensity of the same part of the crystal with polarization direction 11.25° and 100.25° of the polarizing plate are collected and represented as dashed line and solid line respectively.

Whatever the excitation polarization, the fluorescence spectra are the same. The band at 547nm is highly polarized parallel to the long axis of the crystal.

All the emission spectra are composed of two major bands occurring at 547nm and 570nm and a minor one at 620nm from the same part of the crystal.

Fig. 3. 26 shows the emission spectra as a function of the direction of the analyser in radian for the range of wavelength 485-685nm.

The fluorescence collected through a polarizer making an angle θ with the axis A1 is a function of the orientation of the transition dipoles in the crystal but also of the birefringence of the crystal.

The birefringence of the crystal will rotate the polarization of fluorescence by an amount that depends on the depth at which the fluorescence is produced in the crystal. This is complex to model. But we want to attribute the fluorescence bands to different emitters in a range from 560nm to 800nm. The birefringence varies smoothly from 0.13 to 0.23. Thus we shall interpret the abrupt change in polarization to change in emitters.

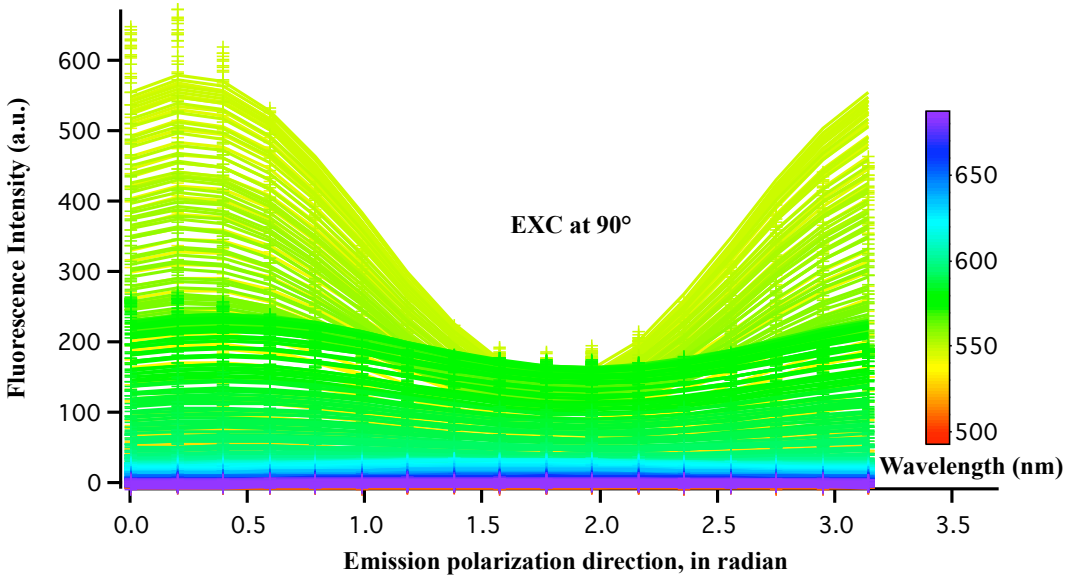

Figure 3. 26: Polarized emission spectra of the crystal excited with the polarization light at angle of 90°, Excitation 343nm wavelength. Fluorescence intensities are collected at wavelength between 485 and 685nm as the function of the analyzer angle in radian (0-3.14).

The angular dependence that is observed has been adjusted as:

$$I_\theta = \text{Offset}(\lambda) + \text{Amp}(\lambda)\cos 2(\theta - 0.2) \qquad \text{Eq. 3. 26}$$

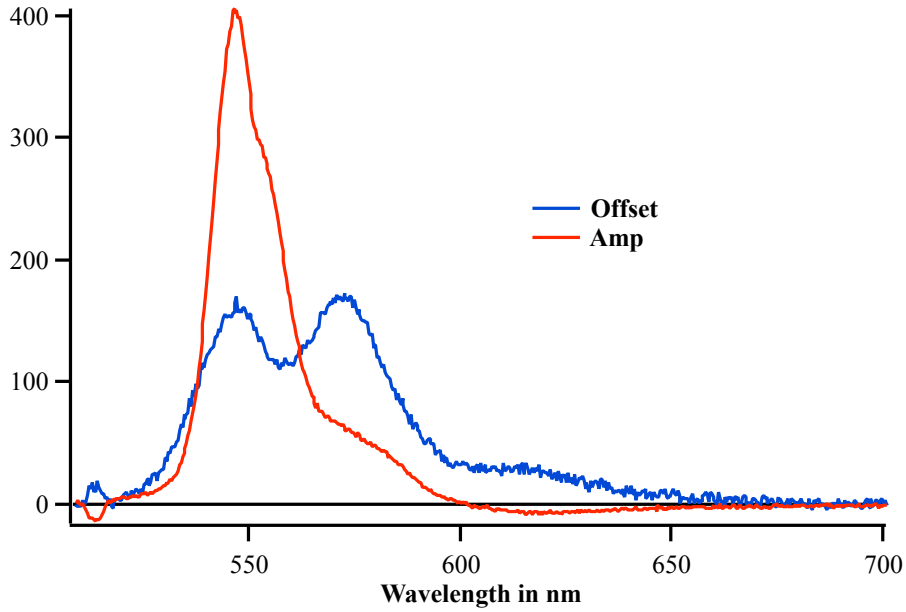

Figure 3. 27: The fluorescence angular dependent offset and amplitude plotted as the function of wavelength. Blue-offset, Red-Amplitude, according to the function:
$I_\theta = \text{Offset}(\lambda) + \text{Amp}(\lambda)\cos 2(\theta - 0.2)$

The spectrum of the polarization independent part of the fluorescence shows three bands at 547nm, 570nm and 620nm. The spectrum of the polarization dependent part of the

fluorescence shows that these three bands differ in their polarization properties: the 547nm band is polarized along A1; the 620nm band is polarized along the A2 direction.

3.4.3. Calculation of the fluorescence spectra

The emission spectra can be calculated using the dipolar-coupling model.

Each exciton can contribute to the fluorescence proportionally to its population, which is given by the Boltzmann equilibrium. Indeed the equilibration time between excitons can be calculated and is in the range of femtosecond[38]. On the **Fig. 3. 28** the fluorescence spectrum has been calculated based on the Boltzmann distribution among excitons and the oscillator strength of the excitons. The broadening of the spectrum has been done using the convolution of the 0K spectrum by the room temperature absorption spectrum.

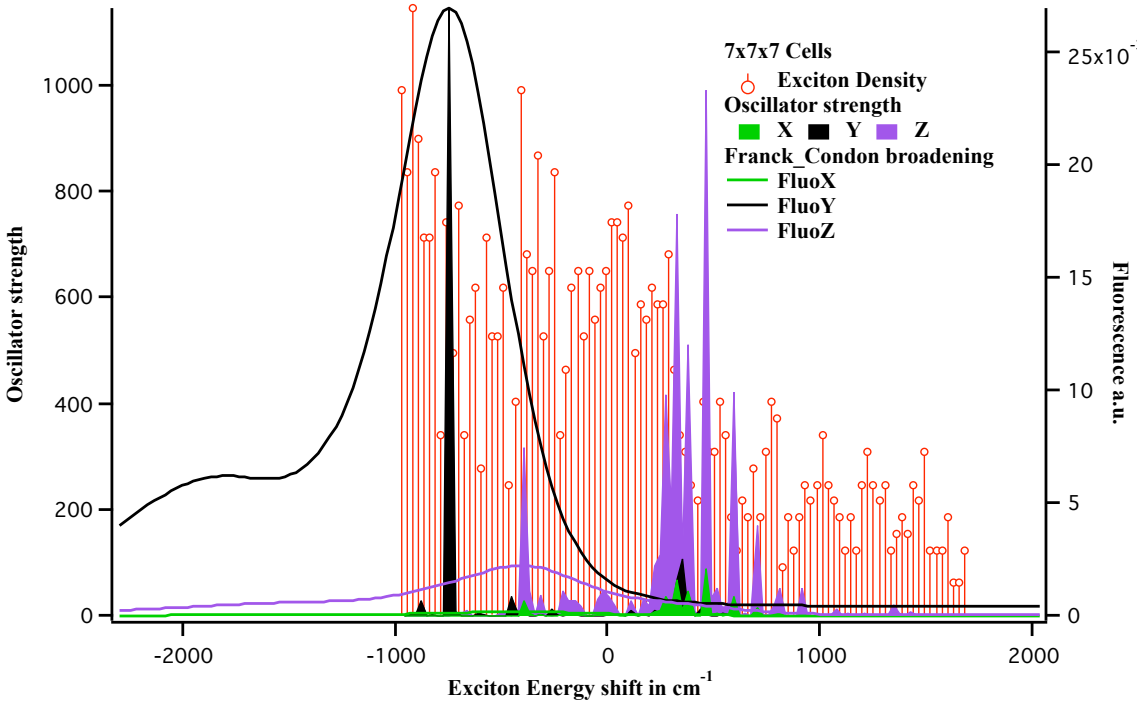

Figure 3. 28: The exciton density (red stick histogram), the oscillator strength density that bear these excitons are represented (black and violet histograms) as well as the fluorescence spectra (black line for Y polarization and violet line for Z polarization). The fluorescence is dominated by the lowest exciton that bears significant oscillator strength. The other emissive excitons are not populated at room temperature. The fluorescence is polarized along Y. By comparison with the experimental data we can conclude that the Y direction of the crystalline structure is the long axis of the crystal.

It can be seen on the **Fig. 3. 28** that the fluorescence is dominated by the lowest exciton bearing some oscillator strength at -800cm^{-1}. It is polarized along the Y direction and has a wavelength of 537nm. The fluorescence observed at 547nm and polarized along the long axis direction can be attributed to this transition. The difference comes from the Stokes shift due to the change in Van de Waals interaction ΔW (**Eq. 3.11**) that we have neglected. The shoulder that is predicted at -2000cm^{-1} comes from the choice in the broadening model. The Franck Condon broadening convolutes the transitions by the absorption spectrum that contains the vibrational structure. We do not know if this vibrational structure survives in the crystal.

The model does not predict the band at 570nm. The intensities of emission are nearly isotropic. We shall assume that it comes from a defect. Since a degeneracy of the transitions is not probable based on the symmetry of the crystal, this means that the 570nm transition is polarized perpendicular to the plan of the glass plate.

The model does not predict the band at 620nm either. We shall assume that it also comes from a defect. The emission intensity is along the A2 direction, the small axis of the crystal.

3.5. Time resolved fluorescence of the single crystal

The attribution of the emission at 570nm and 620nm to traps can be confirmed by the time resolved fluorescence spectra.

We have observed the fluorescence decay of single crystals. They have a sufficient photo stability to allow a recording of their fluorescence lifetime and their time resolved fluorescence spectra. The FLIM image of **Fig. 3.29** reveals some heterogeneity in the structure of the crystal presented. It agrees with some heterogeneity in the lifetimes that are observed between different crystals.

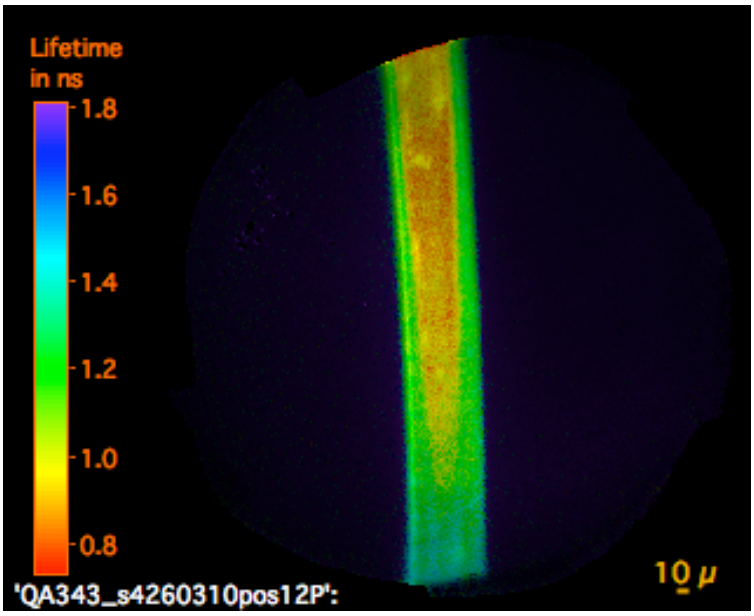

Figure 3. 29: The FLIM image of an AdamBodipy single crystal under excitation at 343nm along the long axis. No polarization on the detection. The lifetime is estimated from the average arrival delay of the photons with respect to the laser. The color codes for the lifetime of each pixel of the image. The brightness code for its intensity. The red area in the center of the crystal has a shorter lifetime. It could be due to the presence of more quenching sites or less long-lived traps.

By selecting a line in the previous image, with a slit and by spreading the spectrum of the fluorescence using a grating, it is possible to create an image on the time resolved detector where the horizontal axis codes for a wavelength and the vertical axis codes for a position along the crystal. On **Fig. 3.30** one can see a very short decay at 540nm, 1.2ns decay at 560nm and a long decay beyond 610nm. At the top of the crystal, the red domain (<0.8ns) is larger: all three decays seem to be shorter.

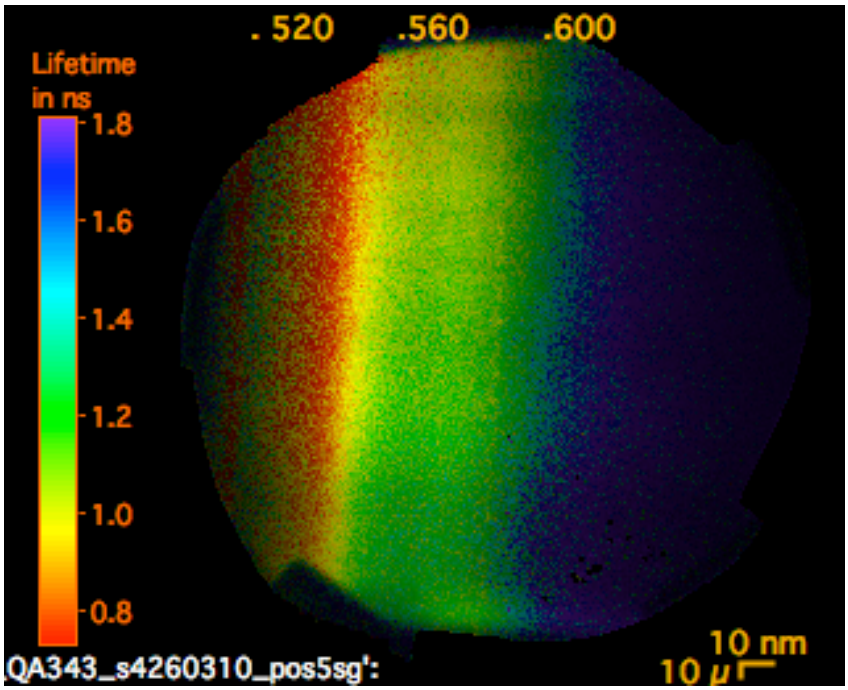

Figure 3. 30: FLIM spectra. A fraction of the fluorescence image is selected by a vertical slit. A grating is used to spread the spectrum on the detector. The color scale codes for the lifetime of each pixels, with the color scale on the left, and the brightness codes for its intensity. The abscise codes for the wavelength and the ordinate for the position in the crystal.

It is possible to extract the time resolved spectra from the data that have been used to build the FLIM image. This has been done on **Fig.3.31,** where the fluorescence spectra at different delay times have been collected.

The time resolved spectra have been normalised to the same area in order to check the presence of isosbestic points that would show the presence of only two fluorescent states[26]. The isosbestic point is not perfect, in particular the spectrum at time 0ps is too small at 569nm.

This is confirmed by the analysis of the number of components in this family of decays. The diagram inserted in the figure shows that two components contribute to 94% but that two more are contributing to more than 1% of the signal[27]. For 94% of the signal we observe the disappearance of the 547nm emission to the benefice of the 620nm fluorescence. The 547nm is the fluorescence of the lowest emissive exciton that is produced by the light absorption. This exciton diffuses toward traps and disappears to the benefice of the trap emissive at 569 and 620nm.

The fluorescence decay for a given wavelength can be constructed from the data by gathering the photons collected in a column of the image. Three typical decays are selected and shown on **Fig. 3.32**.

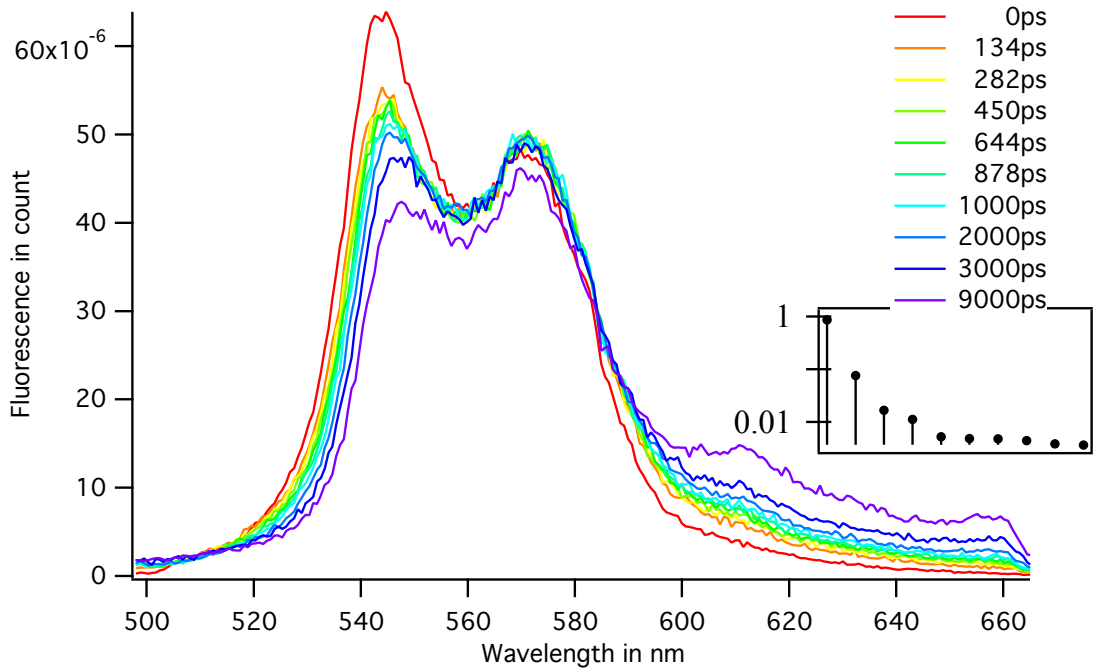

Figure 3. 31: Fluorescence spectra at different delay times have been collected from FLIM image of **Fig. 3. 30**

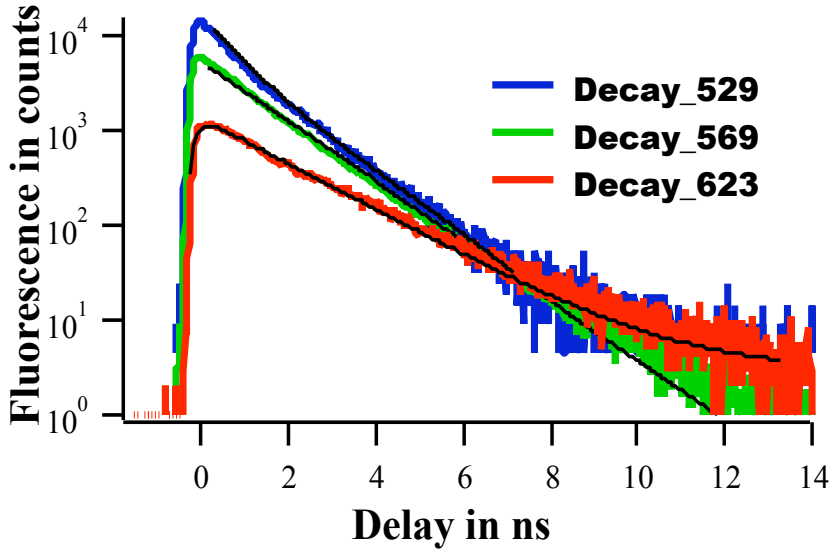

Figure 3. 32: Three typical decays at 529 nm, 569nm and 623 nm that are selected from FLIM image **Fig. 3. 30**.

The fluorescence decay at 529nm is biexponential with two lifetimes of 0.7ns (70%) and 1.6ns (30%). The fluorescence decay of the 569nm emission is almost exponential with a lifetime of 1.2ns. The 623nm rises in less than 0.17ns and decays in 1.9ns.

The fluorescence spectra obtained from the polarization study (**Fig. 3.25**) and those obtained from the FLIM (**Fig. 3.31**) are quite similar and support a quite consistent model. The crystal fluorescence is polarized and narrow at 547 nm. The crystal fluorescence disappears in 0.7ns to the benefit of two types of traps. The traps have different polarization as well as different fluorescence decays.

By comparing the experimental fluorescence with the calculated one in **Fig 3.34**, we can conclude that the Y-axis of the crystalline structure is the long axis of the microcrystals. The 570nm traps emit orthogonally to the microcrytal plate and the 620nm traps emit along the short axis.

3.6. Molecular organization from the absorption spectra:

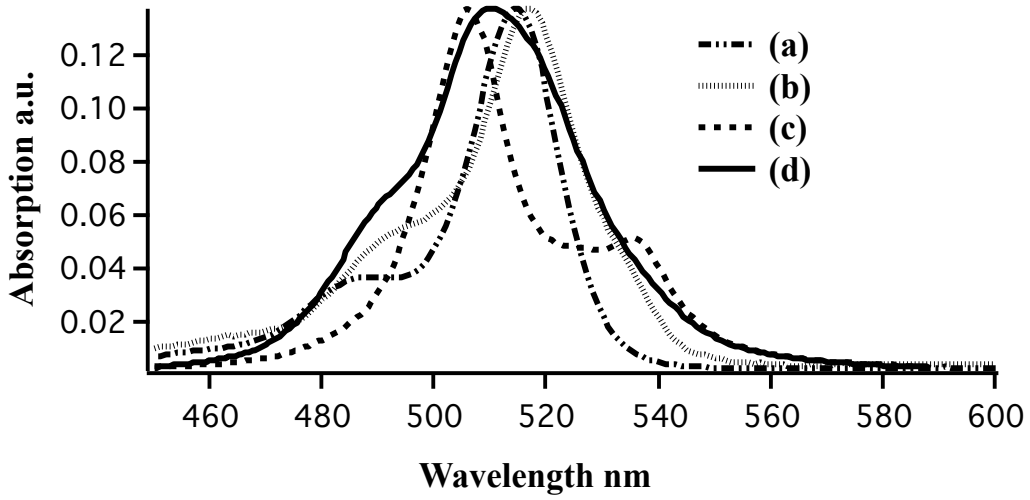

Figure 3. 33: Measured and calculated absorption spectra of Adambodipy. (a) is a molecular solution in THF/EtOH=3:7 (b) Adambodipy NPs obtained by MFD; (c) calculated absorption of an isotropic mixture of crystals; (d) calculated absorption assuming an amorphous phase (See text). This shows that we have produced amorphous nanoparticles.

A typical adambodipy molecular absorption spectrum in THF/EtOH=3:7 is presented on **Fig.3.33 (a)**, with the main band at 514nm and a shoulder at 487nm. All the nanoparticles suspensions that have been produced in the MFD have very similar

absorption spectra. They all exhibit a main band at 517nm and a shoulder around 493nm. A typical spectrum is showed on **Fig. 3.33(b)**. The amplitude of the absorbance increases as the concentration of the Adambodipy in the samples increases (imposed by the flow rates ratio).

The experimental and the theoretical spectra for amorphous phase exhibit a similar shape; whereas a red shifted band (due to the coupling for J-aggregate) is expected on the absorption spectrum of the crystalline phase. This indicates that the nanoparticles that we have produced are made of Adambodipy gathered in an amorphous phase.

3.7. Molecular organization from the fluorescence spectra:

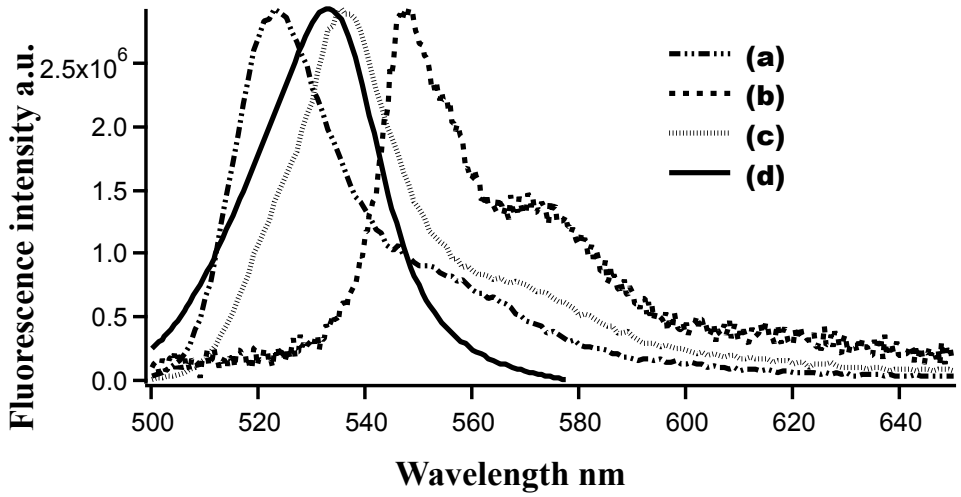

Figure 3. 34: Measured and calculated fluorescence spectra of Adambodipy: (a) = molecules dissolved in THF/Ethanol (λ_{ex}=495nm). (b) = crystal (λ_{ex}=515nm). (c) Suspension of nanoparticles (λ_{ex}=495nm). (d) is the calculated fluorescence spectrum of Adambodipy nanoparticles in an amorphous phase. The comparison shows that we have produced amorphous nanoparticles.

We have overlaid the typical fluorescence spectra of Adambodipy in solution and from various samples of this molecule in solid states. In **Fig. 3. 34** (a) is the typical fluorescence spectrum for BODIPY derivatives, with an intense band at around 527nm.

The spectrum obtained for the crystal (b) in **Fig. 3. 34** is far different from the others: there is a strong red shift (compared to the main band of the spectrum for solution) and a doubling of this band between 560 and 580nm. As the X-ray diffraction has confirmed the

crystalline structure, those bands at 548 and 574 nm can be attributed to the crystalline phase of the Adambodipy in solid state.

For the sample prepared with CTACl concentration below CMC, in the microfluidic device (c), The main band was at 537nm, between the spectra of the crystal and that of the Adambodipy solution.

Finally the simulated fluorescence spectrum (d) was done assuming a disordered structure at room temperature T=300K and with a linewidth of 250cm^{-1}. The main band was found at 534nm that was close to the experimental spectrum (c), confirming the nanoparticle amorphous structure.

3.8. Time-dependent density functional theory (TDDFT)[39,40]

3.8.1. Introduction

Time-dependent density-functional theory (TDDFT) is a density-functional method for calculating excited states. TDDFT is formally exact, and improves the wavefunction-based methods that are consuming huge computer time. It is also computationally more efficient and scales better than ab-initio methods. It can be used in large systems, up to thousand atoms, though in practice one has to approximate the exchange-correlation functional, which contains all the many-body effects. And it is a good approach to access the optical properties of large molecular systems containing hundreds of atoms.

3.8.2. Density Functional Theory (DFT)

The conventional approach to quantum chemistry uses the wave function ψ as the central quantity to solve the Schrödinger equation (SE), however the wave function is a very complicated quantity for the systems that contain many atoms and many more electrons. Considering a system of N-electron interacting with each other through Coulomb potential and subjected to an external potential $v_{ext}(\vec{r})$. The SE for it could be written as:

$$H\psi(x_1, x_2, \cdots, \cdots, x_N) = E\psi(x_1, x_2, \cdots, \cdots, x_N) \qquad \text{Eq. 3.27}$$

Where the x_i denotes the space, r_i and spin σ_i variables of the electrons.

Hamiltonian consists of the kinetic energy T, the nuclear-electron interaction V_{ne} and the electron-electron interaction V_{ee} respectively as follow

$$H = T + V_{ne} + V_{ee} \qquad \text{Eq. 3.28}$$

Then the SE could be rewritten as:

$$\left(-\frac{1}{2}\sum_{i}^{N} {\nabla_i}^2 + \sum_{i}^{N} v_{ext}\,(\vec{r}_i) + \sum_{i<j} \frac{1}{r_{ij}} \right)\ \psi(\vec{r}_1, \vec{r}_2, \dots, \vec{r}_N) = E(\vec{r}_1, \vec{r}_2, \dots, \vec{r}_N) \quad \text{Eq. 3.29}$$

The terms in the bracket are related to kinetic energy, the nuclear-electron interaction and the electron-electron interaction. Then the difficulty arises mainly due to the electron-electron interaction, which should be reflected in the wave functions along with it being antisymmetric. Thus the unmanageable numbers of variables may make a computational treatment very difficult. The better solution instead of the exact calculation is to get approximate solutions of the Schrödinger equation.

Density Functional Theory (DFT) is based on this attempts, it is a remarkable theory that built around the idea of an electron density $\rho(\vec{r})$, and allows us to obtain information on the electronic structure of molecules. It was widely used in the condensed matter physics and quantum chemistry because of its good balance between accuracy and computational cost.

The electron density $\rho(\vec{r})$ of a molecule represents the number of electrons per unit volume at some position $\vec{r}$ in a molecule or in an atom. Total electron density due to N electrons can be defined as N times the integral of square of wave functions over the spin coordinates of all electrons and over all but one of the spatial variables.

$$\rho(\vec{r}) = N \int \cdots \int |\psi(x_1, x_2, \cdots, \cdots, x_N)|^2\, ds_1 dx_2, \cdots, \cdots, dx_N \qquad \text{Eq. 3.30}$$

$\rho(\vec{r})$ is the probability of finding any of the *N*-electrons within a volume element d(*r*) with arbitrary spin. Unlike the wavefunction, the electron density is observable and can be measured experimentally, e.g., by X-ray diffraction.

Various theories have been developed starting from Thomas-Ferm, Hartree, Hartree-Fork now to the modern density-functional theory. Some theories that are related to the thesis are introduced here briefly.

DFT theory was then developed by Hohenberg and Kohn[41] and in the work of Kohn and Sham[42] in 1964. Some of the work is captured as follow.

3.8.3 Hohenberg-Kohn theory

Hohenberg and Kohn (HK) established the two theorems, which constitute the theoretical foundation of DFT:

1. Theorem 1: (The Existence Theorem)

For a non-degenerate system of interacting electrons in an external potential $v_{ext}(\vec{r})$, ($v_{ext}(\vec{r})$ is the electric potential of the nuclei) there is a one-to-one correspondence between $v_{ext}(\vec{r})$ and the ground-state charge density $\rho_0(\vec{r})$. The total ground state energy of an electron system can be written as a functional of the electronic density. The useful consequence is that if $\rho_0(\vec{r})$ is known $v_{ext}(\vec{r})$ is known, a Hamiltoninan can be constructed and all the properties of the system can be calculated. The direct connection means that the density completely determines all the properties of a given many body system. This includes the kinetic energy T_o and the electron-electron repulsion E_H.

2. Theorem 2: (The Variation Theorem)

The ground state charge density minimizes a variational expression for the ground state energy. The energy of an interacting-electron system in an external potential $v_{ext}(\vec{r})$ can be expressed as a function of the electronic density, $\rho(\vec{r})$, of the form:

$$E_{v_{ext}}[\rho] = V_{ne}[\rho] + T[\rho] + V_{ee}[\rho] = \int v_{ext}(\vec{r})\,\rho(\vec{r})d\vec{r} + F_{HK}[\rho] \qquad \text{Eq. 3.31}$$

Where $V_{ne}[\rho]$ and the integral is the electrostatic interaction of the electron with the nuclei. $F_{HK}[\rho]$ is the remaining unaccounted parts of the energy: the kinetic energy $T[\rho]$ and the electron-electron repulsion $V_{ee}[\rho]$.

In addition to minimize the energy, this density $\rho_0(\vec{r})$ has to maintain the total charge constant and equal to the number of electrons N.

$$\int \rho(\vec{r})d\vec{r} - N = 0 \qquad \text{Eq. 3.32}$$

Based on these constraints and theorems, Kohn and Sham have shown REF that the ground state electron density will be expressed as:

$$\rho(\vec{r}) = \sum_i n_i e|\psi_i(\vec{r})|^2 \qquad \text{Eq. 3.33}$$

Where the orbitals $\psi_i(\vec{r})$ can be obtained by solving the one electron Schrödinger equation of a fictitious non-interacting system. Where $\vec{r}$ stands for the three dimensions of space.

$$\varepsilon_i \psi_i(\vec{r}) = \left[-\frac{1}{2}\nabla^2 + v_s(\vec{r})\right]\psi_i(\vec{r}) \qquad \text{Eq. 3.34}$$

where the KS effective potential $v_s(\vec{r})$ is defined by:

$$v_s(\vec{r}) = \int \frac{\rho(\vec{r},t)}{\left|\vec{r}-\vec{r}'\right|}\, d\vec{r}' - \frac{\delta E_{xc}[\rho]}{\delta\rho(\vec{r},t)} + v_{ext}(\vec{r}), \qquad \text{Eq. 3.35}$$

$E_{xc}[\rho]$ is the part of the e-e interaction that is not known and that has to be approximated.

To complete this equation, the total electronic energy may be calculated from Kohn-Sham orbitals in the expression as follow:

$$E = \sum_{i=1}^{N} \varepsilon_i - \frac{1}{2} J[\rho] + E_{xc}[\rho] - \int v_{xc}\,[\rho](\vec{r})\rho(\vec{r})d\vec{r} \qquad \text{Eq. 3.36}$$

Thus the calculation of the energy of the ground state and of his electron density reduces to the solution of a Schrödinger equation in 3 dimensions.

Different types of DFT can be performed. They differ by the way the electron electron repulsion $E_{xc}[\rho]$ is approximated and by the way the orbital $\psi(\vec{r})$ are describe numerically.

3.8.4. Time-dependent density functional theory (TDDFT)

The main limit of standard DFT is that it is a ground-state theory, thus not strictly applicable to the simulation of excited state properties. A powerful method to solve the problem is the Time-dependent density functional theory (TDDFT), which has been shown to consistently give accurate excitation energies and oscillator strength of large molecular systems containing hundreds of atoms. It is basically an extension of the ground state DFT to deal with the time-dependent external perturbations, and it was Runge and Gross[43,44] who formalized the TDDFT and extended the HK theorems into the time domains. They proved that two spatially different external potentials could not induce the same time-dependent densities.

3.8.5. Analysis of Adambodipy from Molecular orbital theory and TDDFT results

The calculation of the crystal spectrum using the Frenkle exciton model is based on the value of the coupling elements given in **Eq. 3.17**. This coupling element can independently be obtained from the splitting of the excited state energy of a dimer as calculated by the TDDFT[31]. We have thus calculated the excited state of the monomer and two representative dimers of the crystal. Computation of small molecular aggregates is a typical technique to determine inter-chromophore interactions in molecular assemblies, and this allows determination of aggregation type, that are of H or J type, and electronic coupling energies[45,46].

The calculation were conducted by using 6-311+g(d,p) basis set. This means that the orbital $\psi_i(\vec{r})$ that are used to numerically describe $\rho(\vec{r})$ are a linear combination of Gaussian Type Orbitals (GTOs) as indicated by the "g". The 6-311g basis sets is a triply split valence basis set, which is triple-zeta in the balance part but only minimal in the core. For the atom calculated in this set, the number of primitives required to represent the atom is 6 GTOs for the core orbitals 1s, then 3 GTOs for inner valence, 2 different GTOs for outer valence. (d,p) means that a set of *p*-type functions have been added on the Hydrogen, d-type functions add on to all other atoms to account for polarization effect. '+" means that diffuse orbitals have been added for atoms other than Hydrogen for a better description of the excited state. The e-e interaction operator $E_{xc}[\rho]$ used is based on two hybrid exchange-correlation functional, B3LYP and PBE1PBE[47], including 20% and 25% of Hartree-Fock (HF) exchange respectively. The theory has been shown to be suited for determination of spectroscopic properties of organic molecule[48] using Gaussian03 software.[49] It has been applied successfully to azabodipy[50].

The basics of π-orbitals, the excitation of electrons from π-bonding to anti-bonding orbitals will be shortly reviewed in the following sections as obtained from the TDDFT calculation.

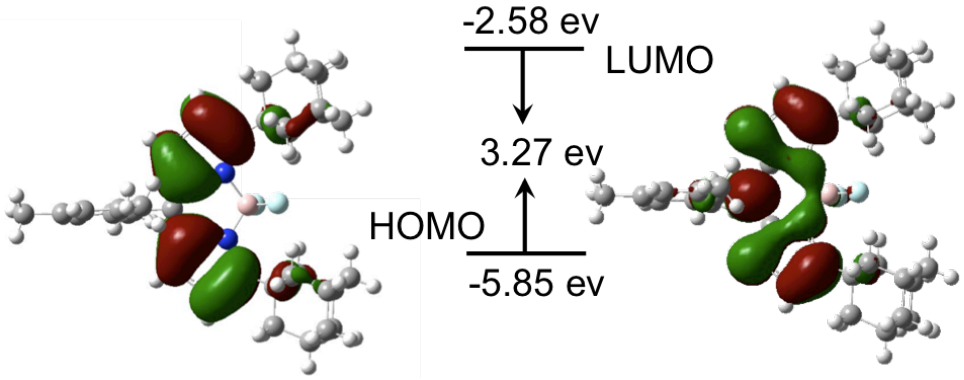

Figure 3. 35: Highest occupied molecular orbital (HOMO, left) and lowest unoccupied molecular orbital (LUMO, right) of the Adambodipy. The energy of the transition obtained by TDDFT is too high by 20% with respect to the measured one.

In the ground state, the highest occupied molecular orbital (HOMO) and the lowest unoccupied molecular orbital (LUMO) of the molecules are the π and π* orbitals centered on the BODIPY dye. Adambodipy with adamantyl groups in the 3,5-position displays mixed orbital contribution for the lowest energy excitation.

	Monomer	**Dimer 1**	**Dimer 2**
L+2	-0.11	-0.09	-0.19
L+1	-0.18	-2.55	-2.59
LUMO	-2.58	-2.59	-2.6
HOMO	-5.85	-5.84	-5.86
H-1	-6.92	-5.86	-5.87
H-2	-6.95	-6.77	-6.9
H-3	-7.24	-6.79	-6.92

Table 3. 6: The molecular orbitals of Adambodipy monomer and two of its' dimers and their energies (ev), HOMO: the highest occupied molecular orbitals (H) and LUMO: the lowest occupied molecular orbitals (L). The numbering H-1 is the orbitals with number of HOMO-1 and the L+1is the orbital with number of LUMO orbital+1 and so on

Wavelength	Oscillator Strength	Major contributions
419	0.5576	H→L (71%)

Table 3. 7: Calculated wavelength, oscillator strength, and principal orbital contribution of the lowest energy transitions of Adambodipy. Wavelength given in nm, H = HOMO, L = LUMO. Level of calculate: B3LYP/6-311+g(d,p).

The absorption spectrum of the Adambodipy in vacuum was calculated with TDDFT. The results are listed in **Table. 3. 8** and **3. 9**, and convoluted by a Gaussian profile in **Fig. 3. 38.**

As expected, the lowest-energy transition has remarkable oscillator strength and characteristically appears as a main peak in the linear absorption spectra. According to the table, we have vertical transition 1 at 419 nm (23866 cm^{-1}), with an oscillator strength f=0.56 for Adambodipy. This has to be compared with the experimental values 516nm for the absorption and the 0.29 for the oscillator strength. The calculations revealed a higher excitation energy, which means a smaller wavelength.

The experimental energy of the transition is a safe measurement of the transition energy since Bodipy has very small solvatochromism and the gas phase calculation should be close to the experimental one. The oscillator strength calculation is based on the measurement of the molar extinction coefficient. The critical step is the accurate weighting of less than 10mg of the pure dye. We have not redone these measurements. The discrepancy could also come from the fact that the Frank Condon factor evaluates the transition probability between vibrational levels. This discrepancy has been observed by other authors[28].

For the dimers calculations we use the geometries extracted from the experimental X-ray crystallographic data. In addition to the single molecule shape, we consider dimers generated from the coordinates of two nearest neighbor pairs in the unit cell. Two pairs of dimers with two different signs of the coupling element were chosen. The two pairs have the largest coupling elements and dominate the spectral properties of the Adambodipy crystal. The same TDDFT parameters were used then for the monomer. The TDDFT results are shown as follow.

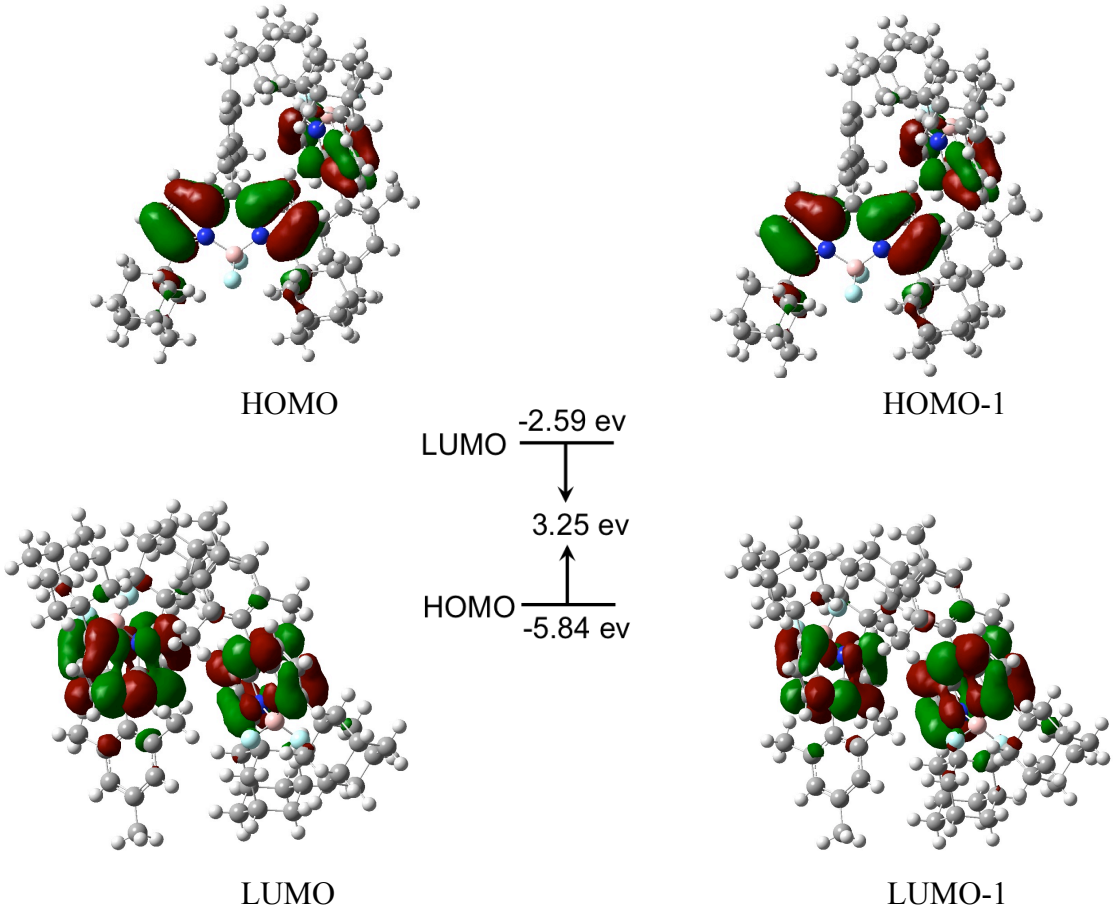

Figure 3. 36: Spatial plots of selected frontier molecular orbitals of Adambodipy dimer 1 obtained from TDDFT study

According to Kasha theory, the first excited state of the isolated molecule should split into a pair of states for the dimer. Depending on the orientation of the transition moments of the molecules, either the lower or higher energy state would acquire a larger oscillator strength, and these two classes are classified as J or H aggregate as mentioned in former section **Fig. 3.10**

We examine dimer 1 and dimer 2 according to H, and J –aggregate cases separately, and we list the calculated information in the **Table 3.8**, and **3.9** and plot the calculated excitation energies for both the dimers compared to the single molecule excitation energies in **Fig. 3. 38**

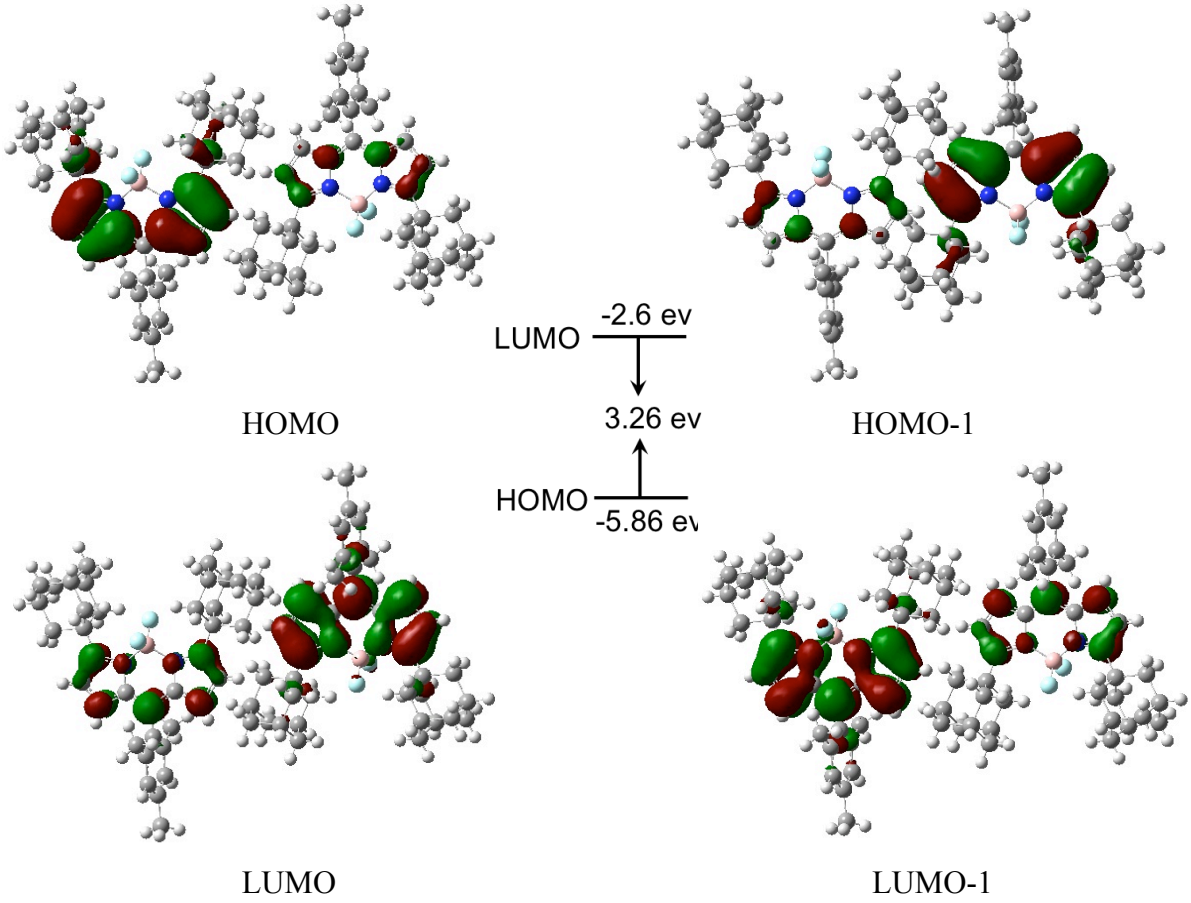

Figure 3. 37: Spatial plots of selected frontier molecular orbitals of Adambodipy dimer 2 obtained from TDDFT study

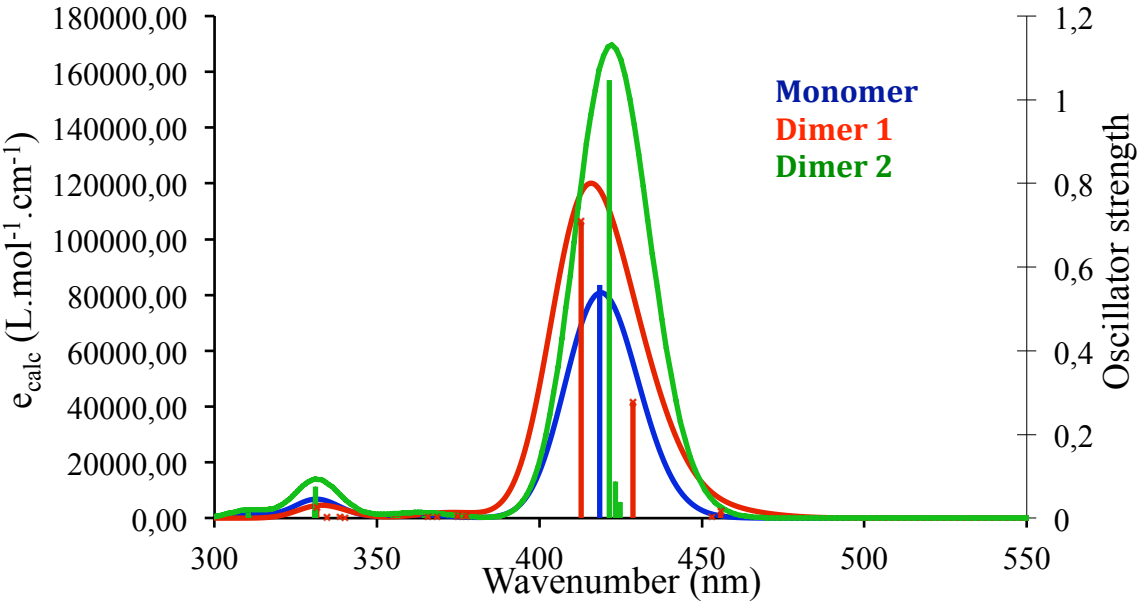

Figure 3. 38: Excitation energy of monomer (Blue), dimer 1 (Red) and dimer 2 (Green) as the

function of wavenumber and convoluted by Gaussian expression separately. Dimer 1 is an H dimer since the higher transition gains oscillator strength.

From **Fig. 3. 38**, dimer 1 with parallel orientation of the molecules forms H-aggregates in crystals exemplified by a blue-shifted first optical states compared to the corresponding properties of the monomer. The states split up and down from the isolated molecule. For the dimer 2 the splitting is not seen but an increase of the oscillator strength (above one) is observed.

Wavelength (nm)	Oscillator Strength	Major contributions	
456	0.0155	H×L (66%)	H×L+1 (-18%)
453	0.0029	H-1×L (41%)	H-1×L+1 (33%)
429	0.2779	H-1×L+1 (45%)	H×L (-17%)
413	0.7081	H-1×L (-31%)	H×L+1 (36%)

Table 3. 8: Calculated wavelength, oscillator strength, and principal orbital contribution of the lowest energy transitions of dimer 1 of Adambodipy. Wavelength given in nm, H = HOMO, L = LUMO. With method of B3LYP/6-311+g(d,p)

The table list 3.8 and 3.9 show the results of time-dependent density functional theory (TD-DFT) calculation for dimer 1 and dimer 2; including the corresponding wavelengths (in nm), the energies (in eV), the oscillator strength (*f*) and the orbitals involved in the transitions

Wavelength (nm)	Oscillator Strength	Major contributions		
425	0.0387	H×L (87%)		
423	0.0883	H-1×L+1 (51%)	H-1×L (29%)	H×L+1 (-17%)
422	1.0463	H-1×L+1 (41%)	H×L+1 (18%)	H-1×L (-12%)
417	0.0004	H-1×L (35%),	H×L+1 (34%)	

Table 3. 9: Calculated wavelength, oscillator strength, and principal orbital contribution of the lowest energy transitions of dimer 2 of Adambodipy. Wavelength given in nm, H = HOMO, L = LUMO. With method of B3LYP/6-311+g(d,p)

This information shows that the peak of the wavelength of maximum absorption at wavelength 413 nm for dimer 1 and 422nm for dimer 2.

TDDFT results for dimer H related to exciton splitting:

Vertical transition 3: 429 nm (23310 cm^{-1}) with f=0.28

Vertical transition 4: 413 nm (24213 cm^{-1}) with f= 0.71

Exciton splitting: 451 cm^{-1} (= (VT2-VT1)/2)

TDDFT results for dimer J related to exciton splitting:

Vertical transition 3: 422 nm (23697 cm^{-1}) with f=1.05

Vertical transition 4: 417 nm (23981 cm^{-1}) with f= 0.01

Exciton splitting: 142 cm^{-1} (= (VT2-VT1)/2)

3.9. Conclusion

We have successfully prepared Adambodipy micro-crystals by reprecipitation in solution at low supersaturation. X-ray crystallography firstly helps to understand the relative orientation of fluorescent molecules in the solid, and the optical properties, birefringence, dichroism and the fluorescence polarization of a monoclinic crystal were confirmed by the polarized optical spectroscopy. The slow and fast axes have been determined under a cross polarizer set up, and the refractive indexes were measured separately from the transmittance spectra. The difference of $\Delta n=0.15$ confirms the birefringence property of the crystal. The absorbance shows polarization dependence, which is associated with the alignment of the Adambodipy molecules in the crystal.

We have shown that the Frenkel exciton theory is convenient to calculate the absorption lineshapes of the Adambodipy crystal with dipolar coupling approximation. TDDFT method did not provide the transition energy or the oscillator strength of the molecule. But it provides the direction of the transition moment and an estimation of the coupling in dimers, and providing a quite reliable description of excited states in monomer and two dimers (H-dimer and J-dimer) system. The coupling predicted by the dipolar approximation agrees with the one obtained from the TDDFT calculation of dimers. The shape of the spectra strongly depends on the electronic transitions (allowed) in Y and Z direction and (forbidden) in X direction. The comparison with the experimental spectra is limited to the bandwidth due to the bad dynamics of our spectrometer on small micro-crystals. For the comparison to the experimental results obtained at room temperature, a Lorentzian convolution is chosen as the simplest calculation.

The analysis of the fluorescence of the microcrystals shows that the fluorescence of the exciton predicted by the dipolar coupling is only one half of the fluorescence. But the polarization studies and the time resolved fluorescence studies show that the other half of the fluorescence is due to defects. We have identified 2 of them with the polarization and energy.

A simple way to simulate the absorption spectra of the nanoparticle suspension was introduced here by randomly orientating the directions of transition moments in the crystal model. The product from microfluidics was confirmed to be an amorphous phase by comparison with the calculated absorbance and fluorescence spectra.

Reference:

[1] Opanasyuk, O.; Johansson, L. B. A. *"Extended Forster theory: a quantitative approach to the determination of inter-chromophore distances in biomacromolecules."* Phys Chem Chem Phys, **2010**, *12*, 7758-7767.

[2] Newton, M. D. *"Quantum Chemical Probes of Electron-Transfer Kinetics - the Nature of Donor-Acceptor Interactions."* Chem Rev, **1991**, *91*, 767-792.

[3] Prytkova, T. R.; Kurnikov, I. V.; Beratan, D. N. *"Coupling coherence distinguishes structure sensitivity in protein electron transfer."* Science, **2007**, *315*, 622-625.

[4] Simpson, W. T.; Peterson, D. L. *"Coupling Strength for Resonance Force Transfer of Electronic Energy in Vanderwaals Solids."* J Chem Phys, **1957**, *26*, 588-593.

[5] MacColl, R. *"Cyanobacterial phycobilisomes."* J Struct Biol, **1998**, *124*, 311-334.

[6] Ren, Y.; Chi, B.; Melhem, O.; Wei, K.; Feng, L.; Li, Y.; Han, X.; Li, D.; Zhang, Y.; Wan, J.; Xu, X.; Yang, M. *"Understanding the electronic energy transfer pathways in the trimeric and hexameric aggregation state of cyanobacteria phycocyanin within the framework of forster theory."* Journal of computational chemistry, **2013**.

[7] Kasha, M. *"Energy Transfer Mechanisms and the Molecular Exciton Model for Molecular Aggregates."* Radiat Res, **2012**, *178*, Av27-Av34.

[8] Gresser, R. *"Azadipyrromethenes as Near-infrared Absorber Materials for Organic Solar Cells: Synthesis and Characterization of Structure-property Relationships."* **2011**.

[9] M. Kasha, H. R. R., M. Ashraf El-Bayoumi. *"The exciton model in molecular spectroscopy."* Pure Appl. Chem., **1965**, *11*, 371-392.

[10] Rajeshwa, K. *"Photoelectrochemistry."* The Electrochemical Society, Inc., **1997**.

[11] Kasha, E. G. M. a. M. *"The molecular exciton model."* Physical Processes in Radiation Biology, Academic Press, , **1964**, 23-42.

[12] Davydov, A. S. *"Theory of Light Absorption of Molecular Crystals."* Naukova Dumka, **1951**.

[13] Mcrae, E. G.; Kasha, M. *"Enhancement of Phosphorescence Ability Upon Aggregation of Dye Molecules."* J Chem Phys, **1958**, *28*, 721-722.

[14] Knox, R. S. *"Theory of excitons."* Academic Press, **1963**.

[15] Agranovich, V. M. *"Excitations in Organic Solids."* Oxford University Press, **2008**.

[16] Fidder, H.; Knoester, J.; Wiersma, D. A. *"Optical-Properties of Disordered Molecular Aggregates - a Numerical Study."* J Chem Phys, **1991**, *95*, 7880-7890.

[17] May, V.; Kühn, O.; Wiley InterScience (Online service): Charge and energy transfer dynamics in molecular systems. 3rd ed.; Wiley-VCH ;
John Wiley [distributor]: Weinheim
Chichester, 2011; pp 1 online resource.

[18] Hecht, E. *"Optics."* 4th ed. ed.; Addison Wesley, **2002**.

[19] "Olympus Microscopy Resource Center". Olympus America Inc., 2011-11-13.

[20] Swanepoel, R. *"Determination of the Thickness and Optical-Constants of Amorphous-Silicon."* J Phys E Sci Instrum, **1983**, *16*, 1214-1222.

[21] Singh, J. *"Optical Properties of Condensed Matter and Application."* Wiley, **2006**.

[22] Jiang, H.; Tan, K. J.; Zhang, K. K.; Chen, X. D.; Kloc, C. *"Ultrathin organic single crystals: fabrication, field-effect transistors and thickness dependence of charge carrier mobility."* J Mater Chem, **2011**, *21*, 4771-4773.

[23] Beugnis, A. *"Microscopie Des Milieux Cristallins."* Presses académiques européennes, **1969**. pp 190.

[24] Lemaistre, J. P. *"A two-dimensional model for energy transfer in pure and mixed J-aggregates."* Chem Phys, **2007**, *333*, 186-193.

[25] Pope, M.; Swenberg, C. E.; Pope, M. *"Electronic processes in organic crystals and polymers."* 2nd ed.; Oxford University Press, **1999**.

[26] Dreuw, A.; Head-Gordon, M. *"Single-reference ab initio methods for the calculation of excited states of large molecules."* Chem Rev, **2005**, *105*, 4009-4037.

[27] Seth, M.; Ziegler, T. *"Calculation of excitation energies of open-shell molecules with spatially degenerate ground states. II. Transformed reference via intermediate configuration Kohn-Sham time dependent density functional theory oscillator strengths and magnetic circular dichroism C terms."* J Chem Phys, **2006**, *124*.

[28] Adamo, C.; Jacquemin, D. *"The calculations of excited-state properties with Time-Dependent Density Functional Theory."* Chem Soc Rev, **2013**, *42*, 845-856.

[29] Cranswick, R. D. L. M. D. *"International Tables for Crystallography."* 3rd Revised edition ed.; Kluwer Academic **2008**; *Vol*. B.

[30] Tretiak, S.; Mukamel, S. *"Density matrix analysis and simulation of electronic excitations in conjugated and aggregated molecules."* Chem Rev, **2002**, *102*, 3171-3212.

[31] Quarti, C.; Fazzi, D.; Tommasini, M. *"A density matrix based approach for studying excitons in organic crystals."* Chem Phys Lett, **2010**, *496*, 284-290.

[32] Bruno, I. J.; Cole, J. C.; Edgington, P. R.; Kessler, M.; Macrae, C. F.; McCabe, P.; Pearson, J.; Taylor, R. *"New software for searching the Cambridge Structural Database and visualizing crystal structures."* Acta Crystallogr B, **2002**, *58*, 389-397.

[33] Eisfeld, A.; Briggs, J. S. *"The J- and H-bands of organic dye aggregates."* Chem Phys, **2006**, *324*, 376-384.

[34] Valeur, B. *"Molecular Fluorescence Principles and Applications."* Wiley-VCH **2001**.

[35] A.Thorne, U. L., S. Johansson. *"Spectrophysics: Principles and Applications "*; Springer; 1 edition, **1999**.

[36] Spano, F. C.; Clark, J.; Silva, C.; Friend, R. H. *"Determining exciton coherence from the photoluminescence spectral line shape in poly(3-hexylthiophene) thin films."* J Chem Phys, **2009**, *130*.

[37] David S. Kliger, J. W. L. *"Polarized Light in Optics and Spectroscopy."* Academic Press, **1990**.

[38] Lemaistre, J. P. *"Intraband relaxation and dephasing of Frenkel exciton states in one-dimensional J-aggregates."* J Lumin, **2004**, *107*, 332-338.

[39] K. I. Ramachandran, G. D., K. Namboori. *" Computational Chemistry and Molecular Modeling: Principles and Applications."* Springer, **2008**.

[40] Cleophas Muhavini, W.: *"Theoretical Investigation of Ruthenium Photosensitizers."* Universite de Grenoble, **2006.**

[41] Hohenberg, P.; Kohn, W. *"Inhomogeneous Electron Gas."* Phys Rev B, **1964**, *136*, B864-&.

[42] Kohn, W.; Sham, L. J. *"Self-Consistent Equations Including Exchange and Correlation Effects."* Phys Rev, **1965**, *140*, 1133-&.

[43] van Leeuwen, R. *"Causality and Symmetry in Time-Dependent Density-Functional Theory."* Phys Rev Lett, **1998**, *80*, 1280-1283.

[44] Runge, E.; Gross, E. K. U. *"Density-Functional Theory for Time-Dependent Systems."* Phys Rev Lett, **1984**, *52*, 997-1000.

[45] Spano, F. C. *"Excitons in conjugated oligomer aggregates, films, and crystals."* Annu. Rev. Phys. Chem. , **2006**, *57*, 217-243.

[46] Magyar, R. J. T., S. . *"Dependence of Spurious Charge-Transfer Excited States on Orbital Exchange in TDDFT: Large Molecules and Clusters."* J. Chem. Theory Comput., **2007**, *3* 976–987.

[47] Ernzerhof, M.; Perdew, J. P.; Burke, K. *"Coupling-constant dependence of atomization energies."* Int J Quantum Chem, **1997**, *64*, 285-295.

[48] Jacquemin, D.; Perpete, E. A.; Ciofini, I.; Adamo, C. *"Accurate Simulation of Optical Properties in Dyes."* Accounts Chem Res, **2009**, *42*, 326-334.

[49] M. J. Frisch, G. W. T., H. B. Schlegel, G. E. Scuseria, M. A. Robb, J. R. Cheeseman, J. A. Montgomery, Jr., T. Vreven, K. N. Kudin, J. C. Burant, J. M. Millam, S. S. Iyengar, J. Tomasi, V. Barone, B. Mennucci, M. Cossi, G. Scalmani, N. Rega, G. A. Petersson, H. Nakatsuji, M. Hada, M. Ehara, K. Toyota, R. Fukuda, J. Hasegawa, M. Ishida, T. Nakajima, Y. Honda, O. Kitao, H. Nakai, M. Klene, X. Li, J. E. Knox, H. P. Hratchian, J. B. Cross, C. Adamo, J. Jaramillo, R. Gomperts, R. E. Stratmann, O. Yazyev, A. J. Austin, R. Cammi, C. Pomelli, J. W. Ochterski, P. Y. Ayala, K. Morokuma, G. A. Voth, P. Salvador, J. J. Dannenberg, V. G. Zakrzewski, S. Dapprich, A. D. Daniels, M. C. Strain, O. Farkas, D. K. Malick, A. D. Rabuck, K. Raghavachari, J. B. Foresman, J. V. Ortiz, Q. Cui, A. G. Baboul, S. Clifford, J. Cioslowski, B. B. Stefanov, G. Liu, A. Liashenko, P. Piskorz, I. Komaromi, R. L. Martin, D. J. Fox, T. Keith, M. A. Al-Laham, C. Y. Peng, A. Nanayakkara, M. Challacombe, P. M. W. Gill, B. Johnson, W. Chen, M. W. Wong, C. Gonzalez, J. A. Pople. Inc. Wallingford CT, **2004**.

[50] Gresser, R.; Hummert, M.; Hartmann, H.; Leo, K.; Riede, M. *"Synthesis and Characterization of Near-Infrared Absorbing Benzannulated Aza-BODIPY Dyes."* Chem-Eur J, **2011**, *17*, 2939-2947.

Chapter 4 Production of nanoparticles in a microfluidic system

4.1. Micro-fluidic precipitation method

In this thesis, we developed a three-dimensional hydrodynamic focusing microfluidic device for the production of Adambodipy nanoparticles. Compared to the old reprecipitation method by bulk (cf. in Chapter 1&2), microfluidic setup is better in controlling the flows and their merging, and, hopefully, the location of the mixing, nucleation and growth areas. The super saturation conditions were thus limited and controlled[1,2] by the characteristic dimensions of the microchannels and by the flow rates.

4.1.1. Micro-fluidic technology

In crystallization and precipitation methods, besides the formation of the expected solid phase, controlling the mean size and the size monodispersity of nanometer size crystal, known as NCs, or in more general structure - nanoparticles (NPs), is often a critical issue. This is obtained by having a short nucleation time followed by a uniform growing rate[3,4]. Those two processes are governed by the local supersaturation. An efficient mixing of reagents rapidly raises the concentration above the critical nucleation threshold. Supersaturation is then partially relieved by a short intense burst of nucleation that lowers the precursor concentration below the critical level. The newly formed nuclei are then allowed to grow to reach the desired average particle size[5]. The reproducibility of the process is also a challenge, as the mixing is very sensitive to the hydrodynamics.

There has been tremendous interest in the development of microfluidic methods for chemical synthesis of NPs with uniform and tunable distributions of size[6] and shape[6,7]. In Chan et al (2003)[8], they give a more detailed investigation of continuous and controlled CdSe nanocrystal preparation. About controlling particle diameter and reproducible preparation of particles, also the effort towards narrower, monodisperse particle-size distributions was made in some applications[9-11]. Many authors demonstrated that the ability to reproducibly control temperatures and concentrations on the scale of micrometers and milliseconds in micro-fluidic reaction systems allows tuning of the size of the resulting NCs[4,8].

Based on these results from initial investigations, one can anticipate that micro-reactors are likely to provide cost-effective and environmental friendly technologies for the rational design and synthesis of NPs. Also, process scale-up either by utilizing several thousands of micro-reactors in parallel or using continuous-flow reaction protocols can provide several

advantages in large-scale production of NPs[12]. Some of the unique features of micro-fluidic reactors are the ability to:

1. Efficiently mix reagents under highly controlled laminar flow
2. Control properties of nanomaterials by controlling their formation at the desired nucleation or growth stage
3. Continuously vary the composition of a reaction mixture by varying differential injection rates of the inlet channels
4. Operate within continuous flow regimes allowing additional reagents to be added downstream as required
5. Investigate the fundamentals of NP formation through spatial resolution
6. Scale up the synthesis with controlled kinetic parameters.[13]

We want to produce nanoparticles or even better, NCs of Adambodipy. In this size regime, nanoobjects are large enough to exhibit the intense luminescent properties of bulk crystals but are small enough to exhibit unique size-dependent properties due to quantum confinement and high surface-area-to-volume ratios[14].

In our research, NPs containing Adambodipy were prepared using the micro-fluidics technology. We use the micro-fluidic systems that operate in a continuous flow mode, which allowed continuous generation of desired particle formulations. The micro-fluidic hydrodynamics focusing technique can offer the capability to reduce the mixing time below the millisecond[15]. In such a Micro-Fluidic-Device (MFD) the fluid streams flowing toward one another can merge and form a very sharp and well-defined interface by virtue of laminar flow[16] and insure a good reproducibility of the experiments.

4.1.2. Microfluidic device (MFD) design

In recent years, the development of micro-fluidic systems has been attracting scientific and industrial attention. The selection of materials for microfluidic device depends on careful material selection to match mechanical, electrical and other properties to functionality.

There are several basic criteria rule for the materials of micro-fluidic reactors, and they are:

1. Easy and fast (around one day or less) to fabricate.
2. Inexpensive and readily available

3. Non-toxic or bio-compatible
4. Rigid (for the substrate, packaging, and possibly flow layer) or flexible (for the gasket) as necessary
5. Reproducibility.

The most important constraints for the materials used to fabricate microfluidic for synthesis of nanomaterials are that they are temperature-resistant in quantum dots particular application, compatible with solvent, smooth enough, rigid enough, and of the right size to be used with available microfabrication process, such as photolithography, hot embossing powder blasting, injection molding or laser micro forming.[17]

The properties of the fluid flow layer material determine many factors in the microfluidic experiments, such as the possible channel dimensions, the patterned method, the reactivity with solutions to be pumped through the micro channels. Traditionally, microfluidic devices are made of silicon and glass since the fabrication processes are well developed but the techniques used are expensive and time consuming. Polymers have also used to fabricate microfluidic device because of their relatively low cost and simple fabrication process, and some of them are quite well known, such as polymethyl methacrylate (PMMA), PC, polystyrene (PS), polydimethylsiloxane (PDMS). The fabrication is easy, and their use as materials reduces the time, complexity, and cost of prototyping and manufacturing [18,19].

Among these polymers, PDMS (see the structure on **Fig.4. 1**) has been one of the most actively developed polymers for micro-fluidics[20]. The advantages of PDMS material for micro-fluidics applications also include elasticity, ease of bonding, permeability to gases for some biological applications,[21] and optical transparently from 240–1100nm with a refractive index around 1.41. It has negligible birefringence, therefore it is possible to enclose optofluidic components in PDMS and couple light through PDMS with minimal loss due to absorption[22]. The main limitation of use is the chemical compatibility of the PDMS. Except water and few solvents as methanol, ethanol or acetonitrile, PDMS can be swelled or dissolved by most organic solvents[23](see **Table 4. 1**). PDMS is hydrophobic and could adsorb hydrophobic molecules on to its surface.

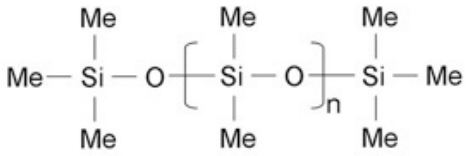

Figure 4. 1: Polydimethysiloxane (PDMS)

PDMS is useful for applications at room temperature, and also useful for large-scale production. With our experiment, according to soft-lithography techniques, primarily based on printing and molding, this polymer-based micro-fluidic reactor is likely to be the preferred choice for on-chip synthesis of nanomaterials.

Property	Characteristics	Consequence
Optical	Transparent; UV cutoff, 240 nm	Optical detection from 240 to 1100 nm
Electrical	Insulating; breakdown voltage, 2×10^7 V/m	Allows embedded circuits; intentional breakdown to open connections
Mechanical	Elastomeric; tunable Young's modulus, typical value of ~750 kPa	Conforms to surfaces; allows actuation by reversible deformation; facilitates release from molds
Thermal	Insulating; thermal conductivity, 0.2 W/(m · K); coefficient of thermal expansion, 310 μm/ (m · °C); stable up to ~300°C	Can be used to insulate heated solutions; does not allow dissipation of resistive heating from electrophoretic separation
Interfacial	Low surface free energy ~ 20 erg/cm2	Replicas release easily from molds; can be reversibly sealed to materials; not wetted by water unless oxidized to SiOH presenting surface
Permeability	Low permeability to liquid water; permeable to gases and nonpolar organic solvents	Contains aqueous solutions in channels; allows gas transport through the bulk material; incompatible with many organic solvents
Reactivity	Inert; can be oxidized by exposure to a plasma	Unreactive toward most reagents; surface can be etched; can be

		modified to be hydrophilic and also reactive toward silanes
Toxicity	Nontoxic	Can be implanted in vivo;

Table 4. 1: Basic mechanical properties of PDMS[24].

In the thesis, in order to detect the Adambodipy precipitation process under microscope, also for easy reproducibility, PDMS was chosen for fluid flow layer material due to the ease of bonding and also transparent optical properties.

4.1.2.1. Soft lithography technique

The micro-fabrication technique developed for constructing complex 3-D channel paths PDMS device is one of the easiest method for the rapid prototyping MFD. Soft lithography combined with replica molding and rapid prototyping is the method used in our research.

The 2-D patterned layer was fabricated using conventional photolithography technology and the layout for each layer was drawn using a computer-aided design program (ADOBE ILLUSTRATOR). The mold is obtained by photolithography of the negative SU-8 photoresist through a mask printed on a transparent with a resolution of 3600 dpi. The main steps of the replication are sketched in **Fig. 4. 2** below. The procedure is detailed in Chapter 6.

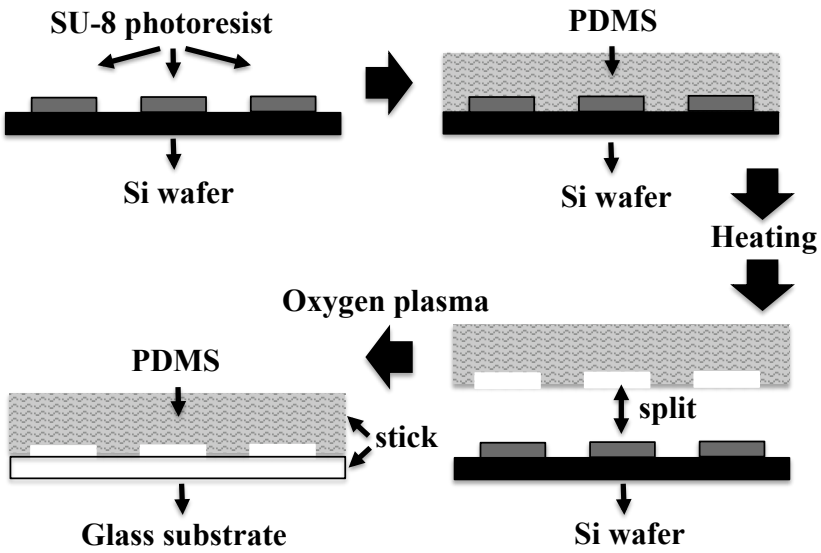

Figure 4. 2: (a) A master for each layer was formed on a silicon wafer using SU-8 photoresist and standard photolithography procedures. (b) Next, the PDMS prepolymer mixture was poured onto the master and heated at 75°C for 2 hours. (c) After cold down, we can easily peel the PDMS replica from the master. (d) After exposure to O_2 plasma the PDMS block and the glass substrate are sealed.

4.1.2.2. MFD mold pattern used in the thesis

To realize the hydrodynamic focusing of the organic stream containing the solute to crystallize by the surrounding of an aqueous flow, a PDMS mold with a 4 channels junction was built with 3 inlet branches and a main channel between the junction point and the outlet, as shown on **Fig. 4. 3.** Between the two side inlet branches, the third inlet is insured by a capillary silica tube (Polymicro, OD = 150µm, ID = 20µm) and inserted in this channel, then glued to fix it and avoid leakage. This configuration is used to introduce the organic solution of Adambodipy in THF/ EtOH, due to the limitation of chemical compatibility of the PDMS with organic solvents[25]. By this way the focused stream is confined in the middle of the main channel and avoid any further contact of the organic mixture with the wall. After that, PTFE tubes are inserted into the reservoirs and connected to 10 mL plastic syringes (ID=14.5mm) set that was placed on the syringe pumps (Harvard type PHD 2000 for side flows). The capillary silica tube is also connected to a syringe-pump for injection (Harvard Picoplus11), with 100µl syringe (ID=1.46mm). The device is placed under a binocular, equipped with a camera, to control the stability of the flows during the production of NPs.

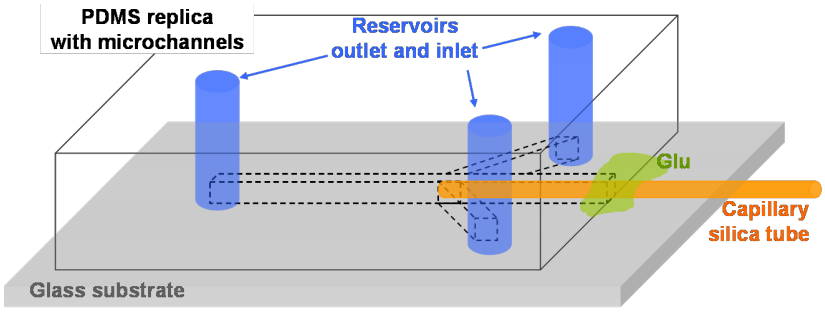

Figure 4. 3: Microchannel patterned in PDMS block, sealed to the glass substrate with the inserted capillary silica tube

4.1.3. Design and Improvement of the micro-fluidic systems for NPs production

Several 3D hydrodynamic focusing MFD were fabricated and used in our experiment. Their designs as well as their performance were modified to improve the research related to the limitation of the condition in different experiment.

4.1.3.1. MFD1

Firstly, with the MFD 1, we have used a capillary with a flat edge and the side channels have a 45° angle with the main channel. Then, a crystal is systematically nucleated at the edge

of the capillary and it grows on the periphery of the capillary flow (**Fig. 4.4**). The flow was not blocked and the focusing still occurred but this growing crystal consumed the solute.

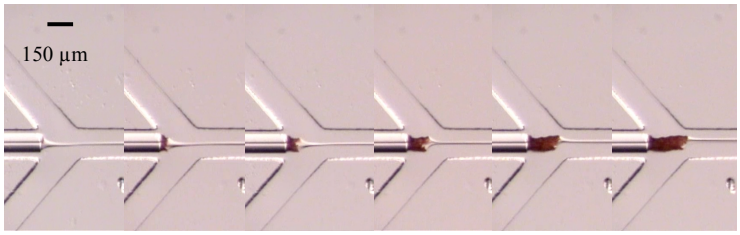

Figure 4. 4: MFD 1- capillary of flat end, with the crystal synthesis at the edge. Pictures taken after 0, 2, 6, 10, 14 and 18 minutes of run.

4.1.3.2. MFD2

To overcome the formation of this sheathing crystal growing at the edge of the capillary, we have improved our MFD. We still keep the Y-type device but we change:

-The shape of the capillary edge. In order to do that, we provide a set-up to polish the tip. (See details in Chapter 6)

-The angle between the side channel and the channel in the center was reduced.

With those improvements the crystallization on the periphery of the capillary disappeared as shown on **Fig.4. 5**. Those pictures also exhibit the reduction of the width of the focused stream as the flow rate ratio (Qc/Qs) decreases.

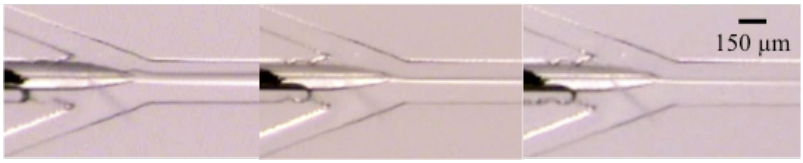

Figure 4. 5: MFD2- taped capillary and smaller angle between the side flow channels. The pictures show the effect of the flow rate ratio on the width of the focused stream. The side flow rate was fixed at Qs = 10 µL.min^{-1} and the capillary flow rate changes from (a) Qc= 3 µL.min^{-1} (b) Qc= 0.5 µL.min^{-1} to (c) Qc = 0.2 µL.min^{-1}

For all the samples produced in MFD2, the surfactant CTACl was added in both organic and aqueous solution. The concentration of Adambodipy in the THF-EtOH mixture was kept at 0.2 mg.ml^{-1}.

4.1.4. Preparation of NPs containing Bodipy derivatives

We are interested in the development of micro-fluidic methods for chemical synthesis of Adambodipy nanoparticles with uniform, stable and tunable distributions of size as demonstrated previously with the production of rubrene nanoparticles[26].

The set-up of the experiment is illustrated as the scheme in **Fig.4. 6**. The solutions of Adambodipy were prepared in a mixture of tetrahydrofuranne (THF) with ethanol (EtOH), so called THF/EtOH organic solution (Volume ratio of THF/EtOH=3/7), or for some samples in THF only. The concentrations of Adambodipy were 0.1g.L^{-1}, 0.2 g. L^{-1} and also 0.5 g. L^{-1}. CTACl was used as surfactant in this experiment and has been added either to the organic mixture or to the aqueous solution or even to both at a concentration of 10^{-2} mol.L^{-1}. The critical micelle concentration of this surfactant is around 1.3 10^{-3} M (cf. in Chapter 1).

The side flow rate varied between 10 to 50 µL.min^{-1} and the capillary flow rate range between 0,4 to 3 µL.min^{-1}.

For the further analysis, DLS and spectroscopic measurements, the volume required and collected at the outlet of the device is between 500µL and 1mL, which correspond to a run time between 10 and 40 minutes depending on the flow rates.

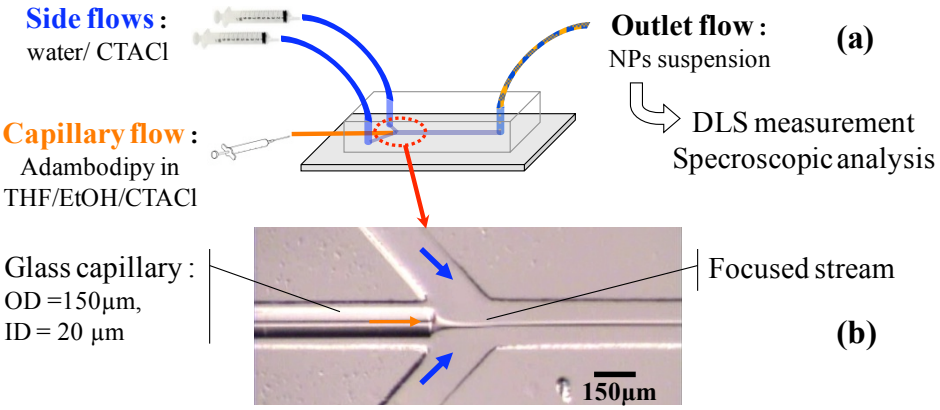

Figure 4. 6: The first microfluidic device, MFD 1. (a) Microchannel patterned in PDMS block, sealed to the glass substrate with the inserted capillary silica tube. The device is connected for feedings and withdraws. (b) Details of the cross-junction area under microscope with the laminar flow of ethanol/THF mixture from the capillary surrounded by water flows

4.2. Nanoparticle analyses

4.2.1. Adambodipy NPs produced in MFD technology

Many operating parameters may affect the production of the nanoparticles, such as the MFD configuration as mentioned before, the concentration of initial Adambodipy solution, the concentration of the surfactant, etc. We have used DLS to characterize the sample and its size distribution. DLS is a powerful method to measure the particle size, by characterizing its Brownian motion. According to the Stokes-Einstein formula shown below, the particles are treated as point objects with no mass and density, the movement of particles during diffusion is size dependent.

$$D = \frac{k_B T}{3\pi\mu a} \qquad \text{Eq. 4. 1}$$

where k_B is the Boltzmann constant and T is absolute temperature. Throughout in this thesis we use this expression to estimate D, μ is the fluid's dynamic viscosity, the diffusion coefficient for Adambodipy NPs with a given particle size a.

The molecular organizations of the Adambodipy in the NPs were studied through their absorption and fluorescence spectra. We have varied the following operating conditions:

1. Different microfluidic device, MFD1 and MFD2, with different shape of the edge of the silica capillary.
2. The side flow rate from 0.5 to 3 $\mu L.min^{-1}$ for the aqueous solution.
3. The capillary flow rate from 10 to 50 $\mu L.min^{-1}$ for the organic solution
4. The Adambodipy concentration in the organic mixture from 0.1 to 0.5 $mg.mL^{-1}$.
5. The presence or not of surfactant in the aqueous or organic solutions, also with different concentration, 10^{-2} M higher than CMC, or 10^{-3} lower than CMC
6. The nature of the mixture containing the Adambodipy, THF or THF-EtOH (3-7 v/v)

4.2.2. Spectroscopy and DLS results for NPs obtained in MFD1

Several samples were collected from MFD1 whereas a crystal was growing at the edge of the silica capillary tube. We were not convinced by the impact of this crystal on the properties

of the particles. Among several samples, 4 of them are presented in the **Table 4. 2**, with DLS histogram displayed in **Fig. 4.7**.

Concentration of Adambodipy (mg/ml)	Q_c/Q_s $\mu l.min^{-1}/\ \mu l.min^{-1}$	Acquisition time Acq/s	Size peak (nm)
0.2	0.5/10	30/90	153-651
0.2	1/20	60/60	193-6500
0.2	1.5/30	30/90	273-460
0.2	2/40	60/60	204-2465

Table 4. 2: Few samples with the same flow rate ratio Q_c/Q_s equals to 0.05

The **Fig. 4. 7** shows the size of the samples varied from 100 nm to few µm in the same flow rate ratio 0.05. The distribution can be quite narrow as **Fig. 4. 7(c)** or very broad as **(b)** and **(d)** and widely distributed. Sometimes several populations were clearly distinguished as in **(a).**

(a)

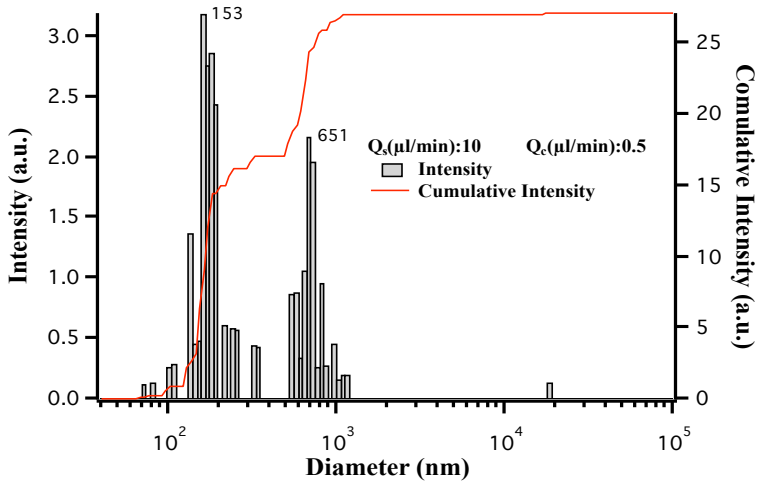

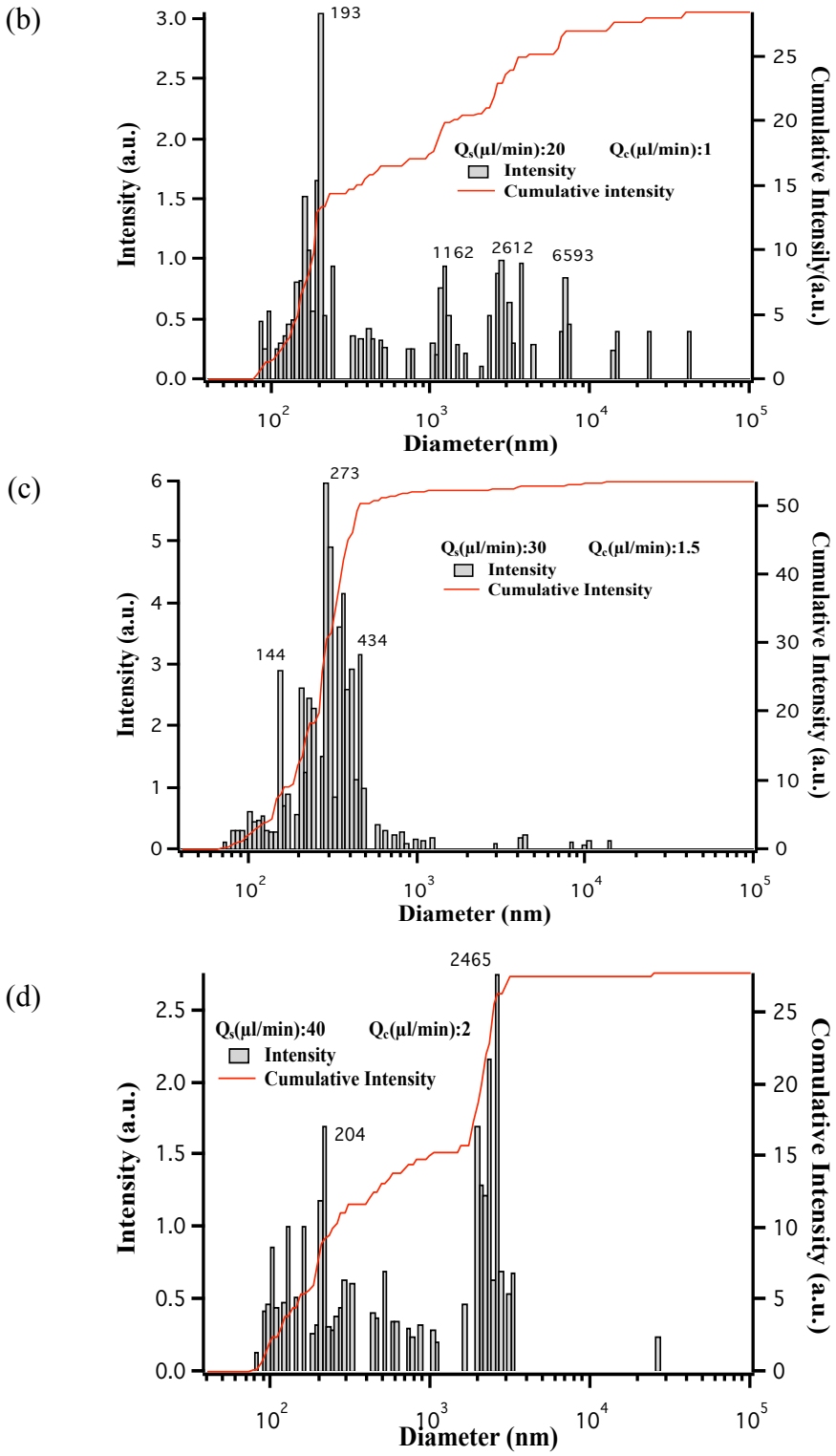

Figure 4. 7: DLS size distribution histograms of NPs obtained in MFD 1 with different flow rates (in $\mu l.min^{-1}$) set: a) Q_s=10, Q_c=0.5. b) Q_s=20, Q_c=1, c) Q_s=30 Q_c=1.5, d) Q_s=40, Q_c=2. Concentrations of CTACl = 10^{-2}M in water and of Adambodipy = 0.2mg/ml in THF/EtOH=3/7 (v/v).

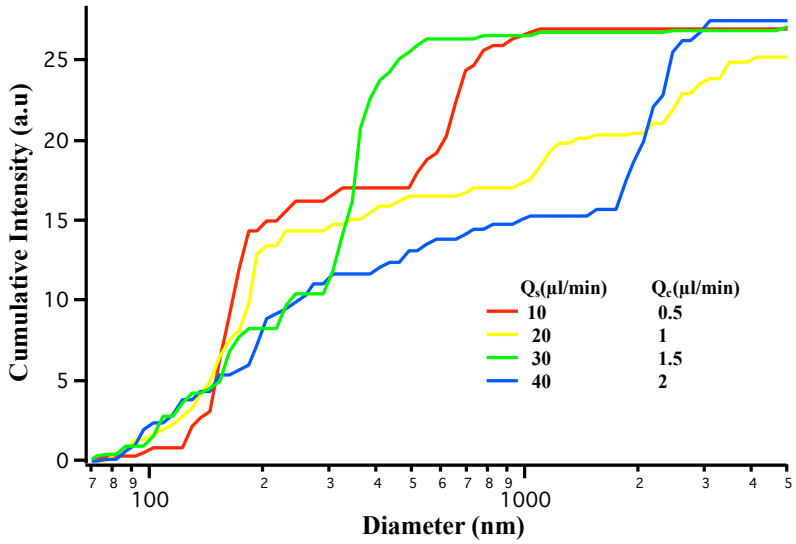

Figure 4. 8: Comparison of the cumulated intensity curves of the size distribution for different flow rates ratio extracted from Fig.4.7

After overlaying the cumulated intensity curves of size distribution for several flow rates with fixed flow rate ratio 0.05 in **Fig. 4. 8**, two size populations of aggregates are observed in the products. Small aggregates are mainly with a similar radius in the range of 150-250nm and larger aggregates with a radius over 1000nm. We shall see later that the populations of small particles have the size expected for a flow ratio of 0.05 when non-crystals do not deposit on the tip. The crystallization on the tip of the capillary tube induces a large heterogeneity in the samples, mainly for a size of the NPs above 300nm.

We have measured the absorption and fluorescence spectra of the samples made with CTACl (10^{-2}M) in MFD 1.

According to **Fig. 4. 9** the sharp peak (516 nm) near the main band of fluorescence curves is due to the reflection (excitation light scattering). The main absorption band at 516 nm is attributed to the 0-0 vibrational band of a strong S_0->S_1 transition and main emission band at 527 nm is due to the transition S_1->S_0. The particles emission is further seen at 632nm and 670nm. Their intensities slightly change from one sample to another. Also, we can conclude that whatever their fluorescence, all the particles have the same absorption. The fluorescent band at 632nm may be due to a special arrangement of the molecules in the NPs.

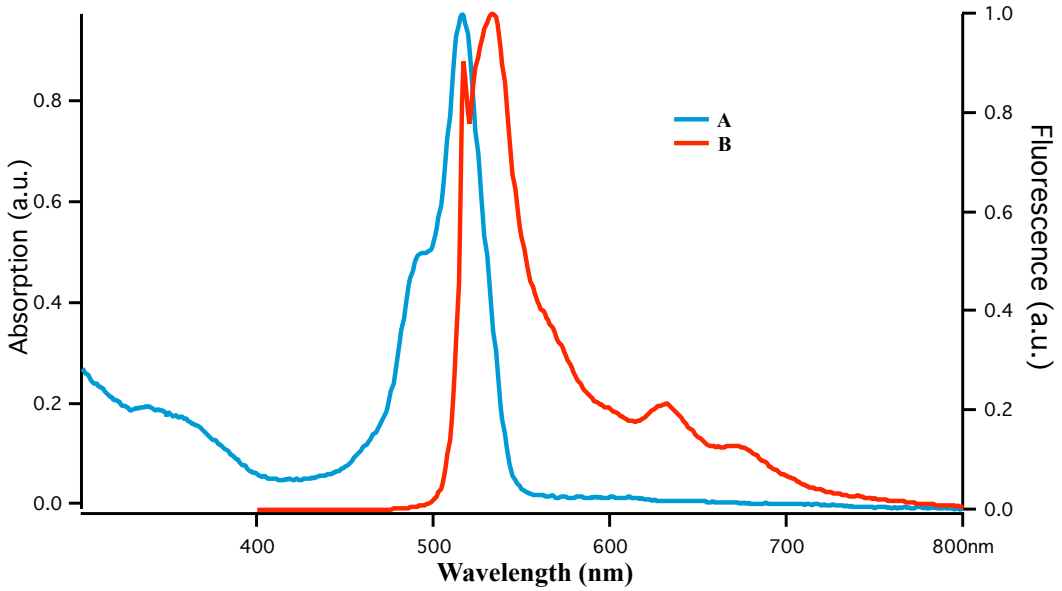

Figure 4. 9: Spectrum A and B are represented absorption and fluorescence for the sample with Adambodipy concentration 0.2mg/ml, with flow rate 10µl/min for the side flow and 0.5µl/min in the centre. The mixtures are done with CTACl (10^{-2}M) in the side flow. Emission spectrum λex=516nm; Absorption spectrum before dilution (λmax_abs=516nm);

This special arrangement can be induced by the excitation (excimer, exciton) or already present in the NP (defect). When several species are present, or when a sole species exists in different forms in the ground state (aggregates, complexes, tautomeric forms, etc.), the excitation and absorption spectra are no longer superimposable.

Here we have observed that the shape of excitation and absorption spectra are superimposable, and then we can confirm that there is a single species in the ground state. So the appearance of longer wavelength emission band is likely to be induced by excitation (for instance excimer formation).

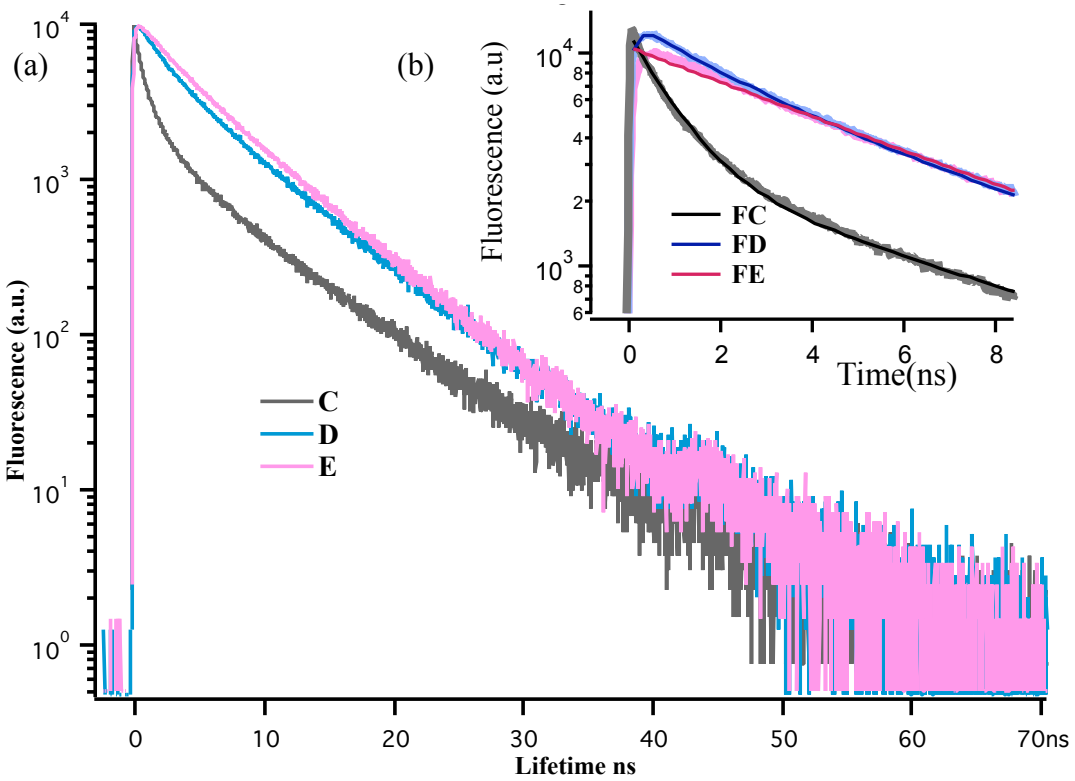

Figure 4. 10: (a) C, D and E are represent the lifetime decays at 533nm, 630 nm and 672 nm with fitting curves FC, FD FE in (b) of partial enlargement of the lifetime decay, in order to see the rising part of the fluorescence decay for each.

Many aromatic hydrocarbons can form excimers. The fluorescence band corresponding to an excimer is located at wavelengths higher than that of the monomer and does not show vibronic bands [27].

From **Fig. 4.9**, we noticed that there are two more bands after the main one at 533nm, at 630nm and 670nm seperately. The fluorescence decay curves were then obtained at those wavelengths with the time-correlated single-photon-counting method by using a titanium-sapphire laser (see **Fig. 4. 10**). Comparing to the fluorescence decay at 533nm, the lifetime decays collected at 630nm and 670nm clearly show a fluorescence rising at the beginning, and the lifetime corresponding to the rising of the fluorescence was 0.1 ns, we can calculate the lifetime by fitting functions as following (see insert **Fig. 4. 10 (b)**).

We supposed that we got single molecules and excimer during the experiments and we would be in the case of dissociation of the excimer within excited-state. It is a straightforward matter to argue that the band at 533nm belongs to monomer, also the excimer bands have lifetime decays were collected 630 nm and 672 nm.

Firstly, we try to fit those fluorescence decays by **Eq. 4.2,** with two species. (Related to **§ 2.1.2.**)

$$I_t = A\left[exp^{(-t/\tau_{pos})} - exp^{(-t/\tau_{neg})}\right] \qquad \text{Eq. 4.2}$$

The result was not satisfying, as it cannot be well fitted; nonetheless, we tried to fit the decays with **Eq. 3** with three species.

$$I_t = A\left[exp^{(-t/\tau_{pos1})} + exp^{(-t/\tau_{pos2})} - exp^{(-t/\tau_{neg})}\right] \qquad \text{Eq. 4.3}$$

According to the results, we got:

Table 4. 3: Parameters according to the fitting function (Eq. 3).

Sample 10-0.5	**A**	τ_{pos1}	τ_{pos2}	τ_{neg}
At 533nm		6.4ns (23%)	0.92ns (77%)	
At 630nm	$6.8e^3$	6.6-6.7ns	2,3-2.6ns	0.11ns
At 672nm	$5.5e^3$	6.4ns	4.4ns	0.13ns

4.2.3. Spectroscopy, DLS results of MFD 2

The concentration of adambodipy in the organic solution was fixed at 0.35mM. The flow rate Q_c / Q_s was kept higher than 0.025 otherwise particles could not be detected in DLS. It was kept lower than 0.075 otherwise Bodipy crystals grow on the nozzle. The micro-fluidic systems were improved to overcome the formation of crystals at the edge of the capillary, as detailed in the § 4.1.2.

Nevertheless, the DLS measurements showed the presence of particles. During the analyses the signal of the detected particles increased as the concentration of the Adambodipy in the samples increased (imposed by the flow rates ratio).

Among the number of samples taken for different flow rate ratio, several of them seem to confirm the hypothesis that the flow rate ratio would determine the particle size, and three of them are presented as follow.

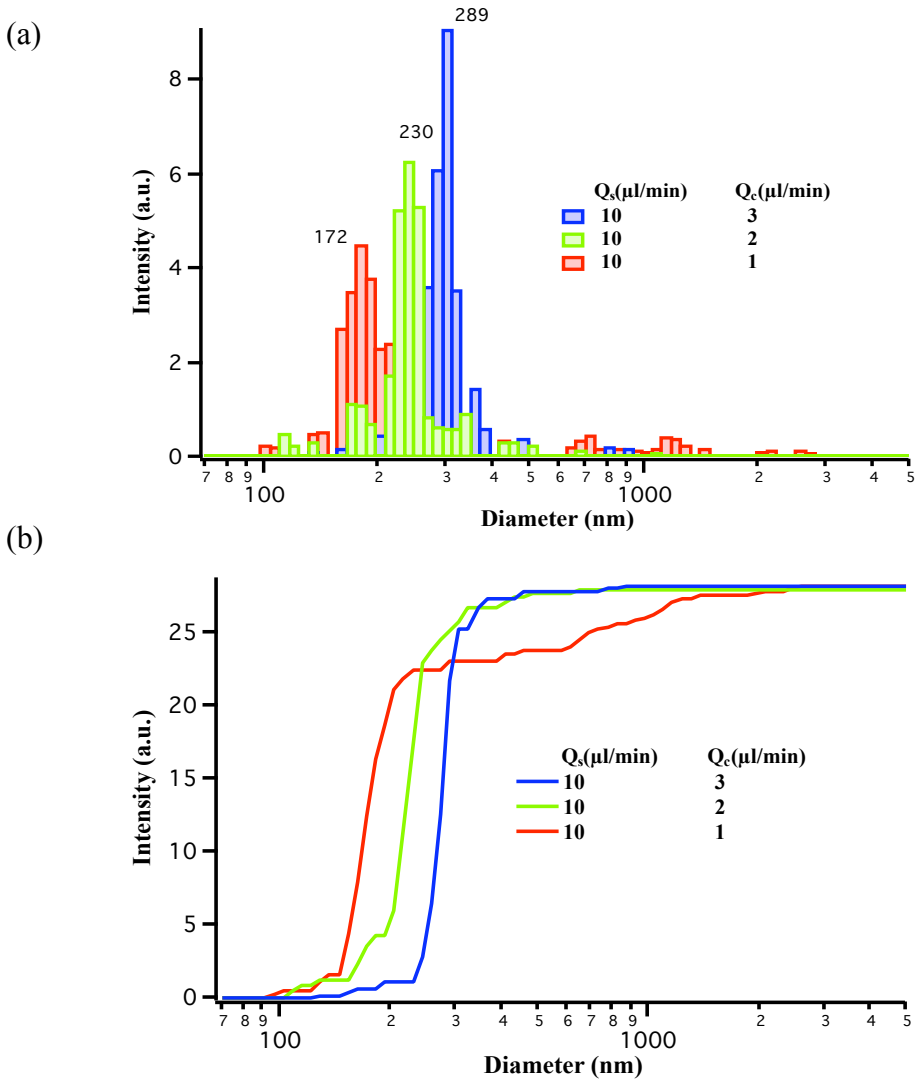

Figure 4. 11: DLS analyses for different flow rates ratio in MFD2. (a) Comparison of the size distribution for different flow rates ratio (b) Comparison of the cumulated intensity curves of the size distribution for different flow rates ratio. The concentration of Adambodipy solution is 0.2mg/ml, Concentration of CTACl=10^{-2}M.

Compared with the DLS results of MFD1 in **Fig.4.7** and **4.8**, the DLS results shown in **Fig.4.10** indicate a unimodal population of radius for aggregates, and the large radius population disappeared. That is the main progress for the use of MFD2 compared with MFD1, to remove the production of big aggregates.

Also, as shown on **Fig.4.10 (a)**, when keeping the side flow as a constant of 10µL.min^{-1}, size distribution of NPs can be tuned by decrease of the center flow from 3 to 1, the NPs become smaller, from 289 to 172 nm as mean diameter.

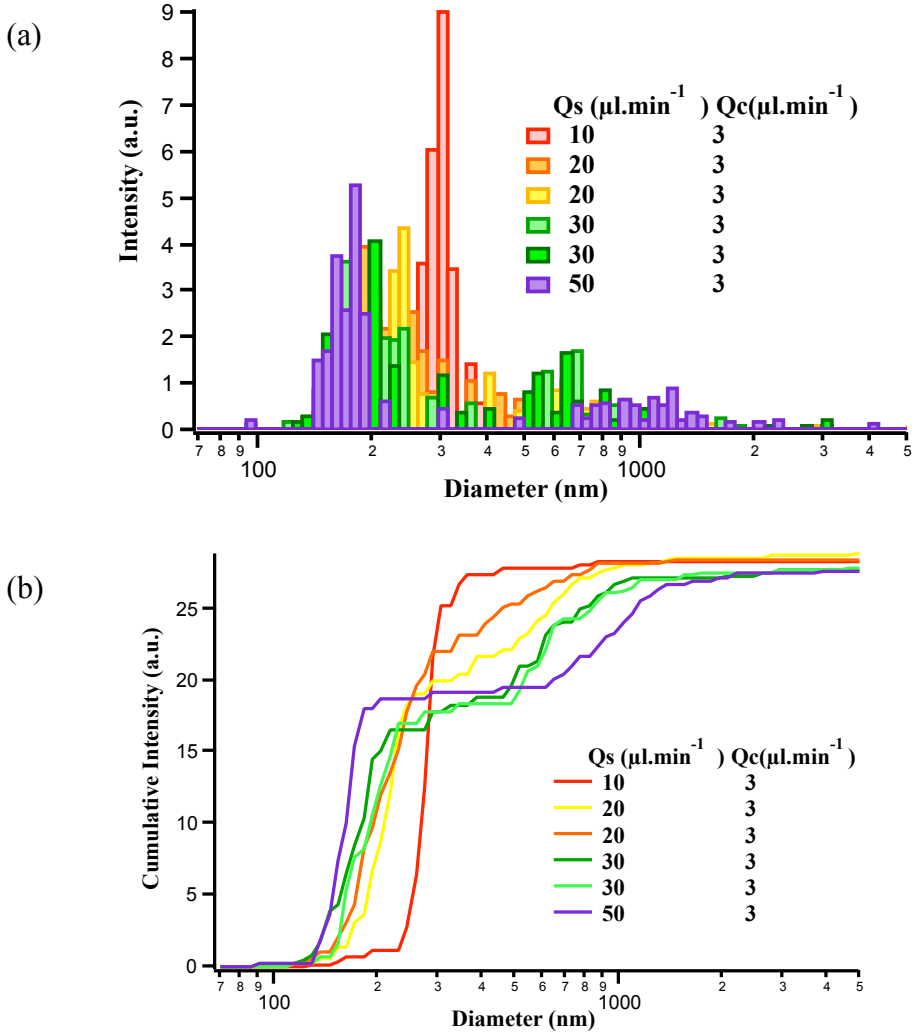

Figure 4. 12: DLS analyses for different flow rates ratio in MFD2. (a) Comparison of the size distribution for different flow rates ratio (b) Comparison of the cumulated intensity curves of the size distribution for different flow rates ratio. The concentration of Adambodipy solution is 0.2mg/ml, Concentration of CTACl=10^{-2}M.

Compared with the **Fig.4.10**, **Fig.4.11** demonstrates that with the use of the MFD 2, the size of NPs can be tuned by varying the side flow rate Qs, while keeping the center flow rate Qc as constant.

As Qs increases, from 10 to 50 µL.min^{-1}, whereas Qc/Qs decreased, the NPs become smaller, from 300 to 180 nm. The radius of NPs can be plot as the function of Qc/Qs in **Fig.4.17**, and is closed to linear relationship. The experiments are reproducible and we could then concludes the main effect is the flow rate ratio Qc/Qs.

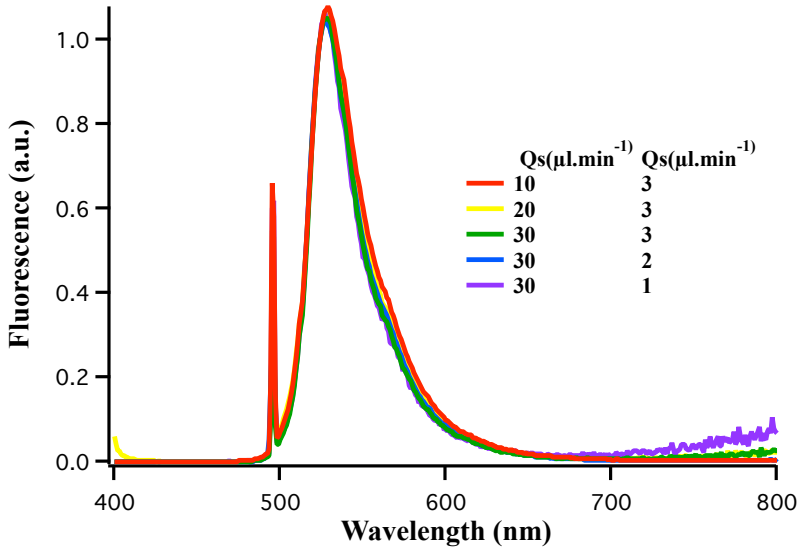

Figure 4. 13: Normalized Fluorescence spectra of the samples prepared with various flow rates in µL.min^{-1} (Qs-side flow; Qc-capillary flow,). The concentration of Adambodipy solution is 0.2mg/ml, λexc=495nm.

For the emission spectroscopy, from **Fig.4.13** we noticed that with different flow rates, those samples had quite similar emission profile and no additional "red" band appeared beyond the main one at around 523nm compared with the emission profile of the samples from MFD1 in **Fig. 4.9**. The main band (523nm) was located at the same position as the Adambodipy in solution of THF/EtOH=3:7 with CTACl 10^{-3}M.

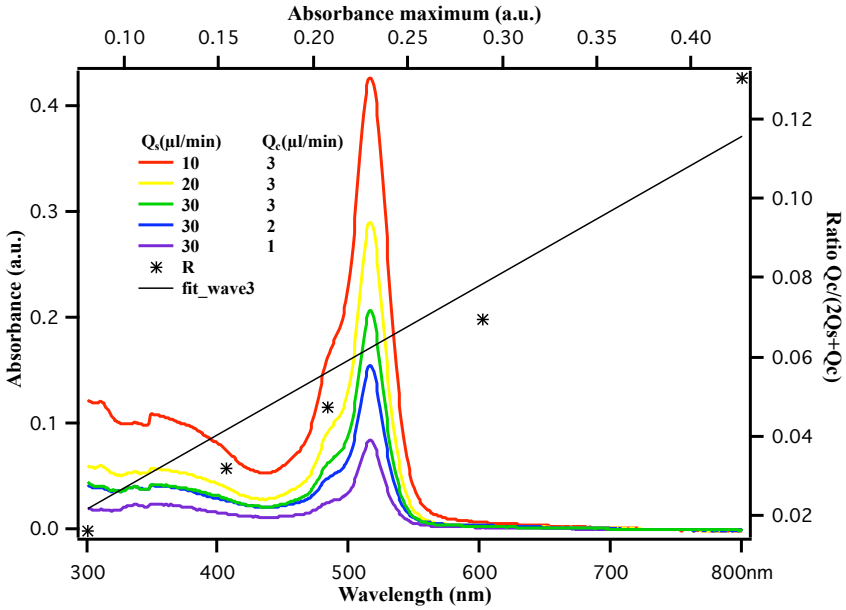

Figure 4. 14: Variations in Absorption intensity measured after collecting samples at the end of micro-fluidic channel for different dilution factors, which is Qc/(2Qs+Qc).

The absorption intensity at 516nm (maximum) as a function of flow rate ratio due to the increasing concentrations of Adambodipy molecule are depicted in **Fig.4.14**. As the flow rate ratio increases, the absorption at the maximum of the band decreases. This curve proved that we got a quite good MFD system and a good agreement between intensity of the absorption band and flow rate ratio. Also, the curve is reproducible.

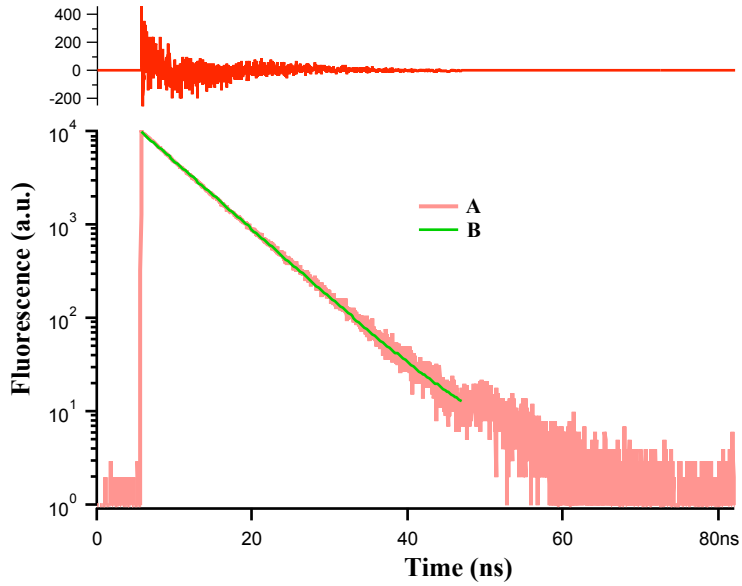

Figure 4. 15: Fluorescence decay curve A, with a fitting curve B with monoexponential function. The sample is prepared with a side flow rate Qs=10 µL.min^{-1} and a capillary flow rate Qc=0.5µL.min^{-1} under CTACl 10^{-2} M with MFD2.

The fluorescence time decays were measured for most of the samples collected with MFD2 under the same surfactant concentration 10^{-2} M. They all reveal the same decay curve. As example, **Fig. 4.15** shows a monoexponential decay (resulting in a straight line in log. scale). Which means in MFD 2 we got mainly one product and the lifetime was 5.93ns± 0.05ns.

In contrast, the fluorescence decay of the sample with MFD 1, in **Fig. 4.10**, is very fast and multiexponential. The spectroscopic properties, and particularly fluorescence spectrum and time decay, are similar to those obtained for the single molecule in DCM solution.

4.2.4. Effect of CTACl

In order to determine the effect of surfactant, several nanoparticle samples are collected under the same conditions, i.e., flow rate ratio, initial concentration of Adambodipy organic solution, but with or without CTACl.

As it was suggested for the samples prepared by the bulk method in presence of CTACl, the micelles may trap the Adambodipy but with very small size that cannot be detected by DLS. The former MFD producing process was implemented with a concentration of CTACl 8 times higher than its CMC (1.3×10^{-3}M), and then has created a large amount of micelles. The further experiments are done with concentration of CTACl below its CMC at a concentration of 1×10^{-3}M. Then the NPs suspension samples are collected and analyzed as follow:

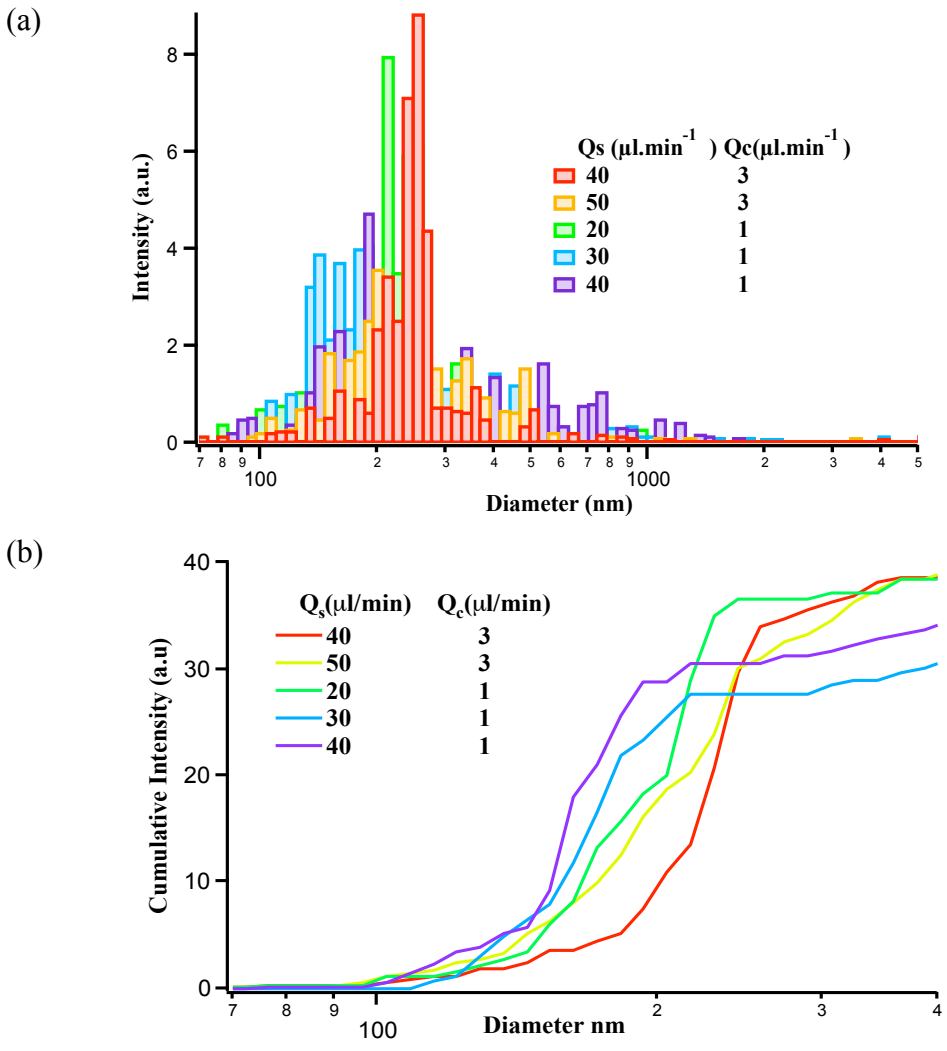

Figure 4. 16: DLS analyses for different flow rates ratio in MFD 2. Size distribution histogram of Adambodipy NPs produced at flow rates Q_S=20 µL.min^{-1} and Q_C=1 µL.min^{-1}. (b) Comparison of the size distribution for different flow rates ratio (c) Comparison of the cumulated intensity curves of the size distribution for different flow rates ratio. Those NPs suspension samples are collected with concentration of CTACl=10^{-3}M, $C_{Adambodipy}$=0.2mg/ml in THF/EtOH=3/7 (v/v) as organic solution.

According to the results of DLS measurements that are shown in **Fig. 4.16**, as Q_c/Q_s decreases, from 0.075 to 0.025, the NPs become smaller, from 240 to 160 nm. In addition, the DLS intensity decreased, due to the lowering concentration of the organic solution of Adambodipy.

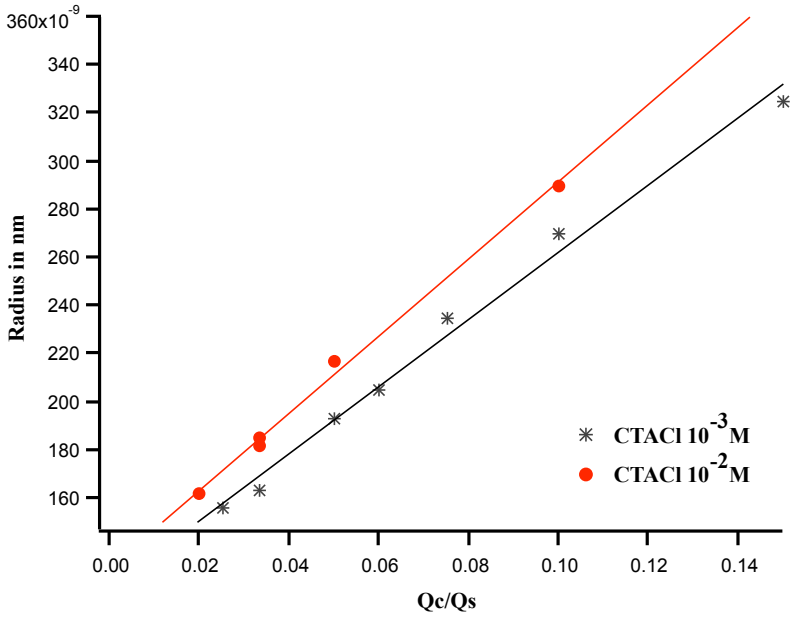

Figure 4. 17: Radius of NPs suspension for MFD 2 as the function of Qc/Qs under different concentration of CTACl 10^{-2}M and 10^{-3}M. The concentration of Adambodipy solution is 0.2mg/ml.

The radius of NPs with low concentration of CTACl can be also ploted as the function of Qc/Qs in **Fig. 4.17**, which is also closed to linear relationship and fits the same trend as the plot of radius of NPs that obtained with high concentration of CTACl. This similarity can be related to the hydrodynamics coupled with the diffusion in the microdevice. The supersaturation governed the kinetics of nucleation and growth mechanisms and finally the size of the NPs.

The Adambodipy NPs suspensions that obtained from MFD 2 with concentration of CTACl under CMC were also analyzed by absorption and fluorescence spectroscopies. For all the samples obtained at different flow rates ratio the spectra are identical except their intensities following the dilution effect. Typical fluorescence and absorption spectra obtained for Adambodipy in solution and in solid states (NPs and microcrystal) are overlaid on **Fig. 4.18**.

On the fluorescence spectrum obtained under the microscope set-up (cf. Chapter 6) for the microcrystal produced by recrystallization method[28] (curve C **Fig. 4.18 (a)**), there is a red shift (24 nm compared to the main band at 523nm for the Adambodipy in solution. The band

at 547nm can be attributed to the crystalline structure of the Adambodipy obtained from the X-ray diffraction (data not shown). The band at 573nm is characteristic of the crystal and we know from polarization experiments that it is the superposition of the vibrational structure and of a trapped exciton[29].

The sample B prepared by MFD 2 exhibits a main fluorescence band at 529 nm and a shoulder around 570 nm between the adambodipy monomer (in solution) and its crystalline phase. This suggests that the sample B is in an amorphous phase or a poorly crystallized phase. It agrees with the fact that the MFD preparation methods can be considered as fast precipitation processes.

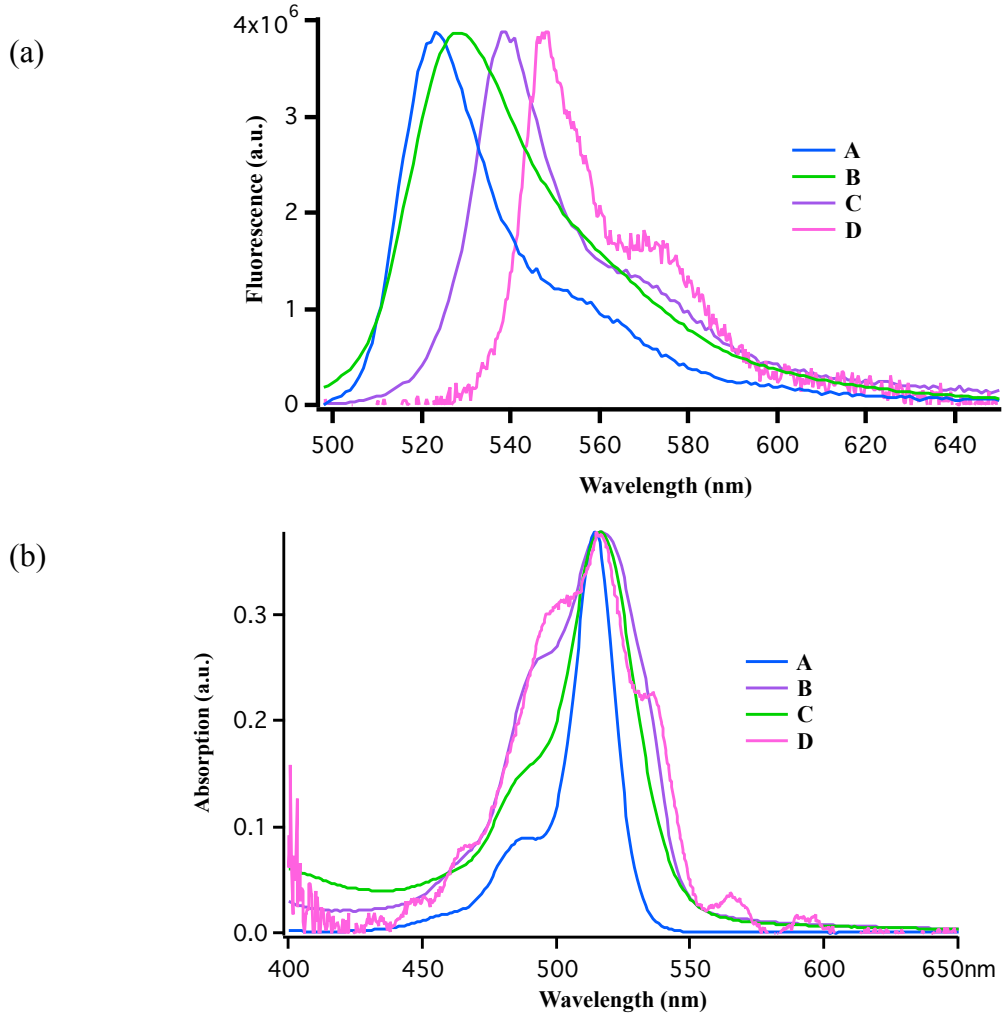

Figure 4. 18: (a) Fluorescence spectra for sample A: solution of adambodipy in EtOH/THF=7:3 with CTACl(10^{-3}M). For sample B and C represent the NPs suspensions produced with MFD 2, with high concentration of CTACl (10^{-2}M) and low concentration of CTACl (10^{-3}M) respectively. All those samples are excited at 495nm with the same other experimental parameters. Then the fluorescence spectrum D is for the single crystal sample, excited at 343nm with main bands detected at 547 and 573nm. – (b) Absorption spectra for the same samples A, B, C and D.

Fig. 4.18(b) shows absorption spectra for molecules in solution (A), for NPs suspensions produced by MFD (B) and the micro-absorption spectrum of an adambodipy single crystal (D). They exhibit absorption maxima (λ_{max}) at 514nm for the molecules, and 517nm for the sample B and sample C. In microcrystal, the absorbance peaks are leveled off by a measurement artifacts (light leaks around the crystal and interference building between the two faces of the crystal). The shoulder at 540nm is characteristic of the crystalline state and is not seen in the sample B from MFD. The difference of the absorption spectra between sample B and microcrystal D confirms that samples produced by MFD are amorphous.

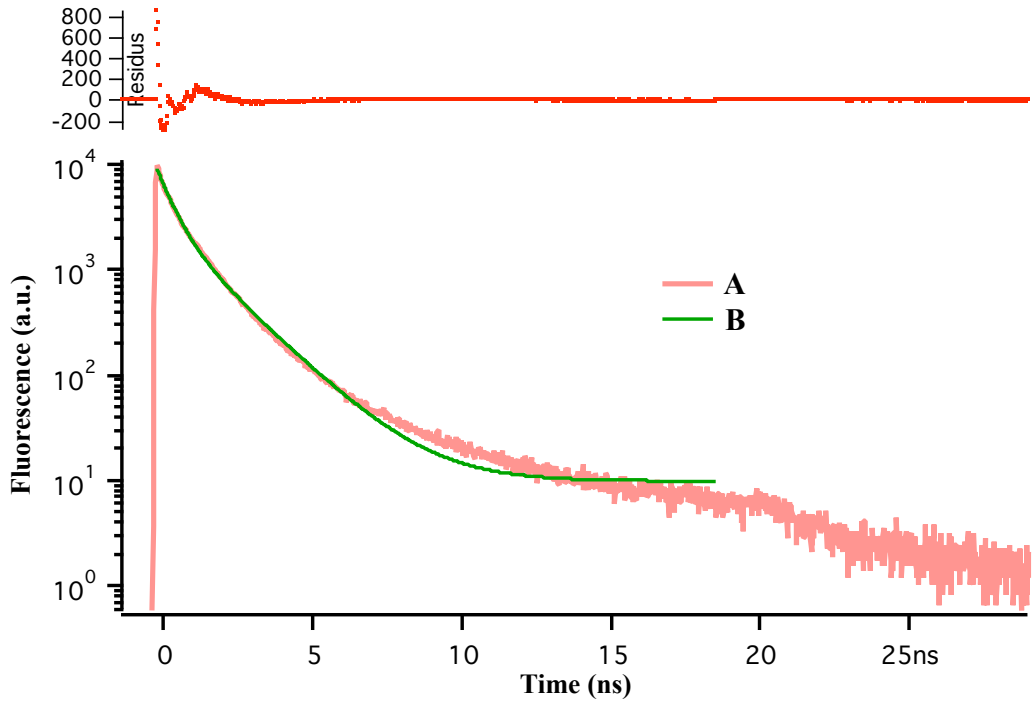

Figure 4. 19: Fluorescence decay curve A, with a fitting curve B with bi-exponential function. The sample is prepared with a side flow rate Qs=20 µL.min^{-1} and a capillary flow rate Qc=3µL.min^{-1} under CTACl (10^{-3} M) with MFD2.

The fluorescence time decays are almost the same for all the samples collected with MFD 2 and under a concentration of CTACl that equals to 10^{-3} M, and the typical curves are shown in **Fig. 4.19.** The decay exhibits a bi-exponential lifetime behavior associated to the NPs components contribution. Here the short and long lifetime components give approximate values of 0.48ns for 62% and 1.6 ns for 38%.

To record those spectra the samples were sometimes diluted with the same mixture THF-EtOH- water-CTACl than the one obtained after mixing of the side and capillary flows with their corresponding flow rates.

Then, the main results concerning the particle size are that without CTACl in the mixture big particles are obtained, with peaks detected by DLS over 1µm. And few results are shown in the **Fig. 4.20.**

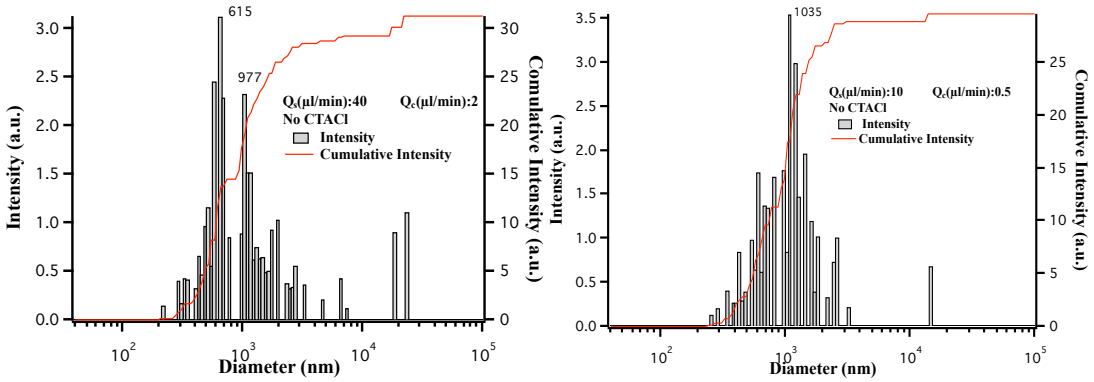

Figure 4. 20: DLS graph of flow rate a) Q_s=40 µl.min^{-1}, Q_c=2 µl.min^{-1}. b) Q_s=10 µl.min^{-1}, Q_c=0.5 µl.min^{-1}, without surfactant, $C_{Adambodipy}$=0.2mg/ml in THF/EtOH=3/7 (v/v) as organic solution.

There is an obviously increase on the average diameters for NPs suspension samples without surfactant in **Fig. 4.20**. This shows that CTACl have the ability to stabilize Adambodipy nanoparticles and avoid the aggregation and formation of large particles.

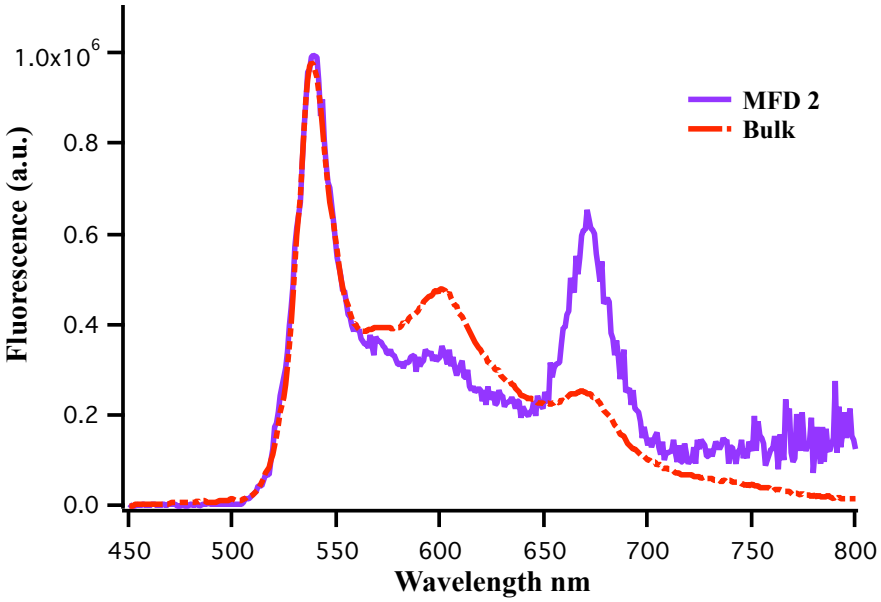

Figure 4. 21: Fluorescence spectra according to the NPs suspensions synthesized without surfactant CTACl, 'Bulk' represents sample 8 from bulk method in Chapter 2(§ 2.4); 'MFD 2' represents the NPs suspension with Q_s=40 µl.min^{-1}, Q_c=2 µl.min^{-1} regarding to the sample in **Fig. 4.20**

In conclusion, in the presence of high concentrations of CTACl that above CMC, all the NPs suspension spectra from either bulk method or MFD method under different device or flow rate condition exhibit the same band located at 523 nm. They are all similar to the one

presented for monomer in THF-EtOH solution that defined in Chapter 2, which related to Adambodipy molecules trapped in micelles.

Without CTACl in the mixture, the absorption and fluorescence spectra were all similar to the samples obtained by the bulk method without CTACl in **Fig. 4.21**. The fluorescence spectra in **Fig.4.21** show a remarkable red shift of 10 nm compared to the band at 523nm for both the monomer in solution with THF-EtOH solution and the NPs suspension with high concentration CTACl (**Fig. 4.13**), however they are located at the same position at 539nm with the NPs suspension with low concentration CTACl according to NPs in solid phase (**Fig. 4.18**). According to the former analysis and the calculated amorphous phase NPs in Chapter 3, this red-shifted band represents the amorphous phase NPs. And the appearance of the bands at higher wavelength 600- and 670 nm may represent big aggregates.

So with the presence of CTACl under CMC, by 3D-hydrodynamic focusing method with MFD 2, we obtained narrow distributed amorphous phase NPs with tunable size from 150-300nm.

4.2.5. Aging

By reexamining the samples from several flow rate ratios in the former experiments after several days (from 1 to 20 days), we found that the NPs suspension samples are quite stable with the presence of surfactant. These experiments and this trend are also reproducible.

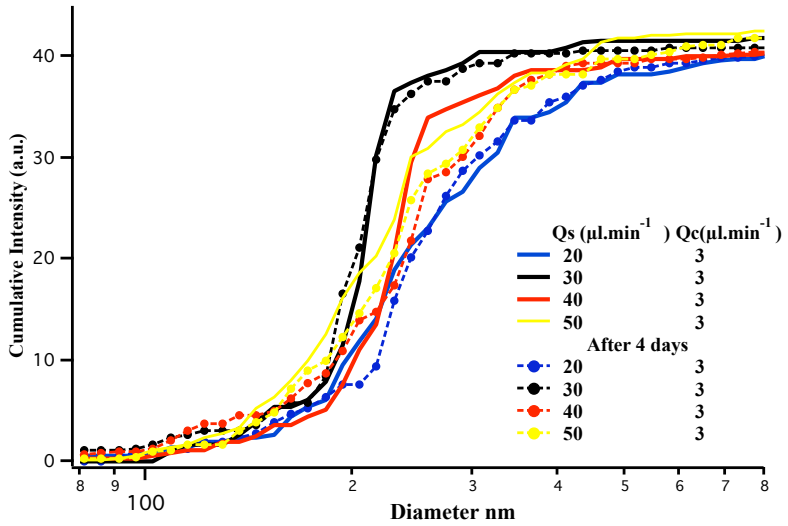

Figure 4. 22: Comparison of the cumulated intensity curves of the size distribution for fresh samples (solid line) obtained at various flow rate ratios, and for corresponding samples reexamined (dash line)

after 4 days (same color for same flow rate ratios). Those NPs suspension samples are collected with concentration of CTACl=10^{-3}M, $C_{Adambodipy}$=0.2mg/ml in THF/EtOH=3/7 (v/v) as organic solution.

4.3. Extra spectroscopy analysis, time resolved area-normalized emission spectroscopy (TRANES)

To get a better understanding about the decay of the emission and to have the different species presented in the system, the fluorescence spectra were reconstructed at different time after excitation and normalized to the same area (**Fig. 4.23**).

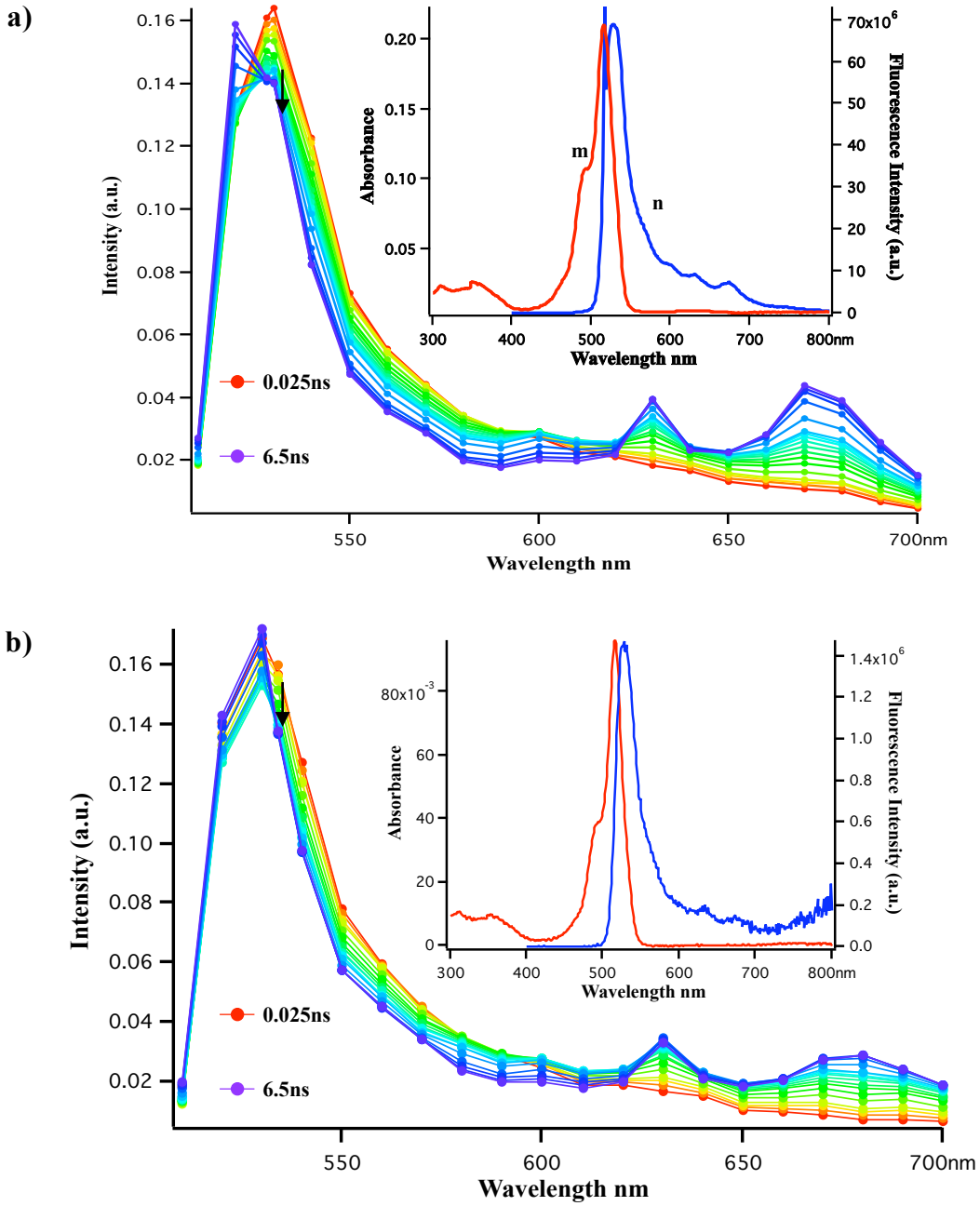

Figure 4. 23: TRANES spectra for time decay of the NPs suspension sample collected from MFD1 under flow rate (a) 10-0.5, and (b) 30-1.5 both with initial concentration of Adambodipy 0.2mg/ml and

high concentration of CTACl 10^{-2}M, with their fluorescence (blue) and absorption (red) spectra on the right hand side. The spectra have been normalized to the same area under the curves to compensate for the decay due to intramolecular deactivation.

This method has been first developed by Pansu, R. B.[30]and then advertised by Koti and co-workers, as TRANES (time resolved area-normalized emission spectroscopy)[31]. It can help us to identify and to understand the heterogeneity of the samples. TRANES were obtained in four steps in this experiment.

a) Collect fluorescence decays every 10 nm intervals start from 510nm to 700nm of emission spectrum.
b) Construction of TRES (Time resolved emission spectra) by using steady state fluorescence spectrum and the wavelength-dependent decay parameters.
c) Normalizing the area of TRES to a constant value (usually to the area of spectrum at time t=0 ns) to obtain TRANES.

The presence of the isoemissive point in the delayed traces indicates the existence of only two emissive species in the sample during the time range were the isoemissive point exists.

We have used this method to several samples from MFD1, and only the normalized curves of NPs suspension sample collected under flow rate 10-0.5 and 30-1.5 were shown in **Fig.4.23 (a), (b)** as typical**.** TRES spectra (not shown) show a continuous shift of spectral peak with time. Absence of an isoemissive point TRANES shows that the fluorescence emission in the NPs suspension originates from three or more emissive species. There is an obviously blue shift for both flow rate at the same band of 530nm. This is due to the disappearance of the NPs fluorescence compared to that of the molecules in micelles that has a longer lifetime. The sample has two small bands at wavelength around 630 and 670nm that we can observe again in the normalized time decay curves at the same positions. These long live emissions can be attributed to excimer that acts as traps. This red emission is not produced directly by the laser pulse. We do not see isobestic points on these spectra since the two processes: micelle and exciton emission are independent. The two-isobestic points spoil one another.

4.4. Conclusion

In summary, we have presented a three-dimensional hydrodynamic focusing microfluidic system to produce adambodipy organic nanoparticles and to control the precipitation process. This technique prevents the contact of the dye solution flow with the channel walls, and the micro-fluidic system has been developed to allow controlling the focused stream through the flow rates ratio. We get a better control of the process inside the MFD and also a more stabilized focused stream by using a polished cone shape at the end of the capillary in the center, with suitable Y-type device.

We succeed in preventing any crystal deposition on the tip of the capillary tube by modified the MFD system. This optimized MFD2 gives NPs of Adambodipy with very promising fluorescent properties. Changing operating conditions can modify the size distribution of the samples collected from MFD2. The ability to control the distribution of the NPs by changing the flow rates seems to be a very important issue in our experiment. Indeed the flow rates affect the residence time and also the nucleation and growth processes as the diffusion kinetics depends on the width of the focused stream, which will be confirmed in Chapter 5 by the kinetic study. The reproducibility of the MFD method was also checked, and with Adambodipy in our experiment, the DLS results demonstrate that the nanoparticles of controlled mean size between 150-300nm can be synthesized by varying the focusing ratios. With a higher focusing ratio (Qs/Qc), smaller nanoparticles can be produced thanks to faster and more efficient mixing condition.

By bulk and MFD methods, the reprecipitation of Adambodipy leads to NPs.

With the presence of CTACl above CMC (1.3×10^{-3}M), the results from MFD may split into micelle and nanoparticle synthesis. Due to the high concentration of the surfactant, we have spontaneous formation of micelles, which dissolve Adambodipy; whereas with surfactant concentration below CMC, only the amorphous nanoparticles are presented in the suspensions. The amorphous phase was confirmed by their absorption spectrum identical with the one calculated in Chapter 3. Thus one striking result is that in presence of CTACl in high concentration, the main emission band is preserved and no J-type aggregates can be found. In the case of MFD1 system, excimers were proved to beformed. When no surfactant is present, a significant red-shift of the main Adambodipy band is observed as well as the appearance of relatively intense red-emitting bands (above 600nm). The main-band shift may be attributed to the presence of aggregates. Recorded decays in the main band show a multiexponential

behaviour (shorter than Adambodipy in solution), this is also consistent with the presence of aggregates. At longer wavelengths, decays show a rising time. Such results are consistent with the presence of excimers. Concerning the single crystal study, which has to be pursued, the emission is not only significantly red-shifted but also doubled. As a former conclusion we would say that the red-shift (compared to solution) of the main emission band is a clue for a solid-state particle formation (Chapter 3)

In further work, we will try to find more suitable and removable surfactant to find a better condition for MFD. Once the surfactant removed, we may be able to observe the morphology of the NPs by AFM.

Furthermore, as we are convinced from the spectroscopy measurement, that we can get NPs, but no NCs of Adambodipy by MFD method. We are wondering if, by changing the conditions of the experiment, we can get NCs, which are more photostable without excimer. However no experiment have been performed concerning the photostability of the NPs yet.

Reference:

[1] Su, Y. F.; Kim, H.; Kovenklioglu, S.; Lee, W. Y. *"Continuous nanoparticle production by microfluidic-based emulsion, mixing and crystallization."* Journal of Solid State Chemistry, **2007**, *180*, 2625-2629.

[2] Génot, V.; Desportes, S.; Croushore, C.; Lefèvre, J.-P.; Pansu, R. B.; Delaire, J. A.; von Rohr, P. R. *"Synthesis of organic nanoparticles in a 3D flow focusing microreactor."* Chemical Engineering Journal, **2010**, *161*, 234-239.

[3] Dushkin, C. D.; Saita, S.; Yoshie, K.; Yamaguchi, Y. *"The kinetics of growth of semiconductor nanocrystals in a hot amphiphile matrix."* Adv Colloid Interfac, **2000**, *88*, 37-78.

[4] Murray, C. B.; Kagan, C. R.; Bawendi, M. G. *"Synthesis and characterization of monodisperse nanocrystals and close-packed nanocrystal assemblies."* Annu Rev Mater Sci, **2000**, *30*, 545-610.

[5] Jeffrey D Winterton, D. R. M., Julian M. Lippmann, Albert P. Pisano, Fiona M. Doyle. *"A novel continuous micro-fluidic reactor design for the controlled production of high-quality semiconductor."* Journal of Nanoparticle Research, **2008**, *10*, 893-905.

[6] Alivisatos, A. P. *"Semiconductor clusters, nanocrystals, and quantum dots."* Science, **1996**, *271*, 933-937.

[7] Puntes, V. F.; Krishnan, K. M.; Alivisatos, A. P. *"Colloidal nanocrystal shape and size control: The case of cobalt."* Science, **2001**, *291*, 2115-2117.

[8] Chan, E. M.; Mathies, R. A.; Alivisatos, A. P. *"Size-controlled growth of CdSe nanocrystals in microfluidic reactors."* Nano Lett, **2003**, *3*, 199-201.

[9] Xu, S. Q.; Nie, Z. H.; Seo, M.; Lewis, P.; Kumacheva, E.; Stone, H. A.; Garstecki, P.; Weibel, D. B.; Gitlin, I.; Whitesides, G. M. *"Generation of monodisperse particles by using microfluidics: Control over size, shape, and composition."* Angew Chem Int Edit, **2005**, *44*, 724-728.

[10] Cabeza, V. S.; Kuhn, S.; Kulkarni, A. A.; Jensen, K. F. *"Size-Controlled Flow Synthesis of Gold Nanoparticles Using a Segmented Flow Microfluidic Platform."* Langmuir, **2012**, *28*, 7007-7013.

[11] Krishnadasan, S.; Brown, R. J. C.; deMello, A. J.; deMello, J. C. *"Intelligent routes to the controlled synthesis of nanoparticles."* Lab Chip, **2007**, *7*, 1434-1441.

[12] Fletcher, P. D. I.; Haswell, S. J.; Pombo-Villar, E.; Warrington, B. H.; Watts, P.; Wong, S. Y. F.; Zhang, X. L. *"Micro reactors: principles and applications in organic synthesis."* Tetrahedron, **2002**, *58*, 4735-4757.

[13] Song, Y. J.; Hormes, J.; Kumar, C. S. S. R. *"Microfluidic synthesis of nanomaterials."* Small, **2008**, *4*, 698-711.

[14] Alivisatos, A. P. *"Perspectives on the physical chemistry of semiconductor nanocrystals."* J Phys Chem-Us, **1996**, *100*, 13226-13239.

[15] Pabit, S. A.; Hagen, S. J. *"Laminar-flow fluid mixer for fast fluorescence kinetics studies."* Biophysical journal, **2002**, *83*, 2872-8.

[16] Andreas. Jahn, J. E. R., Wyatt N. Vreeland, Don L. DeVoe, Laurie E. Locascio, Michael. Gaitan. *"Preparation of nanoparticles by continuous-flow microfluidics."* J Nanopart Res, **2008**, *10*, 925-934.

[17] Madou, M. J. *"Fundamentals of microfabrication."* **1997**.

[18] Becker, H.; Gartner, C. *"Polymer microfabrication methods for microfluidic analytical applications."* Electrophoresis, **2000**, *21*, 12-26.

[19] Soper, S. A.; Ford, S. M.; Qi, S.; McCarley, R. L.; Kelly, K.; Murphy, M. C. *"Polymeric microelectromechanical systems."* Anal Chem, **2000**, *72*, 642A-651A.

[20] McDonald, J. C.; Duffy, D. C.; Anderson, J. R.; Chiu, D. T.; Wu, H. K.; Schueller, O. J. A.; Whitesides, G. M. *"Fabrication of microfluidic systems in poly(dimethylsiloxane)."* Electrophoresis, **2000**, *21*, 27-40.

[21] Jo, B. H.; Van Lerberghe, L. M.; Motsegood, K. M.; Beebe, D. J. *"Three-dimensional micro-channel fabrication in polydimethylsiloxane (PDMS) elastomer."* J Microelectromech S, **2000**, *9*, 76-81.

[22] Fainman, Y. L., L.; Psaltis, D.; Yang, C.;. *"Optofluidics: Fundamentals, Devices, and Applications "*; McGraw-Hill Professional, **2009**.

[23] Lee, J. N.; Park, C.; Whitesides, G. M. *"Solvent compatibility of poly(dimethylsiloxane)-based microfluidic devices."* Anal Chem, **2003**, *75*, 6544-6554.

[24] McDonald, J. C.; Whitesides, G. M. *"Poly(dimethylsiloxane) as a material for fabricating microfluidic devices."* Accounts Chem Res, **2002**, *35*, 491-499.

[25] Jessamine, N. L. P., C.; Whitesides, G. M. *"Solvent Compatibility of Poly(dimethylsiloxane)-Based Microfluidic Devices."* Anal. Chem., **2003**, *75*, 6544-6554.

[26] Genot, V.; Desportes, S.; Croushore, C.; Lefevre, J. P.; Pansu, R. B.; Delaire, J. A.; von Rohr, P. R. *"Synthesis of organic nanoparticles in a 3D flow focusing microreactor."* Chem Eng J, **2010**, *161*, 234-239.

[27] Wakai, N.; Kurihara, N.; Otsuka, A.; Imamura, K.; Takahashi, Y. *"Wintertime survey of LF field strengths in Japan."* Radio Sci, **2006**, *41*.

[28] Yuanyuan LIAO, V. G., Rachel Méallet-Renault, Thanh T. Vu, Jeff Audibert, Gilles Clavier, Robert B. Pansu. *"Spectroscopy of molecular crystals for the structural identification of nano particles."* ICP 2011 (Ed.: C.-H. Tung), Pekin, 2011 07/06, **2011**.

[29] submitted to PCCP

[30] Pansu, R. B.; Yoshihara, K. *"Diffusion of Excited Bianthryl in Microheterogeneous Media."* J Phys Chem-Us, **1991**, *95*, 10123-10133.

[31] Koti, A. S. R.; Periasamy, N. *"Application of time resolved area normalized emission spectroscopy to multicomponent systems."* J Chem Phys, **2001**, *115*, 7094-7099.

Chapter 5 Kinetics study of the formation of organic nanoparticles along a microfluidic device with fluorescence lifetime imaging (FLIM)

The controllable NPs precipitation process by 3D-hydrodynamic microfluidic method was confirmed by the former study with DLS analysis in Chapter 4, the kinetics study was also done experimentally using FLIM techniques and by simulation using the COMSOL software to estimate the variables that govern the whole process. The two main diagnostic experimental techniques employed within this thesis to investigate fluid composition and kinetics of the precipitation process within microfluidic systems used throughout this study are time-resolved single-photon-counting device and time-resolved anisotropy imaging microscopy (details in Chapter 6), which forms the basis of Fluorescence Lifetime Imaging Microscopy (FLIM). The requirements of the FLIM experiment also suggest us to use a new microfluidic system. The fundamental photophysical theories that underpin the research are illustrated in Chapter 3.

A brief description of the kinetics of pressure-driven microfluidic flows, as well as the Fickian diffusion and Maxwell-Stefan diffusion, will be outlined here to provide the understanding necessary to appreciate the models of simulation method and the results.

5.1. Governing equations of kinetics in MFD

Firstly, we state the general principles and equations used to describe the later experimentally performing and to solve the numerical simulation.

5.1.1. Hydrodynamics in the microfluidic device[1]

Hydrodynamic focusing is a technique in which the focusing of a core flow of investigated sample is achieved by allowing two sheath fluids. It is within interest of chemical technology field, mainly in mixing. It was adopted as laminar, diffusion based mixer, and at such small length scales, molecules from the side flow rapidly diffuse across the inlet stream resulting in fast and efficient mixing[2].

We considered both of the properties for controlling the focused fluid and fast mixing in our research. To deal with the kinetic study of precipitation process, the physics behind microfluidics need to be understood, and the effects due to the micro scale of the device need to be examined. Even at higher velocities, the inertial forces are negligible compared to the viscous forces because of the small dimension.

5.1.2. The equation of motion and the Navier–Stokes equation[3,4]

Since the flow in our research is considered as a continuum, the Navier-Stokes equations are applicable. Also because we are modeling the flow of water, mixed with THF/EtOH in microfluidics, where the flow velocities are much smaller than the velocity of pressure waves in the liquid, incompressibility and Newtonian fluid assumptions may be used.

In incompressibility condition, the mass continuity equation becomes:

$$\nabla \cdot \boldsymbol{u} = \mathbf{0} \qquad \text{Eq. 5. 1}$$

where $\boldsymbol{u}$ is the local velocity of the fluid, and ∇ is the del operator, which present the gradient of the vector.

Considering the fluid as a Newtonian fluid, the 2nd Newton law (conservation of momentum) leads to the following Navier-Stokes equation as:

$$\rho\left(\frac{\partial \boldsymbol{u}}{\partial t} + (\boldsymbol{u} \cdot \nabla)\boldsymbol{u}\right) = -\nabla P + \mu\nabla^2\boldsymbol{u} + F \qquad \text{Eq. 5. 2}$$

where ρ is the fluid density, $\boldsymbol{u}$ is the velocity, t is the time, P is the pressure, μ is the fluid viscosity and F is the body force (per unit volume).

If Re<< 1, the non-linear inertial term $(\boldsymbol{u} \cdot \nabla)\boldsymbol{u}$ can be neglected, and the remaining expression leads to the Stokes equations:

$$\rho\frac{\partial \boldsymbol{u}}{\partial t} = -\nabla P + \mu\nabla^2\boldsymbol{u} + F \qquad \text{Eq. 5. 3}$$

The system consists of a microfluidic channel in which the central liquid stream of Adambodipy organic solution flows with water aqueous in sheath.

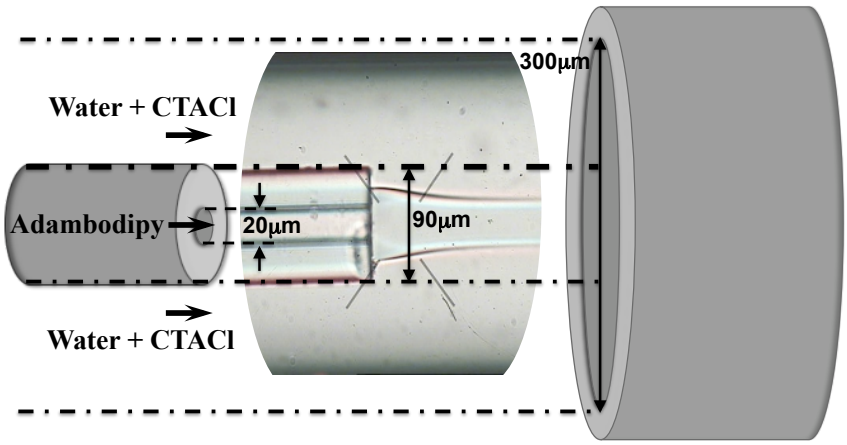

Figure 5. 1: Scheme of the microfluidics

The equation of Re is:

$$Re = \frac{\rho u_{avg} L}{\mu} \qquad \text{Eq. 5. 4}$$

where L is the most relevant length scale, μ is the viscosity, ρ is the fluid density, and u_{avg} is the average velocity of the flow. L is equal $4A/P_w$ to where A is the cross sectional area of the channel and P_w is the wetted perimeter of the channel. In the case of circular channels, L is normally taken as the diameter d (ID) of a channel (200μm in this thesis). Due to the small dimensions of microchannel in the thesis, the Re is much less than 1.0, (around 0.12-0.02 according to total velocity from 0.06-0.01m/s) which is a typical laminar flow.

After applying the steady state in the incompressible Stokes equation presented above, for the Reynolds number<<1 the viscous term dominates, thus the flow can be approximated as creeping flow or Stokes Flow, where the body force of gravity is negligible. The **Eq.5.2** leads to:

$$\nabla P = \mu \nabla^2 \boldsymbol{u} \qquad \text{Eq. 5. 5}$$

In our case, because of the co-axial geometry, we can consider a Poiseuille flow.

The significance of viscous forces is enhanced in the case, and is the determining factor for fluid velocity in the channels due to the large shear rates near channel walls. In our case, the only remaining mechanism of mixing is diffusion across the mutual liquid–liquid interface between the two streams transverse to the direction of flow[5].

5.1.3. Determination of velocity Profile

Besides the pure pressure driven flow, the most common method used to generate fluid transport through microchannel is a pressure-driven setting with a positive displacement, such as syringe pumps. Such system was used in the thesis. One of the fundamental laws of fluid mechanics for macroscale laminar flow is the no-slip boundary condition, which states that, the fluid velocity should match the velocity of the solid boundary, so the fluid velocity at the walls must be zero. It is well accepted except in some applications where it was recently suggested that this condition is not always applicable at the micro- and nano-scale[6,7].

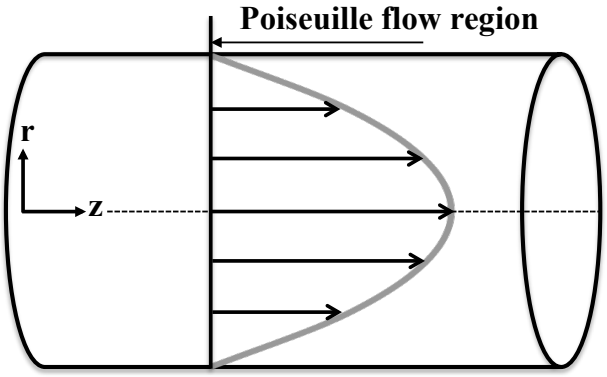

Figure 5. 2: A Poiseuille profile for a laminar flow in a microchannel.

As shown on **Fig. 5.2**, under the no-slip condition, pressure driven flows in the cylindrical microchannels develop a parabolic velocity flow distribution, commonly referred to Poiseuille flow, which has a much higher velocity in the center of the channel, and the velocity of the fluid that close to the walls is zero.

Microfabrication techniques typically fabricate microchannel with no-circular cross-section, but rectangular channel, which is the case in Chapter 4 with MFD 1 and MFD 2. This type of channel creates a more complex distribution of fluid velocities with different parabolic velocity gradients across one or both cross-sectional dimensions[8]. For the MFD 3 designed in this Chapter (**Fig. 5.1**), the Poiseuille profile is obtained. It was also simulated with COMSOL in the later studies and given in Chapter 6, **Fig. 6.10.**

Because of the profile, there is a position-dependent distribution in residence time. In that case, fluids positioned at the center exhibit higher velocity, and have significantly less time to diffuse and mix.

The pressure drops induced by the viscosity and friction forces in the fluid also characterize the flow in microchannel. In a circular microchannel, they can be calculated as following equation:

$$\Delta P = \frac{128 \mu l Q}{\pi d^4} \qquad \text{Eq. 5. 6}$$

where Q is the volumetric flow rate, *l* is the length of the pipe and *d* is its inner diameter. Typically in our experiment, the higher-pressure drops will be created by the center flow through the capillary with OD=20μm, *l*=15cm. For $\mu = 10^{-3}$Pa. s, and Q ranges from 0.5 to 3ml/min, the value for pressure drops ranges from 0.3 to 2 bars.

5.1.4. Diffusion theories: Fickian diffusion and Maxwell-Stefan diffusion.

5.1.4.1. Fickian diffusion theory:

Diffusion is the transfer of species (molecules or particles) from an area of high concentration to an area of low concentration, and the classical description of the diffusion process goes back to Fick. He relates the flux from high concentration regions to low concentration regions with a magnitude proportional to the concentration gradient. The Fick's first law is:

$$J = -D\nabla c \qquad \text{Eq. 5.7}$$

where J is the diffusion flux of the particles in $mol.m^{-2}s^{-1}$, D is the diffusion coefficient in m^2s^{-1}, c is the concentration in $mol.m^{-3}$. In the two or more dimension, the concentration gradient ∇c, it is often called the driving force in the diffusion. The minus sign in the equation means that diffusion is down the concentration gradient.

Considering the species as a sphere, the diffusion coefficient D of the molecule or particles can be estimated by the equations given by the Stokes- Einstein expression (**§ 4.2.1. Eq. 4.1**).

In microfluidic device, where often there is a velocity profile present and the molecule are transported through the channels by convection also.

Then the convection-diffusion equation is written as follow:

$$\frac{dc}{dt} + \nabla \cdot (\boldsymbol{u}c) = D\nabla^2 c \qquad \text{Eq. 5.8}$$

In the equation, the second term represents the convection process while the last term on the right side is related to normal diffusion according to the Fick's law. In the case of an incompressible and stationary flow, where the density of the fluid remains constant, the convection diffusion equation reads:

$$\boldsymbol{u}\nabla c = D\nabla^2 c \qquad \text{Eq. 5.9}$$

where c is the molar concentration, D is the diffusion coefficient, ∇c is concentration gradient. The equation is the same one used in the "Convection-diffusion" module of COMSOL database.

5.1.5.2 Maxwell-Stefan diffusion theory

Although Fick's law provides a reasonable approximation of the diffusion process in many common situations, in some occasion, the Fick's law is not enough to explain the observed experimental behavior. Among this kind of behaviors, the diffusion phenomenon in a multicomponent gaseous mixture was first has been observed, and first accurately described by Maxwell[9] (1867) based upon the kinetics of gases and then extended by Stefan (1871) and known as Maxwell-Stefan theory[10] for transport phenomena. After all, it was generalized by Taylor and Krishna[11] (1993).

The general idea of the Maxwell-Stefan theory is to consider balance between driving forces and friction forces between the diffusing components. The general form of the Maxwell-Stefan for ideal binary system with constant pressure gives:

$$\nabla x_1 = \frac{x_1 x_2}{D_{ij}}(u_2 - u_1) \qquad \text{Eq. 5.10}$$

where x is the mole fraction, D_{ij} is the Maxwell-Stefan binary diffusion coefficient, ,

In this thesis of a binary diffusion system with two diffusing species of water and ethanol, the mutual diffusivity in the system, $D_{W\text{-}E}$, is estimated from the self-diffusion coefficients of the two components D_W and D_E [12], shown as **Eq. 5.11**

$$D_{W-E} = x_W \cdot D_E + x_E \cdot D_W \qquad \text{Eq. 5.11}$$

The mass transfer can also affect the density and the viscosity of the mixture. While in this experiment, the fluids have the different density and viscosity in the inlet channel, side channel and outlet channel since they mixed during the flowing. So we use the Jouyban-Acree model that presented by Acree[13] to correlate different physical or chemical properties in this binary system. Depends on this estimation, an experimentally determined density and viscosity value for the binary mixture of water and ethanol mixtures at different temperature was reported. It gives reliable predictive model constants at temperature between 293 to 323K. The following relation (**Eq. 5.12-13**) is then used by the author to fit the density and viscosity of binary mixture of water and ethanol at 298 K[14]:

$$ln\rho_{m,T} = x_W \cdot ln\rho_{W,T} + x_E \cdot ln\rho_{E,T} - 30.808\left[\frac{x_W \cdot x_E}{T}\right] - 18.274\left[\frac{x_W \cdot x_E \cdot (x_W - x_E)}{T}\right] + 13.890\left[\frac{x_W \cdot x_E \cdot (x_W - x_E)^2}{T}\right] \quad \text{Eq. 5.12}$$

$$ln\mu_{m,T} = x_W \cdot ln\mu_{W,T} + x_E \cdot ln\mu_{E,T} - 724.652\left[\frac{x_W \cdot x_E}{T}\right] + 729.357\left[\frac{x_W \cdot x_E \cdot (x_W - x_E)}{T}\right] + 976.050\left[\frac{x_W \cdot x_E \cdot (x_W - x_E)^2}{T}\right] \quad \text{Eq. 5.13}$$

Where ρ and μ are indicators of density and viscosity; W, E and m subscripts stand for water, ethanol and their mixtures, respectively. The density and viscosity value of water, ethanol at 298K can also be found from the literature. The R^2 values for **Eq. 5.12-13** are 0.986 and 0.945 according to the reference.

5.1.5. Nucleation

The condition of supersaturation is not sufficient for a system to start to crystallize. Before crystals can develop, there must be a process where the first formed solid bodies, embryos, nuclei or seeds with only a few nanometers in size, that act as centers of crystallization.

There mechanisms of crystal nucleation are generally acknowledged: (a) the primary homogeneous nucleation, (b) the primary heterogeneous nucleation, and (c) the secondary nucleation[15].

5.1.5.1. Primary homogeneous nucleation:

If nucleation happens without preferential nucleation sites, nucleus can only be formed by homogeneous nucleation. The classical theories of homogeneous nucleation processes, coming from the work of Gibbs, Volmer, Becker and Döring and others, is based on a condensation of a vapor to liquid, and can be extended to crystallization from melts and solutions. We can quantify these concepts by considering the free energy changes per molecule of the bulk and that of the surface, and the nucleation rate J should be a function of temperature, pressure and the composition of the solution. When keep the temperature and pressure constant, it is a function of the concentration c of the solute going to precipitate.

In a solution that is supersaturated, there is a critical nucleus size that determines a nucleation barrier whose magnitude, Δg (free energy changes) can be expressed as:

$$\Delta g = \frac{16\pi {\alpha_{sl}}^3}{3} \cdot \left(\frac{\Omega}{k_B T \sigma}\right)^2 \qquad \text{Eq. 5.14}$$

Where Ω is the volume per molecule, and α_{sl} is the interfacial free energy, and σ is defined as the absolute supersaturation, (S-1).

The supersaturation S was defined as the ratio of actual concentration of Adambodipy to the solubility C_{eq}. And this is the barrier that determines the kinetics of nucleation.

$$S = \frac{C_{Adambodipy}}{C_{eq}} \qquad \text{Eq. 5.15}$$

where $C_{Adambodipy}$ could obtained from the "Convection-Diffusion module" simulation of COMSOL, and we could also find the C_{eq} from solubility expression.

Then the nucleation rate is given as[16,17]

$$J_{hom} = A_{hom} \exp\left(\frac{-\Delta g}{k_B T}\right) \qquad \text{Eq. 5.16}$$

We could group all of the factors into the coefficient B despite of interfacial energy and supersaturation, and equation then turns to:

$$J_{hom} = A_{hom} \exp\left(-B \cdot \frac{{\alpha_{sl}}^3}{\sigma^2}\right) \qquad \text{Eq. 5.17}$$

5.1.5.2. Interfacial free energy of the nanocrystal:

The free energy of crystal-liquid interfaces α_{sl} is the important role and the main difficulty in the kinetics of nucleation and crystal growth according to the equation given above. Many empirical expressions have been developed so far to determine the value from physical properties that can be directly determined. And among those expressions that correlated solubility with interfacial tension reported by Bennema and Söhnel[18], Nielson and Sohnel[19], and Mersmann[20], or Sangwal's theory[21] that related the interfacial tension to the mole fraction of solute in the solution, the Mersmann expression was widely accepted and used one.

5.1.5.3. Growth controlled for monosized nanoparticle.

Fig.5.3 demonstrates the process of nucleation and subsequent growth of nuclei. According to the figure, nucleation occurs only when the supersaturation reaches a certain

value (C_{nuc}) above the solubility (C_{eq}), which corresponds to the energy barrier defined in **Eq. 14** for the formation of nuclei. After the initial nucleation, the concentration of the solute decreases accompany with the decrease of the volume Gibbs free energy. Once it reaches the critical concentration, the nucleation process will stop and no more nuclei would form. However the growth process will occurs simultaneously when nuclei would form, and continue until the concentration reached the equilibrium concentration C_{eq}, that is solubility.

In this thesis, for the purpose of production of uniform size distribution nanoparticles, it will be the best if all nuclei are created at the same time to produce the particles with the same size; thus, it is highly desirable to have nucleation occur in a very short period of time.

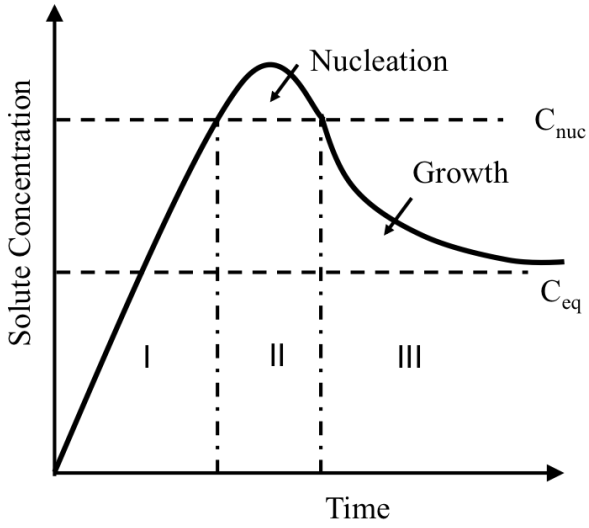

Figure 5. 3: Schematically illustrate the nucleation and growth process[22].

The formation of uniformly sized nanoparticles can be achieved if the growth process is appropriately controlled and the diffusion-limited growth is desired in order to control the size distribution of nanoparticles.

5.2. Kinetics study of microfluidic system combined with fluorescence lifetime imaging microscopy (FLIM) method

5.2.1. Introduction

The fluorescence of molecules is not only characterized by its emission spectrum, it has also a characteristic lifetime. Measurements of fluorophore excited-state lifetimes offer an additional distinguish parameters for imaging applications because fluorescence lifetimes are highly sensitive to physical conditions, such as temperature, pH, oxygen levels, polarity, binding to macromolecules and ion concentration. While it is generally independent of the

effects of concentration, photo bleaching, absorption and scattering that may affect the steady-state measurements[23].

Fluorescence lifetime imaging microscopy (FLIM), a technique to map the spatial distribution of nanosecond excited state lifetimes within microscopic images, was firstly introduced in 1989[24]. The decay profile could be in two or three dimensions, and typically with resolution in the nanosecond range, since the lifetimes of most fluorophores used in many applications fall within this range. The use of FLIM had been restricted to the imaging of biological system[25,26] and on non-flowing systems until recently. Nowadays, many applications had developed FLIM technology and combine the FLIM technique to provide information on mixing processes and efficiency in a continuous-flow microfluidic reactor[27,28].

As Adambodipy display a fluorescence lifetime which is extremely sensitive to its state, as monomer or in solid state, showing 6.5ns in solution to around 1 ns in crystalline phase, the FLIM technique reported in this Chapter demonstrates a superior approach to study the kinetics and imaging of diffusion-based mixing and nucleation process of nanoparticles within microfluidic system.

The technique of FLIM has been well employed to quantitatively and spatially maps the fluid composition within microfluidic systems, and offer *in situ* characterization of the mechanisms of diffusion, nucleation, nanocrystal growth in the continuous-laminar flow.

5.2.2. MFD3 used for FLIM kinetic studies.

The microfluidic device used in the FLIM experiment were first designed and manufactured as MFD2 (Chapter 4, **§ 4.1.2**). In order to avoid the pollution of the hydrophobic PDMS by the spread of fluorescent organic molecules and to decrease the subsequent noises during the FLIM measurement, a new glass microchip was designed.

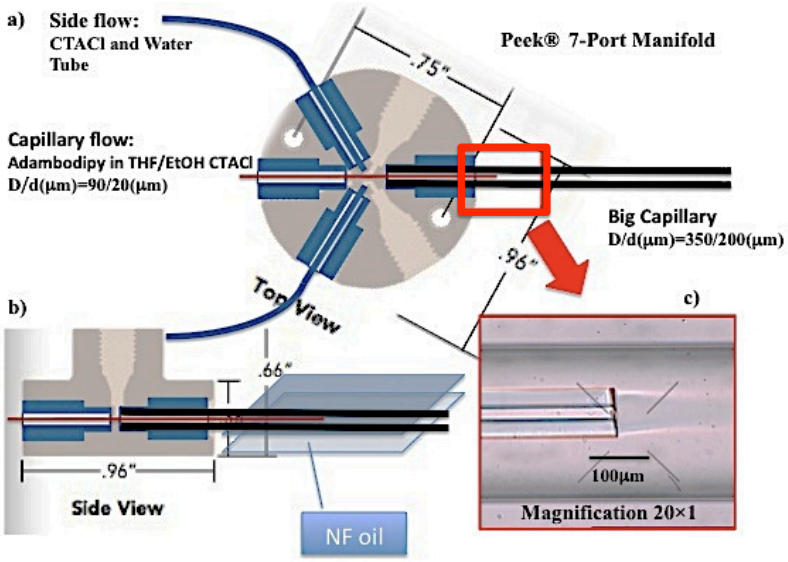

Figure 5. 4: MFD3 diagram of 3D-hydrodynamic microfluidic device with the top view (a) and the side view (b), and details of the cross-junction area of the flow under microscope in (c).

With a PEEK® 7-Port Manifold (Upchurch Scientific®) as a connector, the small glass capillary (Polymicro, ID=20 μm, OD=90 μm) was inserted into a larger one (Polymicro, ID=200 μm, OD=360 μm) as depicted on **Fig.5.1 and 5.4**. The focused stream was created by flowing the organic solution of Adambodipy in THF/EtOH into small capillary and by flowing the surrounding aqueous solution from the two of the side ports to feed the annular region between the two capillaries. The same syringe pumps force the flows into the MFD3.

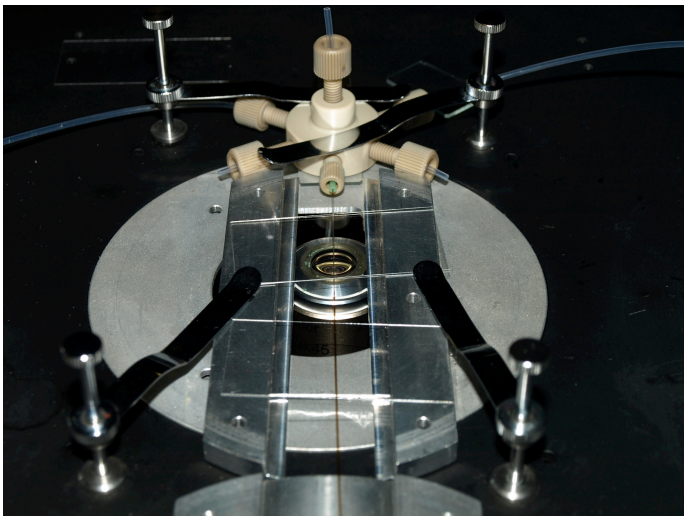

Figure 5. 5: Photography for the real experimental chip.

The photo of the real experimental chip was shown on **Fig. 5. 4**.

Besides the limitation of the unwanted adsorption of the organic molecules on the hydrophilic glass wall, such system shows a cylindrical geometry and symmetry.

5.2.3. Kinetic study of the precipitation process by FLIM

To implement the study with the new set-up, the main difficulties encountered were to avoid the leaks at the connecting ports, to insure the good alignment of the small capillary in the center of the larger one and to focus properly in the mid-plane of the flow. The acquisition of the FLIM images requires also a very good stability of the flow. This is important for the recording of the precipitation area around the central flow.

Before the acquisition of each FLIM image, we must adjust the laser power, and changing the recording time, typically between 5 to 20 minutes to collect enough photons.

Fluorescence lifetime images were taken every few millimeter along the channel. All the round images with 120μm diameter were gathered and displayed in **Fig.5. 6.**

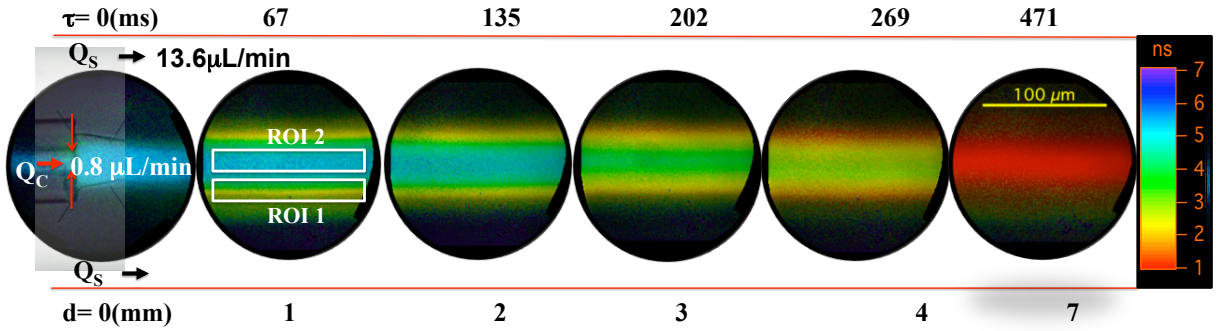

Figure 5. 6: Representative fluorescence lifetime data from 3D- hydrodynamic focusing microfluidic system, represents whole precipitation process from monomer to nanoparticle though the flow. In which the red lines correspond to the geometry of the glass microchip mentioned in 2.1. The central flow of adambodipy organic solution has a concentration of 0.08mM and Qc=0.8 μL/min, sheathed by side flow of water, Qs=13.6μL/min. The time variable is labeled with a rainbow color scale Fluorescence lifetime image at the position 0 was overlaid by a transmission image.

For each image, the mean fluorescence decay is recorded. Those decays along the channel are normalized and gathered in **Fig. 5. 7.** According to the figure, the average lifetime decreases along the focusing flow. This can be related to the mixing of water with the EtOH/THF mixture, which reduces the solubility of Adambodipy and induces its precipitation. As in the theory, that the nucleation and crystallization is mainly depending on the supersaturation, we may suggest that the concentration reaches the minimum saturation required to generate critical free energy for nucleation. The COMSOL simulation will help to estimate this critical supersaturation.

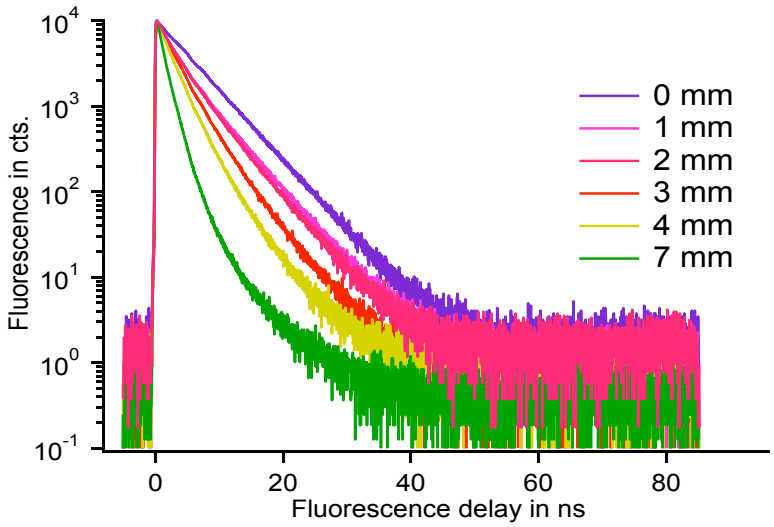

Figure 5. 7**:** Normalized mean fluorescence decays according to the FLIM images shown in Fig. along the flow at different positions.

The Adambodipy in solid state has a shorter fluorescence lifetime and a lower quantum yield (0.9 ns and Φ=0.15) compared to that of the molecule in the organic solution (6.1 ns and Φ=0.48). The decrease of the fluorescence lifetime is due to the depletion of monomer and the precipitation process. The decrease of the quantum yield during the precipitation process was compensated by the increase of the acquisition time and of the laser power.

A significant feature is that the width of focused stream containing the dyes does not enlarge along the flow. Indeed, the diffusion coefficient of the particle is roughly inversely proportional to particle size according to the theory mentioned before (Einstein-Stokes). Therefore, the diffusion coefficient of the particles will decrease during the NCs growth process, and prevents the migration process cross the channel.

According to the **Fig.5. 6**, at position d=0mm, the lifetime of the focused stream looks homogeneous and identical to the monomer solution flowing in and out of the capillary. The corresponding lifetime is accordance with the lifetime 6.1ns measured in cuvette. For the next image at position d=1mm, the heterogeneity appears in the diffusion areas between the organic and the aqueous solutions, where the precipitation process starts.

Two regions of interest (ROIs); ROI 1 and ROI 2 were defined in **Fig. 5. 6** in the middle and at the edge of the focused stream respectively. At each position along the flow, the fluorescence decays are collected in ROI 1 and ROI 2 separately. All those decays exhibit the

same evolution with a continuous decrease of the fluorescence lifetime that can be related to a continuous consumption of Adambodipy molecules from solution to particles.

A principal component analysis (details in Chapter 6) of the data says that three decays are sufficient to describe the data. The first one is the fluorescence of the monomer; the second one is the fluorescence decay of the nanoparticle. A third contribution arbitrary represented by the intermediate decay at d=3mm allows us to describe all the decays. The third compound associated with intermediate contribution is neither the monomer fluorescence nor the NPs fluorescence. It may be a nuclei or a cluster, i.e. the assembly of few molecules with a subcritical size. Their intermediate fluorescence lifetime can be rationalized since lifetime can be a function of the aggregates size. Indeed the excited state (exciton) that is produced by the absorbed photon will diffuse in the nanoparticles and the bigger the nanoparticles are, the higher the number of quencher is in the nanoparticles. When the particle becomes large compared to the diffusion length of the excitation, the quenching should reach a plateau.

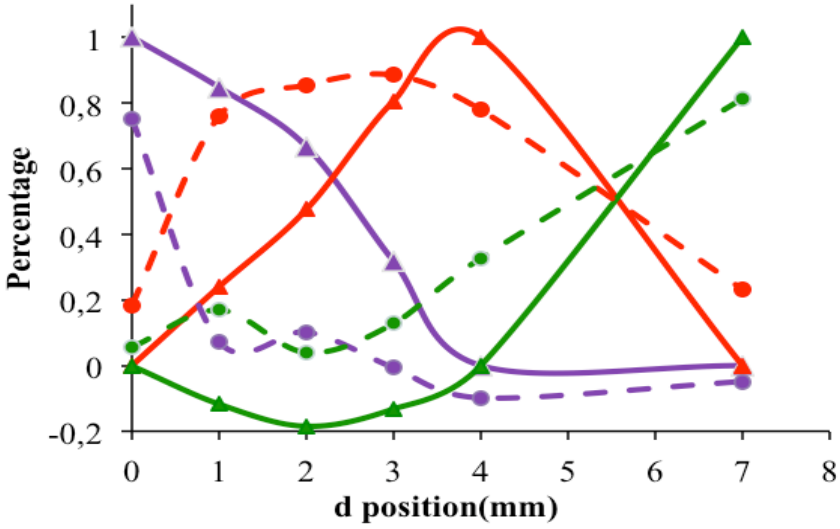

Figure 5. 8: Distribution of the three contributions describing the decays along the channel in the ROI 1 (plain lines) and in ROI 2 (dashed lines). Each color corresponds to a contribution: purple for the long decay (monomer) – red for intermediate decay – green for short decay (NPs)

The **Fig. 5. 8** shows the distribution of the 3 contributions along the channel in the middle of the flow (ROI 1) or at the interface (ROI 2). The evolution of the contribution are similar with a delay of 135 ms (d=2mm) for the consumption of the monomer and a plateau of the intermediate contribution in the ROI 2, i.e. for the mixing area at the edge of the focused stream.

In the middle of the focus stream the monomers concentration decrease slowly over the three first millimeters (*i.e.* in 0.15s) then it drops below 10% of its initial value. From 3mm to 4mm (0.2 to 0.27s) the intermediate species dominate. In both ROIs, they are transformed into stable nanoparticles at 7mm (0.47s). This transformation occurs at a step where there is no more monomer available. Thus the reaction still proceeds after the depletion of the monomers. The transformation of the intermediate species into the stable NPs does not occur by growth, *i.e*. reaction with monomers, but by aggregation, *i.e*. reaction between species of subcritical size.

At the interface there is no more monomer after 0.07s. The intermediate at the interface remains the dominant species up to 0.27s. Indeed monomers can diffuse from the center flow. The new subcritical intermediates are formed from the monomers, faster than they are consumed by aggregation.

As long as the nanoparticle size is smaller than the diffusion length of the exciton, the number of quenchers that are able to kill the fluorescence of the exciton will increase with the volume of the nanoparticle. The decay of the fluorescence is given by the following exponential:

$$S^*(t) = S^*(0)\exp\left[-\left(k_f + n(a)k_Q\right)t\right] \qquad \text{Eq. 5.18}$$

Where k_f is the fluorescence rate, k_Q is the quenching rate, $n(a)$ is the number of quenching sites in a particle of radius a. $n(a) = d_Q\left({}^{a}/_{a_0}\right)^3$, where a_0 is the diffusion length of the exciton, d_Q is the density of quenching sites.

5.3 Numerical analysis by COMSOL 3.4

Modeling and simulation are very powerful and attractive tools in the design and development of engineering system, since it allows us to conduct parametric analysis at a lower cost as compared to an experimental setting. In the research of microscale domain, numerical simulations of microfluidic device design and hydrodynamic flow focusing have been applied to have a better understand of the flow, mixing and transport conditions that correlate to the formation, growth, and closure of these intermediate structures of microfluidics.[29]

There are a variety of numerical softwares that have been successfully used in modeling microfluidic devices, such as COMSOL, CFD-ACE+, Fluent and Coventor[30,31]. These

softwares offer different fundamental equations to governing the physics of boundary conditions.

Among those commercially available modeling softwares that have been successful in modeling microfluidic processes, the multiphysics capabilities of COMSOL brings easy-to-use tools for comprehensive modeling in the study of microfluidic devices.

5.3.1 Numerical model for microfluidic diffusion process

To build the current theoretical models for predicting the kinetic process inside the three-dimensional hydrodynamically focused streams in mcirochannels, this study starts by describing the theory and equations. Then we come to the following built-in modules, Due to the cylindrical symmetry of the device, 2D-Axisymmetric model was chosen here in the first place, and the geometry and the dimensions are those of the experimental device of the glass microchip mentioned in **Fig.5. 4** and **Fig. 5. 5.**

Step 1: The steady state "Incompressible Navier-Stokes"

The steady state "Incompressible Navier-Stokes" (MEMS Module) model, for a laminar flow and a Stokes regime, using the equations from the COMSOL database are similar to **Eq.5. 2** with a difference of identity matrix for iteration, and was first performed to solve for the momentum conservation and the velocity profile for the fluid flow in the channel:

$$\rho\frac{\partial \boldsymbol{u}}{\partial t} - \nabla\cdot[(-p)I + \mu(\nabla\boldsymbol{u} + (\nabla\boldsymbol{u})^T)] + \rho\boldsymbol{u}\cdot\nabla\boldsymbol{u} = F \quad \text{Eq. 5. 19}$$

$$-\nabla\boldsymbol{u} = 0 \quad \text{Eq. 5. 20}$$

where ρ is fluid density, u=(u,v,w) is the flow-velocity vector for a three dimensional fluid, *p* is fluid pressure, I is the unit diagonal matrix, μ is the fluid's dynamic viscosity, and F = (*fx, fy, fz*) is a bulk force affecting the fluid. The initial parameters setting and the result could be found in details in Chapter 6. In our case, $\frac{\partial \boldsymbol{u}}{\partial t}$ and F are equal to 0. Then we obtained the velocity field in microdevice.

Step 2: The "Maxwell-Stefan Diffusion and Convection" module

With the results of the initial calculation of velocity profile, "Maxwell-Stefan Diffusion and Convection" (Chemical Engineering Module) application mode was then applied here to model the mixing of organic and aqueous solutions via counter diffusion along the laminar flow in the capillary of the same dimensions as those used in the experiment.

$$\nabla \cdot \left[-\rho w_i \sum_{j=1}^{N} D_{ij} \left\{ \frac{M}{M_j} \left(\nabla w_j + w_j \frac{\nabla M}{M} \right) + \left(x_j - w_j \right) \frac{\nabla p}{p} \right\} + w_i \rho \, \vec{u} \right] = 0 \qquad \text{Eq. 5.21}$$

$$x_j = \frac{w_j}{M_j} \cdot M \qquad \text{Eq. 5.22}$$

$$\sum_{i=1}^{n} w_i = 1 \qquad \text{Eq. 5.23}$$

where M denotes the total average molar mass of the mixture (kg/mol), M_j gives the molar mass of species j (kg/mol), and w_j is the mass fraction of species j. M can also be expressed in terms of the mass fractions, w_j. M=somme(w_j,M_i)

The solutions were respectively considered as ethanol and water. Then, the value of mutual diffusivity, density and viscosity along the flow of this water-ethanol binary system can be calculated with the input scalar expressions (**Eq. 5.11-13**) with the mass fraction profile results.

Step 3: Redo the steady state "Incompressible Navier-Stokes" calculation.

With more precise consideration, the "Incompressible Navier-Stokes" calculation was redo with the value of mutual diffusivity, density and viscosity at local position coming from the last step.

Step 4: The "Convection and Diffusion" module

Then the velocity field obtained from the "Incompressible Navier-Stokes" simulation was implemented for the calculation of the concentration distribution of the dye using the "Convection and Diffusion" module. The diffusion of Adambodipy specie in water-ethanol system under microfluidic flow conditions was then solved according to the convection-diffusion equation:

$$-\nabla \cdot (-\mathrm{D}\nabla \boldsymbol{c} + \boldsymbol{cu}) = \mathbf{0} \qquad \text{Eq. 5.24}$$

Step 5: Supersaturation profile calculation

With all the final results from the former calculations, those includes density, viscosity, mutual diffusivity, concentration for Adambodipy and mass fraction profile of water and ethanol at local position along the flow, and combine the input scalar expression for solubility and supersaturation of Adambodipy in binary system (**Eq.5.15**), we could run again the "Maxwell-Stefan Diffusion and Convection" module and get the supersaturation profile.

5.3.2. Kinetic study of the precipitation process by COMSOL simulation

The first application of the simulation was to investigate the hydrodynamic focusing under stable flow within the device; we monitored the flow rate ratio from 30 to 45 with a low total flow rate. We record each first FLIM image at position 0. At a fixed position (50µm) far from the transition flow that is present close to the nozzle, the fluorescence intensity profile was plot. We consider the full width at half-maximum (FWHM) of this Gaussian like profile as the width of the focused stream.

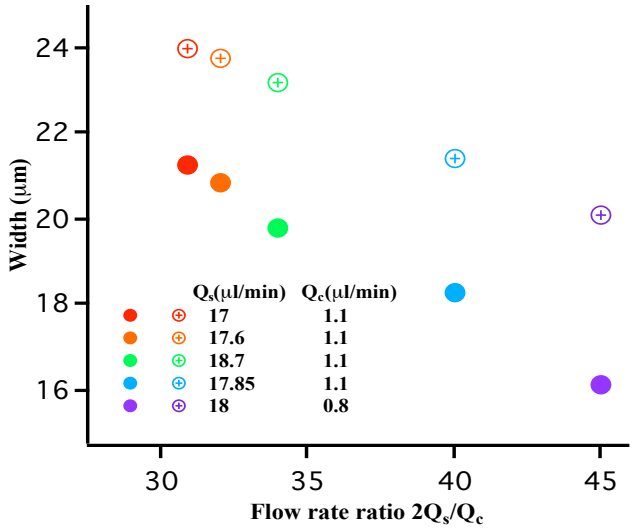

Figure 5. 9: Widths of the focused stream at the position as a function of the flow rates ratios, experimental values ● and numerical values ⊕.

These widths were also determined at the same position along the flow from numerical simulations using Comsol Multiphysics 3.4 software with identical geometry (small capillary OD= 45µm insert into a big capillary channel ID=100 µm), and identical parameters for each flow. One numerical example is given in the figure below the x-axis at position 0 on **Fig. 5. 9**. The hydrodynamic focusing has been simulated including the diffusion of the Adambodipy, its diffusion coefficient was calculated from Stokes-Einstein equation ($4.23\times10^{-10}m^2/s$).

As shown on **Fig.5.9,** as the flow rates ratio Qc/Qs decreases (from 0.143 to 0.030), the width of the focused stream decreases. Therefore as mentioned in a previous work in the group, for the preparation of rubrene particles[32], the kinetic to reach the supersaturation and create nanoparticles can be changed: the precipitation rate will increase as the width decreases. Indeed, the hydrodynamic focusing ratio determines the NPs size.

The second application of COMSOL simulation predicts the velocity and concentration fields, to compare with the experimental data from the FLIM.

The precipitation process is governed by interdiffusion of water and Adambodipy along the channel. The diffusion of the water in the organic solution is much faster with a diffusion coefficient equal to $1.6\times10^{-9}m^2/s^3$, as shown by comparison of top and bottom simulations on **Fig. 5. 10**.

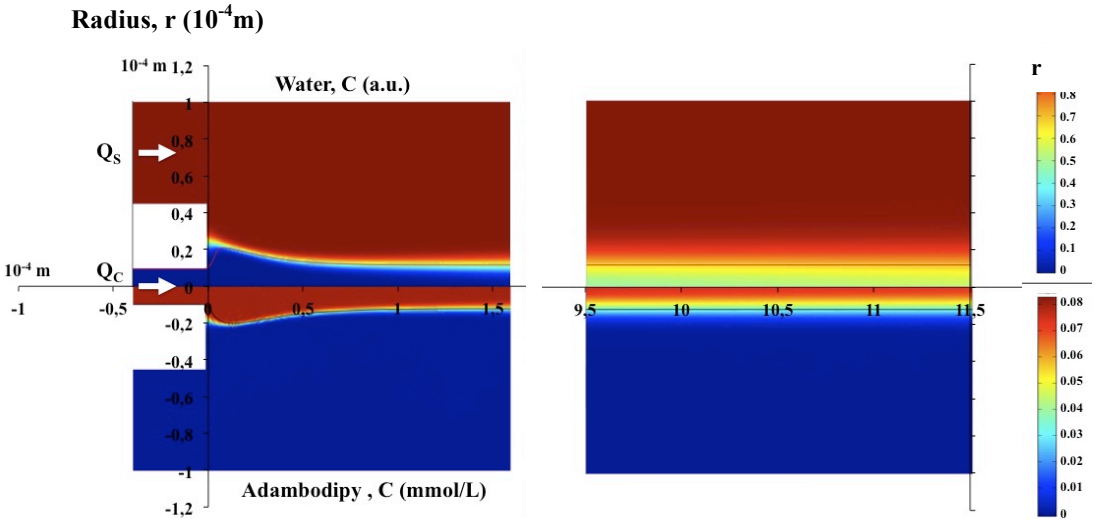

Figure 5. 10: 2D-Axisymmetric geometry of the glass microfluidic device and Comsol simulations of diffusion in hydrodynamic focusing flow, Qc=0.8mL/min and Qs=13.6mL/min, Cadambodipy=0.08mM. Concentration distributions of water (above the x axis) and of adambodipy (below x axis) along the 200mm of the channel at position 0 (a) and at position 1mm (b). The streamline is to indicate the interface between the two solutions.

In first approximation, we can neglect the diffusion of the Adambodipy. The simulation of the water diffusion at 1mm (**Fig. 5. 10 (b)**) indicates that the water has reached the middle of the focused stream. Nevertheless, the percentage of the water is below 65% at r<10µm, whereas for concentration 0.08mM Adambodipy, this water content is expected to start a precipitation. As a consequence, the fluorescence lifetime remains long inside the focused stream as demonstrated in the FLIM image (**Fig. 5. 6**). At the interface for 10µm <r< 12µm, the high water concentration induces nucleation and shorter lifetime (**Fig. 5.6, 5.10**).

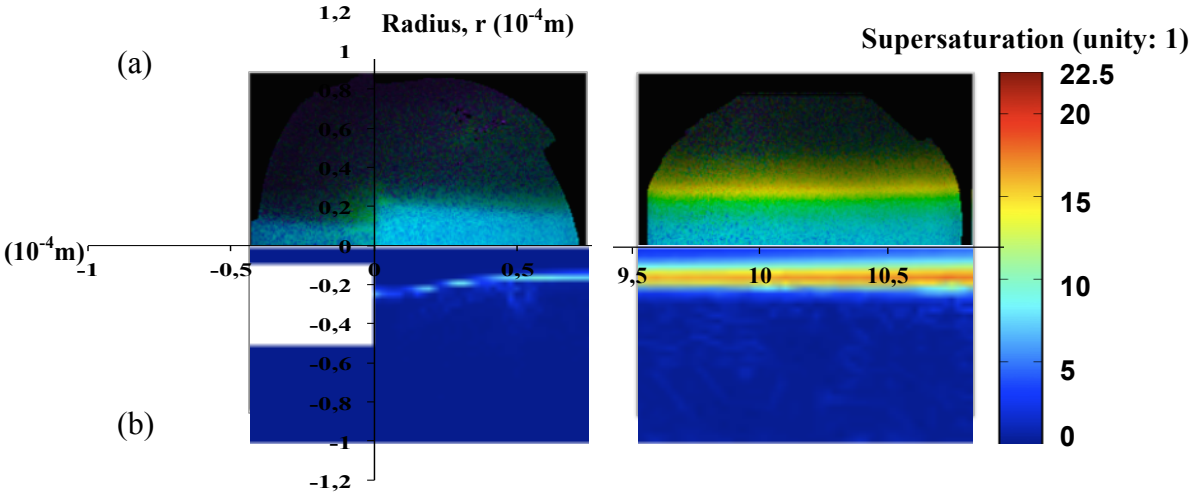

Figure 5. 11: The comparison of real experimental FLIM imaging in (a) with the 2D-Axisymmetric geometry of the glass microfluidic device and Comsol simulations of Adambodipy supersaturation profile under the same condition (b), initial concentration of 0.08mM and with flow rate Qc=0.8 mL/min, Qs=13.6 mL/min along the hydrodynamic focusing flow, same image as in **Fig. 5.6**. The simulated supersaturation variable is labeled with a rainbow color scale with unit 1.

We see on the FLIM image that the first nucleation has already started at 0.9mm±50µm. From the comparison of the simulation with the experiment we can conclude that the supersaturation required for nucleation to occur is when $8<\frac{C_{Adambodipy}}{C_{eq}}<15$. The simulation explains why under these mixing conditions we do not observe the formation of a crystalline tube at the tip of the capillary: the super saturation is lower than that required for nucleation to occur.

The COMSOL simulation does not include the nucleation process. The molecules are allowed to diffuse, the super saturation is calculated but the precipitation process is not included. Thus, after the beginning of the precipitation, the supersaturation is over estimated.

5.4 Conclusion

FLIM implemented with the microfluidic system can measure in situ the evolution of the dye and of its state in the focused stream. The mixing of the solvents inside the channel and the study the crystallization process are followed from few milliseconds to a second. The multi-exponential fluorescence decays and its evolution suggest that, from the monomer in the solution, a new emerging nanostructures compete and then turn into nanoparticles. Combined with the DLS measurements, the size distribution of the nanoparticles display a dynamic width-dependent of the focusing stream, which is directly linked to the flow rate ratio.

A numerical method with COMSOL was applied for kinetic analysis of this diffusion controlled process occurring in the microfluidic device. The simulation predicts the species diffusion and supersaturation field and can highlight the experimental precipitation phenomenon.

Reference:

[1] M, D. *"Hydrodynamic Focusing in Microfluidic Devices "*; InTech, **2012**; *Vol*. Chapter 2. pp 29-54.

[2] Knight, J. B.; Vishwanath, A.; Brody, J. P.; Austin, R. H. *"Hydrodynamic focusing on a silicon chip: Mixing nanoliters in microseconds."* Phys Rev Lett, **1998**, *80*, 3863-3866.

[3] Zhigang Wu, K. H. *"Microfluidic Hydrodynamic Cell Separation: A Review."* Micro and Nanosystems, **2009**, *1*, 181-192.

[4] Bruus, H. *"Theoretical Microfludics."* Oxford University Press, **2008**.

[5] Kumar, C. S. S. R. *"Microfluidic Devices in Nanotechnology: Applications."* Wiley, **2010**.

[6] Tretheway, D. C.; Meinhart, C. D. *"Apparent fluid slip at hydrophobic microchannel walls."* Phys Fluids, **2002**, *14*, L9-L12.

[7] Yamaguchi, Y.; Takagi, F.; Watari, T.; Yamashita, K.; Nakamura, H.; Shimizu, H.; Maeda, H. *"Interface configuration of the two layered laminar flow in a curved microchannel."* Chem Eng J, **2004**, *101*, 367-372.

[8] Emmelyn, M. G.: *"The Application of Fluorescence Lifetime Imaging Microscopy to Quantitatively Map Mixing and Temperature in Microfluidic Systems."* The University of Edinburgh **2007.**

[9] Clerk Maxwell, **J.** *"On the Dynamical Theory of Gases."* Royal Society of London, **1867**; *Vol*. 157.

[10] Lu, K.: *"Modelling of Multicomponent Diffusion and Swelling in Protein Gels."* University of Canterbury, **2011.**

[11] Taylor, R. K., R.;. *"Multicomponent Mass Transfer."* Wiley, **1993**.

[12] Darken, L. S. *"Diffusion, Mobility and Their Interrelation through Free Energy in Binary Metallic Systems."* T Am I Min Met Eng, **1948**, *175*, 184-201.

[13] Acree, W. E. *"Mathematical Representation of Thermodynamic Properties .2. Derivation of the Combined Nearly Ideal Binary Solvent (Nibs) Redlich-Kister Mathematical Representation from a 2-Body and 3-Body Interactional Mixing Model."* Thermochim Acta, **1992**, *198*, 71-79.

[14] Khattab, I. S.; Bandarkar, F.; Fakhree, M. A. A.; Jouyban, A. *"Density, viscosity, and surface tension of water plus ethanol mixtures from 293 to 323 K."* Korean J Chem Eng, **2012**, *29*, 812-817.

[15] Mersmann, A. *"Crystallization Technology Handbook."* CRC Press; 2 Rev Exp edition, **2001**.

[16] Abraham, F. F. *"Homogeneous Nucleation Theory."* Academic Press, **1974**.

[17] Nielsen, A. E. *"Kinetics of precipitation "*; Pergamon Press, **1964**.

[18] Bennema, P.; Sohnel, O. *"Interfacial Surface-Tension for Crystallization and Precipitation from Aqueous-Solutions."* J Cryst Growth, **1990**, *102*, 547-556.

[19] Nielsen, A. E.; Sohnel, O. *"Interfacial Tensions Electrolyte Crystal-Aqueous Solution, from Nucleation Data."* J Cryst Growth, **1971**, *11*, 233-&.

[20] Mersmann, A. *"Calculation of Interfacial-Tensions."* J Cryst Growth, **1990**, *102*, 841-847.

[21] Sangwal, K. *"On the Estimation of Surface Entropy Factor, Interfacial-Tension, Dissolution Enthalpy and Metastable Zone-Width for Substances Crystallizing from Solution."* J Cryst Growth, **1989**, *97*, 393-405.

[22] Lamer, V. K.; Dinegar, R. H. *"Theory, Production and Mechanism of Formation of Monodispersed Hydrosols."* J Am Chem Soc, **1950**, *72*, 4847-4854.

[23] Sud, D.: *"Wide-field Time-domain Fluorescence Lifetime Imaging Microscopy (FLIM): Molecular Snapshots of Metabolic Function in Biological Systems."* The University of Michigan, **2008.**

[24] Bugiel, I. K., K. Wabnitz, H. *"Investigation of cell by fluorescence laser scanning microscopy with subnanosecond time resolution."* Lasers in the Life Sciences, **1989**, *3*, 47-53.

[25] Gadella, T. W. J.; Jovin, T. M. *"Oligomerization of Epidermal Growth-Factor Receptors on A431 Cells Studied by Time-Resolved Fluorescence Imaging Microscopy - a Stereochemical Model for Tyrosine Kinase Receptor Activation."* J Cell Biol, **1995**, *129*, 1543-1558.

[26] Haj, F. G.; Verveer, P. J.; Squire, A.; Neel, B. G.; Bastiaens, P. I. H. *"Imaging sites of receptor dephosphorylation by PTP1B on the surface of the endoplasmic reticulum."* Science, **2002**, *295*, 1708-1711.

[27] Elder, A.; Schlachter, S.; Kaminski, C. F. *"Theoretical investigation of the photon efficiency in frequency-domain fluorescence lifetime imaging microscopy."* J Opt Soc Am A, **2008**, *25*, 452-462.

[28] Redford, G. I.; Majumdar, Z. K.; Sutin, J. D. B.; Clegg, R. M. *"Properties of microfluidic turbulent mixing revealed by fluorescence lifetime imaging."* J Chem Phys, **2005**, *123*.

[29] Auro Ashish Saha, S. K. M. *"Modelling and Simulation."* I-Tech Education and Publishing, **2008**; *Vol*. 17.

[30] Glatzel, T.; Litterst, C.; Cupelli, C.; Lindemann, T.; Moosmann, C.; Niekrawietz, R.; Streule, W.; Zengerle, R.; Koltay, P. *"Computational fluid dynamics (CFD) software tools for microfluidic applications: A case stud."* Computers & Fluids, **2008**, *37*, 218-235.

[31] Glasgow, I.; Aubry, N. *"Enhancement of microfluidic mixing using time pulsing."* Lab Chip, **2003**, *3*, 114-120.

[32] Genot, V.; Desportes, S.; Croushore, C.; Lefevre, J. P.; Pansu, R. B.; Delaire, J. A.; von Rohr, P. R. *"Synthesis of organic nanoparticles in a 3D flow focusing microreactor."* Chem Eng J, **2010**, *161*, 234-239.

Chapter 6. Experimental section

6.1. Microfluidic device fabrication and improvement

6.1.1. Material

Adamantyl mesityl BODIPY (Adambodipy) (from Dr.Gilles CLAVIER and Dr. Marina DVORKO) molecule was synthesized and purified in the laboratory (not published yet). The organic solvent tetrahydrofuran (THF) and absolute ethanol (EtOH) are purchased from SDS (SpectroscopicGrade). The water has been deionised. The surfactant cetyltrimethylammonium chloride (CTACl) was used as a stabilizing agent and purchased from TCI-Tokyo.

6.1.2. Fabrication of two layers microfluidic device

According to the Soft lithography technique, PDMS elastomers, Sylgard® 184 from Dow Corning®, was used here as fluid flow layer materials. Sylgard is a two part resin system containing vinyl groups (part A) and hydrosiloxane groups (part B) shown in Figure below. Two components as elastomer base and silicone elastomer curing agent were mixed in the volume ratio of 10:1 (A: B). Mixing the two part components together leads to a cross-linked network of dimethyl siloxane groups. Because this material is flexible, it can be unmolded (peeled off) from the SU-8 master, leaving the master intact and ready to produce another device. These samples have different base/agent ratios, which mean different degrees of cross-linking, and 10:1 is the most widely used type[1].

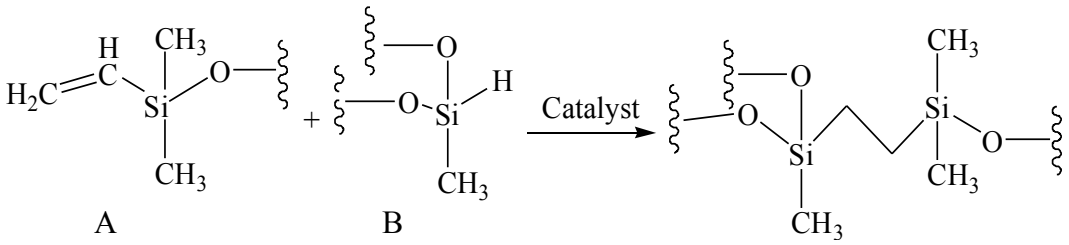

Figure 6. 1: PDMS crosslinking

With the ultrasonic operation (TRANSSONIC DIFITAL S, *ε*lma®), the two components are well mixed, and then set the mixture under 100 torr for around 30 min for evacuation until almost all the bubbles are eliminated from the mixture.

After the pretreatment, the mixture is then poured on the wafer mold and cured at 75 °C for 2h. After that the PDMS replica can be easily peeled off from the master, and then the replica and glass coverslip (Marienfeld Micro Slides, Germany) are activated by O_2 plasma (HARRICK PLASMA CLEANER/ STERILIZER (PDC-002) for 20 s and sealed each other.

With oxygen plasma in our research, whereby the surface Si-CH_3 groups along the PDMS backbone will react with the oxygen species in the plasma at high pressure and then transform into Si-OH groups. The produced silanol surfaces are easily transformed with alkoxysilanes and can easily mate with glass surface. The steps are presented in **Fig. 6. 2**

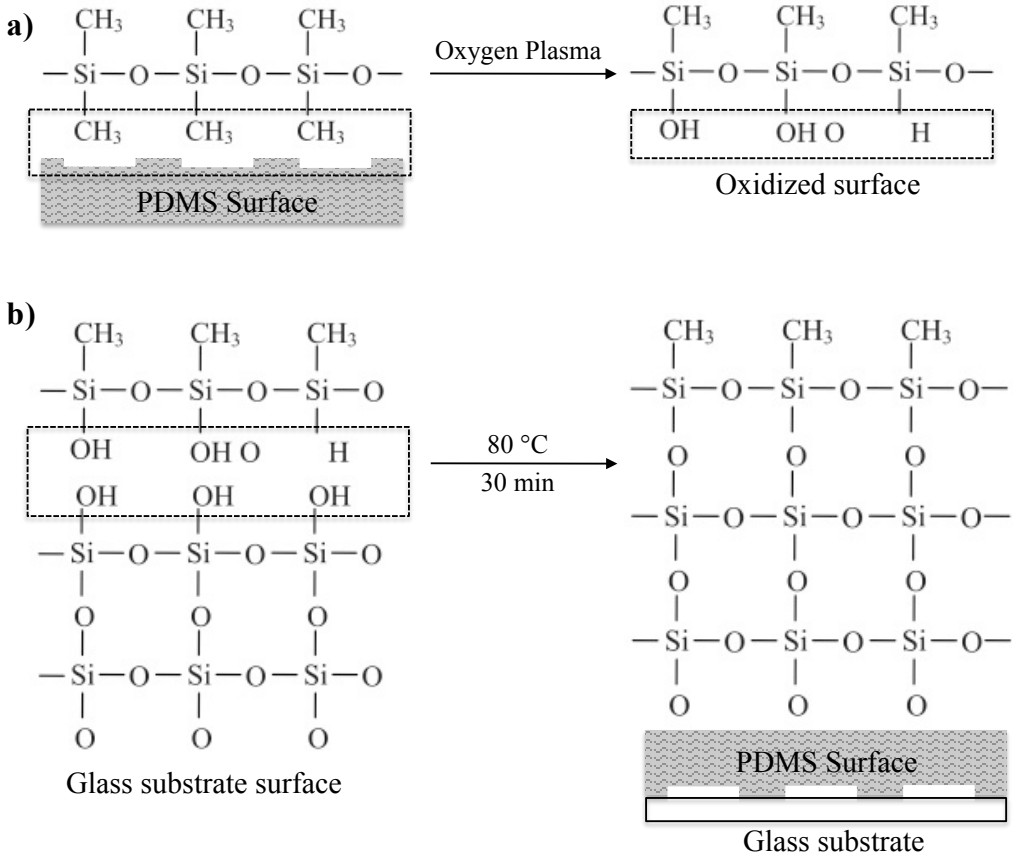

Figure 6. 2: a) The surface of PDMS was modified by O2 plasma. b) Covalent binding of a PDMS slab to a silica surface,

Centimeter lengths of multi-mode optical fiber TSP 20150 from Polymicro USA were prepared, then burning their protective Polyimide mechanical cladding and remove the burned out layer with ethanol. Then put the optical fiber into the embedded center channels until their front ends made contact the across section.

6.1.3. Microfluidic device improvement

To overcome the formation of crystals at the edge of the capillary changes were introduced in the microdevice.

Beside the change in the pattern of the Y-type junction, with a reduced angle between the side channels and the main channel, the end of the capillary was polished to a cone shape by using the millstone used for removal of the organic layer of metal electrode from MECAPOL.

A photo of our set-up for the polishing is illustrated below, which includes the millstone for polish and also the capillary emerging from a syringe needle to handle it firmly. (**Fig.6 .3**) The balloon is to avoid the dust blocking the capillary from inside.

Figure 6. 3: Millstone (MECAPOL P 220 U); Capillary (150 20mm) Needle Microscopy, balloon

6.2. Spectroscopic measurement

6.2.1.UV-visible absorption spectroscopy

The UV-visible absorption spectra were recorded on double beam Uvikon 943, or Cary-5000 spectrophotometers in the lab. The samples of NPs suspension are checked with quartz cells (Bodelsheim, France) with an inner path length of 10 mm.

6.2.2. Steady state fluorescence spectroscopy

The fluorescence of the samples were recorded on FluoroMax-3, and FluorologFL3-221 spectrophotometers.

FluoroMax-3: A Xenon arc lamp (150W) was used as the light source. The spectral range went through 200 to 900 nm. The band pass of the monochromator of excitation and emission were automatically adjusted via the software (0.5 to 10 nm).

Fluorolog FL3-221: A Xenon arc lamp (450W) was used as the light source. The spectral range covers from 200 to 1300 nm. The band pass of the monochromator of excitation and emission were automatically adjusted via the software (0 to 30 nm). The excitation and emission beam can be polarized independently.

6.2.3. Time-resolved spectroscopy

The fluorescence decay curves were obtained with the time-correlated single-photon-counting method by using a titanium-sapphire laser pumped by an argon ion laser (82 MHz, 1

ps pulse width, repetition rate lower to 4 MHz thanks to a pulse-picker, a doubling crystal was used to reach 495 nm excitation).

When deconvolution is required, the time profile of the exciting pulse is recorded under the same conditions by using a scattering solution (suspension of colloidal silica "Ludox"). And the number of fluorescence pulses must be kept much smaller than the number of exciting pulses (<0.01-0.05)[2].

To estimate the quality of the fit for single-photon counting data, the weighted residuals were calculated as follow:

$$\chi_r^2 = \frac{1}{v}\sum_{i=1}^{N}\left[\frac{R(t_i) - R_c(t_i)}{\sigma_i(i)}\right]^2 \qquad \text{Eq. 6. 1}$$

where N is the total number of data points and $\sigma(i)$ is the standard deviation of the i th data point. v is the number of degrees of freedom, χ_2 is equal to the variance of the weighted residuals. A fit was said to be appropriate for χ_2 values was closed to 1[2].

6.2.4. Time-resolved single photon counting spectroscopy and fluorescence lifetime imaging (FLIM)

6.2.4.1. FLIM equipment

Fluorescence lifetime imaging (FLIM) with time-resolved single-photon-counting device and time-resolved anisotropy imaging microscopy are used to visualize the precipitation process along the microchannel. The fluorescence generated in the sample is guided to a time-resolved single-photon-counting photo-multiplier (QA) from Europhoton Gmbh (Berlin http://www.europhoton.de/).

The experimental device is shown in **Fig.6. 4**. The pulse laser source is an Ytterbium TPulse200 from Amplitude Systèmes (Pessac France). It is injected into the microscope (Nikon 2000 TE) through the epi-illumination port of an inverted microscope (Nikon S-Fluor, 40, 0.90 NA). The spectra (absorption and fluorescence) are collected by means of a fiber-coupled spectrometer (Ocean Optics, Inc., ZD2000).[3]

The FLIM measurement is done with a multi-channel plate photo-multiplier working in the single photon counting mode. For each photon, its position and arrival time are measured and stored. From these data files both intensity and lifetime image can be calculated.[4]

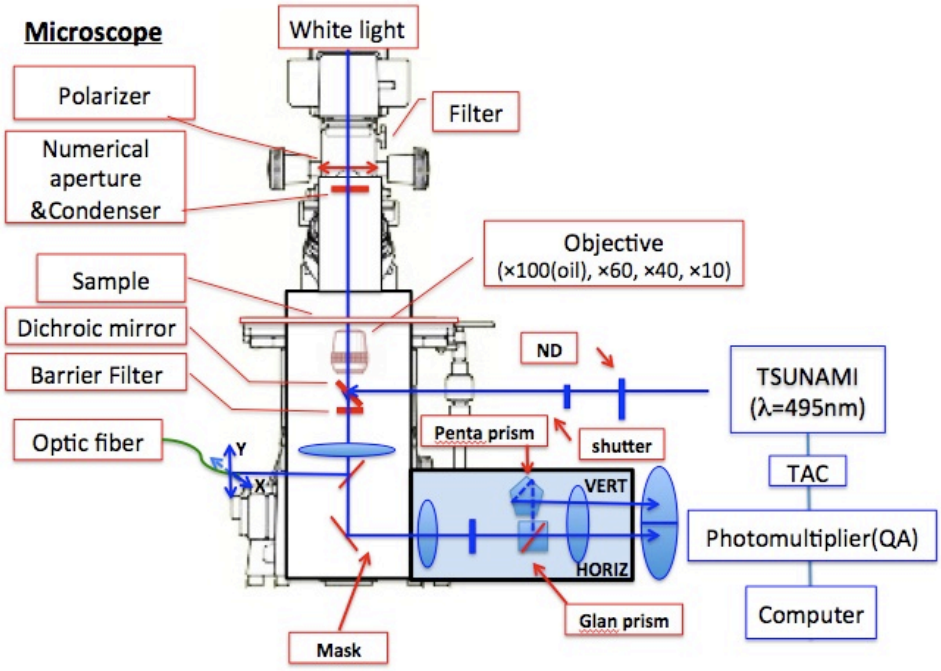

Figure 6. 4: Time-resolved single-photon-counting device

The main part of this equipment is a multi-channel plate photo-multiplier working in the single photon counting mode shown in the **Fig. 6.5.** It detects the delay between the laser pulse and the arrival of the photon on the photomultiplier for each photon and also the absolute arrival time and the position of the photon on the photocathode are measured. The histogram constructed by the number of photons collected per pixel, which gives an image of photon intensity of the sample. The number of photons was collected as a function of absolute arrival time. It gives the evolution of the global fluorescence intensity and a way to monitor photobleaching. And we can also calculate the average fluorescence lifetime τ for each pixel by dividing the sum of all the delays between the laser pulse and the exact moment that the photon is collected.

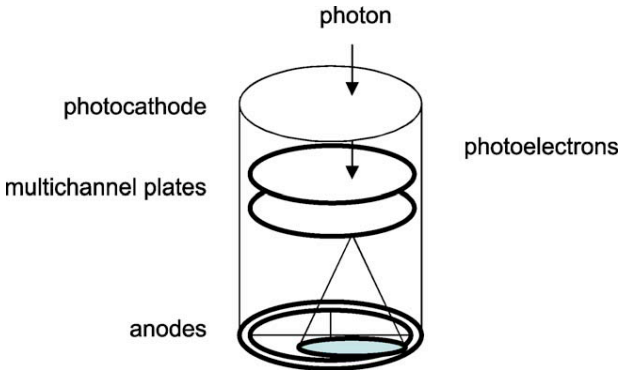

Figure 6. 5: Multi-channel plate photo-multiplier

Fluorescence decay curves were constructed as the histogram of the number of photons collected as a function of the fluorescence delay. The collection is done over all the pixels in a specific area. Unless otherwise stated, the fluorescence lifetimes given in this paper correspond to the global fluorescence decay, i.e. the decay corresponding to the whole QA image. The instrument response time is 150 ps (FWHM) and the spatial resolution of our set-up is 300 nm (FWHM)[4].

Besides the experiment which was analyzed and detailed in Chapter 5, **Fig.6.6** shows two other examples of kinetic evolution in the microfluidic device during the precipitation of Adambodipy.

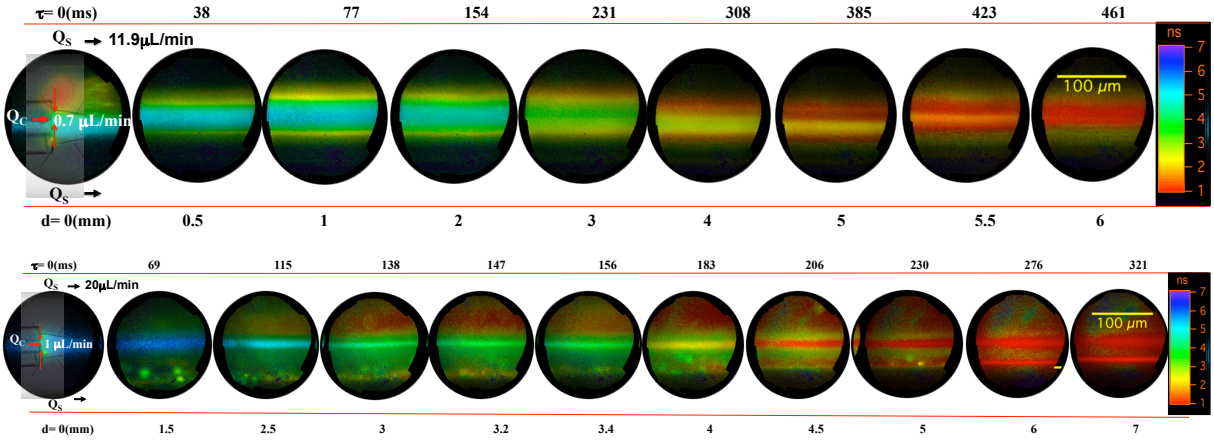

Figure 6. 6: Representative fluorescence lifetime data from 3D- hydrodynamic focusing microfluidic system, represents whole precipitation process from monomer to nanoparticle though the flow. In which the red lines correspond to the geometry of the glass microchip mentioned in 2.1. (a) The central flow of Adambodipy organic solution has a concentration of 0.08mM and Qc=0.7 μL/min, sheathed by side flow of water, Qs=11.9μL/min. (b) The central flow of Adambodipy organic solution has a concentration of 0.13mM and Qc=1 μL/min, sheathed by side flow of water, Qs=20μL/min. The time variable is labeled with a rainbow color scale Fluorescence lifetime image at the position 0 was overlaid by a transmission image.

6.2.4.2. Emission polarization experimental set-up

White light, bright field- polarizing microscopy, used for absorption measurement and neutral axes determined:

The polarizer is a standard multi-coated glass polarizer from Nikon (Nikon C-SP 754097).

The second one witch works as an analyzer is cut in a TECHSPEC® visible linear polarizing laminated film from Edmund Optics. This film is laminated in cellulose triacetate (CTA)

Fluorescence wide field microscopy set-up that used for emission measurement of the single crystal:

1. The laser polarization is controlled with a half wave plate on a motorized rotating stage.
2. Zero order Half-Wave PlateWPH05M-355 nm is used for 343nm excitation.
3. Achromatic Half-Wave Plates AHWP05M-600 nm with range 400-850nm, is used for 515 nm excitation

6.2.5. Determination of fluorescence quantum yield

The fluorescence quantum yield Φ_f presents one of the most fundamental properties for a fluorophore and is also important for the characterization of novel fluorescent probes. According to the definition of the Φ_f, it is the ratio of the number of the emitted photons (n_{em}), to the number of absorbed photons n_{abs}.

$$\Phi_f = \frac{n_{em}}{n_{abs}} \qquad \text{Eq. 6.2}$$

Since the reliable measurements of these quantities can be hard to obtain, a better method is to use a standard reference to determine the quantum yield.

Considering the easiest situation, for species in dilute solution, It's preferable to measure the fluorescence spectrum and compare its integrated intensity with the same quantity for a reference solution of known quantum yield that can be to be excited at the same wavelength and whose emission spectrum is close to that of the tested compound[5]. The similarity of the two emission spectra is recommanded for spectrometers whose sensitivity correction curve is not perfect. The quantum yield is calculated using **Eq.6.3.**

$$\Phi_f^i = \frac{F^i f_s n_i^2}{F^s f_i n_s^2} \Phi_f^s \qquad \text{Eq. 6.3}$$

Where Φ_f^i and Φ_f^s are the quantum yield of the sample and that of standard; F^i and F^s are the integrated emission intensity of the corrected spectra of the sample and reference spectra; f_i and f_s are the absorbance factor of the sample and standard at the excitation wavelength ($f_x = 1 - 10^{-Ax}$), n_i and n_s are the refractive indices of the sample and the reference

solution[5]. The refractive indices correct for the collection angle of the fluorescence. The collection angle is fixed in air by the spectro-fluorometer but change in the sample depending on its refraction index.

The standard reference compound used in the thesis for the determination of the fluorescence quantum yield was Rhodamine590.

6.2.6. Principal component analysis[6].

Principal component analysis (PCA) is probably the most popular multivariate statistical technique and it is used by almost all scientific disciplines, and it was widely used for investigations on the physic-chemical properties of chemical or biological systems where it is used for the analysis of the spectra of mixtures. It can replace the analysis of families of spectra through isosbestic points. It is also a well-know statistical technique to analyze a series of fluorescence or absorption spectra and the related concentrations. The analysis of effect of the controllable variable such as pH, concentration, temperature, or time reveals the nature of the contributing species and leads to a full understanding of the underlying reaction mechanisms and the corresponding equilibrium or kinetic constants[7-9].

The steps in conducting PCA could be concluded as follow[10]:

1. Initial extraction of the components, normally is equal to the number of variables being analyzed.
2. Determining the number of components that are truly meaningful and worthy of being retained for rotation and interpretation.
3. Rotation to a Final Solution
4. Interpreting the Rotated Solution
5. Extracted the contribution of the rotated solution to the data.

In the thesis, the logarithm of fluorescence decays that were collected through FLIM should depend linearly on probability of components. We have applied PCA to this linear problem and to obtain the principal contributions using the data analysis in the environment of Igor pro©.

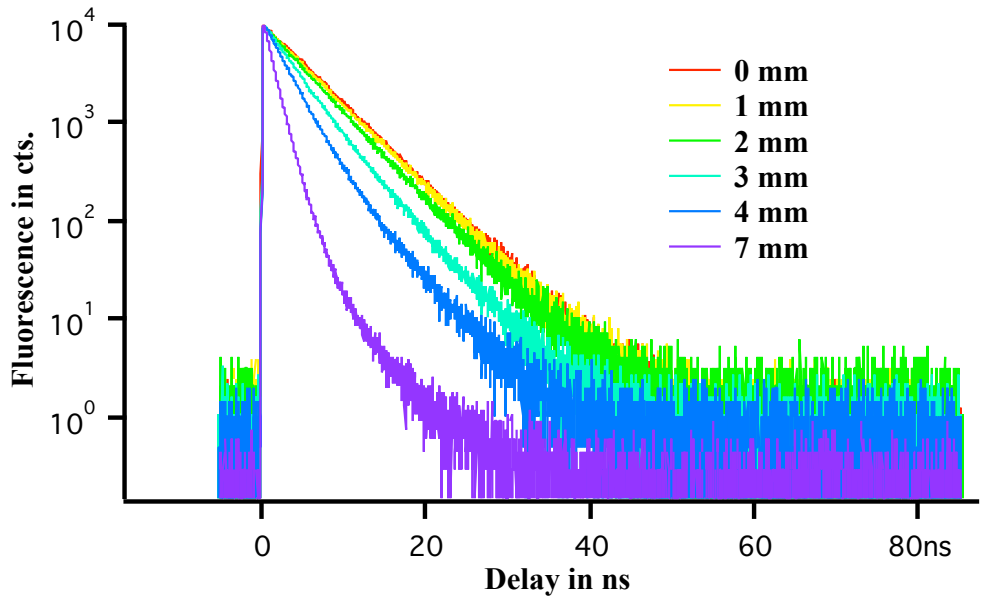

Figure 6. 7: Normalized mean fluorescence decay collected on the ROI1 in Chapter 5 Fig.5.7, at the center position of FLIM.

The number of components extracted in a principal component analysis is equal to the number of observed variables being analyzed. However in this experimental case, we assume that only three components are important, while two components are not sufficient: the monomer, NPs and intermediate nucleus. Indeed they account for significant amounts of the variance as shown on **Fig. 6. 7**. The proposed decays shown on **Fig. 6. 7** do not fit with the requirement of a concentration (they are negative at some times). (Step 2). But any linear combination of the principal components will describe the data equality well. We have to do a rotation to construct physically acceptable decays. As a first component we have chosen a linear combination of the principal components that fits the decay of the monomer as it is measured at short mixing time. We have chosen as third component a combination that fits the decay of the nanoparticles as it is measured for long mixing time. We have chosen as second component a combination that fits an intermediate decay.

It appears that the decays become faster with the precipitation process. Decays at position 0 mm, 4 mm and 7 mm are selected as model decays for the monomer, nucleus and NPs separately. And the amounts of those three decays are presented in Chapter 5.

Then the quality of the description of the data by the three decay components can be illustrated by the weighted residuals on **Fig. 6. 8**, and the result show that the quality of the description of the data by those three components is correct.

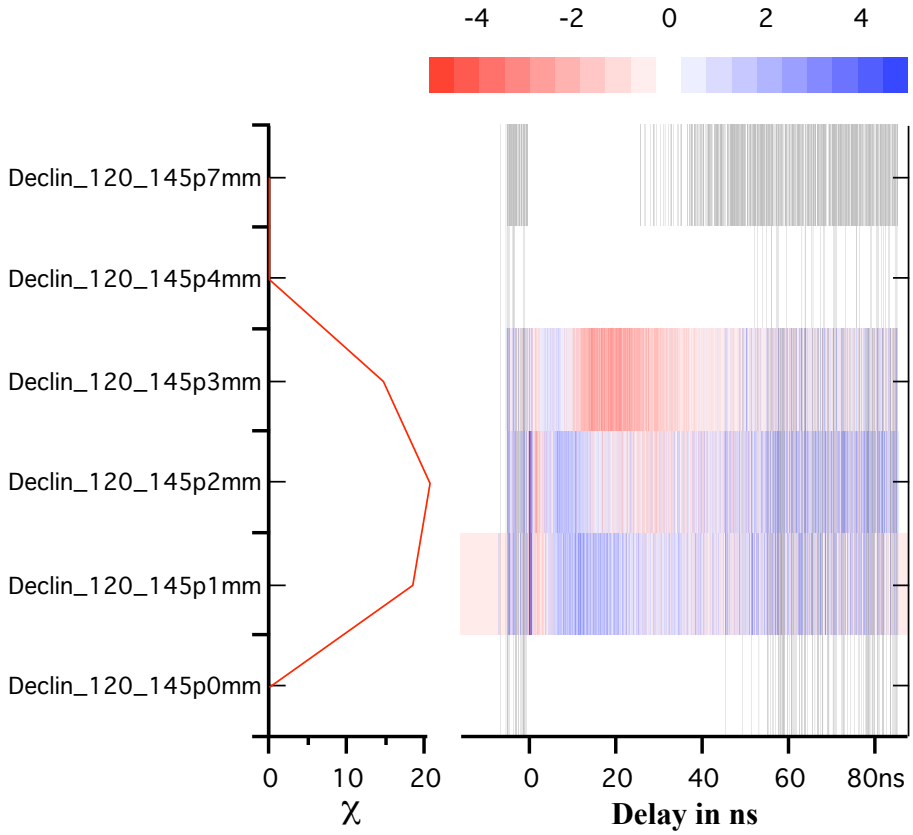

Figure 6. 8: The quality of the description of the data that collected on ROI 1 by the three decay components is shown. The weighted difference between the data and their description is plotted in red white blue color scale, and it can be seen that most of the points are around zero, with white color.

The figure contains two plots with a common vertical axe that lists the name of the decay curves. The left plot gives the χ^2 that is the variance of the distribution of the differences between the data and their approximation by the model. χ^2 is zero for the two extreme curves that have been used as references. It should be close to 1 for the others. The right image displays the same difference between data and approximation point per point. The random change of color means a random change in sign of this difference that is a sign of goodness of the fit.

Thus the logarithm of the decays can be described the sum of threes curves, and represent the monomer, intermediate decay and NPs decay.

6.2.7. Dynamic light scattering (DLS)

The Adambodipy NPs suspension was analyzed by a dynamic light scattering analyzer (DL135 Particle Size Analyzer, Cordouan Technologies), which equipped with a 15 mW diode laser, operating at 650 nm. The configuration allows also the photo-detector to collect

the back-scattered laser light signal, at an angle of 135°. This apparatus offers a configuration, able to analyze as small as 50µL sample volume. The main limitation concerns dilute suspensions (2 10^{-3}g.L^{-1}), when the signal is difficult to discriminate from noise. Each adambodipy nanosuspension sample was analyzed at =20°C, with a viscosity equal to 1.003cP. An acquisition lasts for 45 seconds, is repeated 30 times and generates a size distribution curve using a Padé-Laplace algorithm. The 30 curves are cumulated to give a histogram of the size distribution.

6.2.8. Crystallization of Bodipy derivatives :

The curve of solubility of the Adambodipy molecule in organic-water mixture was obtained in the following way: 1. The partial dissolution of Adambodipy powder was done in several organic-water mixtures with percentage of water varying from 10 to 90%. After 2 days under stirring we obtained saturated mixtures – 2. The clear supernatant was then collected, analysed by spectrophotometry and compared to a calibration curve.

Based on the saturation curve, a concentration of 0.2 g.L^{-1} of Adambodipy in THF-water mixtures with water 40% (W/W percentage) led to a low supersaturation in order to reduce the nucleation rate and favour the growth. In this experiment, the micrometer-sized crystals were obtained by pouring under vigorous mixing a volume of water into Adambodipy organic mixture (THF/EtOH=3/7 v/v) to reach a low supersaturation that closed to 1, in order to reduce the nucleation rate and favour the growth process. The procedure was reproducible.

6.2.9. X-ray diffraction

The orange-red prismatic (0.42 × 0.36 × 0.28 mm) Adambodipy crystal structure determination was carried out using single crystal X-ray diffraction. Adambodipy single crystal was mounted on a Rigaku rotating-anode diffractometer, equipped with a MM007 HF generator, delivering filtered Cu-Ka radiation (l = 1.54187 Å) enhanced and collimated by Osmic confocal optics and with a Rapid II Curved Image Plate. The reflections were corrected for Lorentz and polarization effects but not for absorption. The structure was solved by direct methods with SHELX97-S programiand refined by full matrix least squares, based on F2, using the SHELX97-L software through the CRYSTALBUILDER interface.[11] All non-hydrogen atoms were refined with anisotropic thermal parameters. Hydrogen atoms were generated in idealized positions, riding on the carrier atoms, with isotropic thermal parameters. The final cycle refinement including 392 parameters converged to R1 = 0.0491 (4393 data

with I > 2σ(I)) and wR2 = 0.1488 (all 5756 data), Goodness of Fit S=1.152, max./min. residual electron density 0.238/-0.205. Crystal data of C38 H45 B F2 N2 were recorded at 200 K. CCDC reference number is 852756.

6.2.10. Atomic force microscopy

The NanoWizard® 3 BioScience atomic force microscope (AFM, JPK, Berlin, Germany) is capable of high-resolution image for the crystal terrace and the nanostructure of the surface. It has been used here to image the needle shaped Adambodipy crystals. The crystal was first moved to the microscope cover slips No. 1 borosilicate glass, 0.15 mm thickness, and then repeatedly washed with water. Imaging was done in intermediate-contact mode using commercial silicon nitride cantilevers (ACTA probe, rectangular, no coating, Applied NanoStructures, Inc.) and a scan rate for a 512×512 pixel image from 0.2 to 1 Hz. Height analysis was performed using the JPK software.

Figure 6. 9: The NanoWizard® 3 BioScience atomic force microscope[12]

6.3. TDDFT calculations with Gaussian 09 parameters

6.3.1. The Split-Valence Basis Sets[13]

However, it seems that there is no way to avoid wavefunctions in molecular calculations and for accurate calculations they have to be used as a mapping step between the energy and density. The disadvantage for pure DFTs is that they fail to provide meaningful results for molecular systems.

The Slater method[14] formulated in 1951 gives the first modern chemical approach to the DFT. Then it was developed as an approximate solution to the Hartree Fock (HF) equations, in conventional wave function based approaches. In that case, a very general overview of the typical kinds of basis sets that is almost universally chosen to construct the approximate wave function are given as follow.

A basis set is a set of wave functions that describes the shape of atomic orbitals (AOs), that could be written as:

$$\Psi = a_1\phi_1 + a_2\phi_2 + \cdots a_k\phi_k \qquad \text{Eq. 6.4}$$

where k is the size of the basis set, $\phi_1, \phi_2, \ldots, \phi_k$ are the basis functions and a_1, $a_2, \ldots, a_k$ are the coefficient of ϕ on the basis set.

It was first proposed by John C. Slater to use basis sets for orbital computation, and this set is named Slater Type Orbitals (STOs). In the computation, those one-electron ions give atomic orbitals, which are a product of a radial function that depend on the distance of the electron from the nucleus and a spherical harmonic[15]. Apart from Slater Type Orbitals, Gaussian Type Orbitals (GTOs), which is much easier to compute, are also used to describe AOs. Although STOs describe the shape of AOs more closely than GTOs, it is faster to compute several GTOs and combine them to describe an orbital than to compute one STO. This is why combinations of GTOs are commonly used to describe STOs, which in turn, describe AOs in most of the computation methods[16].

These basis sets are also called Pople basis sets, and it was first proposed by John Pople in the late 1970. Pople basis sets allow specifying the number of GTO's to use for core and valence electrons separately (size adjustable) and makes the total function more accurate and reliable. The method offers an improved description of molecular properties over the minimal representation, and still small enough to be broadly applicable. If we generate an atom centered Cartesian coordinates with *x*, *y*, *z*, GTO of the general form can be written as:

$$\Psi_{GTO}(x, y, z) = x^l y^m z^n e^{-\zeta r^2} \qquad \text{Eq. 6.5}$$

where *l*,*m*,*n* are positive integers which more or less describe the angular momentum of the orbital, and *r* is the radial distance to the atomic center. Spherical orbitals are usually given by *l*=*m*=*n*=0, a p*x* orbital is given by *l*=1,*m*=*n*=0, a d*xy* orbital is given by *l*=*m*=1, *n*=0, etc.

The smallest possible basis set is called the *minimal basis set*, and it contains one orbital for every orbital we usually think of for an atom (including occupied and unoccupied orbitals). Obviously it is not capable of giving highly accurate results.

One solution is to have *twice* as many basis functions as in a minimum basis; this is called a double zeta basis set (the zeta, ζ, comes from the exponent in the GTO). Then, with the Hartree-Fock procedure to weight each atomic orbital basis function more or less, we could get a better description of the wave function.

Split-valence with double-zeta basis is typically presented as X-YZg, depends on the two numbers after the hyphens. In this case, X represents the number of primitive Gaussians comprising each core atomic orbital basis function, which means the number of sp-type inner shell GTOs. Then Y and Z indicate that the valence orbitals are composed of two-basis function each, with a linear combination of Y and Z primitive Gaussian functions respectively. In other words, Y is the number of inner valence s- and p-type GTOs, and Z is number of outer valence s- and p-type GTOs. While "g" indicates that GTOs are used. The split-valence triple- and quadruple-zeta basis sets are also used, denoted as X-YZWg, X-YZWVg etc.

The 6-311g basis sets is a triply split valence basis set, which is triple-zeta in the balance part but only minimal in the core. For the atom calculated in this set, the number of primitives required to represent the atom is 6 GTOs for the core orbitals 1s, then 3 GTOs for inner valence, 2 different GTOs for outer valence (triple zeta), in total (3+1+1)×(valence electrons).

6.3.2. Polarized Basis Sets

When bonds are formed in molecules, the atomic orbitals will polarized from their original direction to have optimal bonding. The phenomenon leads to an extension of basis set Gaussian functions. It typically for one unit higher in angular momentum than what are present in the ground state of the atom are polarization functions, which also increase the flexibility of the basis set in the valence region in the molecule. Adding p, d and f function to basis sets respectively can mimic the distortion of s, p and also d orbital, and in Pople type, it was noted by 6-311g (d) when add a single set of cartesian d-type function on to atoms other than Hydrogens and (d,p) when add a set of *p*-type polarization functions on to Hydrogens, d-type functions add on to all other atoms, f-type functions add on to transition metals.[15,16].

6.3.3. Diffuse Basis Sets

Another extension is the diffuse valence function. It modifies the Pople basis set by letting the electron move far away from the nucleus, creating diffuse orbitals. This modification is always added to the basis set in the computation of anions and molecules with higher bond length or in the calculations of electronically excited states and used to better describe the long-range tails of the orbitals, noted by "+" or "++". "+" is when diffuse functions added on to atoms other than hydrogen and "++" is when diffuse functions added on to all atoms .

6.3.4. Hybrid DFT method

Hybrid DFT method includs a mixture of Hartree-Fock exchange with DFT exchange-correlation. It is available via keywords in the computation of Gaussian software.

One widely used hybrid DFT method is PBE1PBE developed by Perdew, Burke and Ernzerhof, often also abbreviated as PBE0 [17]. The "0" in the acronym tells that the method is parameter free, and it uses a 3:1 mixture of DFT and exact (HF) exchange energies. B3LYP is also one of the most popular DFT model. This method is called to be a hybrid, because is uses corrections for both gradient and exchange correlations[18].

6.4. COMSOL test modeling

6.4.1. Model Navigator

1. Open a new file and click "Multiphysics"
2. Click "Add Geometry…" and add "Axial symmetry (2D), with independent variables as r, phi and z.
3. In the Model navigator, select "Axial symmetric (2D)" in the Space dimension list.
4. Under "Application Modes", ", open Comsol Multiphysics>Fluid dynamics> Incompressible Navier-stokes > Steady-state analysis. Choose Lagrange – p2-p1 for element type. Click "Add". This is the Ruling application mode by default.
5. Under "Application Modes", open Comsol Multiphysics>Fluid dynamics>Convection and Diffusion> Steady-state analysis.
6. Under "Application Modes", open Comsol Multiphysics> Chemical Engineering Module> Maxwell-Stefan Diffusion and Convection > Steady-state analysis.

6.4.2. COMSOL model description:

6.4.2.1. Model description

The physical domain of the model is a 3-dimensional channel with two inlets, one belongs to the inner capillary that introduces the organic solution, which is Adambodipy in THF/EtOH, and one belongs to the outside big capillary for aqueous solution. Due to the COMSOL memory limitation for operating system, we simulate only the first 0.2mm distance from the cross section, and place the top at $z=3\times10^{-4}$m as inlet and z=0 as outlet of the channel.

At the inlet position, initial values for velocity, concentration, mass fraction, and also the diffusion coefficient of each flow for simulation were given. The experimental device was described in Chapter 5, MFD3. The simulation domains were constructed to a 2D-asymmetry system as shown in **Fig.6. 10**

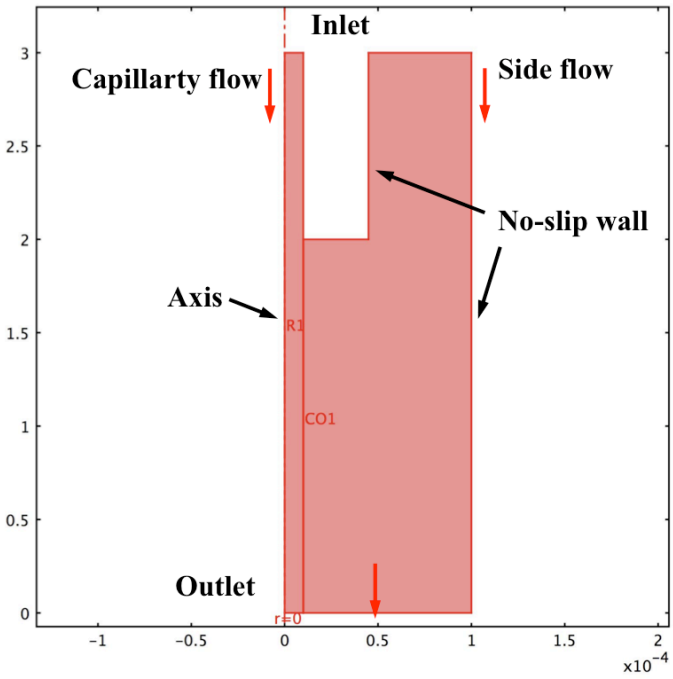

Figure 6. 10: microfluidic geometry built in COMSOL. 3.4, 2D-asymmetry system, with the boundary unit (m)

6.4.2.2 Constants and variables

There are several ways to input necessary parameters and equations into COMSOL. The "constant" option is used to define global parameters, which can be used for the whole

geometry, subdomains and in different modules required in the simulation. The physical parameters of this work are defined in **Table 6.1**.

The scalar expressions are used to define variables as a function of local variable that are valid at any point and at any time of the simulation. We have input the equation for mutual diffusion coefficient, viscosity and density (given in Chapter 5 Eq. 15, 16 and 17) for this binary system, also the Adambodipy solubility in the system (given in Chapter 2, Eq. 23), and absolute saturation expressions (C/ C_{sat}-1) in the scalar expressions setting in the program.

Parameter	Value	Unit
Density of ethanol (ρ_{org})	789	$kg{\cdot}m^{-3}$
Viscosity of ethanol (μ_{org})	$1.2\ 10^{-3}$	Pa·s
Density of water (ρ_{aq})	1000	$kg{\cdot}m^{-3}$
Viscosity of water (μ_{aq})	10^{-3}	Pa·s
Molar mass of water (M_H2O)	18	g/mol
Molar mass of ethanol (M_ETH)	46	g/mol
Self-diffusion coefficient of water (D_W) [19]	$2.299\cdot10^{-9}$	$m^2\cdot s^{-1}$
Self-diffusion coefficient of water (D_E) [20]	$1.07\cdot10^{-9}$	$m^2\cdot s^{-1}$
Boltzmann constant (k_B)	$1.3806488\cdot10^{-23}$	$m^2kg\cdot s^{-2}K^{-1}$
Temperature (T)	298.15	K
Avogadro constant (NA)	$6.02\cdot10^{23}$	mol^{-1}

Table 6. 1: Operating and physical conditions:

6.4.2.2. Computation

Step1: Computation of the hydrodynamics

Application mode type: Incompressible Navier-Stokes (MEMS Module)

Application mode name: mmglf

Solver manager:

- Initial value: Initial value expression
- Values of variables not solved for and linearization point: Use setting from initial value frame

Number of degrees of freedom	106443
Number of mesh points	6341
Number of elements	12344
Triangular	12344
Quadrilateral	0
Number of boundary elements	404
Number of vertex elements	9
Minimum element quality	0.6738
Element area ratio	0.1813

Table 6. 2: Mesh statistics used for the calculation

Analysis	Stationary
Linear system solver	Direct UMFPACK
Matrix symmetry	Automatic
Linearity	Automatic
Relatively tolerance	0.0000001
Maximum number of iteration	40

Table 6. 3: Solver parameter

We first mesh with parameters in **Table 6. 2**. We fixed the initial velocity at a value of 0.04246 m/s for side flow and 0.01810 m/s for center flow, according to the flow rate 13.6μl/min and 0.8μl/min. The other boundary conditions where no slip along the wall and the atmospheric pressure at the outlet. and calculated from the given surface of the channel, we solve the model Incompressible Navier-Stokes (MEMS Module) with stationary solver for velocity distribution over the channel.

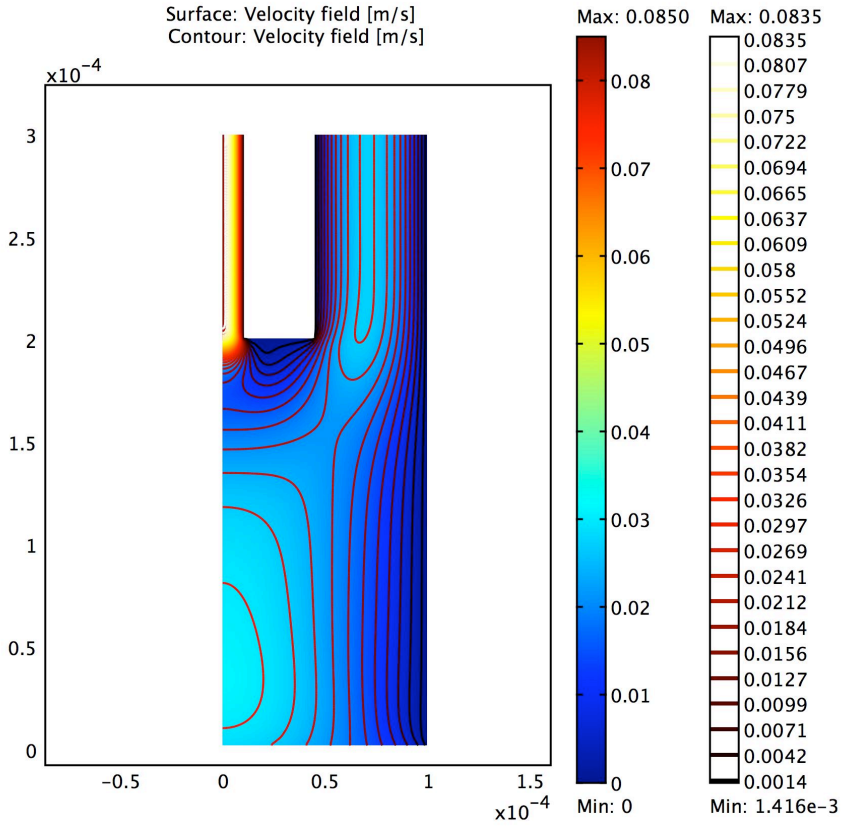

Figure 6. 11: velocity profile (m/s), boundary unit (m)

The result of velocity field is plotted with 15 contour levels in **Fig. 6. 11.**

Step 2: Computation of the Ethanol/Water mixing.

Application mode type: Maxwell-Stefan Diffusion and Convection (Chemical Engineering Module)

Application mode name: chms

Solver manager:

- Initial value: Initial value expression evaluated using using current solution (solution of Step1)
- Values of variables not solved for and linearization point: current solution.

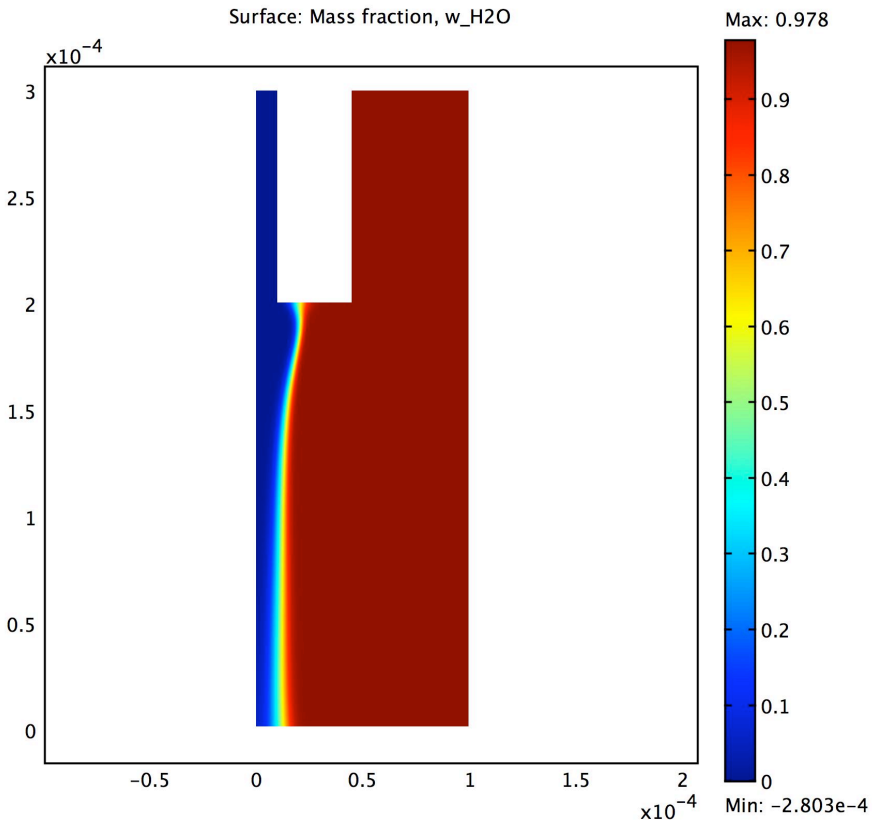

Figure 6. 12: Water mass fraction profile (Unit:1)

The numerical solution of water mass fraction is obtained by applying Maxwell-Stefan Diffusion and Convection module with Eq. 16, 17 in Chapter 5. The initial values for the velocity will be the solved velocity values obtained at the end of the step 1. The initial values for concentration are given as 0 for side flow and 0.08 mol/m^3 (concentration of Adambodipy solution for FLIM experiment). The numerical profile of mass fraction of water that diffused in EtOH is shown in **Fig. 6. 12**. Mass fraction value decreases as color changes from red to blue.

Density and viscosity of the mixture varies with the mass-fraction of water. Their values are calculated according to the Eq. in Chapter 5 and included in the simulation using ”scalar expression”. The plot of the density profile and the viscosity profile are shown in **Fig 6. 13, Fig 6. 14** separately.

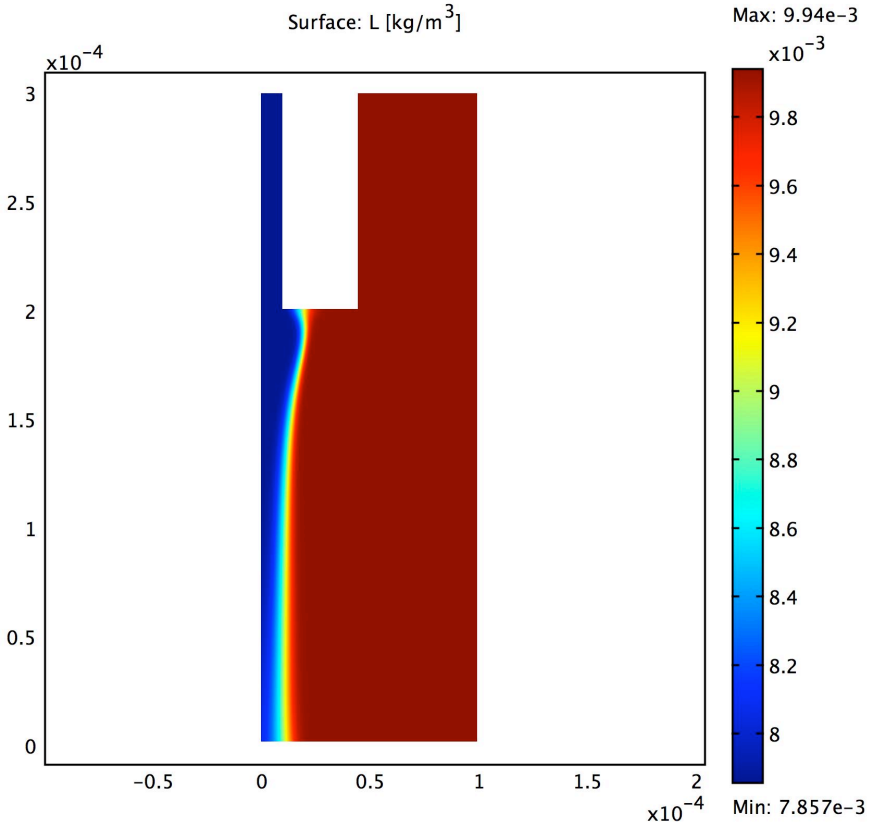

Figure 6. 13: Density profile,L (Unit: kg/m^3)

The density profile agrees with the transmission image (**Fig. 6. 13(a)**). Indeed The refraction index that is proportional to the density and depends on the composition. The refraction index gradient is responsible of the refraction of the light at the Ethanol/Water boundary. We have not achieved the simulation of the transmission image with Comsol. But with this in mind we have measured the refraction index as a function of the mixing ratio. This is shown in **Fig. 6.14**. where refraction index of mixtures water/Ethanol/THF have been measured for water percentage range is $[0, 1]$, EtOH $[0,\ 0.4]$, THF$[0, 0.4]$. It fits the intensity of the transmission image **Fig. 6. 14 (c)**.

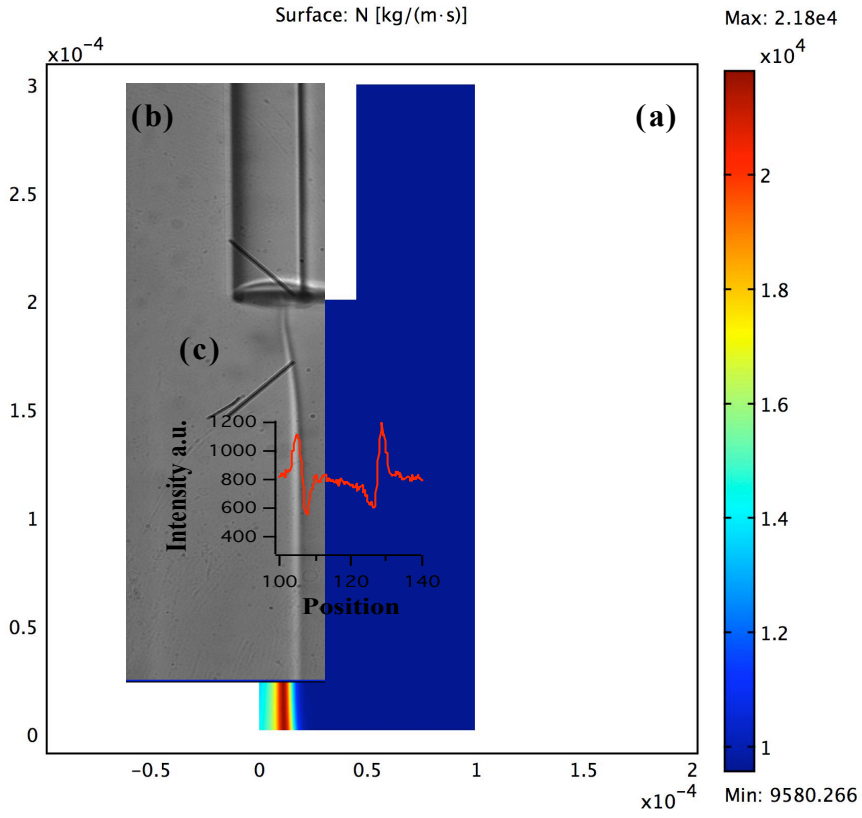

Figure 6. 14: (a) Viscosity profile, N (Unit: kg/(m.s)) (b) Transmission image of the flow in capillary, (c) Intensity of the transmission image cross the center flow.

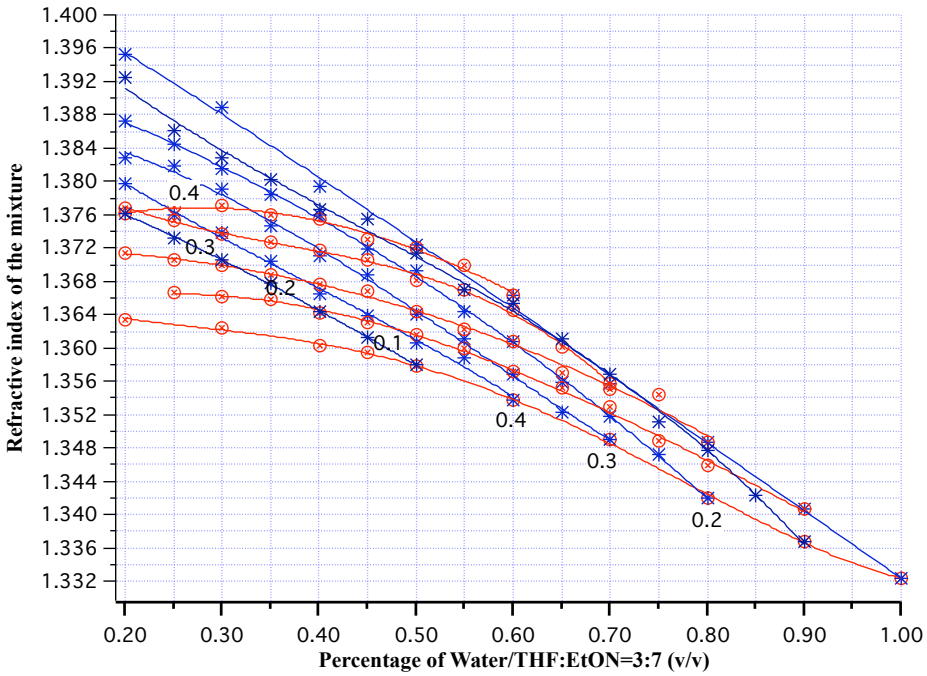

Figure 6. 15: Refraction index of mixtures water/Ethanol/THF have been measured for water percentage range is [0, 1] shown in x axis, EthOH [0, 0.4] in red curves, THF[0, 0.4] in blue curves

Step 3:

Redo the Step 1

There is no significant change for the obtained velocity profile and the mass fraction profile after the recalculation.

Step 4: Diffusion of the Bodipy in the Ethanol/water gradient

Application mode type: Convection and Diffusion (MEMS Module)

Application mode name: chcd

Solver manager:

- Initial value: Initial value expression evaluated using current solution (result from Step 3)
- Values of variables not solved for and linearization point: Current solution

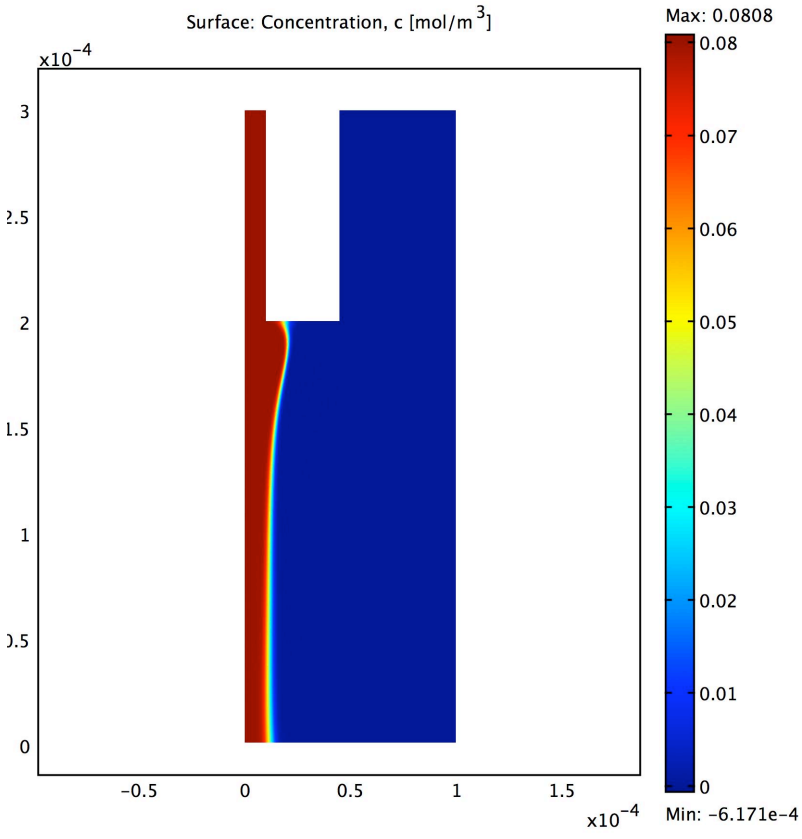

Figure 6. 16: Concentration profile, c (Unit: mol/m^3)

The numerical solution of Adambodipy concentration is obtained by applying the Convection and Diffusion Module with Eq. in Chapter 5. Since the Adambodipy molar

fraction (Concentration<0.08mol/m^3) is small, the viscosity and density of the solvent will not be modified. The velocity and viscosity values obtained in the former part of the simulation will be used as initial values for the variables during the simulation. The numerical profile of concentration is shown in **Fig. 6. 16.** Concentration decreases as color changes from red to blue as the Adambodipy of concentration diffused into aqueous solution over the channel. The concentration profile agrees with the fluorescence image taken from the experiments. This is particularly true close to the nozzle, when there is no precipitation.

The concentration profile obtained at Step 4 does not include the nucleation and precipitation but is used for the further simulation of supersaturation profile.

Step 5: Calculation of the supersaturation map.

The scalar expressions are used to intermediate local quantities but also to plot such quantities. The supersaturation can be defined as the ratio C/ C_{sat}. Where the concentration profile C was obtained at step 4. C_{sat} is the saturation concentration this is was measured at **§ 2.4.2**. The saturation concentration is a function of the solvent composition and can thus be measured at each point. The supersaturation profile was plotted in **Fig. 6. 17**.

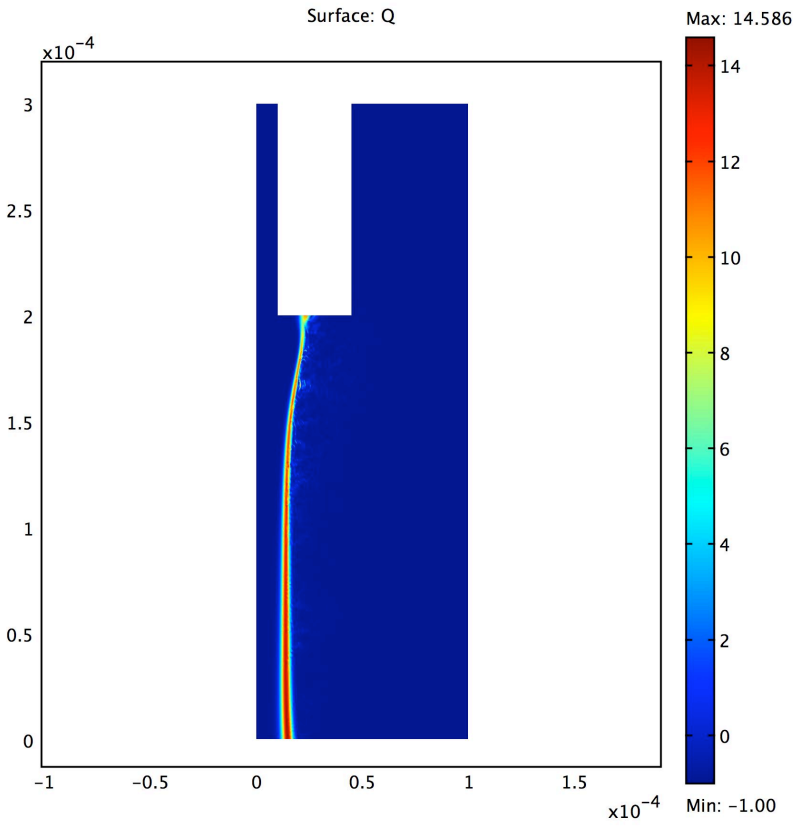

Figure 6. 17: Absolute Supersaturation profile, Q= C/ C_{sat}-1 (Unit: 1)

The supersaturation profile shows that the supersaturation is not maximal at the contact with the nozzle. The solvent gradient is there but Adambodipy that diffuses is still not there. This may explain that in a narrow concentration rang we can avoid crystallization on the nozzle.

In the blue area outside the frontier we see filaments that are due to the digitalization of the computation. This numerical noise is amplified since we are dividing a concentration that is almost zero by a saturation concentration that is almost zero.

Reference:

[1] *"Information about Dow Corning® Brand Silicone Encapsulants. Product nformation. Dow Corning and Sylgard are registered trademarks of Dow Corning Corporation. ©2000-2008 Dow Corning Corporation. All rights reserved. Form No. 10-898I-01."*

[2] Hof, M. H., R.; Fidler, V. *"Fluorescence Spectroscopy in Biology: Advanced Methods and their Applications to Membranes, Proteins, DNA, and Cells."* **2005**.

[3] Spitz, J. A.; Yasukuni, R.; Sandeau, N.; Takano, M.; Vachon, J. J.; Meallet-Renault, R.; Pansu, R. B. *"Scanning-less wide-field single-photon counting device for fluorescence intensity, lifetime and time-resolved anisotropy imaging microscopy."* J Microsc-Oxford, **2008**, *229*, 104-114.

[4] Badre, S.; Monnier, V.; Meallet-Renault, R.; Dumas-Verdes, C.; Schmidt, E. Y.; Mikhaleva, A. I.; Laurent, G.; Levi, G.; Ibanez, A.; Trofimov, B. A.; Pansu, R. B. *"Fluorescence of molecular micro- and nanocrystals prepared with Bodipy derivatives."* J Photoch Photobio A, **2006**, *183*, 238-246.

[5] Brouwer, A. M. *"Standards for photoluminescence quantum yield measurements in solution (IUPAC Technical Report)."* Pure Appl Chem, **2011**, *83*, 2213-2228.

[6] Abdi, **H.** W., L. J.;. *"Principal Component Analysis."* Wiley Interdisciplinary Reviews: Computational Statistics, 2 **2010**.

[7] Al-Soufi, W.; Novo, M.; Mosquera, M. *"Principal component global analysis of fluorescence and absorption spectra of 2-(2 '-hydroxyphenyl)benzimidazole."* Appl Spectrosc, **2001**, *55*, 630-636.

[8] Al-Soufi, W. N., M.; Mosquera, M.; Rodríguez-Prieto, F. *"Reviews in Fluorescence 2009: Principal Component Global Analysis of Series of Fluorescence Spectra."* Springer New York, **2011**.

[9] Jolliffe, I. T. *"Principal Component Analysis."* 2nd ed. ed.; Springer, **2002**.

[10] Hatcher, L. *"A Step-By-Step Approach to Using the Sas System for Factor Analysis and Structural Equation Modeling."* SAS Institute Inc., **1994**.

[11] Welter, R. *"The CRYSTALBUILDER project: an easy way for single crystal structure analysis."* Acta Cryst., **2006**, s252.

[12] http://www.jpk.com/index.27.en.html.

[13] Wolfram, K. M. C., H.;. *"A Chemist's Guide to Density Functional Theory."* Wiley-VCH Verlag GmbH, **2001**; *Vol*. 7.

[14] Slater, J. C. *"A Simplification of the Hartree-Fock Method."* Phys Rev, **1951**, *81*, 385-390.

[15] K. I. Ramachandran, G. D., K. Namboori. *" Computational Chemistry and Molecular Modeling: Principles and Applications."* Springer, **2008**.

[16] Tomberg, A. *"Gaussian 09W Tutorial: An introduction to computational chemistry using G09W and avogadro software."* Barrett Research Group, http://barrett-group.mcgill.ca/tutorials/tutorials.php.

[17] Ernzerhof, M.; Perdew, J. P.; Burke, K. *"Coupling-constant dependence of atomization energies."* Int J Quantum Chem, **1997**, *64*, 285-295.

[18] Raghavachari, K. *"Perspective on "Density functional thermochemistry. III. The role of exact exchange" - Becke AD (1993) J Chem Phys 98:5648-52."* Theor Chem Acc, **2000**, *103*, 361-363.

[19] Holz, M.; Heil, S. R.; Sacco, A. *"Temperature-dependent self-diffusion coefficients of water and six selected molecular liquids for calibration in accurate H-1 NMR PFG measurements."* Phys Chem Chem Phys, **2000**, *2*, 4740-4742.

[20] Guevara-Carrion, G.; Nieto-Draghi, C.; Vrabec, J.; Hasse, H. *"Prediction of Transport Properties by Molecular Simulation: Methanol and Ethanol and Their Mixture."* J Phys Chem B, **2008**, *112*, 16664-16674.

General Conclusion and Perspectives

The results obtained in this thesis can be divided into two different aspects of the research on fluorescent organic nanoparticles: their spectroscopy and their preparation. The main conclusions are summarized as follows:

First, fluorescence organic microcrystals from Adambodipy was obtained by the precipitation method with typical size $100\times10\times1\mu m^3$. We have shown that these crystals are birefringent and dichroic. For that we have added polarization control on our spectrometer inside the microscope. It appears that the absorption measurement under our microscope levels at high values that preclude the correct measurement of the microcrystal absorption peaks. The birefringence was measured along the two neutral axis using the Swanepoel method.

We have written a software for the calculation of the absorption and fluorescence spectra of nanoparticles made of N×N×N cells (N<11) based on X-ray crystallography information. We use for that the Frenkel exciton theory with the dipole-dipole coupling approximation. The values of the coupling elements were estimated from a classical model. But we have compared this value with the one that can be deduced from the TDDFT calculation of an Adambodipy dimer. The order of magnitude is satisfying. But it appears that the calculation of a dimer is long and heavy. As expected, the shape of the calculated spectra strongly depends on the electronic transitions (allowed) in Y and Z direction and (forbidden) in X direction. The calculated fluorescence spectra predict only one transition where two extra red shifted bands are present. Polarization and fluorescence lifetime studies show that these emissions come from defect of the crystalline structure.

Second, in conclusion of the work described in Chapter 4 and 5, the 3D hydrodynamic focusing micro-fluidic technology was used for produce highly fluorescence organic nanoparticles with controllable narrow distribution, high stability and reproducibility.

This technique prevents the contact of the dye solution flow with the channel walls, and the micro-fluidic system has been developed to allow the control of the focused stream through the flow rates ratio. We get a better control of the process inside the MFD and succeed in avoiding any crystal deposition on the tip of the capillary tube by modifying the

MFD. We further move a glass tubing microfluidic solution to avoid the adsorption of fluorescent molecules into the PDMS.

The stability of the colloidal suspension of nanoparticle was achieved using th surfactant CTACl. In the presence of CTACl above CMC (1.3×10^{-3}M), we shaw that the fluorescent molecule distributes into micelle and nanoparticle, whereas with surfactant concentration below CMC, only the amorphous nanoparticles are presented in the suspensions. With Adambodipy, the size of the nanoparticles range from 100 to 200nm in diameter and scales linearly with the inner flow diameter. Indeed the flow rates affect the residence time and also the nucleation and growth processes, as the diffusion kinetics controls the supersaturation and depends on the width of the focused stream. The reproducibility of the MFD method was also checked.

We have used COMSOL to simulate the mixing and diffusion steps of the precipitation. We have included in the simulation the mixing of ethanol and water as well as the diffusion of the Adambodipy. From our measurements of the saturation of Admabodipy in a mixture of ethanol and water, we have been able to produce with COMSOL the map of the super saturation in the microdevice.

Then we exploit the benefits offered by Fluorescence Lifetime Imaging Microscopy (FLIM) to image the precipitation process. The lifetime decreases when going from molecules to nanoparticle. The images obtained by FLIM closely resemble those predicted by COMSOL.

In conclusion, the ability to control the size distribution of the FONs by changing the flow rates was a very important issue in our experiment; especially the method can be fully controlled and illustrated with the combination of FLIM technology, then confirmed by the prediction from the simulation model of COMSOL.

This work opens new research directions. We wish to further reduce the size of the nanoparticles. For that we shall further reduce the size of the inner flow using new microfluidic devices. The comparison of the COMSOL simulations, which produce the supersaturation map can be compared with the FLIM images. From this comparison we should be able the determined the concentration at which nucleation starts. The spontaneous nucleation remains random. In order to improve the size dispersity we plan to regulate the nucleation by focusing the laser in the domain of super stauration.

When we shall have nanoparticles with sizes that compare with the diffusion length of the exciton we shall evaluate these nanoparticles as ultrbright nanosensor where not only the surface fluorescence can be quenched by surface reactions but also that of the core.

Finally, this micro-fluidic technique, once completely optimized, can be used to synthesize NPs of other BODIPY derivatives, with fluorescence emission shifted in the near-IR range, compatible with applications in biology. Also, further experiments will be carried out to get monodisperse size NPs with fully controlled spectroscopic properties.

Conclusion générale et perspectives

Pendant cette thèse nous avons travaillé sur deux aspects des nanoparticules organiques fluorescentes d'AdamBodipy : leur spectroscopie et leur production avec des tailles contrôlées.

Nous avons produit des microcristaux d'AdamBodipy par précipitation dans des solutions de sursaturation faible. Nous avons développé notre montage de microscopie pour mesurer leur spectroscopie d'absorption et de fluorescence polarisée dans la gamme 380nm à 900nm sur une surface de 10µm. Nous avons ainsi pu mesurer la biréfringence et le dichroïsme des microcristaux. Il apparaît que la mesure de l'absorption est handicapée par la lumière transmise vers le détecteur hors du champ de mesure.

Nous avons écrit un logiciel pour le calcul des spectres d'absorption et de fluorescence en utilisant la théorie du couplage dipolaire pour les excitons de Frenkel. Le programme s'applique à des nanoparticules formées de N×N×N (N<11) mailles cristallines. Nous avons voulu comparer le couplage biomoléculaire estimé pour cette théorie avec la valeur donnée par le calcul par TDDFT de dimères. L'ordre de grandeur est vérifié. Nous n'avons pas calculé plus de dimères car le calcul reste lourd et long.

La comparaison entre les spectres d'absorption théoriques et calculés est satisfaisante. Pour la fluorescence nous avons montré que les bandes rouges, non prévues pas la théorie, étaient des défauts. Nous avons pu reproduire les spectres des nanoparticles produites dans notre micro-dispositif en simulant une forme amorphe.

La focalisation hydrodynamique 3D, nous a permis de produire des nanoparticules de taille contrôlée sans qu'il y ait précipitation de l'AdamBodipy sur les parois. En réglant le rapport des flux entre la solution organique de colorant et la solution aqueuse non solvant, nous avons pu ajuster la taille des nanoparticules entre 100 et 300nm.

Nous avons simulé la précipitation des nanoparticules par COMSOL en introduisant une l'hydrodynamique de mélange par diffusion mutuelle de l'eau et de l'éthanol et de diffusion du colorant dans ce mélange. Nos études de la solubilité de l'AdamBodipy dans des mélanges organiques/eau, nous ont permis de déterminer la loi de solubilité et d'obtenir des cartes de la super-saturation dans le microdispositif. Nous avons utilisé l'imagerie de fluorescence pour suivre le processus de précipitation. Les images obtenues sont semblables à celles calculées par COMSOL On observe une précipitation à l'interface entre les deux solvants ainsi qu'une précipitation en masse après un temps de résidence qui dépend du rapport des flux. Les

déclins de fluorescence collectés en différents points du canal microfluidique peuvent être attribués à trois espèces : le monomère, la nanoparticule et une espèce intermédiaire, un germe.

Ce travail ouvre de nombreuses perspectives. Nous souhaitons réduire encore la taille des nanoparticules en réduisant encore la taille du flux central. Pour cela il faut de nouveaux dispositifs microfluidiques. La comparaison de la simulation COMSOL, qui fournit les domaines de sur saturation, avec les images devrait nous fournir la sur saturation critique à laquelle la nucléation démarre. La nucléation spontanée reste aléatoire. Pour affiner la distribution en taille, nous souhaitons régulariser la nucléation en focalisant un laser dans le domaine de sur saturation critique.

Si nous disposons de nanoparticules de taille comparable à la distance de diffusion de l'exciton, nous pourrons valider ces nanoparticules comme des capteurs ultralumineux dont la fluorescence de surface comme du cœur sera sensible au quenching de surface.

Appendix 1. Igor script for simulation

With the following code example, the crystal structure are built and analyzed.

Step 1: Build Adambodipy single crystal structure

The code below was built to load the Adambodipy single crystal structure information from the ".cif " file from X-ray diffraction. Then a Cartesian coordinate system was built to describe the crystal structure.

```
// NbreMolecule number of molecules describe in the CIF
// NbreMoleculeMaille number of molecules in a cell
// Coord[0][NbreMolecule][NbreAtome][0...2] contains the coordinates [0..2] of the atomes in the molecules of cell 0. (Coordinate in cell unite)
// NumCellsTot number of cells in the nanoparticle
// CoordCell[NumCellsTot][0...2] coordiantes of the cell in cell units.
// dipole[CellNumber][MolinCell][0,2] coordinates of the dipole in cell units.
// dipole[CellNumber][MolinCell][3,5] de 3 a 5 coordinates of the center of the dipole in cell units.
// DMU moment de transition en Debye
// LongCell[0...2][0...2] transformation matrix of the cell coordinates to Cartesian coordinates in nm
// CellParam=(a, b, c, alpha, beta, gamma) geometric description of the cell.
// ExcitonStates [CellNumber* MolinCell][k] contribution of each dipole to the exciton k whose energy is W_eigenValues[k]
// TransitionMoments[k][0...2] //Exciton k Transition Moment
macro ReadAdamantane()
variable pipe

string ligne,clef

Make/O/N=(125,4,6,4) Coord

Coord=0

variable/G NbreAtome=0

Variable/G NbreMolecule=0

// Opens the X-ray diffraction data file .cif

Open /R  /M="Select a CIF Xray dataFile" /T=".CIF" pipe
```

```
do
FReadLine  pipe, ligne
while (strsearch(ligne,"_symmetry_equiv_pos_as_xyz",0)==-1)
FReadLine  pipe, ligne;print Ligne
…
…
do
FReadLine  pipe, ligne
//instead of the whole molecules, we select 4 atoms, B1, C3, C6, C13 to present the molecule structure//
while (cmpstr(ligne," _atom_site_label "+"\r")!=0)
Clef="B1 B"
do
FReadLine  pipe, ligne
while (strsearch(ligne,Clef,0)==-1)
print ligne
Ligne=Ligne [strsearch(ligne, Clef, 0) + strlen(Clef), inf]
LireCoord(ligne)
…
…
Clef="C6 C"
FSetPos pipe, 0
do
FReadLine  pipe, ligne
while (strsearch(ligne,Clef,0)==-1)
print ligne
        Ligne=Ligne[strsearch(ligne,Clef,0)+strlen(Clef),inf]
LireCoord(ligne)
```

```
close pipe
NbreMolecule=1
End
//
```

By symmetry property of the crystal, unit cell with four molecules can be describe by the code below:

```
Macro MakeCell0bySymetrie()
Variable NumMol=0
variable NumCell=0
translateToCell0(NumCell,NumMol)
        AppendMolecule(NumCell,0)
variable NewMolecule=NbreMolecule
variable/G NbreMoleculeMaille=NbreMolecule
If(1)
Coord[NumCell][NewMolecule][*][0,2] = −Coord[NumCell][NumMol][r][s]
translateToCell0(NumCell,NewMolecule)
        AppendMolecule(NumCell,NewMolecule)
NbreMoleculeMaille+=1
Endif

If(1)
…
…
```

After that, the crystal can be built up by setting the number of unit cell.

Step 2: Calculate the dipole coupling term, exciton states and oscillator strength

The code below is to calculate the interaction among molecules in the crystal as coupling term and represent the obtained values in matrix shown in Figure 3. 18 in Chapter 3.

```
Macro MakeCouplages()

Make/O/N=(NbreMoleculeMaille*NumCellsTot,NbreMoleculeMaille*NumCellsTot) couplages

Make/O/N=3 PQ,M_Product

PQ[*]=dipole[0][0][p]

Cristal2Cartesian(PQ)
```

```
//Geometrical length of the dipole.//
variable/G AL2=PQ[0]^2+PQ[1]^2+PQ[2]^2

Couplages[*][*]=CouplageDipolaireEtenduVect(p,q)

KillWaves/Z  PQ

silent 1

DoWindow MatriceCouplage

if (V_Flag!=1)
        Display
        appendImage couplages
        ModifyGraph mirror=2
        ModifyGraph height=(Plan,1,left,bottom)
        SetAxis/A/R left
        ModifyImage couplages ctab= (*,*,Rainbow,0)
        Label left "Molecule N° in the small crystal"
        Label bottom "Molecule N° in the small crystal"
        TextBox/C/N=text0/A=MC/X=29.25/Y=37.63 FormeCrystal
        DoWindow /C MatriceCouplage
else
        DoWindow/F MatriceCouplage
        TextBox/C/N=text0 FormeCrystal
endif

end

Function CouplageDipolaireVectoriel(Molp,Molq)
        Variable Molp,Molq
```

```
wave LongCell=LongCell

wave dipole=dipole

wave CoordCell=CoordCell

NVar epsilon=epsilon

NVar DMU=DMU

Variable R=0,p1p2=0,p1R=0,p2R=0,norme=0

Variable NumCellp,NumMolp,NumCellq,NumMolq

NumCellp=MolNum2CellNumber(Molp)

NumMolp=MolNum2PositionInCell(Molp)

NumCellq=MolNum2CellNumber(Molq)

NumMolq=MolNum2PositionInCell(Molq)

Make/O/D/N=3 PQ,P1,P2

PQ=dipole[NumCellp][NumMolp][p+3]-
dipole[NumCellq][NumMolq][p+3]//+CoordCell[NumCellp][p]-CoordCell[NumCellq][p]

P1=dipole[NumCellp][NumMolp][p]

P2=dipole[NumCellq][NumMolq][p]

Cristal2Cartesian(PQ)

Cristal2Cartesian(P1)

norme=sqrt(P1[0]^2+P1[1]^2+P1[2]^2)

P1/=norme

Cristal2Cartesian(P2)

norme=sqrt(P2[0]^2+P2[1]^2+P2[2]^2)

P2/=norme

R=sqrt(PQ[0]^2+PQ[1]^2+PQ[2]^2)
```

```
        p1p2=MatrixDot(P1,P2)

        p1R=MatrixDot(P1,PQ)

        p2R=MatrixDot(P2,PQ)

if (Molp==Molq)

return 0

else

//Interaction term is expressed in wavenumbers, the transition moments are in Debye (1 Debye
=3.33×10^-30 Coulomb meter), R is the vector between two molecules //
return 5.04*DMU^2*(p1p2 - 3*p1R*p2R/R^2)/R^3

endif

end function

…

…
Macro CalculDipolesListe(TransitionMoment,translate,ChargePosition)
//Transition moment is 5.6 debye coming from TDDFT calculation//
        variable TransitionMoment=5.6,translate=-0.1,ChargePosition=0.9
        prompt translate "Translation du moment de transition en fraction de la distance BC13"
        prompt ChargePosition "distance entre charges en fraction de la distance C3C6"
        prompt TransitionMoment "Transition Moment in Debye"
        //DMU represent transition moment//
        Variable/G DMU=TransitionMoment
        Coord[*][*][*][*]=Coord[0][q][r][s]+CoordCell[p][s]
// dipole[NumCell][NbreMolecule][0,2] from 0 to 2 represent the coordinates of dipole
dipole[NumCell][NbreMolecule][3,5] from 3 to 5 represent the coordinates of molecule from the
center//
//dipole[*][0][0,2]=-dipole[p][0][r] // This was tested to check that changing the direction of the
transition moment on one family of molecule was not changing the eigenvalues and spectral densities
//dipole[0][0][0,2]=-dipole[0][0][r]// This was tested to check that changing the direction of the
transition moment on one molecule was not changing the eigenvalues and spectral densities
//dipole position from the coordinates of atome 3 and 1 and CoordCell in cristalographique unites
        dipole=0
```

```
        dipole[*][*][0,2]=(coord[0][q][1][r]-coord[0][q][3][r])*ChargePosition // dipole coordinates
from the coordinates of atome 3 and 1 in cell [0] in cristalographique unites
        dipole[*][*][3,5]=(coord[0][q][3][r-3]+coord[0][q][1][r-3])/2+CoordCell[p][r-
3]+translate*(coord[0][q][2][r-3]-coord[0][q][0][r-3])/4

// Aleatoire
if(0)
variable cell,mol,theta,Phi
silent 0
cell=0
do
mol=0
do
theta=enoise(2*Pi)
        dipole[cell][mol][0,2]=cos(theta)*(coord[0][mol][1][r]-
coord[0][mol][3][r])+sin(Theta)*(coord[0][q][2][r]-coord[0][q][0][r])/4
mol+=1
while(mol<NbreMoleculeMaille)
cell+=1
while (cell<NumCellsTot)
print "rotation aleatoire des molecules dans le cristal"
endif

if(0)  //rotation
variable cell,mol,theta
theta=getvalue("Angle en ° de rotation des dipoles",45)
theta*=Pi/180
silent 0
mol=0
do
        dipole[*][mol][0,2]=cos(theta*mod(mol,2))*(coord[0][mol][1][r]-
coord[0][mol][3][r])+Sin(Theta*mod(mol,2))*(coord[0][q][2][r]-coord[0][q][0][r])/4  //de 0 à 2 //
dipole coordinates from the coordinates of atome 3 and 1 in cell [0] in cristalographique unites
mol+=1
while(mol<NbreMoleculeMaille)
print "rotation des molecules dans le cristal de",theta/pi*180,"°"
endif
```

```
//        dipole[*][*][0,2]=coord[0][q][0][r]-coord[0][q][2][r]  //transition moment along NI
//        dipole[*][*][3,5]=(coord[0][q][0][r-3]+coord[0][q][2][r-3])/2+CoordCell[p][r-3] //transition moment along NI
//        variable Theta=Pi/4
//        dipole[*][*][0,2]=coord[0][q][1][r]-coord[0][q][3][r]*cos(Theta)+coord[0][q][0][r]-coord[0][q][2][r]*sin(Theta)  //de 0 à 2 // dipole coordinates from the coordinates of atome 3 and 1 in cell [0] in cristalographique unites
visualisation()
end macro
```

Then the code to calculate the density of excited states, also oscillator strength as follow:

```
Macro ExcitedStates()
MatrixEigenV /SYM/EVEC couplages
killwaves/Z Excitonstate
rename M_eigenVectors, Excitonstate

Make/O/N=100/O W_eigenValues_Hist
Histogram/B=1 W_eigenValues,W_eigenValues_Hist
W_eigenValues_Hist/=numpnts(W_eigenValues)
pauseupdate
duplicate/O W_eigenValues_Hist,
DensiteEtats,DensiteSpectraleX,DensiteSpectraleY,DensiteSpectraleZ,DensiteSpectrale

duplicate/O W_eigenValues,ForceOscillateur,TransitionMomentX,
TransitionMomentY,TransitionMomentZ,TransitionMomentsPowder,DMKT,temp2
Make/O/N=(Numpnts(W_eigenValues),3) TransitionMoments
TransitionMomentX=0;TransitionMomentY=0;TransitionMomentZ=0;
Make/O/N=3 tempTM
variable K=0
tempTM=dipole[MolNum2CellNumber(K)][MolNum2PositionInCell(K)][p]
Cristal2Cartesian(tempTM)
      TransitionMomentX[]+= Excitonstate[K][p]*tempTM[0]
      TransitionMomentY[]+= Excitonstate[K][p]*tempTM[1]
      TransitionMomentZ[]+= Excitonstate[K][p]*tempTM[2]
      K+=1
while (K<NbreMoleculeMaille*NumCellsTot)
      TransitionMoments[][0]=TransitionMomentX[p]
```

```
        TransitionMoments[][1]=TransitionMomentY[p]
        TransitionMoments[][2]=TransitionMomentZ[p]
    ForceOscillateur[]=(TransitionMomentX[p]^2+TransitionMomentY[p]^2+TransitionMomentZ[p]
^2)*(W_eigenValues[p]+19400)*3.43184E-15
    DMKT[]=(TransitionMomentX[p]^2+TransitionMomentY[p]^2+TransitionMomentZ[p]^2)
    temp2=DMKT*4E8/(W_eigenValues[p]+19400)^2*0.0094627;Histogram/P/B=1/W=temp2
W_eigenValues,DensiteSpectrale
    temp2=TransitionMomentX^2*4E8/(W_eigenValues[p]+19400)^2*0.0094627;Histogram/P/B=1/
W=temp2 W_eigenValues,DensiteSpectraleX
    temp2=TransitionMomentY^2*4E8/(W_eigenValues[p]+19400)^2*0.0094627;Histogram/P/B=1/
W=temp2 W_eigenValues,DensiteSpectraleY
    temp2=TransitionMomentZ^2*4E8/(W_eigenValues[p]+19400)^2*0.0094627;Histogram/P/B=1/
W=temp2 W_eigenValues,DensiteSpectraleZ
```

Step 3: Plot the absorption and fluorescence spectra

```
Macro Spectre(centrale,theorie)
        variable centrale=19400
        string Theorie
        prompt centrale "energie de la transition dans le vide en cm-1"
        prompt theorie "Largeur Homogene en cm-1" ,popup,
"LargeurHomogene;Franck_Condon;Self_Consistant"

duplicate/O DensiteSpectrale AbsPoudre,FluoPoudre
duplicate/O DensiteSpectraleX AbsX,FluoX
duplicate/O DensiteSpectraleY AbsY,FluoY
duplicate/O DensiteSpectraleZ AbsZ,FluoZ
Variable T=300
FluoX*=exp(-x/0.695028718/T)
FluoY*=exp(-x/0.695028718/T)
FluoZ*=exp(-x/0.695028718/T)
FluoPoudre*=exp(-x/0.695028718/T)

InsertPoints  0, 50, AbsPoudre, AbsX,AbsY,AbsZ,FluoPoudre,FluoX,FluoY,FluoZ
// Increase the size of absorption with respect of density of state to have room form line shape to decay
InsertPoints  numpnts(AbsPoudre), 50, AbsPoudre,
AbsX,AbsY,AbsZ,FluoPoudre,FluoX,FluoY,FluoZ
```

```
SetScale/P x, DimOffset(DensiteSpectrale, 0)-
50*deltax(DensiteSpectrale),deltax(DensiteSpectrale),"cm-1", AbsPoudre,
AbsX,AbsY,AbsZ,FluoPoudre,FluoX,FluoY,FluoZ
Make/O/N=401
SetScale/P x -deltax(DensiteSpectrale)*200,deltax(DensiteSpectrale),"cm-1", Spectrehomogen
```

List of Figure

List of Table

Publications and Communications

Publications

Yuanyuan Liao, Valérie Génot, Rachel Méallet-Renault, Thanh T. Vu, Jean-Frédéric Audibert, Jean-Pierre Lemaistre, Gilles Clavier, Pascal Retailleau, Robert B. Pansu, *"Spectroscopy of BODIPY in solid phase: crystal and nanoparticles."* Phys Chem Chem Phys, **2013**, *15*, 3186-3195.

Communication oral

Yuanyuan Liao, Valérie Génot, Rachel Méallet-Renault, Thanh T. Vu, Jean-Frédéric Audibert, Gilles Clavier, Robert B. Pansu. *"Spectroscopy of molecular crystals for the structural identification of nano particles."* XXV International Conference on Photochemistry - ICP 2011 (Ed.: C.-H. Tung), Pekin, China, 07 to 12 August 2011

Yuanyuan Liao, Valérie Génot, Jean-Frédéric Audibert, Robert B. Pansu. *"Spectroscopy of BODIPY solid phase: Micro-Crystal and Amorphous Nanoparticles, and Microfluidic Precipitation."* Journées de printemps du groupe Français de Photochimie, Photophysique et Photosciences (GFP2P) - Université Joseph Fourier (Amphi Nanobio), Grenoble, 30 to 31 May 2013.

Communication with posters

Yuanyuan Liao, Valérie Génot, Rachel Méallet-Renault, Thanh T. Vu, Jean-Frédérique Audibert, Gilles Clavier, Robert B. Pansu. *"Study of a new BODIPY derivative in solid state: nanoparticles and micro-crystals."* "Summer School Nanosciences Ile de France" - C'Nano Centre de competences en Nanoscience, Au Domaine du Tremblay, Paris, 19 to 24 June, 2011.

Yuanyuan Liao, Valérie Génot, Jean-Frédéric Audibert, Robert B. Pansu. *"In situ kinetics study of the formation of organic nanoparticles by fluorescence lifetime imaging microscopy (FLIM) along a microfluidic device."* Proceedings of the 3rd European Conference on Microfluidics - Microfluidics 2012 - Heidelberg, 03 to 05 December, 2012.

Yuanyuan Liao, Valérie Génot, Jean-Frédéric Audibert, Robert B. Pansu. *"In Situ Kinetics Study Of The Formation Of Organic Nanoparticles By Fluorescence Lifetime Imaging Microscopy (FLIM) Along A Microfluidic Device."* International workshop PICS 2012 - Chemometrics in time-resolved and imaging spectroscopy Instrumental measurements and data analysis, Lille France, 03 to 04 December, 2012.